Dissertation
submitted to the
Combined Faculty of Natural Sciences and Mathematics
of the Ruperto Carola University Heidelberg, Germany
for the degree of
Doctor of Natural Sciences

Presented by Mgr Ewa Sitarska
born in: Warsaw, Poland
Oral examination on 12.03.2021 Heidelberg, Germany

Deciphering the role of curvature-sensitive BAR domain proteins for cell migration

Referees: Dr. Jonas Ries

Prof. Dr. Ulrich Schwarz

Abstract

Cell motility has a critical role in a range of biological processes including development, immunity and disease. Navigation through complex and ever-changing environments often relies on the activity of actin-rich protrusions at the leading edge, also referred to as lamellipodia. Lamellipodia are known to exhibit areas of continuously rearranging membrane curvature, and their dynamics determines motion persistence. One group of proteins interesting in the context of membrane curvature are BAR domain proteins. However, whether and how these curvature-sensitive proteins contribute to leading edge dynamics and function, remains poorly understood. Here, we use neutrophils as a vertebrate model system of a highly migratory cell type. By combining RNAseq with a localization screen we identify two BAR proteins that are relevant for cell surface organization during migration: SH3BP1 and Snx33.

First, using fluorescent imaging and Atomic Force Microscopy, we show that SH3BP1 responds to changes in membrane mechanics and, vice-versa, modulates membrane tension. Using microfluidics, we further demonstrate that SH3BP1 is important for cell navigation through complex environments. Namely, its knockout displays increased cell speed and decision making during directed cell migration. Next, we used the above techniques complemented with machine learning-based segmentation for time-resolved TIRF microscopy to understand the role of Snx33. We show that motion persistence and directionality, in both freely moving and environmentally constrained cells, depends on Snx33 activity. Specifically, Snx33 has an inhibitory effect on the lamellipodia dynamics by regulating WAVE2-driven actin polymerization. Our work exposes a novel mechanism by which cells steer protrusions upon encountering obstacles that facilitates efficient migration. In summary, we discovered novel functions of the curvature-sensitive proteins SH3BP1 and Snx33 in regulating cell surface mechanics and efficiency of directed cell migration.

Zusammenfassung

Die Motilität von Zellen spielt eine entscheidende Rolle in einer Reihe von biologischen Prozessen, wie die embryonale Entwicklung, im Immunsystem und bei Erkrankungen. Die Zellfortbewegung durch komplexe und sich stetig verändernde Umgebungen hängt häufig von der Aktivität aktin-reicher Ausstülpungen an der leading edge (Vorderseite der Zelle) ab, die als Lamellipodien bezeichnet werden. Lamellipodien weisen Bereiche auf in denen sich die Membrankrümmung kontinuierlich verändert und ihre Dynamik die Bewegungspersistenz bestimmt. BAR-Domänenproteine sind eine Gruppe von Proteinen, die im Zusammenhang mit der Membrankrümmung von Interesse sind. Ob und wie diese krümmungssensitiven Proteine zur Dynamik und Funktion der leading edge beitragen, ist jedoch aktuell wenig erforscht. In dieser Arbeit wurden Neutrophile als Wirbeltiermodellsystem eines sehr beweglichen Zelltyps verwendet. Durch die Kombination von RNAseq mit einem Lokalisierungsscreening wurden zwei BAR-Proteine identifiziert, die für die struktuelle Organisation der Zelloberfläche während der Zellmigration relevant sind: SH3BP1 und Snx33.

Zunächst wurde mithilfe von Fluoreszenzmikroskopie und Rasterkraftmikroskopie gezeigt, dass SH3BP1 auf Veränderungen in der Membranmechanik reagiert und umgekehrt die Membranspannung moduliert. Außerdem konnte mithilfe von Mikrofluidik nachgewiesen werden, dass SH3BP1 für die Zellnavigation in komplexen Umgebungen wichtig ist, da durch den Knockout des Proteins eine erhöhte Zellgeschwindigkeit und beschleunigte Entscheidungsfindung während der gerichteten Zellmigration gemessen werden konnte. Als nächstes wurden die obigen Techniken durch Maschine learning basierender Segmentierung zeitaufgelöster TIRF-Mikroskopiedaten ergänzt, um die Rolle von Snx33 zu verstehen. Es konnte gezeigt werden, dass die Bewegungspersistenz und -richtung sowohl in frei beweglichen als auch in bewegungs-eingeschränkten Zellen von der Snx33-Aktivität abhängt. Insbesondere hat Snx33 eine hemmende Wirkung auf die Lamellipodiendynamik, indem es die WAVE2-gesteuerte Aktinpolymerisation reguliert. Diese Arbeit enthüllt einen neuartigen Mechanismus, mit dem Zellen die Bildung von Ausstülpungen steuern, um auf Hindernisse zu reagieren und eine effiziente Migration zu ermöglichen. Zusammenfassend wurden neue Funktionen der krümmungssensitiven Proteine SH3BP1 und Snx33 in der Regulierung der Zelloberflächenmechanik und der Effizienz der gerichteten Zellmigration entdeckt.

Acknowledgements

I am filled with a lot of gratitude for all the contributions from the people who I worked and spent time with during the preparation of this thesis, and I would like to take the chance to say how thankful I am!

I would like to thank Alba, my supervisor, for giving me this great opportunity to embark on my PhD journey and study such a fascinating topic. Thank you for all your support. The many interactions and discussions we had, certainly shaped my view on science and I am very glad that I had the possibility to be a part of your lab from the very beginning!

Many thanks to my Thesis Advisory Committee, Dr. Alba Diz-Muñoz, Prof. Dr. Paul Heppenstall, Dr. Jonas Ries, Prof. Dr. Ulrich Schwarz and Prof. Dr. Michael Sixt who helped to steer the project during exciting discussions.

I must thank my lab members, especially Martin for sharing his expertise and for his kind help, and Silvia, with who we spent a lot of time together brainstorming and analyzing, both in person and virtually, during the last year.

I had a great privilege to learn from and discuss with several people within the EMBL community. Thank you Malte, Diana, Neda and Bea; Faba, Sabine and Stefan; Tischi; Vladimir; Charles and Jelle; Andrea and Moritz; Lucas and Marek; I appreciate a lot all the time spent together and your help as well as many scientific insights and a great atmosphere. Also, many thanks to all the other people who contributed to the development of this thesis in many different ways!

I would like to thank a lot Julian for the great and intense time during our collaboration and Brian for insightful discussions.

I want to give many thanks to my friends for all the moments spent together along this way.

I am very grateful for all the support from my Mom, Dad and brother, who are always there for me, and over all these years, keep inspiring me in many ways.

I am filled with incredible gratitude for the never-ending support and enthusiasm that kept me afloat. Thank you, Kuba, for all, as much long as exciting days in the lab, countless coffee walks and simply being a great partner during this PhD journey!

Contents

List of Abbreviations

ADAM	**A D**isintegrin **A**nd **M**etalloproteinase
AFM	**A**tomic **F**orce **M**icroscopy
BFP	**B**lue **F**luorescent **P**rotein
BSA	**B**ovine **S**erum **A**lbumin
ChoF	**C**hannel **o**f **I**nterest
CIP4	**C**dc **I**interacting **P**rotein **4**
ddH_20	**d**ouble **d**istilled H_20
dHL-60	**d**ifferentiated **HL-60**
dPBS	**d**ulbecco's **P**hosphate **B**uffered **S**aline
DTT	1,4-**D**i**T**hio**T**hreitol
ECM	**E**xtra**C**ellular**M**atrix
EDTA	**E**thylene**D**iamine**T**etraacetic**A**cid
Ena/VASP	**Ena/VA**sodilator **S**timulated **P**hosphoprotein protein family
ER	**E**ndoplasmatic **R**eticulum
ERM	**E**zrin **R**adixin **M**oesin
F-actin	**F**ilamentous **-actin**
FBS	**F**etal **B**ovine **S**erum
FEME	**F**ast **E**ndophilin-**M**ediated **E**ndocytosis
FOV	**F**ield **O**f **V**iew
fMLP	N-**f**ormyl **M**ethionine-**L**eucyl-**P**henylalanine
GAP	**G**TPase **A**ctivating **P**rotein
GDI	**G**uanine nucleotide **D**issociation **I**nhibitor
gDNA	**g**enomic **DNA**
GEF	**G**uanine nucleotide-**E**xchange **F**actor
GFP	**G**reen **F**luorescent **P**rotein
gRNA	**g**uide **RNA**
IRSp53	**I**nsulin **R**eceptor **S**ubstrate **p**rotein of **53** kD
KO	**K**nock**O**ut
LB	**L**uria-**B**ertani Broth
MCA	**M**embrane-to-**C**ortex **A**ttachments
mCherry	**mCherry** fluorescent protein
MIM	**M**issing **I**n **M**etastasis
MTOC	**M**icro**T**ubules **O**rganizing **C**enter
mTORC2	**m**ammalian **T**arget of **R**apamycin **C**omplex **2**
PCA	**P**rincipal **C**omponent **A**nalysis
PCC	**P**earson **C**orrelation **C**oefficient
PCR	**P**olymerase **C**hain **R**eaction
PDMS	**P**oly**D**i**M**ethyl**S**iloxane
PH	**P**leckstrin **H**omology
PIP_2	**P**hosphatidyl**i**nositol-(4,5)-bis**p**hosphate
PIP_3	**P**hosphatidyl**i**nositol-(3,4,5)-tris**p**hosphate
PM	**P**lasma **M**embrane
PTEN	**P**hosphatase and **TEN**sin homologue

PX	**P**ho**x** homology
Rho	**R**as **ho**mologues
RT	**R**oom **T**emperature
SB	**S**cale **B**ar
SEM	**S**canning **E**lectron **M**icroscopy
SEM	**S**tandard **E**rror of the **M**ean
SDS	**S**odium **D**odecyl **S**ulfate
SH3	**S**RC **H**omology **3**
SH3PB1	**S**RC **H**omology **3** **B**inding **P**rotein **1**
SOCE	**S**tore-**O**perated **C**a^{2+} **E**ntry
SR	**S**arcoplasmic **R**eticulum
srGAP	**S**LIT-**R**OBO Rho **G**TPase **A**ctivating **P**rotein
TBST	**T**ris **B**uffered **S**aline with **T**ween 20 Detergent
TIRFM	**T**otal **I**nternal **R**eflection **F**luorescence **M**icroscopy
TRITC	**T**etramethyl**R**hodamineB**I**so**T**hio**C**yanate
WASP	**W**iskott-**A**ldrich **S**yndrome **P**rotein
WAVE	**WA**SP-family **VE**rprolin-homologous protein
WB	**W**estern **B**lot
VCA	**V**erprolin **C**entral **A**cidic

For my parents

Part I

Introduction

Chapter 1

Introduction

1.1 Physical forces in biology

The concept of physical forces shaping the behaviour and processes at the organism, tissue, cell and molecule level has gained considerable interest in recent years. Mechanical stimuli can be transduced into function-relevant biochemical signaling to coordinate the most crucial functions during development (Vining and Mooney, 2017), tissue morphogenesis (Heisenberg and Bellaïche, 2013), stem cell lineage specification (Engler et al., 2006), immune response (Huse, 2017), collective and single-cell migration (Ladoux and Mège, 2017; Saha, Nagy, and Weiner, 2018; Van Helvert, Storm, and Friedl, 2018) as well as disease (Jain, Martin, and Stylianopoulos, 2014) and many more (Figure 1.1). Organs, tissues and cells both exert forces on their surroundings as well as sense and respond to mechanical forces and material properties in their environment such as surface tension in a developing embryo, cytoskeletal muscle contraction, flow-induced shear stresses in blood vessels and pressure arising from substrate stiffness.

Over the years, several molecules have been identified as crucial for mechanotransduction. For example, proteins in the Hippo pathway read the extracellular matrix rigidity and regulate YAP/TAZ to drive transcriptional programs (Low et al., 2014). Additionally, mechanosensitive ion channels (e.g Piezo1/2) sense stretching in the plasma membrane and by switching protein conformations regulate a plethora of processes from osmosis in plants to blood flow in mammalian cells (Ridone, Vassalli, and Martinac, 2019).

Recognition of several molecular components that can either sense of exert mechanical forces would not be possible without the considerable advancement of the available toolkit to study them. Various techniques have been developed to quantify the forces that cells exert on their surroundings including traction force microscopy, micropillars and FRET sensors (Roca-Cusachs, Conte, and Trepat, 2017). To complement them, several methods arose to measure mechanical properties of cells or tissues, such as Atomic Force Microscopy (Müller and Dufrêne, 2011), micropipette aspiration (Hochmuth, 2000) or more recently Brillouin microscopy (Prevedel et al., 2019).

Despite the efforts towards understanding the complexity of mechanochemical feedback driving changes in cells and tissues at several timescales (ranging from days in developmental processes to below seconds at rupture of integrin-ECM bonds) many aspects of how mechanical forces coordinate cell behaviour remain unknown. Over the past years, the cell surface became the tip of the iceberg. Being the physical barrier between the outside and inside of the cell, it creates a very dynamic interface for integration of biochemical signaling (Jarsch, Daste, and Gallop, 2016; Keren, 2011) that can inform cell behaviour through its mechanical properties (Houk et al., 2012; Charest and Firtel, 2006; Goehring and Grill, 2013).

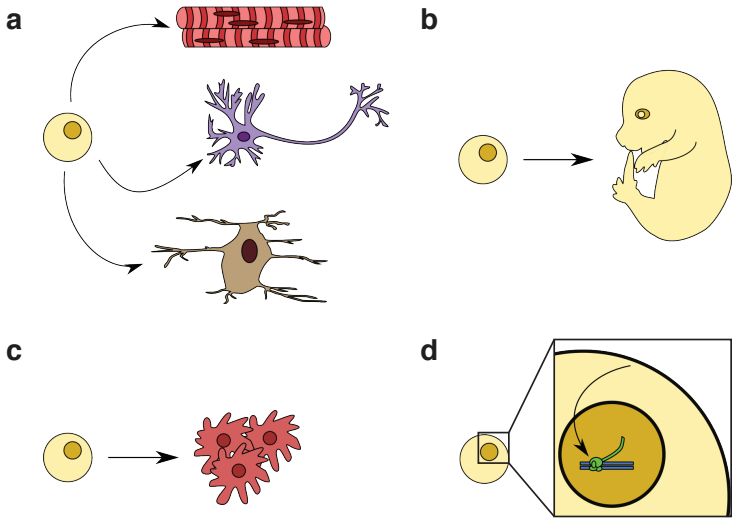

FIGURE 1.1: Mechanical forces shape biological processes. Mechanical forces are key for several processes: a. stem cells lineage specification b. morphogenesis c. control of tumour malignancy and d. regulation of transcriptional programs.

1.2 Cell surface as a mechanosensing platform

1.2.1 Components of the cell surface

The cell surface in eukaryotic cells is a very unique and perplexing physical system that encompasses the plasma membrane (which is a lipid bilayer with transmembrane and membrane-bound proteins and glycoproteins) as well as the underlying actomyosin cortical cytoskeleton (Figure 1.2, Sitarska and Diz-Muñoz, 2020) The underlying cytoskeleton is coupled to the plasma membrane by membrane-to-cortex attachment proteins (MCA) such as ERM (Ezrin, Radixin and Moesin) that have binding sites for both the F-actin domain and for lipids or proteins embedded in the membrane (Fehon, McClatchey, and Bretscher, 2010). Present in most animal cells, the cytoskeletal cortex lying underneath the plasma membrane is a thin, but dense actomyosin meshwork including a milieu of proteins (such as myosin motors) interconnected by the network of spectrins, vinculins, septins and intermediate filaments (Chugh and Paluch, 2018; Diz-Muñoz, Weiner, and Fletcher, 2018; Bridges and Gladfelter, 2015). Cell surface organization and composition of particular proteins differs not only between cell types or subcellular locations, but also over time providing a dynamic platform that can be tailored to a specific function. For example, the cell cortex appears to be uniform during mitosis when cells are round, but in spread or polarized cells reveals substantial heterogeneity (Svitkina, 2020).

A variety of cell surface components have been implicated in sensation or transduction of mechanical stimuli. In turn, improper organization of cell surface may lead to function deficiencies in cells as well as to diseases in organisms. Every component of the cell surface is unique and responsible for fulfilling several functions. To name some examples, ERM proteins in lymphocytes have an important role in

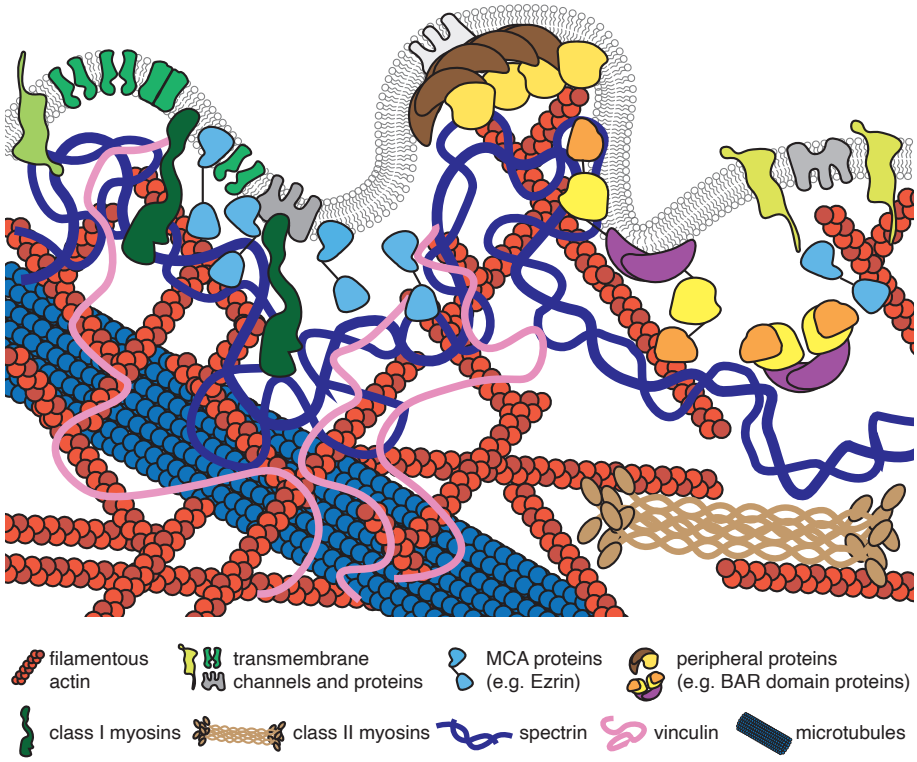

FIGURE 1.2: Cell surface as a mechanosensing platform. Cell surface comprises the plasma membrane with its transmembrane and peripheral proteins, sugars and underlying cytoskeleton. Several components of the cell surface are highlighted in the legend. Components are not to scale. For simplicity sugars are not included.

the regulation of migration and transmigration critical for immune system homeostasis (Liu et al., 2012). Class I myosins enable efficient organization of adhesion and phagocytosis of pathogens and cellular debris (Barger et al., 2019). Vinculins residing at the adhesion sites are force-dependent and thus, influence cell migration (Grashoff et al., 2010; Spanjaard and Rooij, 2013). Interactions of Myosin-II with the spectrin network generate contractile forces that control deformability and shape of red blood cells to enable their circulation in the blood (Smith et al., 2018). Actin-spectrin cytoskeleton is essential for mechanical resilience during capillary flow in red blood cells and touch sensation in neurons (Bennett and Baines, 2001; Krieg, Dunn, and Goodman, 2014). Moreover, cell surface glyocoproteins can sense the mechanical properties of the environment to drive cell motility (Razinia et al., 2017). Not to mention the growing evidence for the important role of transmembrane mechanosensitive channels such as Piezo1/2, that are responding to mechanical forces and their dysfunction may cause a variety of pathological states (Ridone, Vassalli, and Martinac, 2019). Above-mentioned examples highlight the importance of every individual component of the cell surface and their complex interplay in the processes involving responding to mechanical forces. But, the questions remain, how exactly cell surface proteins and their networks are involved in mechanotransduction? What physical properties can be sensed by various components of the cell surface?

1.2.2 Mechanical and physical properties of the cell surface

Cell surface mechanics encompasses mechanical properties of its individual components that give rise to more complex entities such as cell surface tension. Dissecting the individual components: the plasma membrane can be described by in-plane membrane tension and bending rigidity, membrane-to-cortex-attachments have a particular adhesion energy and the cytoskeletal cortex can be characterized by cortical tension and elasticity (Figure 1.3; Diz-Muñoz, Weiner, and Fletcher, 2018). In the following section the particular mechanical properties and their interplay will be discussed.

As a lipid bilayer, plasma membrane can resist deformations such as bending or stretching. Bending rigidity is a measure of the energy required to bend the membrane, usually expressed in kBT or Nm. Experimentally, bending rigidity has been measured in lipid vesicles. Reports infer that it can depend on several parameters including temperature, types of lipids, proteins, sugars and salts (Dimova, 2014). Nevertheless, measurements of bending rigidity in more complex systems remain challenging. For example, it has been approximated to be in the order of 10^{-19} Nm for membranes of red blood cells (Bo and Waugh, 1989; Diz-Muñoz, Fletcher, and Weiner, 2013).

Membrane tension is a measure of the energetic cost of increasing the membrane area and can be measured in $J/m^2 = N/m$. Originally, membrane tension was studied in lipid vesicles, where the force needed to expand the surface area was described as in-plane membrane tension. In vesicles, that have the properties of a 2D liquid, rapid diffusion allows the global propagation of the membrane tension across the membrane. Here, the only external force inducing tension is the pressure across the membrane. This pressure arises from the opposing hydrostatic and osmotic pressures (Gauthier, Masters, and Sheetz, 2012; Diz-Muñoz, Fletcher, and Weiner, 2013). In cells, however, plasma membrane tension also has contributions from its attachments to the underlying cytoskeleton (MCA), peripheral protein binding, and the presence of transmembrane proteins. All of these factors provide additional resistance to membrane area changes (Sitarska and Diz-Muñoz, 2020). Therefore, surface membrane tension is commonly defined as a sum of both in-plane tension (T_m) and MCA (T_{MCA}) (Diz-Muñoz, Fletcher, and Weiner, 2013).

While membrane tension propagation in pure lipid systems is well described, it has been recently questioned whether membrane tension can rapidly travel across the plasma membrane of cells and result in subsequent changes in cell behaviour or can only induce local perturbations (Shi et al., 2018; Cohen and Shi, 2020). Several studies imply that membrane tension could account for long-range signal propagation (Houk et al., 2012; Diz-Muñoz et al., 2016a; Mueller et al., 2017; Graziano et al., 2019; Tsai et al., 2019). For example, micropipette aspiration at the cell rear of fast migrating neutrophils and keratocytes induces changes in the leading edge formation and dynamics (Houk et al., 2012; Mueller et al., 2017). On the other hand, measurements of mechanical coupling between two membrane tethers pulled 5-15 μm apart showed no long-range propagation in a variety of cell types for over 10 minutes (Shi et al., 2018). Explanations of these seemingly opposing results may be possibly found in the diversity of the underlying cytoskeleton structure or membrane deformations that are cell-type dependent, as they can influence diffusion of other molecular components at the plasma membrane. Additionally, it is important to consider the various migration modes and speeds. Cell types whose behaviour is consistent with fast propagation of membrane tension are also the ones displaying the highest velocities in the human body. Several explanations for this intriguing

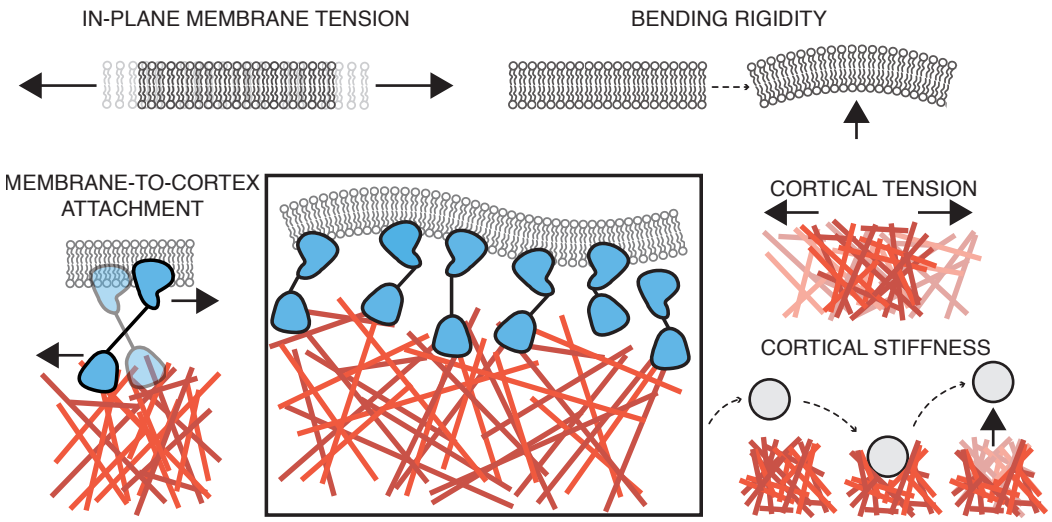

Adapted from Sitarska and Diz-Muñoz, 2020

FIGURE 1.3: Mechanical properties of the cell surface. Cell surface comprises several mechanical properties including in-plane membrane tension, bending rigidity, adhesion of membrane-to-cortex-attachments, cortical stiffness and cortical tension. Components are not to scale. For simplicity membrane binding proteins other than MCA are not included. See Figure 1.2 for completion.

case can be formulated and they require further careful studies. This example highlights only one out of many unanswered questions about cell surface mechanics.

Physical properties of the actin cortex that closely interacts with the plasma membrane include stiffness and cortical tension (Salbreux, Charras, and Paluch, 2012; Diz-Muñoz, Weiner, and Fletcher, 2018). Cortical tension is the force per unit length of the cortex fragment, typically expressed in N/m. It is induced by stresses generated in the contractile network build from myosin and actin filaments acting as semiflexible polymers and it gives rise to cell surface tension (Kruse et al., 2005; Chugh and Paluch, 2018). Cortex stiffness is an apparent elastic response to the deformation of the contractile tension of the cortex that depends on cortical tension, the elastic modulus of the cortex and cell geometry (Salbreux, Charras, and Paluch, 2012). Thus, actin cortex comprises, both, contributions from active stresses coming predominantly from motors activity as well as a passive contribution arising from its viscoelastic response to flow or deformation (Chugh and Paluch, 2018).

1.2.3 Probing and perturbing the cell surface mechanics

It is often challenging to measure directly mechanical properties of particular components of the cell surface and their combinations. However, several indirect ways of determining those mechanical properties were developed. Usually, a combination of direct measurements and mathematical modelling with certain assumptions is applied to dissect the contributions of individual components to cell surface mechanics (Diz-Muñoz, Weiner, and Fletcher, 2018; Chugh and Paluch, 2018).

Current methods used to quantify plasma membrane tension include tether pulling by Atomic Force Microscopy (AFM) cantilevers (Figure 1.4a; Methods 7.19), optical or magnetic tweezers. Tethers are small membrane tubes extracted from the plasma membrane that lack a continuous cytoskeleton. Membrane tension (T) can then be

obtained from the tether force (F_0) and bending rigidity (B) using the following equation:

$$T = \frac{F_0^2}{8B\pi^2} \tag{1.1}$$

where F_0 is the tether force measured by AFM and B is the bending rigidity of the plasma membrane. For measurements in cells we assume that the bending rigidity of the membrane is invariable as we are not able to measure it directly. An estimation of bending rigidity can be obtained through several methods, based on the use of thermal fluctuations, micropipettes, optical tweezers, magnetic and electric fields, among others (Dimova, 2014). The value of bending rigidity in cells was estimated to be 2.7x$10^{-19} Nm$ as it remains challenging to measure the bending rigidity in other systems than *in vitro* (Hochmuth et al., 1996). From these, it was estimated that the membrane tension ranges from 3x10^{-6} N/m to 276x10^{-6} N/m and that the values tend to increase with the speed of cells (Sens and Plastino, 2015; Sitarska and Diz-Muñoz, 2020).

In cells, the measured by AFM static tether force encompasses contributions from in-plane membrane tension and MCA, as discussed previously (Section 1.2.2). Estimation of the MCA effect on membrane tension relies on dynamic tether pulling experiments in which, under certain assumptions, in-plane membrane tension remains constant, but MCA scales with the increasing speed of tether pulling (Figure 1.4b). Different models allow interpretation of these results (Methods 7.30; Hochmuth et al., 1996; Brochard-Wyart et al., 2006).

Cortical tension can be estimated, under certain assumptions, by several techniques including: measuring the pressure needed to aspirate a cell into a micropipette (Evans and Yeung, 1989), the force required to compress the cell between two plates (Yoneda and Dan, 1972), from the cell deformation and the resulting measurement of stiffness (Krieg et al., 2008) as well as from monitoring cortex opening following laser ablation (Mayer, Salbreux, and Grill, 2012).

1.3 Cellular processes controlled by cell surface mechanics

Research in recent decades has established the importance of cell surface mechanics as a physical regulator of several cellular processes. For example, plasma membrane tension was shown to play a key role in cell migration (Diz-Muñoz et al., 2016b; Shah and Keren, 2013) by affecting cell polarity (Tsujita, Takenawa, and Itoh, 2015), cell spreading (Gauthier, Masters, and Sheetz, 2012; Raucher and Sheetz, 2000), leading edge formation (Houk et al., 2012; Diz-Muñoz et al., 2016a), actin polymerization streamlining (Batchelder et al., 2011) as well as other processes such as exocytosis, endocytosis (Boulant et al., 2011; Apodaca, 2002; Dai, Ting-Beall, and Sheetz, 1997) and phagocytosis (Masters et al., 2013).

In turn, cortex contractility drives processes involving cell shape changes such as cell rounding during mitosis (Stewart et al., 2011; Kelkar, Bohec, and Charras, 2020) or migration mode switching (Ruprecht et al., 2015). While cell surface mechanics controls a plethora of cell functions, it is undoubtedly a key player for cell migration as this process requires constant shape control, rapid feedback mechanisms and continuous information processing. Mechanical responses of the plasma membrane and the underlying cytoskeleton that are considerably faster than diffusion of molecules could in principle provide a platform for cellular organization during cell migration.

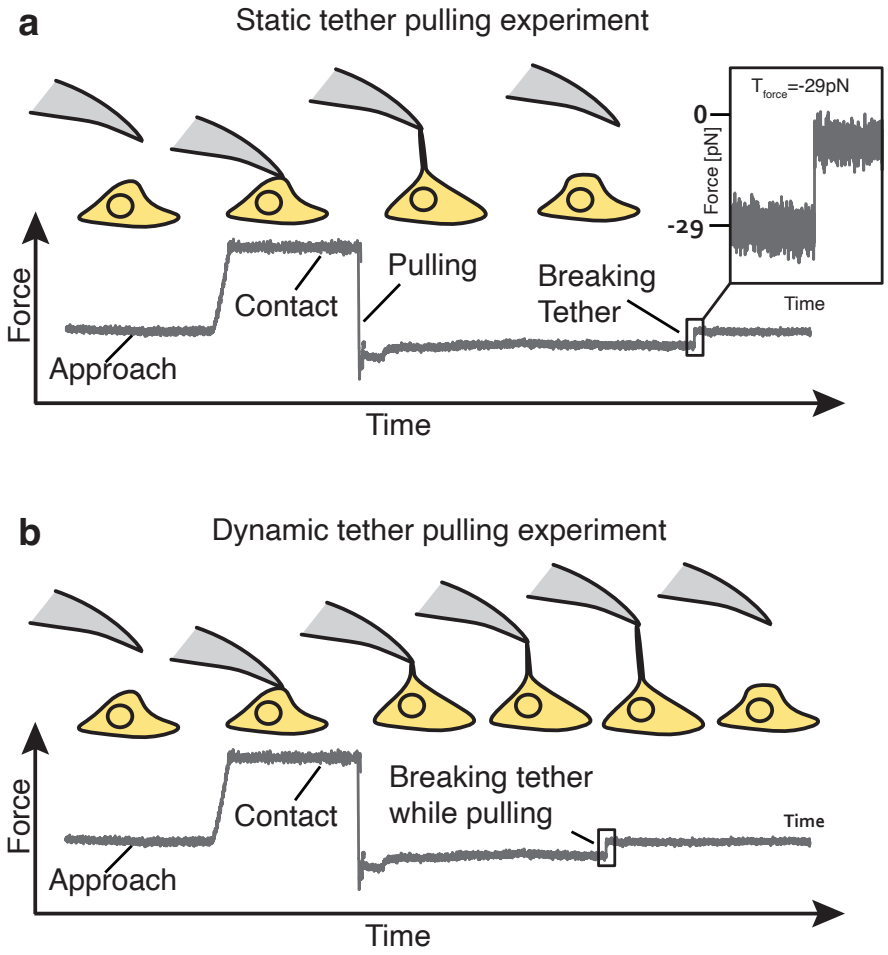

FIGURE 1.4: Membrane tension measurements by Atomic Force Microscopy. a. Static tether pulling experiment in which a membrane tether is pulled and held at a constant length. Once a tether breaks, the difference between the force experienced by a cantilever is defined as the tether force. b. Dynamic tether pulling experiment relies on pulling a membrane tether and measuring the force required to extrude it at variable speeds. Contribution of MCA scales with the speed of tether pulling while T_m remains constant.

1.4 Cell migration

Cell migration is central to a variety of key physiological processes such as development, immune response, wound healing as well as during cancer dissemination. For these to be performed efficiently cells need to respond to a mixture of extracellular cues that may be of biochemical, mechanical or topographical nature, among others. Moreover, cells need to navigate efficiently through a very complex environment that may impose fundamental challenges and require them to dramatically change shape to overcome these difficulties (Yamada and Sixt, 2019). Thus, cell migration is a very finely-tuned process (both from a molecular and physical point of view) in which a complex mixture of information is processed by a cell to adapt and perform its function. To succeed, cells have evolved a variety of strategies enabling them to navigate through intricate and ever-changing surroundings.

Morphological changes are an intrinsic characteristic of cell migration. A key hypothesis for cell migration states that the cell body translocates by adding molecular material to the cell front and inducing a molecular flow. This flow, by coupling to the substrate, generates force to move the cell body forward (Abercrombie et al., 1970). From this, a canonical description of migration was developed that relies on driving cell locomotion by transmission of forces through the dynamics of the actin cytoskeleton (Ridley et al., 2003; Svitkina, 2020). In this view, the molecular machinery of the actin cytoskeleton is providing the force to extend cellular protrusions that adhere to the substrate and in this way induces flow that allows for a rear retraction. This mode of migration was identified based on cell migrating on flat substrates. However, studying cell migration in three dimensional environments uncovered a plethora of different protrusion types and migration modes (Yamada and Sixt, 2019; Kameritsch and Renkawitz, 2020; Bodor et al., 2020).

1.4.1 Modes of cell migration

Early studies of cell migration characterized two fundamental migration modes: mesenchymal and amoeboidal (Figure 1.5a-b). The mesenchymal mode that was most profoundly studied on flat surfaces, is characteristic of fibroblasts, keratinocytes and endothelial cells, among others. In this mode cells perform the three step canonical rhythm: extend their protrusions, adhere to the substrate and retract their rear. The mesenchymal mode is characterized by lower cell velocities ($\sim$ 0.1-0.5 μm/min), spread-out cell morphology and dependence on adhesion that relies not only on actin, but also such proteins as talins and integrins. Consequently, a high contact angle between cell body and adherent substrate is achieved.

In contrast, the amoeboidal mode, is commonly used by leukocytes, including T-cells, neutrophils and dendritic cells as well as cells in developing embryos (Yumura, Mori, and Fukui, 1984; Friedl, Borgmann, and Bröcker, 2001; Diz-Muñoz et al., 2010). Amoebodial migration is distinguished by high velocities ($\sim$ 5-20 μm/min), rounded cell morphology, weak adhesion to the substrate, low contact angle between the cell body and the substrate, as well as dynamic cell shape changes. High velocities are achieved by coordinated action of actin-generated forces and actomyosin contractility. Interestingly, the amoeboidal mode is often observed in cells migrating under confinement or in three dimensional environments (Paluch, Aspalter, and Sixt, 2016). These two migration modes also differ in the way organelles are organised subcellularly. For example, mesenchymally migrating cells usually position their microtubule organizing center (MTOC) and other organelles in front of

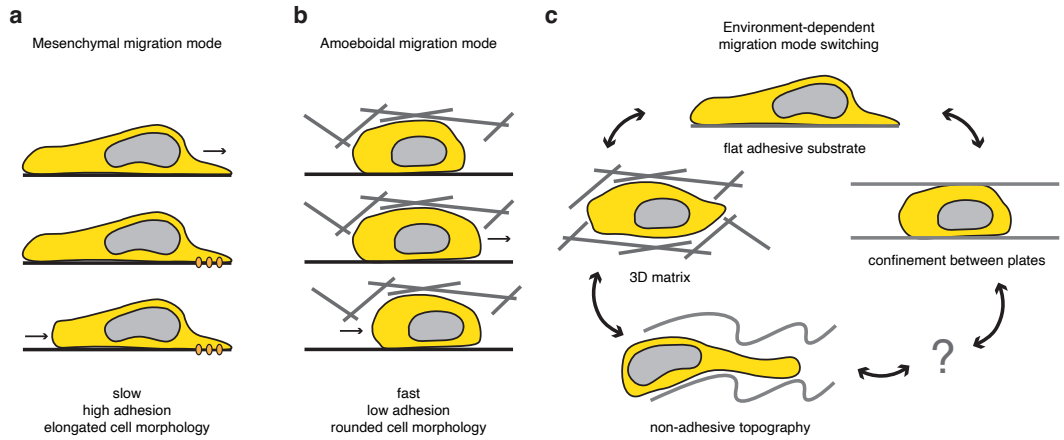

FIGURE 1.5: Modes of cell migration. Schematics of a. Mesenchymal mode. b. Amoeboidal mode. c. Environmental dependence of migration modes.

the nucleus, while amoeboidally migrating cells employ an opposite strategy. Despite a multitude of differences, the mesenchymal and amoeboidal modes are not mutually exclusive. Several cell types can switch from one to the other, depending on circumstances. For example, neutrophils migrate rather in a mesenchymal style when plated on adhesive substrates, but switch to the amoeboid-like manner under confinement (Yip, Chiam, and Matsudaira, 2015).

For a long time, migration was considered to rely strongly on cell adhesion to the substrate. However, many studies showed that different cell types are still motile even in the absence of molecules key for cell adhesion (e.g. talins and integrins) or on non-adhesive substrates (Bergert et al., 2015; Liu et al., 2015b; Ruprecht et al., 2015). More recently, studies showed that even without any coupling to the substrate leukocytes under confinement are able to translocate their bodies using solely topographical features of the substrate (Reversat et al., 2020). These observations were corroborated by the discovery of a variety of non-canonical migration modes observed in three dimensional environment such as gels or *in vivo* (Yamada and Sixt, 2019; Kameritsch and Renkawitz, 2020). For example, recently a hybrid amoeboidal-mesenchymal migration mode was described. In this mode an asymmetric response to hydrostatic pressure allows for the generation of protrusion called lobopodia that drives cellular translocation. Cells that employ this mode need to be strongly attached to the substrate and exert forces on the extracellular matrix, while the nucleus generates anterior pressure by its piston-like movement (Petrie et al., 2012; Petrie and Yamada, 2012).

The increase of the scope of cellular environment under study during the recent years allowed the characterization of new migration modes that strongly depend on the context and available molecular machinery (Yamada and Sixt, 2019). These recent discoveries suggest that we still do not fully understand the key principles of cell motility. Fast migrating cells such as leukocytes were shown to employ a plethora of migration modes depending on biochemical, physical and topographical conditions. Thus, they become perfect candidates for studying the complex mechanisms of adaptation to the environment by migration mode changing (Figure 1.5c).

1.4.2 Types of cell protrusions in migration

Distinct migration modes can be also described in the context of predominant cellular protrusions that are extended in the direction of movement. Cellular protrusions are highly dynamic cytoskeletal-driven structures that are essential for cell migration. They are created by an interplay between different components and forces present at the cell surface. The most well known and studied protrusion is a sheet-like, actin-rich flat protrusion called lamellipodia ($\sim$ 200 nm thick) (Abercrombie et al., 1970). Cultured cells, such as fibroblasts, keratocytes and immune cells extensively generate this type of protrusion on a flat adhesive surfaces.

Another type of protrusions formed during cell migration are blebs (Charras and Paluch, 2008). Blebs are spherical protrusions ($\sim$5 μm in diameter) created by membrane detachment from actin cytoskeleton that are powered by hydrostatic pressure (Paluch and Raz, 2013). Formation of blebs is affected by the levels of myosin contractility and MCA proteins as well as their distribution in cells (Rossy et al., 2007; Diz-Muñoz et al., 2010; Lorentzen et al., 2011; Goudarzi et al., 2012). Zebrafish primordial germ cells perform cell migration with the exclusive use of blebs (Blaser et al., 2006), while other cell types such as neutrophils and keratocytes use lamellipodia (Svitkina et al., 1997). Interestingly, neutrophils devoid of molecular machinery (Arp2/3 complex) required for lamellipodia formation can migrate using bleb-based protrusions provided that they are under confinement (Graziano et al., 2019). Several other cell types, including cancer cell and cells migrating during early development, use both lamellipodia and blebs (Paluch and Raz, 2013).

Lamellipodia are often accompanied by the formation of another protrusion type, namely filopodia. Filopodia are finger-like, actin-rich protrusions ($\sim$200 nm in diameter) that can extend up to 30 μm. Both lamellipodia and filopodia were shown to serve as environmental sensors and to facilitate directional choices (Leithner et al., 2016). Moreover, filopodia were implicated in promoting cell migration *in vivo* during angiogenesis, wound closure and cancer cell extravasation (Wood et al., 2002; Shibue et al., 2012; Wakayama et al., 2015) as well as allowing cell-cell contacts in epithelial and neuronal tissues (Mattila and Lappalainen, 2008).

Lobopodia are a recently described type of cellular protrusions present in the mode of migration lying in-between amoeboidal and mesenchymal. These cylindrical and blunt protrusions at the cell front are formed due to a polarized response to intracellular hydrostatic pressure causing outward deformation of the plasma membrane (Petrie and Yamada, 2012; Yamada and Sixt, 2019). One of the key differences between lamellipodia and lobopodia is a high pressure in the latter, predominantly arising from a dense or highly cross-linked environment and can be employed by primary fibroblasts (Petrie et al., 2012). Because of being pressure-driven, lobopodia resemble rather blebs than lamellipodia from a mechanical point of view.

In a complex environment cellular protrusions are often referred to as pseudopods. Pseudopods are an arm-like protrusions at the leading edge of migrating cancer cells, leukocytes or amoeboidal cells (Li et al., 2011; Fritz-Laylin et al., 2017). Their formation relies on a similar actin-based molecular machinery to lamellipodia, but their morphology is less defined than lamellipodial or filopodial. All the cellular protrusions have one very characteristic feature. Namely, they are created on one side of the cell, breaking its symmetry and creating cell polarity.

1.4.3 Regulation of polarity in migrating cells

Cell polarity emerges from a nonuniform distribution of cell contents from which arises a variety of cell shapes and functions. Motility is a cell function that originates from a front-rear polarity and enables movement in a desired direction e.g. towards an attractant (Woodham and Machesky, 2014). During cell migration a polarized distribution of cell organelles (e.g. nucleus, MTOC), actin cytoskeleton components and its regulatory proteins as well as lipids, surface receptors and adhesion proteins at the plasma membrane can be observed (Ridley et al., 2003). As cell migration exhibits a variety of modes, it requires a certain plasticity of the intracellular organization induced upon cellular response to extrinsic and intrinsic factors. How is this plasticity achieved in a cellular context?

For establishment of polarity a group of small GTPases of the Ras protein superfamily is crucial. They function as molecular switches that can turn on or off several signaling pathways in particular subcellular locations. Within this group of molecules, the Rho (Ras homologues) family proteins, including Cdc42, Rac1 and RhoA, are of particular interest for cell migration, because they regulate and coordinate cytoskeletal remodeling. As molecular switches, Rho family proteins can be found in an active GTP-bound or inactive GDP-bound state. Regulation of Rho proteins is mainly driven through activation by guanine nucleotide-exchange factors (GEFs), deactivation by GTPase-activating proteins (GAPs) or blocking the GTPase cycle by sequestration of GDP-bound form by guanine nucleotide dissociation inhibitors (GDIs). Rho proteins are key for polarity establishment as a high number of their regulators and effectors play substantial roles in cytoskeletal organization. In a simplistic view of the biochemical regulation of cell migration, Rac1 and Cdc42 induce protrusion and adhesion-based forces that are antagonized by RhoA that controls contractility (Raftopoulou and Hall, 2004; Iden and Collard, 2008). Small GTPases can be modulated by a variety of stimuli. In migratory cells, such as Dictyostelium and neutrophils, it was demonstrated that PIP_3 is enriched at the cell front in comparison to PIP_2 (Iglesias and Devreotes, 2012). This accumulation of PIP_3 at the leading edge of migrating cells correlates with Cdc42 activation. Interestingly, a positive feedback loop between Cdc42 and a kinase, that catalyzes the production of PIP_3 from PIP_2 (PI3K), maintains high levels of both PIP_3 and Cdc42 activity. At the same time, it excludes the counteracting phosphataze PTEN (phosphatase and tensin homologue) from the cell front (Iijima and Devreotes, 2002; Funamoto et al., 2002; Raftopoulou and Hall, 2004). Similarly, a positive feedback loop was described for Rac1 and PI3K that leads to extensive lamellipodia formation and membrane ruffling (Raftopoulou and Hall, 2004; Weiner et al., 2002). Rac1 activity also encompasses the recruitment of nucleation-promoting factors such as WASP and WAVE protein families that activate Arp2/3 complex and induce branched actin polymerization (Machesky and Insall, 1998; Weiner et al., 2006).

1.4.4 Components of the actin cytoskeleton machinery in migration

The cell surface includes the underlying cytoskeleton that is a primary driver of cell shape changes and migration. During cell movement, repeated cycles of cell protrusion, attachment to the substrate and retraction are maintained by coordination of actin filaments in space and time. Actin filaments are right-handed helices built from two strands of highly abundant and conserved actin subunits. Actin filaments are polar with the two ends defined as the barbed and the pointed end, from which the barbed end is the one growing faster. A plethora of actin-binding regulatory

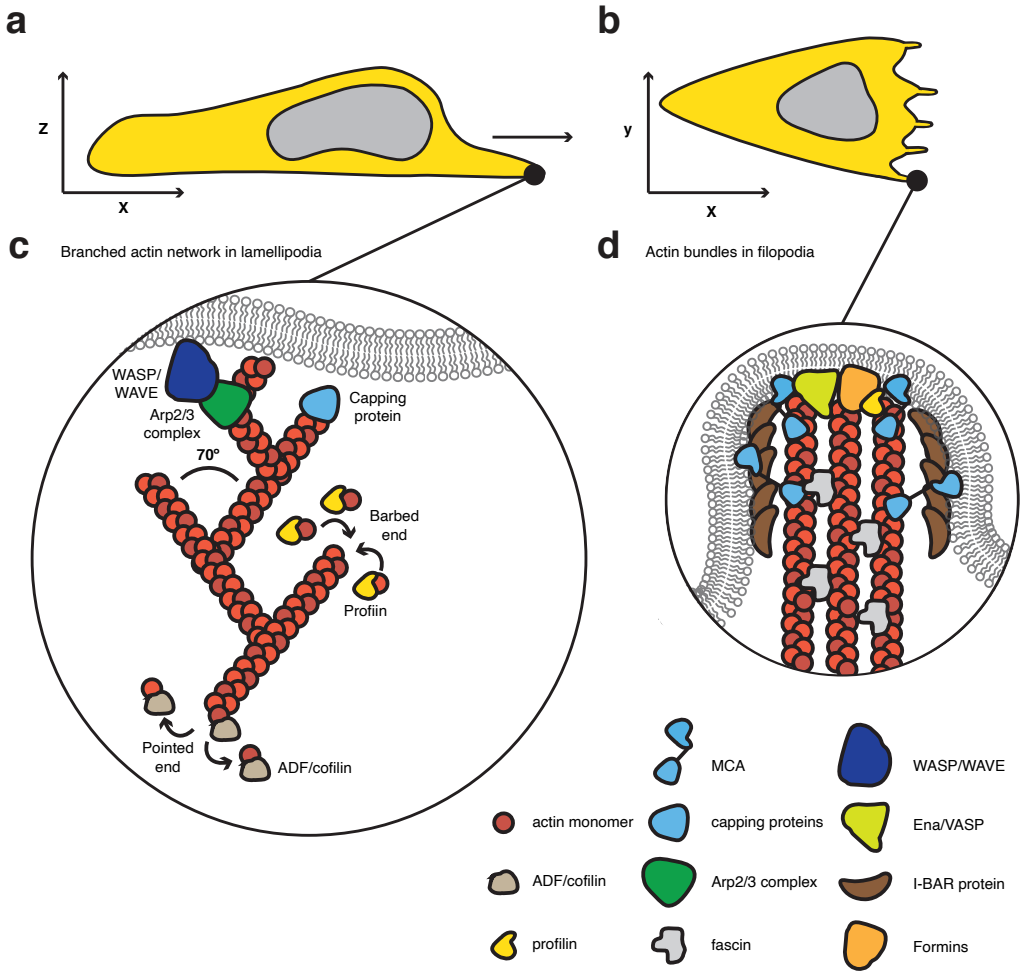

FIGURE 1.6: Actin structure in lamellipodia and filopodia. a. Schematic of a migrating cell extending a flat protrusion, also called lamellipodia in a side view and b. top view. c. Branched actin network in lamellipodia with its regulatory proteins. d. Bundled actin network in filopodia with its regulatory proteins.

proteins coordinate actin filaments nucleation, elongation and disassembly (Pollard, 2016). For example, a lot of non-polymerized actin in the cytoplasm is bound to a small protein called profilin. Interestingly, profilin binding to the barbed end of actin can sterically inhibit nucleation and elongation at the pointed end, but does not impede it at the barbed end. Formins and Ena/VASP proteins promote elongation at the barbed ends of actin filaments by recruiting these actin-profilin complexes, protecting barbed ends from capping and coupling to the plasma membrane.

The main actin structures critical for cell migration are lamellipodia, filopodia, stress fibers and adhesions (Figure 1.6a-b; Svitkina, 2020). Studies of lamellipodial architecture revealed a branched actin network created by an attachment of daughter filaments to a mother filament at an $\sim 70°$angle between their barbed ends (Figure 1.6c). This particular architecture is driven by the Arp2/3 complex. Arp2/3 is a protein complex assembled from 7 proteins, including Arp2 and Arp3 that have a strong structural similarity with actin monomers. Upon Arp2/3 binding to actin filaments, it creates a base for new branched filament growth. At the same time, the Arp2/3 complex is capping the pointed end of a daughter filament to avoid its

elongation. To act, the Arp2/3 complex needs to be activated by nucleating factors. Nucleating factors belong to a Wiskott-Aldrich syndrome protein (WASP) protein family that in mammalian cells include WASP, N-WASP, Scar/WAVE1-3. All WASP family members are intramolecularly autoinhibited and require activation by upstream factors such as Rac GTPases (Chen et al., 2010). The WASP family contains a conserved C-terminal VCA motif (for the verprolin-homology, central and acidic regions) that binds and activates Arp2/3. While WASP/N-WASP exist independently in the cytoplasm, WAVE proteins assemble with four additional proteins (Sra1/Cyfip1, Nap1/Hem-2, Abi and HSPC300) into the WAVE regulatory complex (WRC). The small molecule CK-666 is known to inhibit the Arp2/3 complex-mediated branched actin formation and has been used to investigate lamellipodial networks in a number of studies (Hetrick et al., 2013).

Apart from the Arp2/3 complex, the molecular machinery of branched actin networks consists of the capping protein and ADF/cofilin. Capping protein is a heterodimer built from two similar subunits that bind tightly to the barbed ends of actin filaments. The capping protein cooperates with profilin to limit the number of barbed ends available for growth during actin based protrusion of the leading edge. On the other hand, cofilin is one of the actin severing proteins. Cofilin binds in the barbed end groove of both actin monomers and filaments. An interesting mechanisms is employed to control the severing process. Filaments saturated with cofilin are stable, but binding of small amounts of this protein promotes severing of actin filaments. These small amounts of cofilin, when bound to newly assembled actin filaments at the cell front, increase filament dynamics. Additionally, cofilin can be also inhibited by PIP_2 binding at the plasma membrane providing an extra layer of regulation (Svitkina, 2020; Pollard, 2016).

A different class of actin structures present at the leading edge of cells are filopodia. Actin filaments in filopodia are organized into bundles with the barbed end facing the plasma membrane (Figure 1.6d). These bundles are cross-linked by fascin and attached to the plasma membrane by ERM proteins. For elongation of filopodia, formin and Ena/VASP associate with actin barbed-ends to couple it to the plasma membrane and protect from cofilin-driven depolymerization. Additionally, a membrane binding BAR domain protein IRSp53 was shown to provide a scaffold aiding in the maintenance of the tubular shape of filopodia (Mattila and Lappalainen, 2008). Other BAR domain proteins such as MIM (missing in metastasis) or srGAP2 (SLIT-ROBO Rho GTPase Activating Protein) are also recruited during early filopodia formation to deform the plasma membrane before actin polymerization (Mattila et al., 2007; Saarikangas et al., 2008; Saarikangas et al., 2009; Guerrier et al., 2009).

Actin cytoskeleton plays also a key role in cells connecting with their extracellular environment. For example, actin-rich stress fibers are attached through the plasma membrane to the ECM (extracellular matrix) via integrins. Integrins bind actin filaments inside the cell and extracellular matrix outside the cell with a range of adaptor proteins such as talin and vinculin that are mostly enriched at focal adhesions. Adhesions originally form as the leading edge advances, but are often transient and disassemble rapidly (Burridge and Guilluy, 2016). In motile cells, contractile force can rupture the adhesions and induce a local retraction of the leading edge or, in contrast, strengthen the adhesions and serve as a platform for the next round of protrusion. Usually, adhesions are strengthened at the front and ruptured towards the rear. Typical for filopodia, bundled structures of actin filaments are also present in retraction fibers of migrating cells (Svitkina et al., 1997). Stress fibers and focal adhesions are more abundant in cells in culture as compared to the ones *in vivo*, in 3D environments or on soft surfaces.

Many components of actin networks and their regulators are well described biochemically, but due to their complex interplay and cell type-dependent roles, a lot of processes are still not fully understood. Ena/VASP proteins were previously thought to act rather as negative regulators of cell motility, but a recent study showed that they inhibit lamellipodial microspikes and integrin-mediated adhesion to promote cell migration (Damiano-Guercio et al., 2020).

1.4.5 Force generation by the actin cytoskeleton

Migration, among other cellular functions, requires mechanical forces for protrusion generation and contraction (Mogilner and Oster, 1996). Actin cytoskeleton, that is to a high degree conserved among eukaryotes, is a main driver of force generation. Actin cytoskeleton generates forces by using the energy of ATP hydrolysis to produce protrusive forces by actin polymerization and contraction forces by filament cross-linking by myosin motors. In turn, these forces are transduced by adhesiveness or interaction with the environment (Mogilner and Oster, 2003). It has been proposed that differences in the balance between actin polymerization, myosin contractile forces and actin flow manifest themselves in the migration mode switching particularly in case of amoeboid locomotion (Lämmermann and Sixt, 2009). Interestingly, in immune cells such as neutrophils, dendritic and T cells protrusions were shown to be heavily actin polymerization driven, as they continue to grow upon myosin II inhibition.

1.4.6 Mechanical feedback in the actin cytoskeleton

Recent endeavours revealed the mechanical feedback in the actin cytoskeleton. In a protrusion, the branched actin network induced by Arp2/3 generates tension in the plasma membrane. This tension, was shown to regulate leading edge by acting as a direct physical barrier to prevent actin polymerization (Keren et al., 2008; Houk et al., 2012). *In vitro* reconstitutions showed that tension in the plasma membrane feeds back on the actin network properties. Specifically, mechanical loading increases the network density by changes in the number of filaments and the network architecture (Mueller et al., 2017). Building up on this, Arp2/3-induced actin branches in the lamellipodia of migrating cells that are usually at $\sim 70^{\circ}$angle, broaden the angle upon membrane tension increase. In turn, decrease of membrane tension makes the network less dense and enriches filaments that are position perpendicularly to the plasma membrane (Mueller et al., 2017). Many studies investigated how mechanical load regulates the actin network in a direct manner. Recently, an indirect mechanism of branched actin network modulation was discovered. Namely, elevated membrane tension activates the mTORC2-PLD2 pathway to inhibit WAVE2-Arp2/3-driven actin polymerization, creating a negative feedback loop (Diz-Muñoz et al., 2016a). The mechanics of the molecular machinery that activates mTORC2-PLD2 is not known, but a curvature sensitive protein that activates NWASP/WASP was shown to localize differently to plasma membrane invaginations upon changing levels of membrane tension (Tsujita, Takenawa, and Itoh, 2015). This, suggests that plasma membrane curvature could play a role in transmitting changes in mechanical properties of the membrane into biochemical signaling.

1.5 Cellular plasma membrane curvature

1.5.1 Plasma membrane curvature generation

Cell shape changes are fundamental to several cellular processes such as growth, division and migration (Paluch and Heisenberg, 2009; Bodor et al., 2020). In most types of cells, protrusions that enable locomotion, rely on global or local deformations of the cell surface. These various deformations, in turn, rely on the remodeling of the plasma membrane.

In a pure lipid system, a lipid bilayer remains flat unless the energy necessary to curve the membrane is provided (Helfrich, 1973; Helfrich and Jakobsson, 1990). The energy required to bend the plasma membrane can be provided by changes in the cell surface induced by effects of lipids, cell surface proteins or their combination. Varying lipid headgroups or acyl chain composition change lipid shapes which is an intrinsic way of inducing plasma membrane curvature. Similarly, changing lipid amounts and clustering in both leaflets gives rise to a variety of effects in the spontaneous curvature of the membrane (McMahon and Gallop, 2005; Zimmerberg and Kozlov, 2006; Jarsch, Daste, and Gallop, 2016).

Lipids, such as phosphatidylocholine and phosphatidylserine, form a flat monolayer due to their cylidrical shape. In contrast, lipids with a smaller polar headgroup than phosphatidylocholine can induce inward membrane curvature, because of their conical shape and clustering of headgroups together. The conically shaped lipids include phosphatidylethanolamine, phosphatic acid, diacylglycerol or cardiolipin. On the other side, a large headgroup in lysophosphatidylcholine or phosphatidylinositol phosphate imposes an outward membrane curvature through bending of the monolayer away from the headgroups (Zimmerberg and Kozlov, 2006). Conversely, acyl chain saturation may also induce formation of spontaneous curvature (Bigay and Antonny, 2012; Pinot et al., 2014). Thus, all changes in lipid composition, owing to their modifications, flipping across the membrane or clustering in particular compartments, induce asymmetry that contributes to membrane curvature generation (Poulsen, López-Marqués, and Palmgren, 2008; Graham and Kozlov, 2010; McMahon and Boucrot, 2015).

Plasma membrane remodeling proteins provide another way to induce membrane curvature. It can be realized by an asymmetric insertion into the lipid bilayer of amphiphatic helices or hydrophobic domains, insertion of wedge-shape transmembrane proteins, action of such proteins in coordination with additional membrane-binding domains, oligomerization or assembly of proteins. For example, acetylocholine receptors with transmembrane domains can have a conical shape or can be clustered by attachment proteins to induce membrane curvature (Figure 1.7; Unwin, 2005; McMahon and Gallop, 2005).

Indirectly, the plasma membrane can be bend by electrostatic forces induced by intrinsically curved proteins, oligomers or assemblies acting as a scaffold for the plasma membrane. Additionally, bending can be induced by non-intrinsically curved proteins that create steric constraints by protein crowding or by pushing (or pulling) forces exerted on the plasma membrane by the actin cytoskeleton (Jarsch, Daste, and Gallop, 2016).

1.5.2 Plasma membrane curvature and BAR domain proteins

One group of proteins that are known for their role in sensing and generating plasma membrane curvature are BAR domain proteins (Suetsugu, Toyooka, and Senju, 2010).

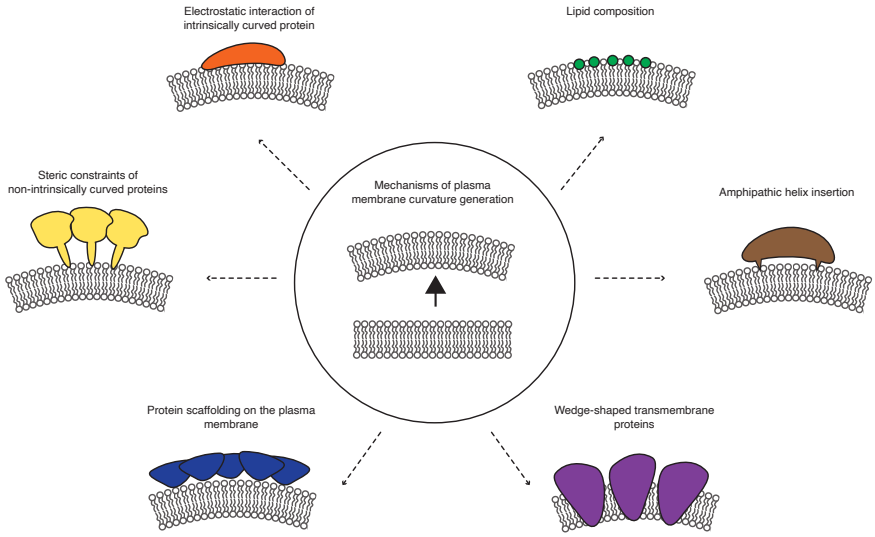

FIGURE 1.7: Mechanisms of membrane curvature generation. Several mechanisms can lead to membrane curvature generation in cells including: intrinsic changes in the plasma membrane by modifying lipid composition; direct action of proteins with amphiphatic helices or wedge-shape transmembrane domains ; indirect action of electrostatic interactions with intrinsically curved proteins, steric constraints of non-intrinsically curved proteins or curved, membrane-bound protein scaffolds. Proteins and lipids are not to scale for simplicity.

When it comes to membrane curvature generation, BAR domain proteins posses most of the critical properties that may induce plasma membrane bending. First, they have an intrinsically curved shape and can interact by their positively charged interface with negatively charged lipids (Peter et al., 2004). Next, a subgroup of N-BAR domain proteins contains amphiphatic helices that can be inserted into the plasma membrane (McMahon and Gallop, 2005). Furthermore, they contain additional membrane-binding domains that are known to stabilize plasma membrane curvature induced by other means. Finally, they are known to oligomerize and form protein scaffolds implicated in the generation of higher order curved structures such as filopodia (Mattila and Lappalainen, 2008). Thus, BAR domain proteins are an interesting group of proteins to study when examining cellular processes that involve plasma membrane curvature changes.

1.5.3 Structural characteristics and membrane binding and bending by BAR domain proteins

The group of BAR domain proteins is characterized by the presence of a BAR domain. Its crystal structure revealed that it consists of approximately 200-280 amino acids that associate in antiparallel fashion to form crescent-shape dimers of varying size and curvature (Tarricone et al., 2001; Peter et al., 2004; Millard et al., 2005). The crescent shape is achieved by two units folding their three long and kinked α helices to form a six-helix bundle adopting a two-fold symmetry. The BAR domain interface is often hydrophobic and interacts with membranes by electrostatic interactions that are non-specific. The BAR domain membrane-interacting surface bears positively charged residues that interact with negatively charged lipid headgroups (McMahon and Gallop, 2005; Suetsugu, Kurisu, and Takenawa, 2014). The structure

of BAR domains has been found to be responsible for membrane curvature sensing and generation both *in vitro* and in cells. Moreover, curvature sensing was shown by a tighter binding to liposomes with an intrinsic curvature closer to the one of a particular BAR domain (Peter et al., 2004). On the other hand, curvature generation was revealed by a multitude of studies showing liposome remodeling and tubulation of cell membranes by BAR domain proteins (Farsad et al., 2001; Mattila et al., 2007; Henne et al., 2007; Itoh et al., 2005; Tsujita et al., 2006; Tsujita, Takenawa, and Itoh, 2015).

Within a group of BAR domain proteins three major subgroups can be distinguished based on their structural characteristics: the classical crescent-shaped BAR with the most highly curved shape, a more extended and less curved F-BAR that binds usually to more shallow curvatures, and the I-BAR with an inverse membrane-interacting surface (Suetsugu, Kurisu, and Takenawa, 2014). The shallower curvature of F-BAR proteins allows for generation of tubules of a larger diameter than the canonical BAR domain (Frost et al., 2008). In BAR and F-BAR proteins the membrane-binding interface consisting of positively charged residues is located on the concave surface of a dimer, while the I-BAR proteins have it located on the convex side (Mim and Unger, 2012). Sequence alignment and superimposition of the existing structures of all three subgroups revealed that BAR and F-BAR proteins have a larger variability in the degree of curvature, while I-BAR proteins are more closely related to each other. The variability in the type of curvature that different BAR domains can adopt arises predominantly from the degree of bending and twisting of three primary helices as well as from the angle of dimerization (Carman and Dominguez, 2018).

Apart from electrostatics, BAR domains can additionally interact with membranes by helical extensions of an amphiphatic nature that may be inserted into the membrane to facilitate curvature generation. Such extensions, described as amphiphatic helices or wedge loops, were observed in all three subgroups of BAR domain proteins, but are most typical for an N-BAR fold present in amphiphysin, endophilin or nadrin (Peter et al., 2004; Gallop et al., 2006; Bhatia et al., 2009).

Most BAR domain proteins contain additional domains that often facilitate membrane binding or are implicated in various protein-protein interactions (McMahon and Gallop, 2005; Suetsugu, Toyooka, and Senju, 2010; Carman and Dominguez, 2018). One of the most common domains present in 50% of all BAR domain proteins is the Src homology 3 (SH3) domain. SH3 domains are known to recognize proline-rich sequences and regulate many cellular processes from cell proliferation, through differentiation to migration (Kurochkina and Guha, 2012). Another common group are domains that are regulated by Rho-family GTPases or can themselves regulate GTPases including such domains as ArfGAP, RhoGAP and RhoGEF (Kreuk and Hordijk, 2012). Approximately 35% of all BAR domain proteins contain domains connected to GTPase regulation. Moreover, membrane binding of BAR domain proteins can be facilitated by the presence of an PH (Pleckstrin homology) or PX (Phox homology) domains that have abilities to bind specific phosphoinositides (Teasdale and Collins, 2011; Suetsugu, Kurisu, and Takenawa, 2014). PX domains are characteristic for all sorting nexins, while PH domains can be found in a variety of BAR domain proteins with a classical BAR domain such as ACAPs, ASAPs, APPLs, GRAFs and oligophrenin-1. Furthermore, some less common auxiliary domains encompass PDZ, WW, WH2 or ANK repeats that have a variety of functions, from controlling actin polymerization to binding to specific motifs.

1.5.4 Cellular functions of BAR domain proteins

BAR domain proteins are a very diverse group as suggested by their low sequence similarity and variable domain architecture. Thus, they are involved in a variety of fundamental processes ranging from embryonic development (Chou et al., 2017) to neurotransmitter release (Ukken et al., 2016). Studies focusing on BAR domain protein overexpression or knockouts in cells and model organisms have elucidated their many facets. Multiple examples show the importance of BAR domain proteins for brain functions. Knockout of the I-BAR IRSp53 in mice impairs their synaptic plasticity and results in hippocampus-associated learning deficiencies (Chou et al., 2017). In *Drosophila*, knockout of BAR-containing sorting nexins diminishes neurotransmitter release (Ukken et al., 2016). Further, BIN1 was found to be an Alzheimer disease risk factor in humans and its regulation of synaptic transmission was elucidated in mice (Chapuis et al., 2013; De Rossi et al., 2020). Several BAR domain proteins (e.g. FBP17 and CIP4) affect the invasive capacity of cancers (Hu et al., 2011; Yamamoto et al., 2011). Moreover, the deregulation of a number of BAR domain protein has been connected to a plethora of vascular disorders and autoinflammatory diseases (Liu et al., 2015a).

As BAR domain proteins were only discovered around 20 years ago, the mechanisms underlying their function in all of the above-mentioned processes and diseases are not fully understood. However, it is well described that BAR domain proteins are implicated in cellular processes including fission of synaptic vesicles, endocytosis, exocytosis, regulation of cell surface receptors shedding, vesicle fusion, ion flux across the membrane or cell-cell fusions. All of these processes are connected to the most prominent actions of BAR domain proteins: membrane remodeling in combination with actin cytoskeleton regulation.

1.5.5 Regulation of actin cytoskeleton and cell migration by BAR domain proteins

Most BAR domain proteins were shown to be implicated in the regulation of actin cytoskeleton assembly. Only by examining their various domains, their potential for actin regulation becomes clear. SH3 domains, present in a vast majority of BAR domain proteins, are known to bind proline-rich motifs in nucleation promoting factors (NPFs) such as WASP/N-WASP, GTPase dynamin and actin nucleation and elongation factors including formins and Ena/VASP-family proteins (Carman and Dominguez, 2018). Next, their RhoGAP, RhoGEF and Arfgap domains regulate the activity of various GTPases such as RhoA, Cdc42 and Rac1 (Elvers et al., 2012). Another layer of regulation capabilities of BAR domain proteins arises from their intramolecular interactions leading to autoinhibition. Specifically, autoinhibition and its release may not only affect membrane binding, but most importantly, interactions with downstream effectors and regulation of Rho GTPases. For example, membrane binding of amphiphysin, endophilin and syndapin is possible only if the autoinhibitory interaction of SH3 and BAR domains are released by dynamin binding to the SH3 domain (Meinecke et al., 2013; Wang et al., 2009).

A growing evidence for BAR domain proteins binding to actin filaments suggests that an even more direct mode of cytoskeletal regulation is plausible (Rocca et al., 2008; Dräger et al., 2017; Chen et al., 2020). Although the functional importance of these interactions is not clear yet, the fact that they may reduce spontaneous polymerization of G-actin imply a role in regulation of actin assembly (Chen et al., 2020). Signaling based on phosphorylation cascades also concerns BAR domain proteins,

as many of them can be phosphorylated and some contain tyrosine kinases that affect downstream signaling (Craig, 2012). For example, phosphorylation of IRSp53 by 14-3-3 affects Cdc42 and downstream cytoskeletal effectors (Kast and Dominguez, 2019b).

Several BAR domain proteins have been implicated in orchestrating cell migration (Table 1.1). Depending on the activity of their BAR domains and auxiliary domains, they can either promote or impair cell migration through modulating cell protrusion formation and dynamics (Guerrier et al., 2009; Parrini et al., 2011; Tsujita, Takenawa, and Itoh, 2015), adhesion turnover (Broussard et al., 2012), polarization (Koduru et al., 2010) and activation of GTPases (Li et al., 2016; Wang et al., 2018; Bendris et al., 2016). Of note, the same BAR domain proteins can affect cell migration differently depending on the cell type, environment or migration mode (Liu et al., 2005; Chen et al., 2016; Parrini et al., 2011). Along with the modulation of cell motility, BAR domain protein deregulation often changes cell morphology (Zhang et al., 2009; Li et al., 2016) and shapes membrane structures (Miki et al., 2000b).

Altogether, a picture emerges that BAR domain proteins are finely-tuned regulators of cell migration in highly dynamic mammalian cells. Their modular architecture, autoinhibition-based activity control and precise subcellular localization are key to provide flexible links between cytoskeleton and the plasma membrane. However, how exactly BAR domain proteins are activated or deactivated to perform their specific functions remains to be elucidated.

1.5.6 The cell surface as a mechanosensing platform for BAR domain proteins

Many studies demonstrated the various cellular functions, interactions and downstream effectors of BAR domain proteins. It is known that their mechanism of action on the actin cytoskeleton often involves interactions with GTPases, nucleation-promoting factors and the resulting activation or deactivation of Arp2/3 (Carman and Dominguez, 2018). Structural studies revealed many diverse shapes that BAR domain dimers can assume and quantified the precise degrees of curvature to which they are expected to bind or bend. Nonetheless, the role of plasma membrane curvature and cell surface mechanics in BAR domain protein regulation is still not fully understood.

The cell surface is an interface for feedback between external forces and downstream biochemical signaling that requires sensors to trigger and regulate cellular behaviour. These sensors could respond to changes of cell surface properties, including membrane tension or membrane curvature. External forces may lead to various plasma membrane deformations, compression or stretching and BAR domain proteins are perfectly designed to detect these changes through their binding or unbinding to the plasma membrane and signal downstream though their other domains. (Diz-Muñoz, Fletcher, and Weiner, 2013; Le Roux et al., 2019).

During recent years, a couple of independent studies suggest direct links between regulation of BAR domain proteins and cell surface properties. FBP17, an F-BAR domain protein, was found to be a part of a feedback loop involving membrane tension and actin polymerization. FBP17 promotes branched actin polymerization through activation of Arp2/3 downstream of WASP/N-WASP. That, in turn, increases protrusive force and membrane tension. Next, high membrane tension inhibits FBP17 bending activity and subsequent actin polymerization that orchestrate leading edge formation and cell migration (Tsujita, Takenawa, and Itoh, 2015). In a

Protein name	BAR domain type	Migration-related functions	References
ASAP1	BAR	ASAP1 promotes metastasis *in vivo* and stimulates tumor cell motility, invasiveness, and adhesiveness *in vitro*; ASAP1 downregulation may inhibit or facilitate cell migration.	Liu et al., 2005; Müller et al., 2010; Chen et al., 2016
APPL1	BAR	APPL1 regulates cell migration through hindering the turnover of adhesion dynamics at the leading edge and inhibiting kinase Akt; APPL1 promotes leptin-induced migration of cancer cells in wound-healing.	Broussard et al., 2012; Ding et al., 2016
BIN3	BAR	BIN3 promotes lamellipodia formation and muscle cell migration through Rac1 and Cdc42.	Simionescu-Bankston et al., 2013
CIP4	F-BAR	CIP4 knockout impairs immune cells adhesion, polarization and transmigration.	Koduru et al., 2010
FBP17	F-BAR	FBP17-mediated activation of WASP/N-WASP regulates leading edge formation and cell migration; FBP17 knockdown decreases number of migrating macrophages.	Tsuboi et al., 2009; Tsujita, Takenawa, and Itoh, 2015
IRSp53	I-BAR	IRSP53 induces membrane ruffling through Rac1-WAVE2-stimulated actin polymerization; IRSp53 regulates filopodia dynamics and cancer cell chemotaxis.	Miki et al., 2000b; Kast and Dominguez, 2019a
IRTKS	I-BAR	IRTKS affects cell shape, promotes cell motility and activation of Rac1 and Cdc42.	Li et al., 2016
MIM	I-BAR	MIM impairs cell motility and affects protrusions formation	Mattila et al., 2007; Li et al., 2016
PACSIN2	BAR	PACSIN2 knockdown promotes cell migration in a wound healing assay through interaction with Rac1.	Kreuk et al., 2011
SH3BP1	BAR	SH3BP1 promotes tumour invasion and contributes to metastasis through Rac1-WAVE2 activation; SH3BP1 regulates protrusion stability and migration it via its GAP activity upon Rac1.	Parrini et al., 2011; Tao et al., 2016; Wang et al., 2018
SNX9	BAR	Snx9 promotes cell migration and metastasis through the activation of RhoA and Cdc42 GTPases and their downstream effectors.	Bendris et al., 2016

srGAP2	F-BAR	srGAP2 negatively regulates neuronal migration through control of filopodia-like protrusions and neurite branching.	Guerrier et al., 2009
srGAP3	F-BAR	srGAP3 inhibits lamellipodia formation and dynamics through Rac1-WAVE1 and lamellipodin; srGAP3 impairs cell migration.	Endris et al., 2011

TABLE 1.1: BAR domain proteins involved in regulating cell migration

different study GRAF1, a BAR protein with a RhoGAP domain, was found to differently localize to the plasma membrane upon changes in membrane tension induced by osmotic shocks. These, led to changes in cell surface localization of Rab8 and its subsequent function in endocytic turnover (Vidal-Quadras et al., 2017). Both studies characterized the dependence of BAR domain proteins localization at the plasma membrane on cell surface mechanical properties, such as the plasma membrane tension.

Plasma membrane deformations are intertwined with changes in cell surface mechanical properties and their detection may inform cell behaviour (Diz-Muñoz, Fletcher, and Weiner, 2013). Recently, it was demonstrated that srGAP2, an F-BAR domain protein, is recruited by the change of membrane curvature induced by cell contacts with a surface. This initiates cytoskeletal polarization that is key for neutrophil adhesion to the endothelium (Ren et al., 2019). Furthermore, engineering of nanostructures that induce membrane curvature in cells resulted in the recruitment of FBP17, a BAR domain protein, and curvature-induced actin polymerization, leading to long-range reorganization of actin cytoskeleton (Lou et al., 2019).

In terms of the above-mentioned mechanisms of BAR domain protein action, a picture emerges, in which BAR domain proteins, while sensing or generating membrane curvature, create molecular platforms that recruit and enable binding and activation/deactivation of various partners, leading to a plethora of finely-tuned cellular processes such as cell migration. Although there are many studies focused on particular biochemical pathways in which BAR domain proteins regulate these cellular processes as well as on their membrane remodeling activity, only a handful of examples illustrate their interplay with mechanical properties of the cell surface. Investigation of how exactly BAR domain proteins are regulated through changes in cell surface mechanical properties may elucidate feedback loops orchestrating dynamic processes and allow understanding of cell interactions and responses to various environmental cues.

Chapter 2

Aims and outline of this study

BAR domain proteins, because of their cell-surface shaping properties, are emerging as a very interesting group of potential sensors and effectors of mechanical properties that organize dynamic cellular functions. Among a plethora of different BAR domain proteins, we set out to identify the most promising ones to shed light on mechanochemical feedbacks that organize cell motility as an example of a complex and fast cellular process.

In Chapter 1, we introduced cell surface, its mechanical properties and the perplexing ways in which it can modulate cellular functions with an emphasis on cell migration. Furthermore, we focused on plasma membrane curvature and the emerging concept that it could be involved in transduction of mechanical forces into biochemical pathways with the use of curvature-sensitive proteins such as BAR domain proteins. In Chapter 3, we present two approaches used to identify BAR domain proteins that could link the regulation of morphological changes during motility to the mechanical properties of the plasma membrane. Using a combination of RNA expression profiling during differentiation into the migratory state of neutrophil-like cells and protein localization upon changes in plasma membrane tensions, we identify two candidates: SH3BP1 and Snx33. In Chapters 4 and 5, we present results revealing the roles of SH3BP1 and Snx33, respectively, for plasma membrane tension, actin cytoskeleton and migration in various environments and discuss the obtained results in the context of most recent studies. Finally, we summarize the contribution of our work to the field and suggest future directions in Chapter 6.

Part II

Results and Discussion

Chapter 3

Identification of relevant BAR domain proteins for cell surface organization and motility

3.1 Assessment of mRNA expression levels of BAR domain proteins in migratory and non-migratory HL-60 cells

The main interest of this thesis is elucidating the role of BAR domain proteins in a complex interplay between the cell surface properties and biochemical signaling relevant for cell motility. BAR domain proteins are a versatile group of proteins (Introduction 1.5.2-1.5.6). Therefore, we collected literature materials about BAR domain proteins taking into account their known functions in controlling protrusion formation and dynamics, cell migration or regulation of the cell surface properties. For the purpose of our study we chose a group of proteins that spanned a versatile spectrum of characteristics (Table 3.1).

In agreement with the aims of the study, we decided to use HL-60 cells as our model system (Figure 3.1a; Methods 7.1). This models' advantage lies in HL-60 cells undergoing dramatic morphological changes during the differentiation process. First, differentiation affects the cell surface by inducing considerable rearrangements of the plasma membrane that can be visualized by polarized Total Internal Reflection Fluorescence Microscopy (pTIRFM) (Figure 3.1b-d; Methods 7.2). Second, the differentiated state ensures high motility of cells that is critical for neutrophils' function in the organism (Figure 3.1b; Fritz-Laylin et al., 2017). HL-60 cells were used previously to study cell surface mechanical properties (Houk et al., 2012; Diz-Muñoz et al., 2016a) and actin cytoskeleton dynamics (Weiner et al., 2006). Furthermore, they were recently employed to explore curvature recognition by WAVE2 complex in coordination with IRSp53, a membrane-sensing BAR domain protein (Pipathsouk et al., 2019).

To confirm that proteins of choice are expressed in HL-60 cells, we performed qPCR experiments (Methods 7.3). As HL-60 cells in a differentiated state are migratory, have increased cell surface dynamics and form lamellipodial protrusions, changes in mRNA levels occurring between undifferentiated and differentiated cells were of a special interest for us. Surprisingly, our most interesting candidates chosen based on the available literature showed a variety of mRNA expression trends during the differentiation process (Figure 3.2). We detected both increases (e.g. GRAF1, ASAP1, Tuba, Snx9) and decreases (e.g. srGAP3, APPL2, AMPH2) in expression levels in differentiated HL-60 relative to undifferentiated HL-60 cells (Figure 3.2). One candidate (MIM) was not expressed in HL-60 cells, although it was detected in

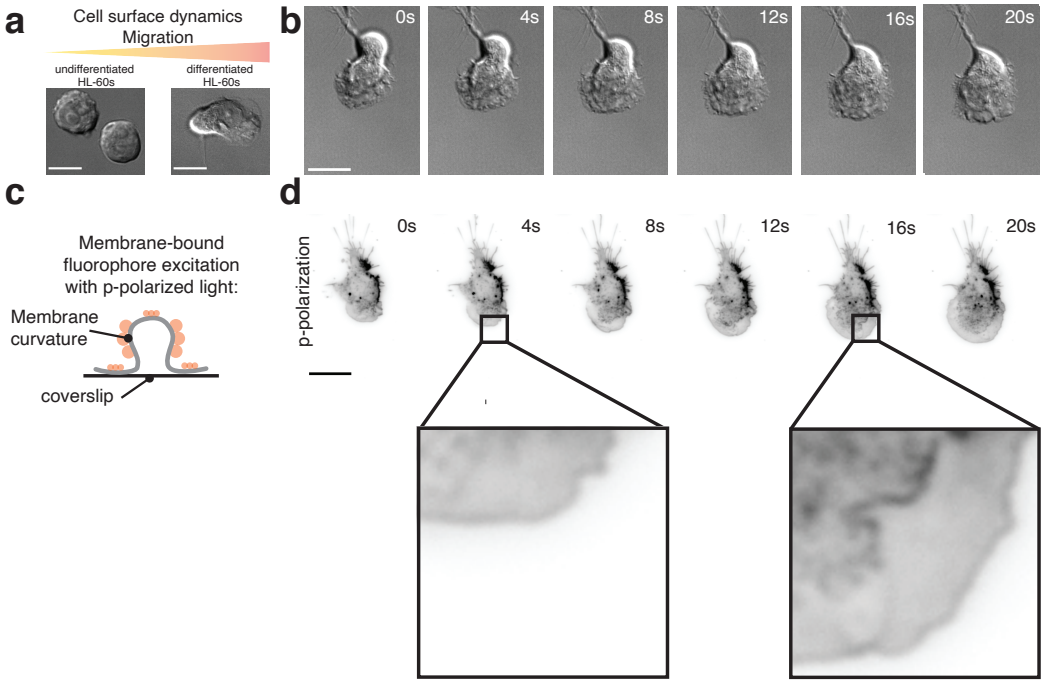

FIGURE 3.1: HL-60 cells as a model system to study cell surface properties relevant for motility. a. Schematic of HL-60 cells changes during transition to a differentiated state. b. Bright-field imaging of dHL-60s. c. Principle and d. imaging of membrane curvature of dHL-60s using pTIRFM highlighting plasma membrane changes. Scale bar = 10 μm.

Protein name	Domains	Relevant functions and interactions	References
AMPH2	BAR, SH3	AMPH2 inhibition of PLD2 affects actin polymerization and membrane tension; Mechanical effects of amphiphysin action depends on their density; AMPH2 interacts with N-WASP	Lee et al., 2000; Sorre et al., 2012; Falcone et al., 2014
ASAP1	BAR, PH, ArfGAP, Ank repeats, SH3	ASAP1 is involved in membrane scaffolding for ciliar protrusions; ASAP1 promotes metastasis *in vivo* and stimulates tumor cell motility, invasiveness, and adhesiveness *in vitro*; ASAP1 downregulation may inhibit or facilitate cell migration.	Liu et al., 2005; Müller et al., 2010; Wang et al., 2012; Chen et al., 2016
APPL1/2	BAR, PH, PTB	APPL1/2 knockout impairs HGF-induced Akt activation, migration and invasion; APPL1 regulates cell migration through hindering the turnover of adhesion dynamics at the leading edge and inhibiting kinase Akt; APPL1 promotes leptin-induced migration of cancer cells in wound-healing.	Broussard et al., 2012; Ding et al., 2016; Tan et al., 2016

CIP4	F-BAR	CIP4 forms lamellipodial protrusions; CIP4 knockout impairs immune cells adhesion, polarization and transmigration.	Koduru et al., 2010; Saengsawang et al., 2012
FBP17	F-BAR, REM-1, SH3	FBP17 localizes to the leading edge in a membrane-tension dependent manner; FBP17-mediated activation of WASP/N-WASP regulates leading edge formation and cell migration; FBP17 knockdown decreases number of migrating macrophages.	Tsuboi et al., 2009; Tsujita, Takenawa, and Itoh, 2015
FCHSD1/2	F-BAR	FCHSD2 interacts with WASP/n-WASP and stimulates F-actin polymerization; FCHSD1 enhances Snx9-dependent actin polymerization; Their homologue Nwk in flies deforms membrane leading to protrusions; FCHSD2 knockout reduces cell migration in wound healing.	Cao et al., 2013; Becalska et al., 2013; Almeida-Souza et al., 2018
GRAF1	BAR	GRAF1 localizes to the PM in a membrane tension-dependent manner; GRAF1 affects cell spreading and migration; GRAF1 activates Cdc42 and RhoA.	Doherty et al., 2011; Francis et al., 2015; Vidal-Quadras et al., 2017
IRSp53	I-BAR, CRIB-PR, SH3, WH2	IRSP53 induces membrane ruffling through Rac1-WAVE2-stimulated actin polymerization; IRSp53 regulates filopodia dynamics and cancer cell chemotaxis.	Miki et al., 2000b; Kast and Dominguez, 2019a
MIM	I-BAR, WH2	MIM impairs cell motility and affects protrusion formation.	Mattila et al., 2007; Li et al., 2016
PACSIN2	BAR, SH3	PACSIN2 interacts directly with actin filaments; PACSIN2 knockdown promotes cell migration in a wound healing assay through interaction with Rac1.	Kreuk et al., 2011; Kostan et al., 2014
SH3BP1	BAR, RhoGAP	SH3BP1 promotes tumour invasion and contributes to metastasis through Rac1-WAVE2 activation; SH3BP1 regulates protrusion stability and migration via its GAP activity upon Rac1.	Parrini et al., 2011; Tao et al., 2016; Wang et al., 2018
SNX9	BAR, PX, SH3	Snx9 promotes cell migration and metastasis through the activation of RhoA and Cdc42 GTPases and their downstream effectors.	Bendris et al., 2016

srGAP3	F-BAR, RhoGAP, SH3	srGAP3 inhibits lamellipodia formation and dynamics through Rac1-WAVE1 and lamellipodin; srGAP3 impairs cell migration.	Endris et al., 2011
Tuba	BAR, multiple SH3, RhoGEF	Tuba stimulates N-WASP-dependent actin assembly and membrane ruffling.	Kovacs, Makar, and Gertler, 2006

TABLE 3.1: BAR domain proteins chosen for the study

another cell line (SCLC21-H) that was used as a positive control (Gene expression relative to GAPDH=0.022, not shown in the Figure 3.2).

Quantification of mRNA expression levels of BAR domain proteins by qPCR experiments allowed us to exclude some candidates due to very low or undetectable expression (e.g. MIM). On the other hand, the unexpected heterogeneity of RNA expression levels trends during differentiation motivated us to investigate it in a more detailed manner. To do so, we performed RNAseq experiments in which we followed mRNA expression daily until 5 days after differentiation (Methods 7.1; 7.4; 7.5). This enabled an improved time resolution as well as an assessment of a higher number of target genes. Differential expression analysis performed using DESeq2 on the Galaxy platform showed high reproducibility of all three biological replicates that cluster together depending on the day of differentiation (Figure 3.3a).

From over 10 000 genes that are differentially expressed during the processes of HL-60 cells differentiation, we focused on the BAR domain candidates. In agreement with our previous results from qPCR experiments, RNA-seq data also showed the heterogeneity of RNA expression (Figure 3.3b-c). We confirmed that several RNA expression trends can be captured. Targets can be up-regulated, down-regulated or show fluctuation over the time course of the differentiation processes (Figure 3.3d).

Analysis of the RNAseq dataset revealed several interesting candidates. As differentiated HL-60 (dHL-60) cells first become migratory at around third day after differentiation, we considered the genes of BAR domain proteins that have up-regulated RNA expression at that day followed by a steady increase as particularly interesting. Following candidates can be found in this category: ACAP1/2, ARHGAP4, ASAP1, BIN2, FES, GAS7, GRAF1/ARHGAP26, FBP17/FNBP1, PSTPIP1/2, SH3BP1, SH3GLB2 and several candidates from sorting nexin family, including Snx18 and Snx33. Additionally, we recognized that the candidates with the highest total RNA expression could be important for controlling processed involving cell surface and migration (BIN2, GRAF1/ARHGAP26, Snx33, srGAP1, Toca1). Lastly, by examining the enrichment of RNA expression in differentiated (migratory) state, we found that BIN2, GRAF1/ARHGAP26, Snx33, srGAP1 and Toca1 have the highest log2 fold change between the two states (Figure 3.3e).

3.2 Assessment of BAR domain proteins' localization upon change of cell surface properties

Simultaneously to performing experiments described in the previous section, a different screening strategy was employed to identify relevant BAR domain proteins (Section 3.1). First, we wanted to understand whether chosen candidate BAR domain proteins are localizing to the plasma membrane. Second, we decided to test

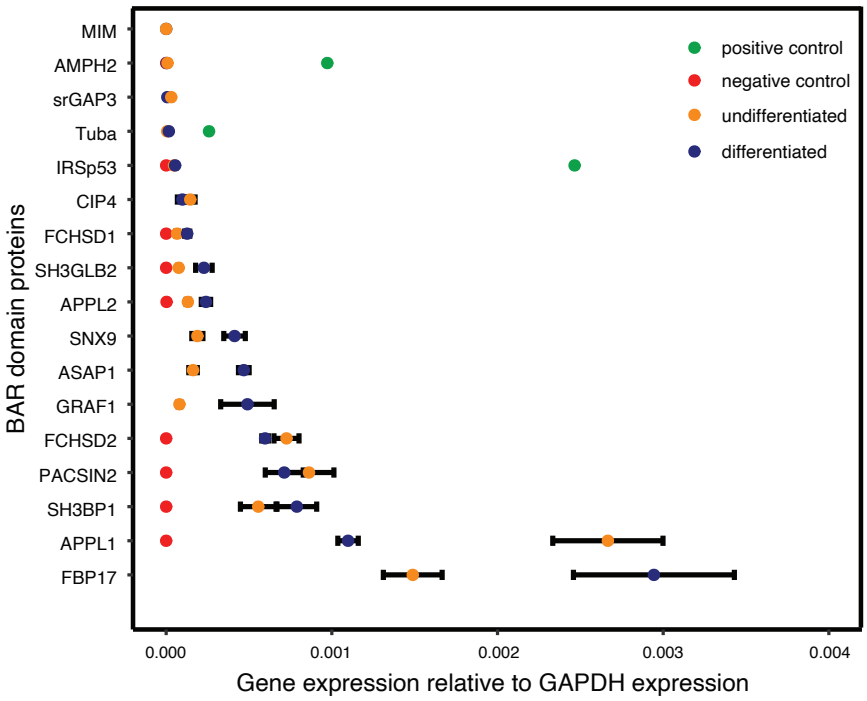

FIGURE 3.2: RNA expression of BAR domain candidates measured by quantitative PCR. Data from 3 biological replicates. Black whiskers show SEM.

whether their localization at the plasma membrane depends on cell surface mechanical properties.

To investigate BAR domain proteins' localization to the plasma membrane, we obtained plasmids of several proteins (Methods 7.6). Next, we cloned plasmids with fluorescently-tagged version of those proteins using either ligation or the Gibson assembly® cloning method (Methods 7.6). We obtained 7 stable HL-60 cell lines expressing eGFP-tagged proteins using lenti-virus transduction (Methods 7.7.2; 7.34). The generated HL-60 cell lines were sorted by FACS for low expression of GFP to avoid overexpression artifacts, and used to assess protein localization at the plasma membrane by Total Internal Reflection Fluorescence Microscopy (Methods 7.7; 7.34). All tested BAR domain proteins localized to the plasma membrane in the form of dynamic puncta (Figure 3.4).

Further, we wanted to test the behaviour of BAR domain proteins upon changes in cell surface properties. We took advantage of the fact that all tested proteins localized to the plasma membrane in the form of puncta when imaged by TIRFM and decided to quantify them. As HL-60 cells change their shape dramatically during migration and the protein puncta are very dynamic, we developed a pipeline of puncta quantification using CellProfiler-3.0.0 (Methods 7.11). It uses multiple time frames to identify and count puncta per cell in the eGFP channel. To make sure that all found puncta are within the cell area, we generated cell lines with an mCherry-CAAX to label the cell membrane in addition to the eGFP-tagged BAR domain protein (Methods 7.34). The pipeline uses the mCherry channel to segment the cell area and counts the number of eGFP puncta within this area.

To change cell surface properties, we decided to affect plasma membrane tension. To this end, we used the Arp2/3 inhibitor CK-666 as it is known to decrease

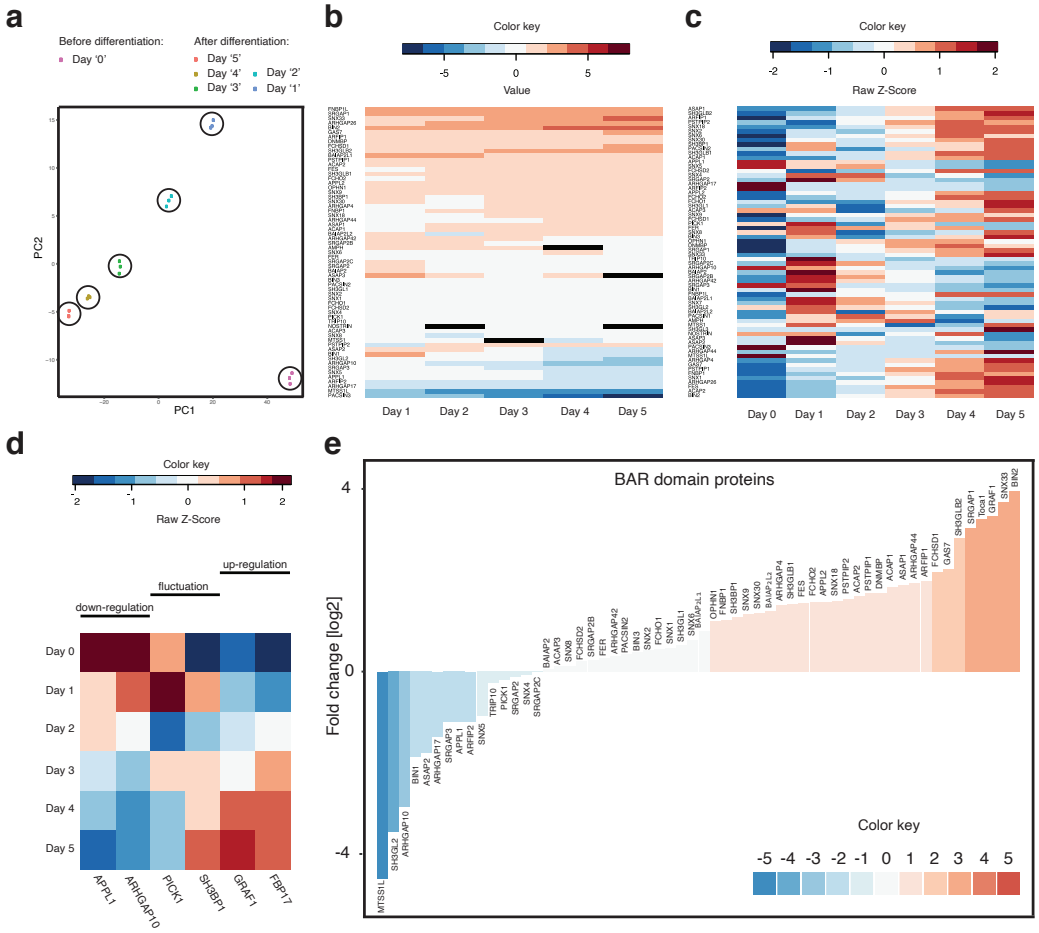

FIGURE 3.3: BAR domain proteins RNA expression measured by RNAseq. a. PCA plot of RNAseq samples from different days of differentiation. b. Results of differential expression analysis using Deseq2: RNA expression of BAR domain proteins presented in b. Log2 scale, all time points are normalized to Day 0. c. Z-Score. Genes are in clustering order. Black represents missing data. d. Examples of RNA expression trends for chosen genes (zoom-in of c.). e. RNA expression enrichment of genes of BAR domain protein in differentiated (migratory) in comparison to undifferentiated HL-60 cells. Bars shown in blue and red are under-expressed and over-expressed in dHL-60 cells, respectively. Data from for 3 biological replicates.

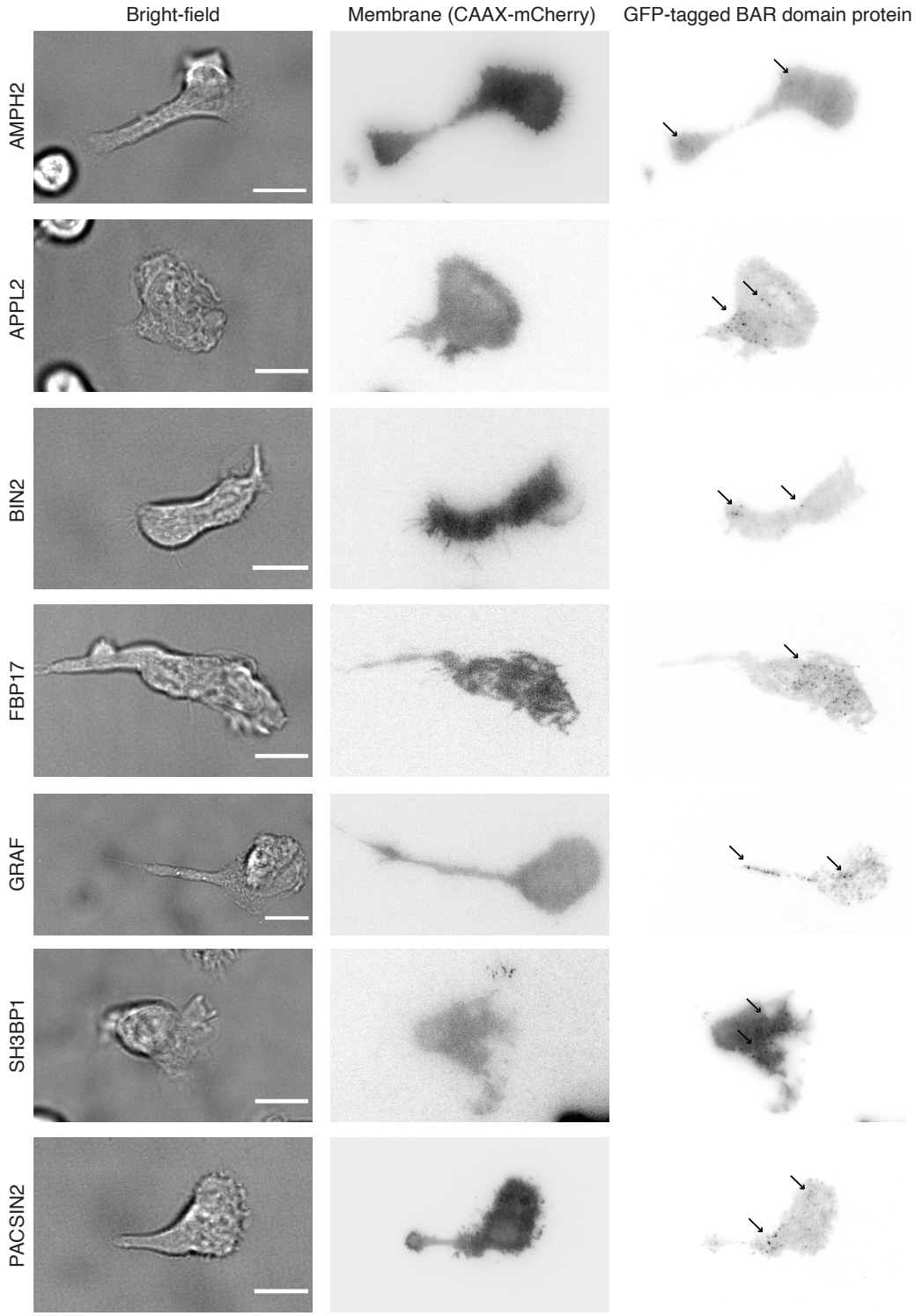

FIGURE 3.4: Bright-field and TIRFM imaging of membrane marker (CAAX-mCherry) and GFP-tagged BAR domain proteins. Black arrows point towards regions with protein puncta. Scale bar = 10 μm

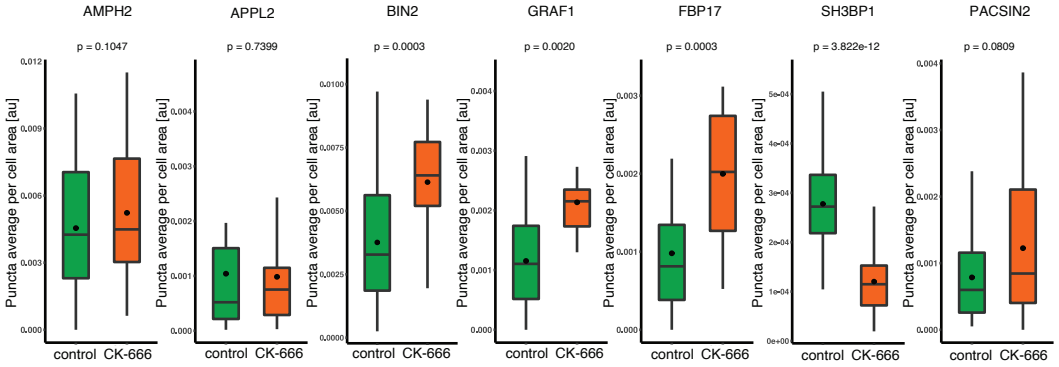

FIGURE 3.5: Analysis of eGFP-tagged BAR domain protein puncta in response to membrane tension changes. Puncta average per cell area in control conditions and upon CK-666 treatment for following eGFP-tagged proteins: AMPH2 (control n=100; CK-666: n=75), APPL2 (control n=12; CK-666: n=11), BIN2 (control n=35; CK-666: n=28), GRAF1 (control n=24; CK-666: n=15), FBP17 (control n=28; CK-666: n=17), SH3BP1 (control n=44; CK-666: n=41), PACSIN2 (control n=62; CK-666: n=51). Each data point is the average of puncta per cell area measured for 9-15 frames of a movie of an individual cell. Black dot indicates the average of all measurements. Statistics: Mann-Whitney-U-Test and T-test.

plasma membrane tension in dHL-60 cells (Diz-Muñoz et al., 2016a). After testing 7 cell lines with eGFP-tagged BAR domains proteins, we found that the puncta number per cell area after CK-666 treatment statistically significantly increased in the ones with eGFP-tagged BIN2, GRAF1, FBP17 with a fold change of 1.6, 1.9 and 2, respectively. Interestingly, in a cell line with eGFP-tagged SH3BP1, we observed an inverted pattern with a 2.3 fold decrease of the puncta number per cell area after CK-666 treatment (Figure 3.5). GRAF1 and FBP17 were already shown to change their localization at the plasma membrane in a tension dependent manner and our results proved to be in agreement with previous findings (Tsujita, Takenawa, and Itoh, 2015; Vidal-Quadras et al., 2017). BIN2 and SH3BP1 were identified as a novel BAR domain proteins that alter their localization at the plasma membrane in response to membrane tension changes. Interestingly, GRAF1/ARHGAP26, FBP17 and SH3BP1 show a similar RNA expression pattern – they are steadily up-regulated during the differentiation process of HL-60 cells (Figure 3.3d).

3.3 BAR domain protein screening conclusions

We employed two distinct screening approaches to shortlist candidates from over 80 BAR domain proteins for the purpose of this thesis. Based on the analysis of our RNAseq dataset, we identified that only BIN2, GRAF1/ARHGAP26 and Snx33 both have an increase in RNA expression when cells first become migratory as well as are greatly enriched in the migratory state of the HL-60 cells. Next, our imaging screen revealed that BIN2, GRAF1/ARHGAP26, FBP17 and SH3BP1 had changes in protein localization at the plasma membrane upon membrane tension manipulation.

As a result of our screening approaches, a number of proteins was identified as interesting, but we decided to focus on SH3BP1 and Snx33 for the purpose of this thesis. SH3BP1 was chosen predominantly because of its novel cell surface-related

behaviour and increase in RNA expression levels in the process of acquiring the migratory phenotype. On the other hand, Snx33 was a clear candidate following the approach of the RNA expression patterns, but so far little is known about its functions regarding cell surface and migration. At the same time, both chosen proteins contain a distinct set of domains (RhoGAP with BAR in SH3BP1 and SH3 with PX and BAR in case of Snx33) that could in different ways contribute to organization of cell surface to ensure motility.

Chapter 4

SH3BP1 (SH3 Domain Binding Protein 1)

4.1 Abstract

Cell surface mechanical properties govern diverse processes ranging from cell migration to stem cell differentiation (Houk et al., 2012; Diz-Muñoz et al., 2016a; Bergert et al., 2020; De Belly et al., 2020). One group of particularly interesting proteins in the context of organization of the cell surface are plasma membrane curvature-sensitive BAR domain proteins that also have the ability to regulate actin cytoskeleton (Diz-Muñoz, Fletcher, and Weiner, 2013; Carman and Dominguez, 2018). Here, we identify a curvature-sensitive SH3BP1 protein with a RhoGAP activity as a novel protein localizing in a tension-dependent manner to the plasma membrane and lamellipodia. By generating an SH3BP1 knockout in highly motile neutrophil-like cells, we discover that it increases membrane tension, alike the depletion of important molecules that organize cell motility including PLD2 and mTORC2 (Diz-Muñoz et al., 2016a). However, in contrast to PLD2 and mTORC2, the elevated membrane tension in SH3BP1 knockout does not depend on enhanced actin polymerization caused by disrupted inhibition of WAVE2 and Arp2/3 complex machinery. Nevertheless, the increase in membrane tension relates to enhanced directed cell migration. Furthermore, neutrophil-like cells devoid of SH3BP1 are more efficient at navigating through challenging environment, suggesting that changes in lamellipodia-driven protrusion dynamics are functionally relevant. Taken together, we found that SH3BP1, an actin remodeling and curvature-sensitive protein, affects cell surface properties such as membrane tension to drive migration in complex environments.

4.2 Introduction to SH3BP1

4.2.1 SH3BP1 domain structure and functions

SH3BP1, often referred to as ARHGAP43, is probably at least as much recognized by containing a BAR domain, as by belonging to the RhoGAP family. First identified as a binding partner of Abl, SH3BP1, encompasses an N-terminal BAR domain, a central RhoGAP domain as well as prolin-rich and SH3-binding sequences positioned closer to the C-terminus (Cicchetti et al., 1992). Among BAR domain proteins, it can be distinguished by the presence of a RhoGAP domain together with only a couple of other BARs (Bargin, GRAF1-3, Oligopherenin-1, RICH1-2) and F-BARs (ARHGAP29, ARHGAP45, GMIP, RhoGAP4, srGAP1-3) (Kreuk and Hordijk, 2012). However, only Bargin, RICH1-2 and SH3BP1 contain solely BAR and RhoGAP domains. In *C. elegans* RGA-8 is a single homolog of both SH3BP1 and RICH1. RGA-8 is known to be involved in morphogenesis and epithelial polarization (Raduwan et

al., 2020). In contrast, in mammalian cells, it is proposed that SH3BP1 and RICH1 acquired distinct functions, suggesting a much more complex and finely-tuned organization of processes involving BAR domain proteins in mammals. For example, during regulation of epithelial junctions they act at various stages. SH3BP1 is recruited quite early during epithelial junction formation and regulates its assembly, while RICH1 is involved once junctions are formed (Elbediwy et al., 2012). Studies about SH3BP1 focus mainly on epithelial cells, their morphology and cell-cell contacts, but it is important to note that SH3BP1 is abundantly expressed in most human tissues (Parrini et al., 2011; Elbediwy et al., 2012; Hak et al., 2018). Thus, its potential roles in other types of cells and tissues are still to be explored.

4.2.2 Cell surface remodeling by SH3BP1

SH3BP1 and membrane protrusions

Several studies indicate that SH3BP1 has a RhoGAP activity towards two important GTPases involved in cell migration, Rac1 and Cdc42 (Parrini et al., 2011; Elbediwy et al., 2012). SH3BP1-based inactivation of Rac1 at the leading edge of migrating cells, most probably, enables the turnover of protrusions and adhesions that are indispensable for efficient cell motility (Parrini et al., 2011). Interestingly, SH3BP1 enhances growth of filopodia during cell-cell junctions formation, a protrusion typically regulated by I-BAR proteins such as IRSp53 (Section 1.4.4; Mattila and Lappalainen, 2008; Elbediwy et al., 2012). On the other hand, it is also found at the leading edge of epithelial NRK and endothelial HUVEC migrating cells, suggesting its relevant role in cell migration relying not only on filopodia, but also on lamellipodia (Parrini et al., 2011; Tata et al., 2014). Additionally, SH3BP1-mediated regulation of Rac1 was found to induce membrane ruffles in fibroblasts (Cicchetti et al., 1995). In turn, knockdown of SH3BP1 impairs dorsal ruffles formation in A431 cells upon EGF-induction. In dorsal ruffles SH3BP1 affects both the regulation of Rac1 and Cdc42 (Elbediwy et al., 2012).

SH3BP1 and actin assembly regulation

SH3BP1 interactions with Rac1 and Cdc42, through its RhoGAP domain, are not the only known way in which this protein could potentially remodel the plasma membrane and the underlying cytoskeleton. It was found to be associated with CD2AP, a protein that regulates actin dynamics by binding to the barbed-end capping protein CapZ. A complex encompassing SH3BP1, CD2AP and capping protein is important for regulation of actin dynamics in cell junctions and protrusion formation (Elbediwy et al., 2012). Regulation of actin dynamics by barbed-end capping can be a powerful mechanism of steering the actin polymerization machinery as well as influence membrane remodeling.

SH3BP1 and membrane remodeling

SH3BP1 is involved in endocytosis, a process that is key for membrane remodeling (Hak et al., 2018). On the other hand, SH3BP1 binding to the exocyst complex (which is a protein complex that tethers secretory vesicles to the plasma membrane) is required for its leading edge localization. The SH3BP1-exocyst complex is proposed to provide a cross-talk between Rac1-WAVE and Ral-exocyst pathways to regulate cell migration (Zago et al., 2019). Besides, SH3BP1-driven inactivation of GTPases

regulating actin assembly was found to be important for another process involving membrane remodeling, namely phagocytosis (Schlam et al., 2015). Interestingly, SH3BP1 interacts also with the cell surface receptor PLXND1 involved in regulation of cell motility in various cell types (Alto and Terman, 2017). Following cell surface receptor activation, SH3BP1 is disengaged from this interaction to inactivate Rac1 (Tata et al., 2014). SH3BP1 emerges as a multifaceted guide of actin remodeling and membrane shaping, not only by its BAR domain but also by its numerous interactions.

4.2.3 SH3BP1 roles in cell migration

Investigation of several interaction partners of SH3BP1 revealed its role for cell migration in wound-healing and cancer cell invasion (Parrini et al., 2011; Wang et al., 2018). Associated with the exocyst complex, SH3BP1 was found to spatially control Rac1 at the leading edge and thus, guide cell migration. Specifically, its depletion from cells led to disorganized protrusions, impaired their velocity and persistence measured in a wound-healing assay. These effects could not be rescued by its RhoGAP or BAR domains alone, only a full-mlength protein counterbalanced migration deficiencies in SH3BP1-depleted cells (Parrini et al., 2011). This, suggests that the curvature-sensitive BAR domain contributes in a important way to the regulation of GTPases at the leading edge to steer migration efficiently. Possibly, the membrane curvature landscape, mechanical properties of the membrane or local phosphoinositide composition could guide the RhoGAP activity.

SH3BP1 and cancer cell migration

More detailed mechanism of SH3BP1 acting in cancer invasion and metastasis was elucidated recently. Various assay's, including scratch, transwell and invasion, using HeLa, Caski, HCCLM3 and Hep3B cells confirmed that SH3BP1 depletion reduces cell invasion, while its overexpression increases it. Moreover, this process was shown to be moderated through Rac1-WAVE2 pathways (Tao et al., 2016; Wang et al., 2018). Previously, it was shown that SH3BP1 mRNA expression is up-regulated in gastric cancer, hepatocellular carcinoma as well as cervical cancer, among others (Tao et al., 2016; Min et al., 2015; Wang et al., 2018). Thus, understanding how SH3BP1 regulates cell migration through cell surface remodeling emerges as an important topic in the control of diseases such as cancer.

SH3BP1 and immune cells

SH3BP1 was also briefly studied in migratory HL-60 cells that are the main focus of this work (Graziano et al., 2017). Its migration characteristics were not discussed in the study as its primary focus lied in investigating the RhoGAP activity of various proteins. Interestingly, generation of the SH3BP1 knockout showed that it plays a minor role in Rac1 activation mediated by PIP_3, but it increases chemoattractant-driven Rac1 activation by nearly 2 fold, measured by phosphorylation of a Rac1 effector Pac (Graziano et al., 2017). This, together with the above-mentioned studies suggests that SH3BP1 might be relevant for membrane and actin remodeling crucial for directed cell migration. Although some proteins relevant for cell surface regulation were studied in the context of SH3BP1, it is still not clear how mechanical properties of the cell surface and the surrounding environment are guided by SH3BP1 activity.

4.3 Results and Discussion

4.3.1 Leading edge enrichment of SH3BP1 is membrane tension and Arp2/3-dependent

In the previous section we revealed that SH3BP1 mRNA expression is enriched in the migratory HL-60 cells, suggesting that it may be important for the migration capabilities (Section 3.1). Several proteins important for the organization of cell motility were shown to localize to the leading edge of migrating cells including WAVE2 (Weiner et al., 2007), active Rac1, Cdc42 (Yang, Collins, and Meyer, 2016; Graziano et al., 2019), and Rictor (He et al., 2013), among others. Interestingly, SH3BP1 was identified at the leading edge of migrating epithelial NRK and HUVEC cells. We wondered whether leading edge localization of SH3BP1 is conserved among different cell lines. TIRFM imaging revealed a fairly uniform distribution of SH3BP1 across the basal plasma membrane with enriched signal only at dynamic puncta (Figure 4.1a; Methods 7.10). However, by performing epifluorescent imaging we observed that SH3BP1 signal is enriched at the leading edge of migrating cells and closely resembles F-actin visualized by phalloidin staining (Figure 4.1b). Thus, the leading edge enrichment of SH3BP1 observed in dHL-60 cells comes predominantly from other sources than from this protein residing at the basal plasma membrane.

Dynamic SH3BP1 puncta on the basal plasma membrane behave in a plasma membrane tension-dependent manner, as showed in the previous section (Figure 3.5). After confirming that SH3BP1 localizes to the leading edge in migrating dHL-60 cells, we asked if its leading edge fraction could also respond to membrane tension changes. Thus, we imaged fixed dHL-60 cells with an eGFP-tagged SH3BP1 and stained F-actin in control conditions and upon Arp 2/3 inhibition by CK-666 (Methods 7.23; 7.25; 7.24; 7.8). CK-666 treatment was previously shown to considerably decrease membrane tension in dHL-60 cells (Diz-Muñoz et al., 2016a). Quantification of protein enrichment at the leading edge uncovered that CK-666 treatment indeed reduces SH3BP1 localization at the cell front by 3 fold (Figure 4.2a-b; Methods 7.12). To corroborate these findings, we performed osmotic shocks that have been broadly used to affect membrane tension (Sinha et al., 2011; Boulant et al., 2011; Diz-Muñoz et al., 2016a; Graziano et al., 2019). Specifically, we performed hyper-osmotic shocks to decrease membrane tension by osmotically-driven water outflux. We found that, similarly to CK-666 treatment, this hyper-osmotic shock decreased SH3BP1 localization to the plasma membrane by 2 fold (Figure 4.2a-b ;Whitacre et al., 2001; Miermont et al., 2019).

To our knowledge, SH3BP1 is only the third BAR domain protein identified to respond to plasma membrane tension changes in cells (Vidal-Quadras et al., 2017; Tsujita, Takenawa, and Itoh, 2015). Interestingly, *in vitro* studies have previously explored the link between membrane tension, curvature-sensitivity and protein density based on BAR protein AMPH2 (Sorre et al., 2012). Furthermore, more recent simulations confirmed that mechanical properties of the membrane can affect BAR proteins association. Specifically, elevated membrane tension alters protein association geometries by impairing their interactions (Simunovic and Voth, 2015). These, and other findings suggest that BAR domain proteins could act as membrane tension sensors and relate changes in plasma membrane mechanics to regulate the cytoskeleton through controlling GTPases (Kreuk and Hordijk, 2012; Diz-Muñoz, Fletcher, and Weiner, 2013). For this, SH3BP1 is a plausible candidate as it contains both curvature-sensitive BAR domain protein and RhoGAP domain that is directly involved in GTPases inactivation.

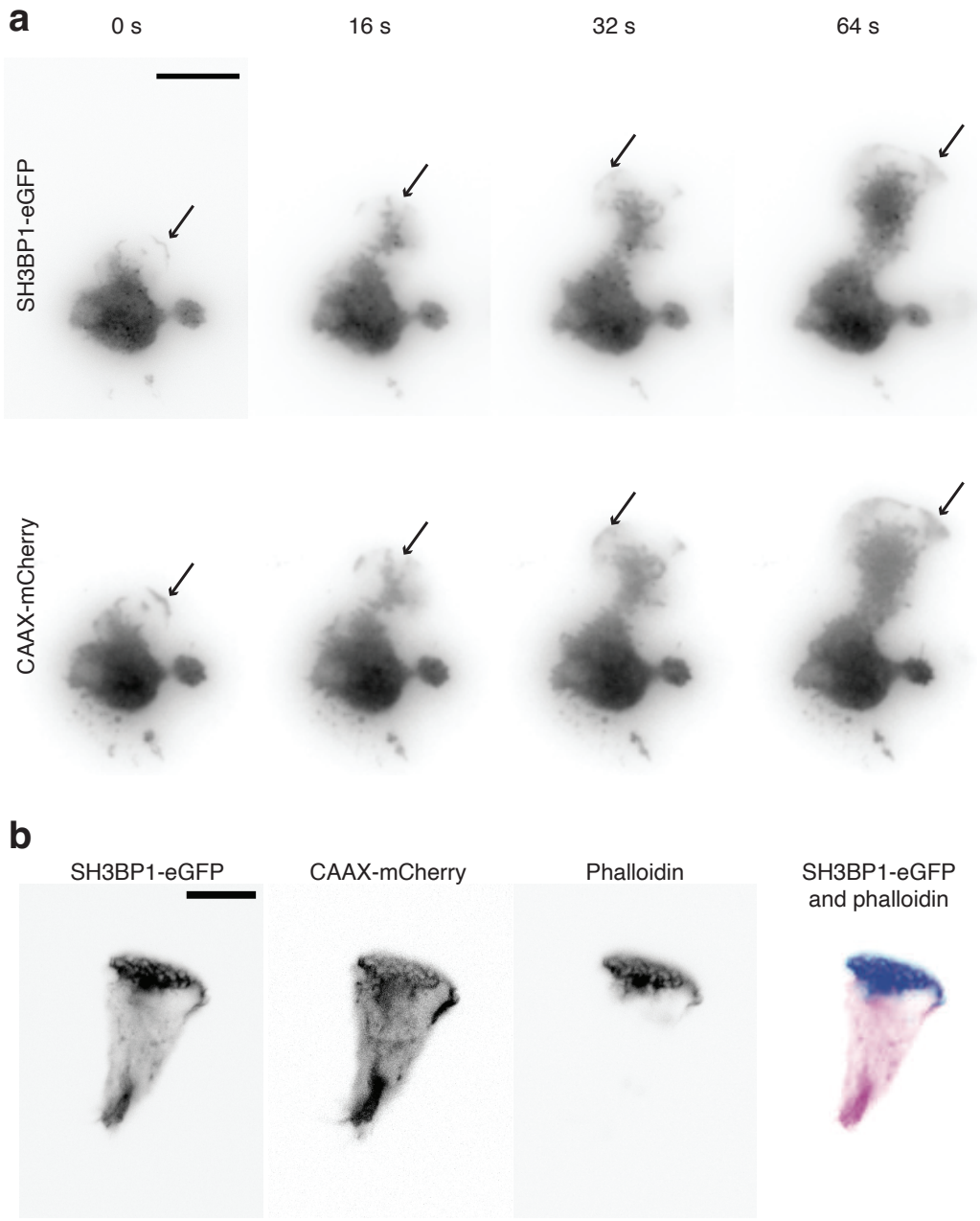

FIGURE 4.1: SH3BP1 localizes to the leading edge of migrating dHL-60 cells. a. Time lapse of TIRFM imaging of an eGFP-tagged SH3BP1 and an mCherry-tagged CAAX (membrane marker) in migrating dHL-60 cells. Arrows point towards the leading edge regions b. Epi-fluorescent imaging of dHL-60 cells fixed during migration expressing an eGFP-tagged SH3BP1, mCherry-tagged CAAX and with visualized F-actin (staining by phalloidin). Scale bar = 10 μm.

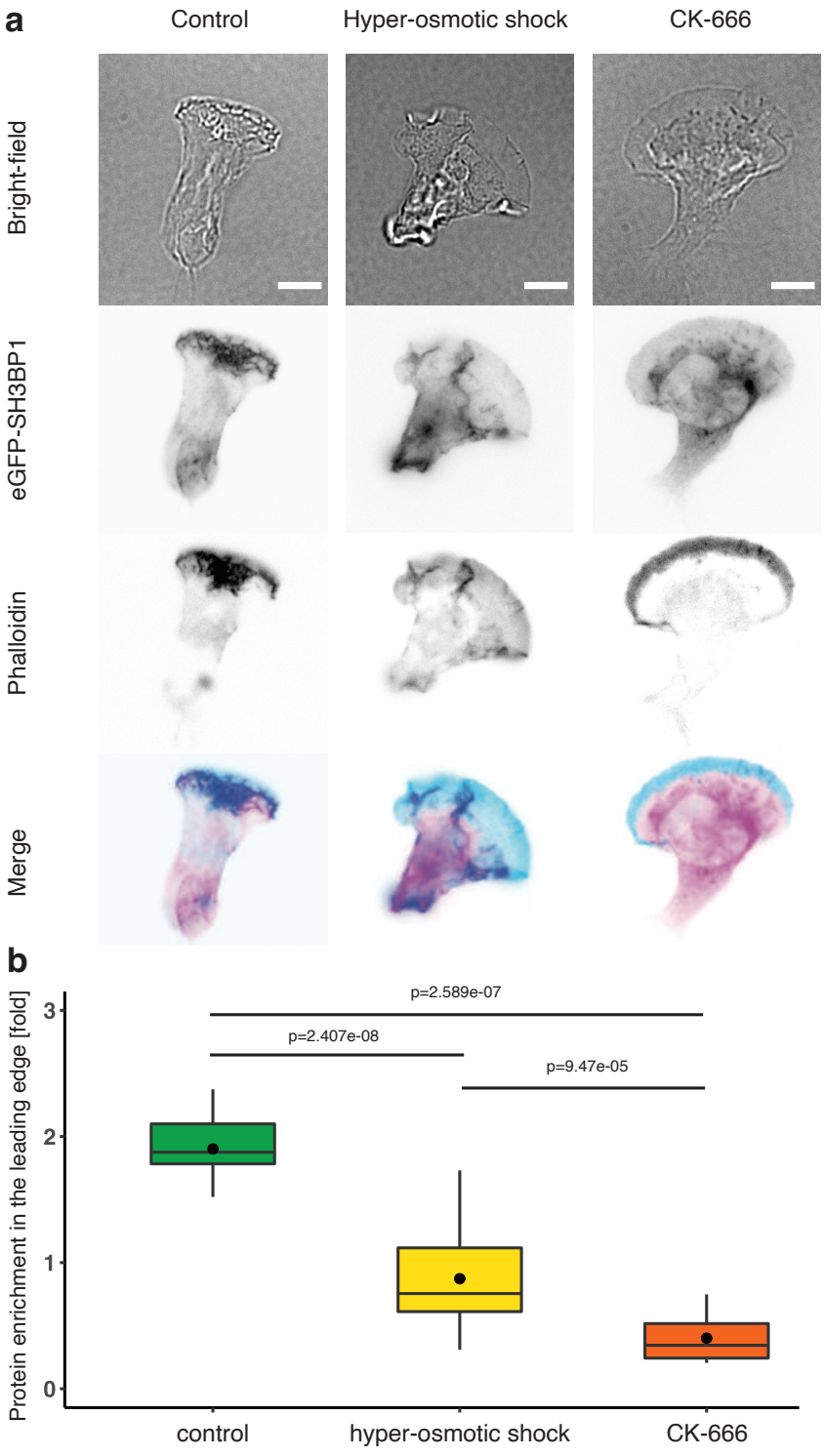

FIGURE 4.2: SH3BP1 localises to the leading edge of dHL-60 cells in a tension-dependent manner. a. Bright-field and fluorescent images of fixed dHL-60s showing eGFP-SH3BP1, phalloidin and their overlay in control conditions, after hyper-osmotic shock or after CK-666 treatment and b. quantification (control: n = 15; hyper-osmotic shock: n = 21; CK-666: n = 11). Scale bar = 10 μm. Data from 2 independent experiments. Statistics: T-test and Mann-Whitney-U-Test.

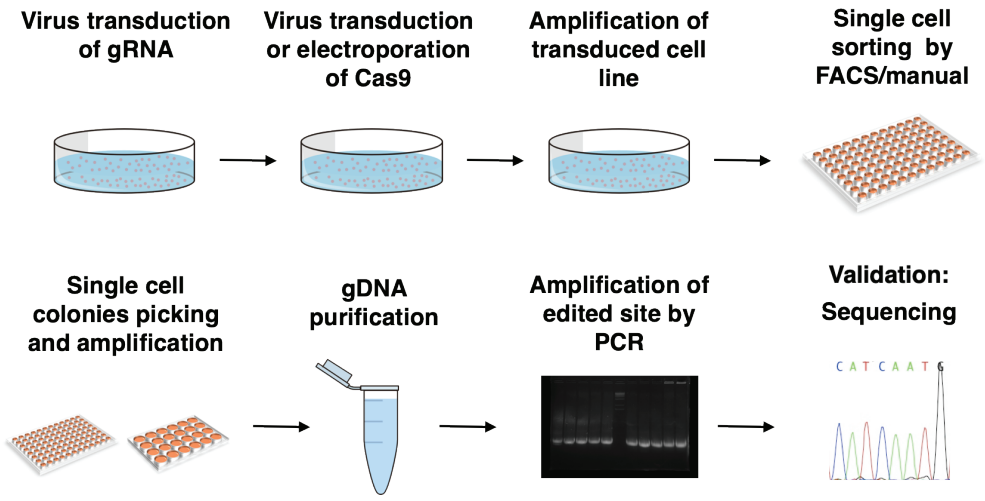

FIGURE 4.3: Schematic of a knockout HL-60 cell line generation using CRISPR/Cas9 technology.

4.3.2 Generation and validation of SH3BP1 knockout HL-60 cell line

To understand the role of SH3BP1 to a greater detail we generated an SH3BP1 knockout cell line using CRISPR/Cas9 technology following a similar strategy as presented previously (Methods 7.13; Graziano et al., 2017; Graziano et al., 2019). Shortly, undifferentiated wild type cells were transduced using lentiviral vectors containing a puromycin-selectable gRNA targeting one of the two different locations aimed at a region at the beginning of the sequence corresponding to exon 1, around 1 and 6 amino acids (prior to BAR domain sequence). Following puromycin selection, cells were transduced or electroporated with lentiviral vectors containing *S. pyrogenes* Cas9 sequence fused to BFP. After recovery and proliferation, BFP-positive cells were single-cell sorted. Single-cell clones were further assessed by gDNA purification and sequencing (Figure 4.3).

Out of 90 single-cell clones screened by sequencing, 7 were identified as potential knockout cell lines due to disruptions of the starting codon caused by a deletion or an insertion of amino acids. These clones were further validated by Western Blotting and clone #45 was identified as the best candidate and is further referred to as the SH3BP1 knockout cell line (Methods 7.15; Figure 4.4a-b). Confocal imaging of migrating dHL-60 cells stained with antibody against SH3BP1 revealed its presence at the leading edge and in the cell body in wild type cells, but its lack in SH3BP1 knockout, as expected (Figure 4.4c; Methods 7.16; 7.17). Next, we validated differentiation efficiency of the SH3BP1 knockout cell line by quantification of CD11b staining using FACS (Methods 7.18). By doing so, we confirmed that SH3BP1 knockout cells do not show any defects in differentiation (Figure 4.4d). Furthermore, we confirmed that the knockout generation procedure using guide RNAs for targeting SH3BP1 sequence does not affect differentiation (Figure 4.4d). To make sure that the SH3BP1 knockout does not affect division of HL-60 cells, we measured the number of cells for over 40 hours of growth in control and SH3BP1 knockout cells. We found no changes in the growth rate between the two conditions (Figure 4.4e). In summary, we validated the generation of an SH3BP1 knockout cell line that can be used to investigate the role of this protein for cell surface properties and migration as it does not influence cell differentiation or division.

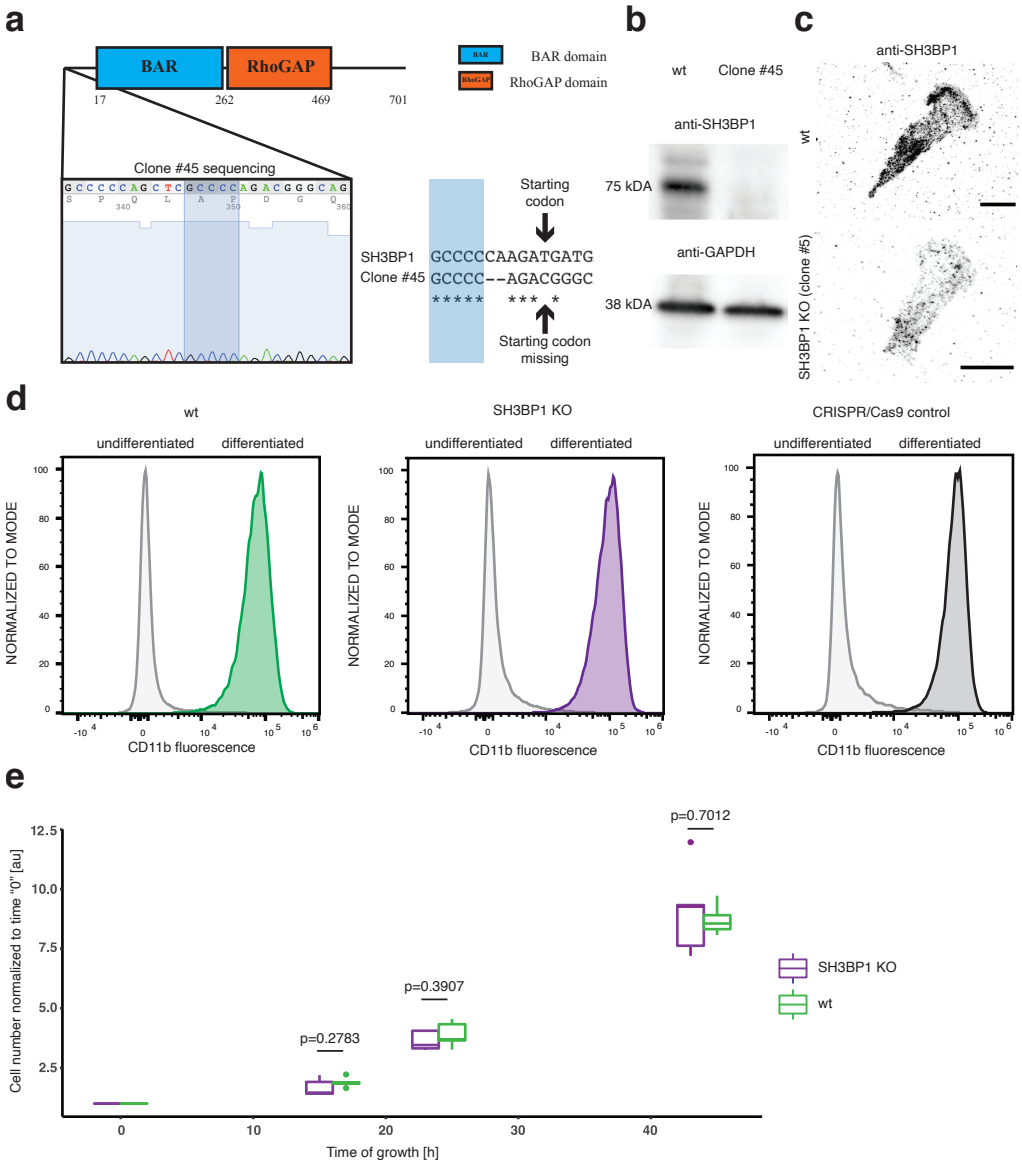

FIGURE 4.4: SH3BP1 knockout cell line validation. a. Clone #45 sequencing confirming disruption of a starting codon. b. SH3BP1 and GAPDH Western Blots of wild type HL-60 cells and promising SH3BP1 KO clone #45. c. Max intensity projections from confocal imaging of migrating control and SH3BP1 knockout dHL-60 cells stained with anti-SH3BP1. Contrast and brightness are adjusted identically. d. Representative histograms of CD11b intensity of wild type, SH3BP1 KO and CRISPR/Cas9 control of HL-60 cells before and after 5 days of differentiation in 1.5% DMSO. e. Growth curves of wild type and SH3BP1 KO cells from 3 independent experiments. Scale bar = 10 μm. Statistics: T-test.

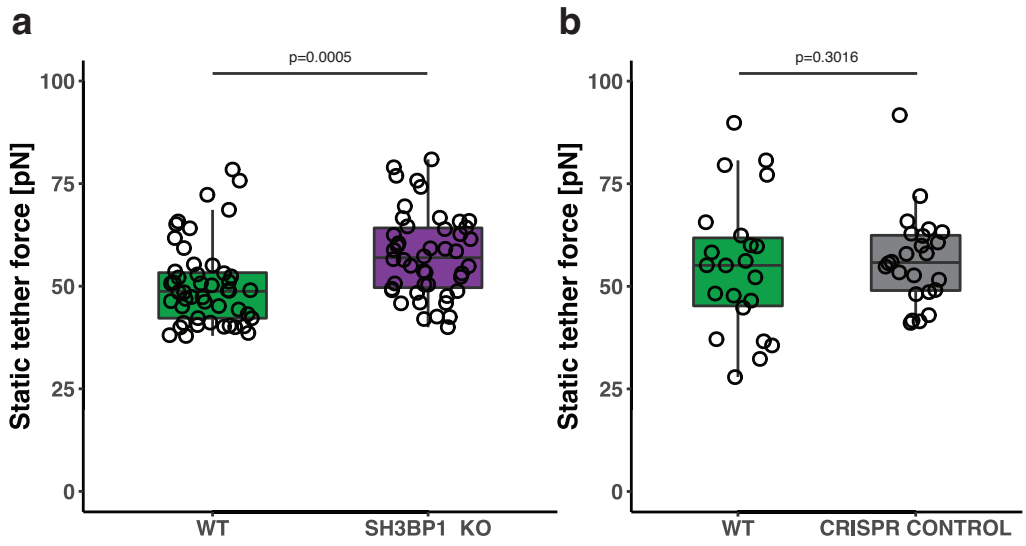

FIGURE 4.5: SH3BP1 knockout increases membrane tension in dHL-60 cells. a. Mean static tether force of wild type (n = 48) and SH3BP1 KO (n = 46) dHL-60 cells from 7 independent experiments. b. Mean static tether force of wild type (n = 24) and CRISPR control (n = 24) dHL-60 cells from 4 independent experiments. For data presented in each plot, the data for all conditions was always collected with the same cantilever per one independent experiment to account for variability introduced by the system. Statistics: Mann-Whitney-U-Test.

4.3.3 Membrane tension is increased in the SH3BP1 knockout cell line

SH3BP1 localizes in a tension-dependent manner to the plasma membrane and the leading edge. Inspired by these observations, we wondered if, in turn, SH3BP1 can contribute to plasma membrane tension homeostasis. To test it, we directly measured the tether force of the SH3BP1 knockout by static tether pulling using Atomic Force Microscopy (Figure 5.15; Methods 7.19; Diz-Muñoz et al., 2016a; Graziano et al., 2019). In a typical experiment, we approach and contact the cell using a cantilever coated with concanavalin A, that is a glycoprotein-binding plant lectin. After the contact, we retract the cantilever to pull an actin-free membrane tether. If a tether breaks before actin polymerizes inside it, we can measure the tether force by analyzing the force experienced by the cantilever before and after the tether breaks.

Static tether pulling experiments revealed an increase in the mean tether force in SH3BP1 knockout (mean = 57.58 pN) in comparison to control cells (mean = 50.37 pN) that corresponds to membrane tension values of 155.52 μN/m and 119.01 μN/m, respectively (Figure 4.5a; Methods 7.19). We wanted to make sure that the observed changes in the tether force are a result of a protein knockout only, and that they do not come from unexpected effects of the specific guide RNAs, the knockout generation protocol or effects of single cell clones. To that end, we compared static tether forces in wild type cells and a single cell clone that went through the knockout generation protocol, but was not edited. As expected, no changes could be observed between the two conditions (Figure 4.5b).

4.3.4 Migration of SH3BP1 knockout cells in complex environments

As changes in membrane tension are related to migration phenotypes, we decided to test if cells devoid of SH3BP1 display differences in cell migration. Several experiments with migrating single cells, including static tether pulling by AFM, require the cells to be placed on a flat substrate. This restraint dramatically changes the amount and types of protrusions as well as environmental cues that are key for guiding cell migration (Fritz-Laylin et al., 2017). To mimic the complexity of a natural *in vivo* environment of neutrophils in which compression forces exist, while keeping a high control over the experimental setup, we decided to take advantage of microfluidic devices, also called micro-fabricated PDMS-based devices. They allow the investigation of cell migration under confinement in a high-throughput manner with the possibility of providing the 3D environment that is tailored to particular scientific questions (Renkawitz et al., 2018; Yamada and Sixt, 2019). To fulfill their function, neutrophils in the *in vivo* setting need to squeeze through tissues, which require high deformation capabilities.

First, we exploited PDMS-based devices with long microchannels containing a constriction in the middle that was mimicking a challenging environment in which cells are required to deform considerably to perform their function (Figure 4.6a). Analysis of migrating dHL-60 cells through microchannels revealed that SH3BP1 knockout cells are more efficient than wild-type cells (Figure 4.6b-c). Specifically, SH3BP1 knockout cells migrate faster through channels and are faster at passing through a constriction that requires high deforming capabilities (Figure 4.6b-c). Further, we tested both cell lines in even more complex environments using microfluidic devices that have a decision point in the middle (Figure 4.7a). In these devices cells encounter channels of different constriction sizes and need to choose the best path and navigate through it. Recent studies revealed that leukocytes, including neutrophils, probe their closest environment and efficiently choose the path of least resistance (Renkawitz et al., 2019). Quantification of time required to pass through a decision point showed that SH3BP1 knockout cells are faster than control cells at navigating efficiently in this type of complex environment (Figure 4.7b-c). Furthermore, the knockout cells are not only faster than the wild-type cells, but they also choose statistically significantly more often the largest pore as confirmed by the distribution of frequency of choosing a particular constriction size (Figure (4.7d). This suggests that SH3BP1 knockout facilitates efficient probing of complex environment to find the path of least resistance.

Interestingly, many of the previous studies observed decrease in migration speed after SH3BP1 depletion. In contrast, we find that SH3BP1 knockout improves cell speed. These discrepancies may be due to differences in the migration assay's employed, as previous studies focused on wound-healing and scratch experiments in which cells move on a flat substrate. Moreover, here, we investigate for the first time the role of SH3BP1 in cells that use the amoeboidal mode of migration. This suggests that SH3BP1 may be an important protein for regulating cell motility, but its function can be adjusted depending on the migration mode and complexity of the surrounding environment. Thus, further experiments are required to dissect the specific role of SH3BP1 in controlling membrane and actin cytoskeleton remodeling in environments of varying complexity.

Previous studies evaluated changes in static tether forces and migration capacities upon depletion of important proteins involved in organization of cell cytoskeleton and motility. For example, knockout of WAVE2 complex and knockdowns of mTORC2 and PLD2 led to an increase in static tether force by around 20 pN, 14

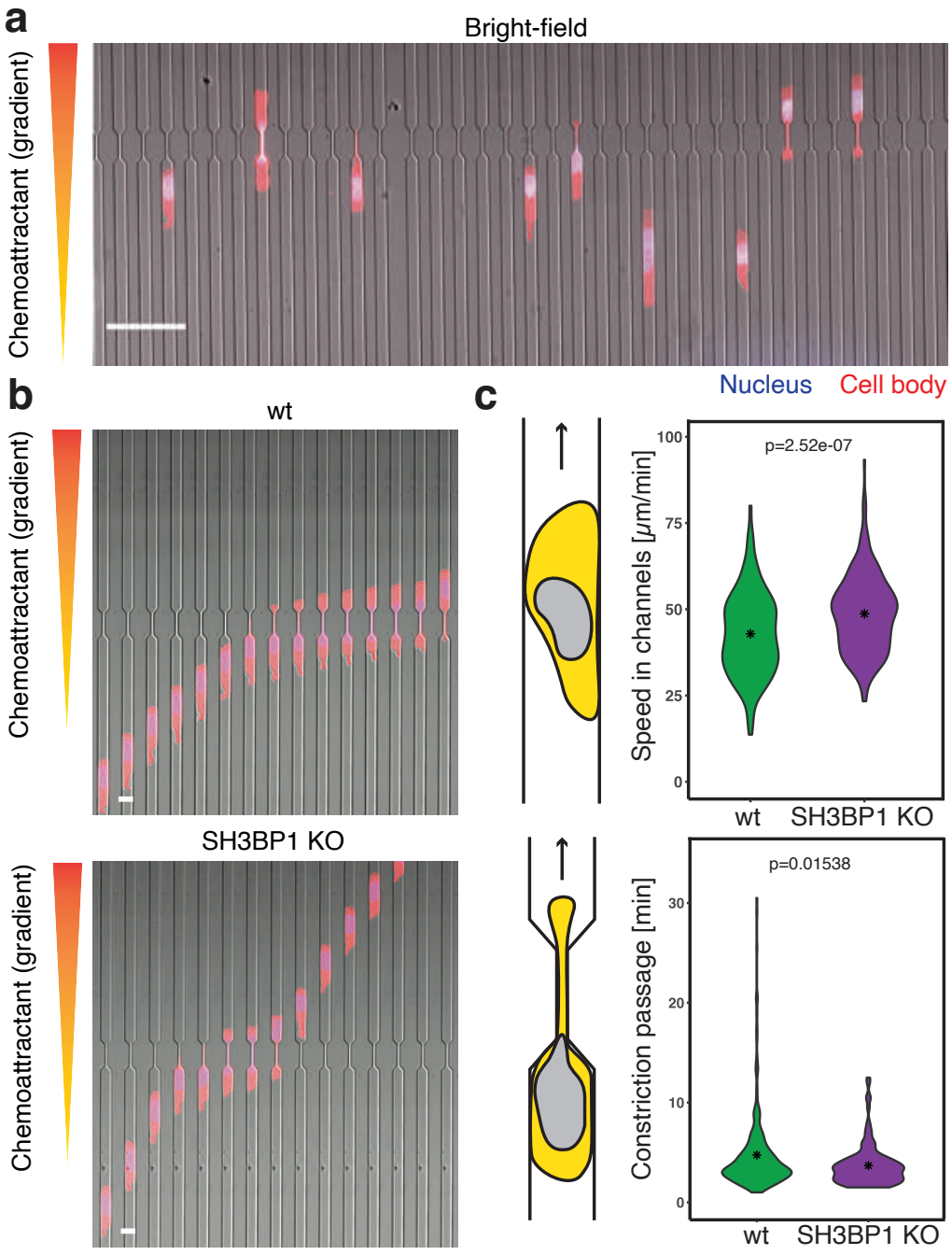

FIGURE 4.6: SH3BP1 knockout migrates and squeezes through a constriction faster in microfluidic devices than wild type cells. a. Overlay of bright-field, nuclei and cell body images of dHL-60 cells migrating in PDMS-based devices. Scale bar = 50 μm. b. Time lapse of wt and SH3BP1 KO cells squeezing through constriction. Time in-between frames is 30 seconds. Scale bar = 10 μm. c and d. Schematics of migration assay using microfluidic devices and quantification of migration speed in straight channels and constriction passage time (n = 235 for wt, n = 207 for SH3BP1 KO). Data acquired jointly with J. Stopp. Data from 3 independent experiments. Statistics: Mann-Whitney-U-Test.

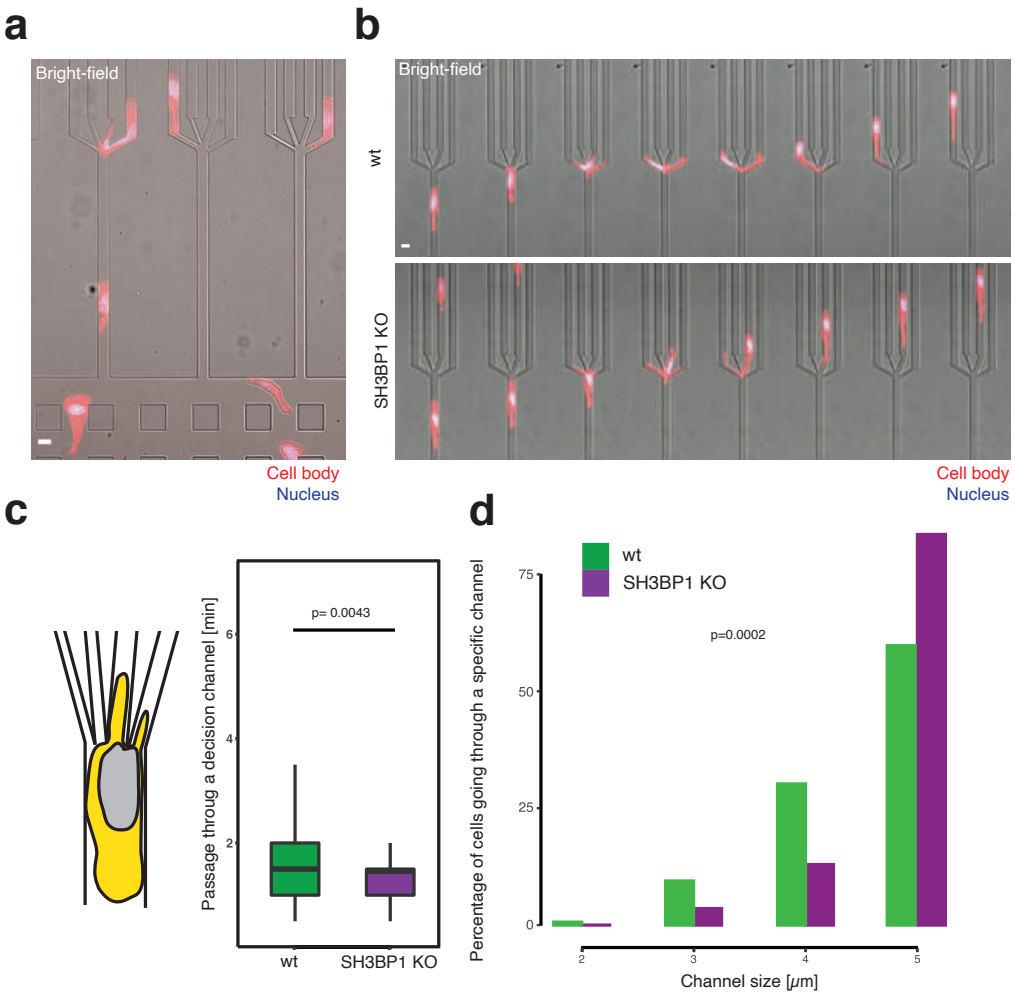

FIGURE 4.7: SH3BP1 knockout migrates faster through a decision point and more efficiently chooses the path of least resistance. a. Overlay of bright-field, nuclei and cell body images of dHL-60 cells migrating in PDMS-based devices with a decision point. b. Time lapse of wt and SH3BP1 KO cells navigating through a decision point. Time in-between frames is 30 seconds. c. Schematic of migration assay using microfluidic devices with a decision point and quantification of passage time (n = 159 for wt, n = 85 for SH3BP1 KO) in dHL-60 cells. d. Frequency of wt and SH3BP1 KO dHL-60 cells choosing a channel of a certain size (n = 159 for wt, n = 85 for SH3BP1 KO). Data from 3 independent experiments. Data acquired jointly with J. Stopp. Statistics: Mann-Whitney-U-Test.

pN and 9 pN, respectively (Diz-Muñoz et al., 2016a; Graziano et al., 2019). Furthermore, knockdown of mTORC2 and PLD2 in HL-60 cells impaired migration, increased actin polymerization upon chemoattractant stimulation, induced more WAVE2 fronts and decreased mTORC2 activation upon membrane tension increase caused by hypo-osmotic shock (Diz-Muñoz et al., 2016a). All the above-mentioned effects result from a disruption of a negative feedback loop in which membrane tension acts both as a direct inhibitor of actin polymerization and an indirect inhibitor of WAVE2 complex through an mTORC-PLD2 pathway (Diz-Muñoz et al., 2016a). A yeast ortholog of mTORC2 was also found to be regulated by plasma membrane tension. Stretching of the yeast plasma membrane changes localization of Slm proteins that promote TORC2-mediated signaling (Niles et al., 2012; Berchtold et al., 2012). In turn, upon decrease in membrane tension, TORC2 is inactivated by PIP_2 (Riggi et al., 2018). In contrast to TORC2, membrane tension-mediated regulation of mammalian TORC2 is less understood.

The increase in membrane tension caused by the SH3BP1 knockout and its enhances migration motivated us to consider it as a potential component of the mTORC2-PLD2 pathway. This hypothesis could be indirectly supported by some of the findings in the field. First, another BAR domain protein FBP17 was proposed to link membrane tension and actin polymerization through modulating NWASP/WASP (Tsujita, Takenawa, and Itoh, 2015). Important to note is that NWASP/WASP belong to the same group of proteins as WAVE2. Furthermore, it was proposed that curvature-sensitivity of BAR domains could be modulated by varying levels of membrane tension. Thus, BAR domain proteins could potentially regulate GAPs and GEFs depending on their membrane binding which can be influenced by membrane tension (Diz-Muñoz, Fletcher, and Weiner, 2013). Second, Rac1, a GTPase, was shown to regulate the activity of mTORC2 upon growth factor stimulation (Saci, Cantley, and Carpenter, 2011). On the other hand, depletion of an essential component of mTORC2 - Rictor, reduces the activity of Rac1 and Cdc42 (He et al., 2013). Interestingly, SH3BP1 has the ability to regulate Rac1 and its loss of function leads to changes in protrusion dynamics and impairs migration, suggesting that there could be a biochemical link between SH3BP1 and mTORC2-PLD2 pathway (Parrini et al., 2011).

4.3.5 The role of SH3BP1 in the mTORC-PLD2 pathway

As the changes in membrane tension and directed cell migration in the SH3BP1 knockout resemble the outcome of disrupting the mTORC-PLD2 pathway, we decided to test whether it is involved in this mechanosensory pathway. To do so, we took advantage of the fact that mTORC2, in response to chemoattractant stimulation or membrane stretching, phosphorylates the serine/threonine protein kinase Akt at position S473. Upon the depletion of mTORC2 or PLD2, Akt phosphorylation is strongly reduced (Diz-Muñoz et al., 2016a). Thus, if SH3BP1 knockout interferes with the mTORC2-PLD2 pathway, a similar effect on mTORC2 activation is expected. We assessed the levels of Akt phosphorylation at S473 by antibody staining of fixed wild type and SH3BP1 knockout cells after exposure to chemoattractant (Methods 7.20). We could observe a slightly lower increase (not statistically significant) in pAkt S473 staining upon chemoattractant stimulation in SH3BP1 knockout cells in comparison to control. This suggests that SH3BP1 might be involved in mTORC2-dependent actin regulation, albeit not as the sole driver (Figure 4.8a). To validate this, we looked into the actin polymerization dynamics that are downstream of mTORC2 and PLD2 (Diz-Muñoz et al., 2016a).

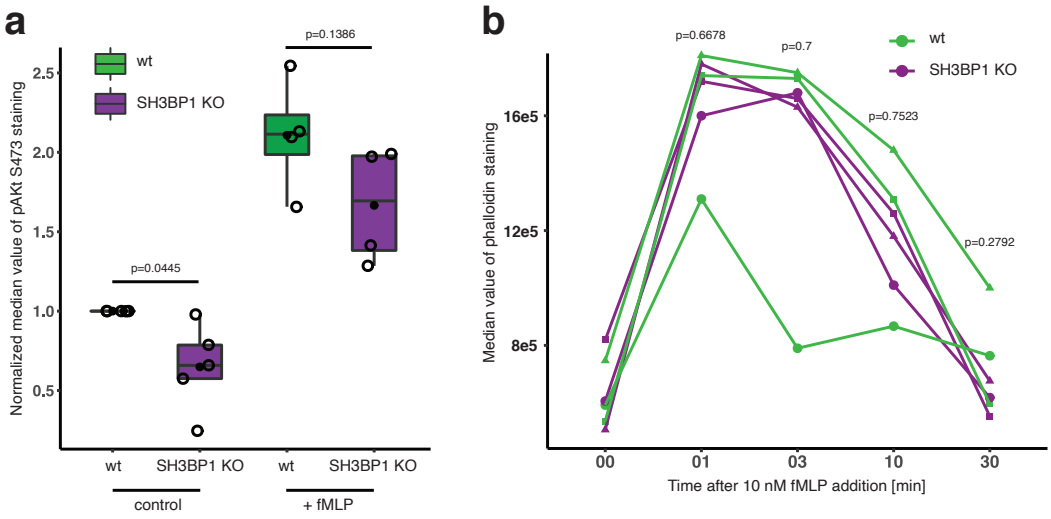

FIGURE 4.8: SH3BP1 knockout mildly affects mTORC2 activation, but does not change F-actin polymerization. a. mTORC2 activation 5 minutes after chemoattractant stimulation (10 nM fMLP) in wild type and SH3BP1 KO dHL-60 cells. Data from 2 independent experiments. b. Median value of phalloidin staining of fixed wt and SH3BP1 KO dHL-60 cells using FACS upon 10 nM fMLP stimulation. Data from 3 independent experiments. Statistics: T-test and Mann-Whitney-U-Test.

Actin levels measured by Western-Blotting in other cell lines were non affected by SH3BP1 knockdown in previous studies (Parrini et al., 2011). However, because of epithelial cells' slow migration in comparison to dHL-60s, actin polymerization dynamics and resulting membrane tension values differ greatly (Sitarska and Diz-Muñoz, 2020). To our knowledge, all measured membrane tension changes in dHL-60 cells were associated with either a decrease or an increase of actin polymerization mediated by WAVE2 and Arp2/3 complex (Diz-Muñoz et al., 2016a; Graziano et al., 2019). Surprisingly, for SH3BP1-mediated membrane tension increase, we did not observe a similar effect (Figure 4.8b; Methods 7.21). One explanation could be that the increase of membrane tension induced by the SH3BP1 knockout is not sufficient to activate the long range-negative feedback program. Alternatively, SH3BP1 could use a different mode of action than the canonical mTORC2-dependent actin regulation. For example, it could affect mechanical properties of the plasma membrane by curvature regulation in a WAVE2-Arp2/3-independent manner. In relation to this hypothesis, a recent study explored a new type of movement in neutrophil-like cells that is not relying on WAVE2-Arp2/3 machinery and proposed that it may be linked to the local membrane curvature (Graziano et al., 2019). Additionally, this work suggests that distinct molecular mechanisms may be activated depending on navigation through different environments.

Moreover, our data suggest that other properties of the actin network such as density or filament elongation could play a role in membrane tension and cell migration regulation. Considering that SH3BP1 is known to be involved in actin remodeling induced by capping protein (Elbediwy et al., 2012), it is tempting to speculate that capping of actin filaments is a potential way of regulating cell surface properties relevant for migration. Deregulation of barbed-end capping could result in changed distribution of the types of actin filaments in the network, promoting long actin filaments. It is still not clear, how different types of filaments contribute to

force generation at the plasma membrane. However, recent work showed that bending long actin filaments provide additional means of force generation (Akamatsu et al., 2020). In endocytosis, self-organization and bending of actin filaments depends on spatial distribution of proteins that link actin and coated endocytic pit that has a high curvature. As suggested, this mechanism may be more general and apply to other types of curved membranes, for example, it could be induced by BAR domain proteins such as SH3BP1. Possibly, changes in actin network properties may underlie improved cell speed in the SH3BP1 knockout.

What are the exact changes in the actin network and how do they affect cell motion, needs to be further investigated using methods that allow for actin network visualization. In relation to this, another study that focused on investigating fast-migrating leukocytes with nonfunctional WAVE2-Arp2/3 complex, showed that diversified protrusions at the leading edge slow the cells down. Apparently, diversified protrusions are key for exploring the surroundings. In contrast, non-branched actin filaments increase speed and directional persistence of cells (Leithner et al., 2016). SH3BP1, together with RacGEFs might promote unceasing GDP/GTP cycling of Rac1 at the leading edge of migrating cells, facilitating turnover of protrusions. Changes in the dynamics of Rac1 inactivation may thus have an effect in cell migration as well as in probing of the surrounding environment. Further experiments, for example by visualizing Rac1 activity at the cell front of SH3BP1 knockout cells in various environmental setups, are needed to explore this direction.

4.3.6 Summary

SH3BP1, a protein characterized by containing BAR and RhoGAP domains, was found to be responsive to membrane tension changes induced by Arp2/3 inhibition and osmotic shocks. To further investigate the role of SH3BP1, we generated a knockout cell line by CRISPR/Cas9 that did not affect differentiation or division. By quantitative measurements using Atomic Force Microscopy, we revealed that SH3BP1 knockout elevates static tether force values that under certain assumptions are directly proportional to membrane tension. To our knowledge, SH3BP1 is the first BAR domain protein proved to be involved in maintaining membrane tension homeostasis in cells, or more globally, affecting cell surface mechanics. However, it does not seem to act through mTORC2 and PLD2, a signaling pathway that was previously identified in neutrophil cells (Diz-Muñoz et al., 2016a). Interestingly, the SH3BP1 knockout makes neutrophil-like cells faster and more efficient at squeezing and path finding than control cells in three-dimentional environments. Our results indicate a complex interplay between migration modes, roles of protrusions and membrane mechanics. In previous work, the lack of SH3BP1-mediated Rac1 inactivation disorganized protrusions. This, resulted in impaired movement of epithelial cells (Parrini et al., 2011). On the other hand, the plasticity and dynamics of protrusions may improve sensing and adaptation to the surroundings to drive efficient migration in complex environments (Leithner et al., 2016). This, can be particularly important for highly motile cells in three-dimentional environment that need to change direction and find the most efficient path, although may be dispensable for other types of migration (Parrini et al., 2011; Fritz-Laylin et al., 2017). Altogether, we found that SH3BP1 plays an important role in directed cell migration as its depletion facilitates efficient path finding.

Chapter 5

Snx33 (Sorting nexin 33)

5.1 Abstract

Neutrophils are highly versatile cells of the innate immune system that form the first line of the host defence when recruited from the blood stream to the sites of inflammation in order to target invading pathogens (Kruger et al., 2015; Lehman and Segal, 2020). To reach the site of inflammation, they need to be highly migratory for which they undergo dramatic morphological changes (Roberts and Hallett, 2019; Kameritsch and Renkawitz, 2020). BAR domain proteins are often associated with changes in cell shape and behaviour (Simunovic et al., 2019). Here, we describe how a curvature-sensitive BAR domain protein, Snx33, contributes to the control of actin-rich protrusions at the leading-edge, also called lamellipodia. We find that Snx33 controls lamellipodia by regulating WAVE2-driven actin polymerization. Moreover, we show that Snx33 knockout displays defective navigation through particular complex environments and cell behaviour upon collisions. Next, based on our results as well as the available literature, we propose a more generalized explanation for how Snx33 affects the regulation of cell migration by inhibitory effects on WAVE2 complex. In summary, we demonstrate that Snx33, a curvature-sensitive and membrane remodeling BAR domain protein, is key to direct cell motility in complex environments by controlling lamellipodia.

5.2 Introduction to Sorting nexin 33 (Snx33)

5.2.1 The biological roles of sorting nexins

Snx33 belongs to a diverse group of sorting nexins (SNX) that are membrane-associated cellular trafficking proteins. They were first identified 24 years ago from a yeast two-hybrid screen set up to look for proteins binding to the EGFR (Kurten, Cadena, and Gill, 1996). Sorting nexins are characterized by the presence of the PX ndomain which binds various phosphoinositides that target sorting nexins to cellular membranes enriched in specific phospholipids. Interestingly, PX domains were found to bind SH3 domains, both intramolecularly and intermolecularly, with their polyproline loop as well as to stimulate phosphoinositide kinases suggesting a positive feedback mechanism of their action (Teasdale and Collins, 2011). Sorting nexins contain several domains, among others, CC, SH3, PXA, and BAR. Thanks to their specific targeting capabilities and the presence of several domains involved in protein-protein interactions, sorting nexins were shown to maintain several cellular functions in endosomal sorting, vesicular trafficking, signaling and regulation of plasma membrane receptors (Worby and Dixon, 2002).

Within the sorting nexins we can distinguish a subgroup, that is characterized by containing a BAR domain, encompassing: Snx1, Snx2, Snx4, Snx5, Snx6, Snx7,

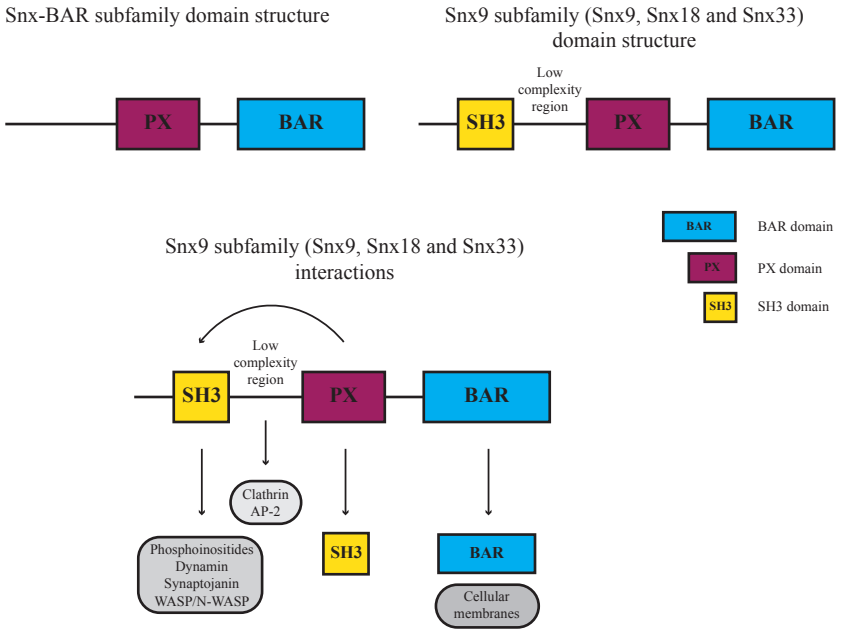

FIGURE 5.1: Domain structures and interactions of Snx-BAR and Snx9 subfamilies. Snx9 subfamily consists of Snx9, Snx18 and Snx33. See text for members of Snx-BAR subfamily.

Snx8, Snx9, Snx18, Snx30, Snx32 and Snx33. So far, Snx-BAR proteins have been shown to coordinate membrane deformation in endocytosis, endosomal sorting and receptor turnover at the plasma membrane. Moreover, defects in functioning of the BAR domain in sorting nexins can lead to neurodegenerative and cardiovascular diseases as well as tumorigenesis (Yang et al., 2019; Zhang et al., 2018). Snx9, Snx18 and Snx33, that belong to the Snx9 subfamily, additionally contain the SH3 (Src Homology 3) domain which mediates interactions with cytoskeletal proteins such as dynamin, synaptojanin, WASP and N-WASP, to name some. The linker region between SH3 and PX domain is referred to as the low-complexity region and can contain sequences with ability to bind clathrin and AP-2 (Weering, Verkade, and Cullen, 2010). As such, sorting nexins containing SH3-PX-BAR domains become interesting candidates for coordinating the processes that occur at the plasma membrane-cytoskeleton interface (Figure 5.1).

5.2.2 SH3-PX-BAR subfamily

Snx9, Snx18 and Snx33, the three members of the Snx9 subfamily of mammalian sorting nexins, have shown to play a role in phagocytosis, autophagy, macropinocytosis and mitosis (Zhang et al., 2009; Wang et al., 2010; Knævelsrud et al., 2013). Interestingly, Snx33 appeared as one of the top hits in the screening platform presented in the previous section (Section 3.1) where we aimed at identifying the BAR domain proteins' RNA expression mostly enriched during the process of HL-60 cells differentiation. Among sorting nexins containing a BAR domain, Snx33 is clearly highly enriched in this process, followed by Snx9 and Snx18 (Figure 5.2).

In *Drosphila*, the Snx9 subfamily is encoded by a single gene *sh3px1*. Intriguingly, depletion of *sh3px1* in S2 cells results in defective lamellipodia formation. On the other hand, its overexpression induces the formation of tubules and protrusions, an

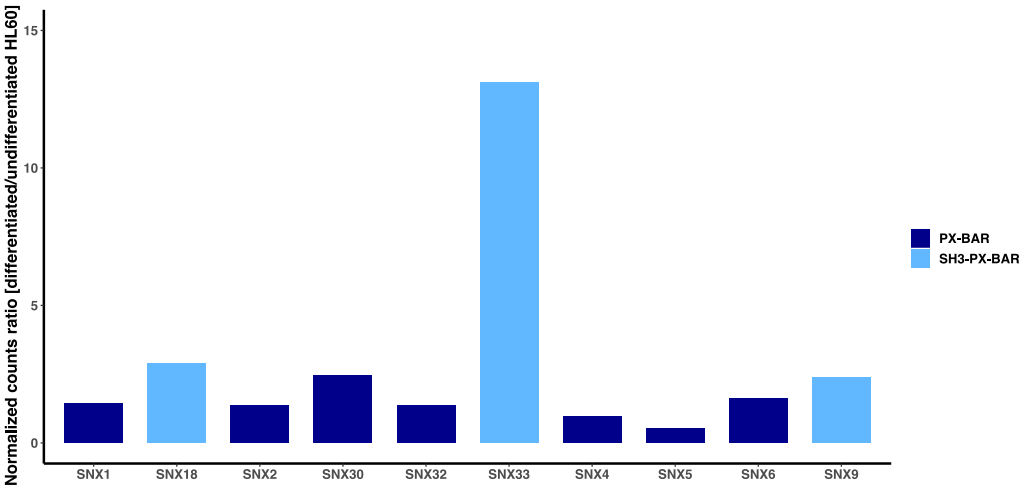

FIGURE 5.2: Normalized counts of non-migratory to migratory HL-60 cells ratio for sorting nexins that contain BAR domain protein. Bars indicate mean of from 3 independent experiments.

effect specific for the PX-BAR domain (Hicks et al., 2015). S2 cells can form lamellipodia once they are attached to the surface, but they are not migratory. Nevertheless, *sh3px1* depletion and overexpression phenotypes clearly indicate a role of the SH3-PX-BAR subfamily in the regulation of lamellipodia formation. The localization and overexpression effects of the mammalian members of the SH3-PX-BAR family have also been tested in S2 cells (Hicks et al., 2015). In agreement with overexpression of *sh3px1*, they did show striking similarities in membrane tubulation, but also differences in localization. In summary, these studies suggest that Snx9 subfamily proteins may have both unique and complementary roles.

5.2.3 Structural and biological insights into sorting nexin 33

Snx33 is one of the most recently discovered and the least explored sorting nexin. As a member of the Snx9 subfamily, it shares its domain structure with Snx9 and Snx18, containing an N-terminal SH3 domain followed by a low-complexity region, a PX domain and a C-terminal BAR domain. Snx33 is ubiquitously expressed in several cell lines and tissues (Zhang et al., 2009; Håberg, Lundmark, and Carlsson, 2008). Little is known about its specific function, but it has been shown to be involved in the regulation of cell shape in HeLa and MCF7 cells (Zhang et al., 2009), affect actin polymerization through the interaction with WASP (Zhang et al., 2009), modulate endocytosis and the shedding of cell surface proteins such as PrPC (prion protein) and APP (amyloid protein precursor) by inhibiting dynamin (Schöbel et al., 2008; Heiseke et al., 2008). Moreover, it plays a role in the maturation of phagosomes containing internalized apoptotic cells in *C. elegans* (Almendinger et al., 2011), is required for fulfilment of cytokinesis in myosin II-dependent manner (Ma and Chircop, 2012) and involved in macropinosome formation (Ma and Chircop, 2012).

Similarly to all known BAR domain proteins, Snx33 forms dimers that act as a functional unit with the ability to bind and deform membranes. Snx33 engages in homodimerization, but conflicting findings have been reported regarding its heterodimerization. One study showed by co-immunoprecipitation that transiently expressed Snx9 and Snx33 can form heterodimers in HEK293T cells (Zhang et al., 2009). In contrast, another study concluded based on immunoprecipatation combined with mass spectroscopy and immunoblotting that neither of the Snx9 family

members exist in the form of intrafamily heterodimers in HeLa cells (Håberg, Lundmark, and Carlsson, 2008). These studies were corroborated by molecular modeling and mutational analysis, as the authors found that amino-acids within the BAR domain of Snx33 that allow homodimerization, at the same time exclude the formation of heterodimers with Snx9, Snx18 and Snx1 (Dislich, Than, and Lichtenthaler, 2011).

Snx33 is often described in the literature as having overlapping functions with its other family members (Snx9, Snx18) because they all share similar domain architecture, have membrane tubulating activity and affect similar processes e.g. endocytosis. On the other hand, there is also mounting evidence that clearly suggests divergent roles of all Snx9 family members. Snx33 shares only by half its sequence similarity with Snx9 and Snx18, and lacks motifs that bind AP-2 and clathrin present in the later two. Snx33 expression is ubiquitous, but its levels differ considerably from Snx18 and Snx9 in various tissues, as it was mainly found in the lung, pancreas and testis (Håberg, Lundmark, and Carlsson, 2008). Interestingly, even at the single cell level, the colocalization of exogenous Snx9 subfamily members could not be detected in HeLa cells, which similarly argues for their independent functions (Håberg, Lundmark, and Carlsson, 2008). Further, while all 3 proteins are known to be involved generally in endocytic processes, when their colocalization with endophilin was tested to investigate their presence in fast endophilin-mediated endocytosis (FEME), only Snx33 was identified with a significant percentage of positive spots indicative of participation in FEME (Hak et al., 2018).

The roles of the three Snx9 subfamily members are difficult to dissect as most studies take advantage of the overexpression or knockdown approaches that often does not allow to undoubtedly rule out their redundant roles. Therefore, in order to clearly understand the redundancy of Snx9 subfamily members as well as their distinct roles, it is needed to use knockout approaches. The observed phenotype in a knockout will be due to the lack of particular protein or cellular adaptation to its absence. Nevertheless, with this approach, distinct functions of a particular protein can be unravelled more probably, as redundant roles that require minimal concentration of this protein, provided in overexpression or knockdown, will not be detected.

5.3 Results and Discussion

5.3.1 Snx33 localizes to the folds at the leading edge of migrating dHL-60 cells

Snx33 is one of the most up-regulated proteins in differentiated and highly migratory HL-60 cells. We decided to test whether it localizes to the leading edge. To do so, we generated a stable cell line (Methods 7.7.2 and 7.7.1) with an eGFP-tagged Snx33 (Methods 7.34) and an mCherry-tagged CAAX motif that targets the plasma membrane. We differentiated (Methods 7.1) fluorescently tagged HL-60 cells and let them migrate for around 15 minutes on fibronectin-coated dishes. After fixation (Methods 7.23), we visualized Snx33, plasma membrane and F-actin (by phalloidin staining) using epifluorescent imaging (Methods 7.24). We observed that Snx33 localizes to the leading edge, where both F-actin and the membrane signal are enriched (Figure 5.3).

We quantified the intensity of Snx33 inside of the leading edge and the cell body, where we used F-actin as a leading edge marker. As a result, the mean intensity of Snx33 was on average higher by a factor 1.7 in the leading edge, when compared to the cell body, clearly showing that Snx33 is enriched in the leading edge (Figure

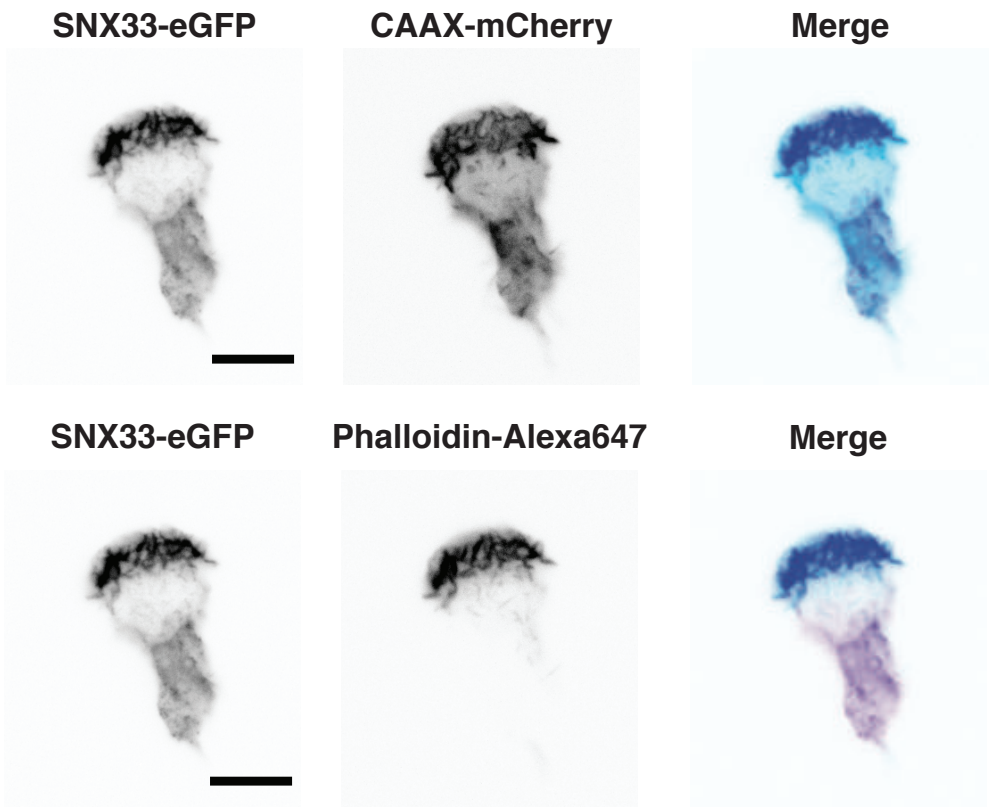

FIGURE 5.3: Epifluorescent imaging of a stable cell line expressing an eGFP-Snx33 and an mCherry-CAAX (membrane), stained with phalloidin. Scale bar = 10 μm.

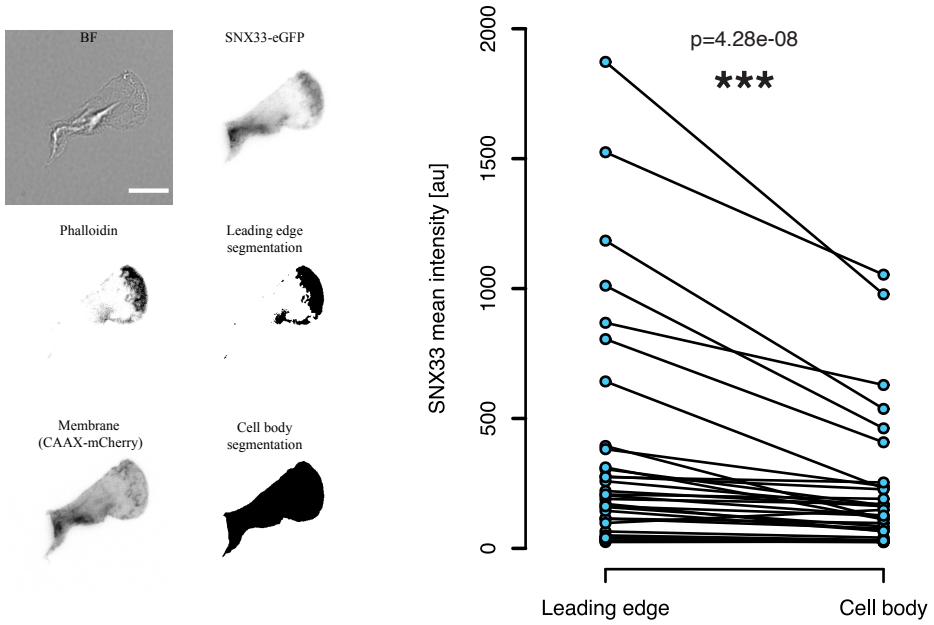

FIGURE 5.4: eGFP-tagged Snx33 mean intensity in the leading edge and cell body. Left panel: Examples of raw images and segmentations (cell body, leading edge). Right panel: Snx33 mean intensity in the leading edge (segmented based on the phalloidin signal) and the cell body (segmented based on the membrane signal field image. n = 33. Statistics: Paired Mann-Whitney-U-Test.

5.4; Methods 7.12). By performing time-lapse imaging of migrating cells, we corroborated the observation that Snx33 is indeed enriched at the leading edge (Figure 5.5; Methods 7.27).

Snx33 is a BAR domain protein and thus, has the ability to bind and deform membranes. We wondered whether its enrichment at the leading edge has a connection with membrane folds on the top part of the plasma membrane. Membrane folds have a very characteristic curvature landscape that we visualized by polarized-TIRFM during live-cell imaging (Methods 7.2) and by Scanning Electron Microscopy (SEM) (courtesy of M. Sandvold Beckwith) in fixed cells (Figure 5.6b-f).

To test if Snx33 resides at membrane folds, we acquired confocal images of migrating dHL-60 cells (Methods 7.17). Next, we measured the Pearson correlation coefficient (PCC) of Snx33 and membrane fluorescent signal in every z-plane from the confocal stack. For quantification, we took advantage of an available Fiji's COLOC2 plugin for colocalization analysis (Methods 7.26), a method used previously in a number of studies (Roca-Cusachs et al., 2013; Aaron, Taylor, and Chew, 2018). After normalization of the number of z-planes in each image, we observed that in the lower z-planes (closer to the coverslip), corresponding to the bottom plasma membrane, PCC values range from 0.2 to 0.3 (low, positive). In contrast, in the upper z-planes, corresponding to the upper parts of the plasma membrane, PCC values fluctuate around 0.4 (medium, positive) (Figure 5.7). Our analysis revealed that Snx33 fluorescence correlates stronger with the membrane fluorescence in the upper z-planes. Thus, it is plausible that Snx33 localizes not only to the leading edge, but more specifically, to the membrane curvature present in the folds in the upper

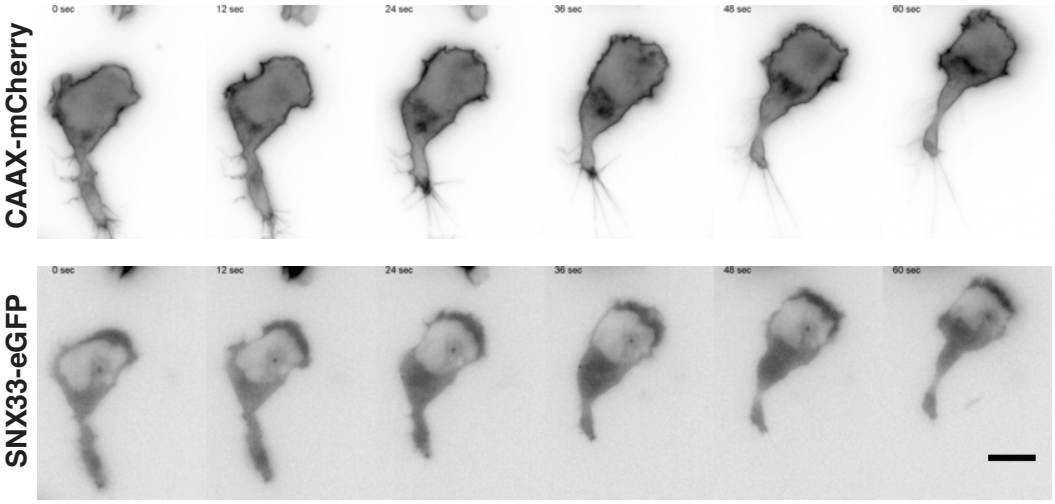

FIGURE 5.5: Time-lapse imaging of eGFP-tagged SNX33 (lower panel) and mCherry-tagged CAAX (upper panel) using epifluorescent microscopy. Scale bar = 10 μm.

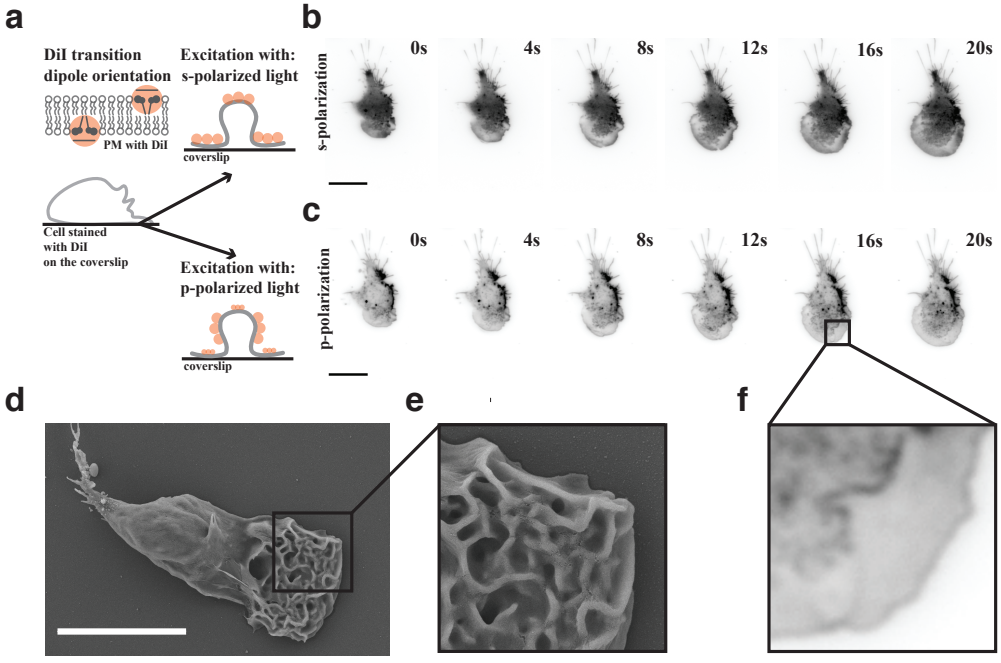

FIGURE 5.6: Membrane folds imaging. a. Schematic illustrating the principles of pTIRFM imaging. b. Time lapse pTIRFM imaging of a migrating HL-60 cell using s-polarization c. Time lapse pTIRFM imaging of a migrating HL-60 cell using p-polarization. d. Scanning electron microscopy (SEM) images of a migrating HL-60 cell. SEM data produced jointly with M. Sandvold Beckwith. e, f. Membrane folds zoom-in of (d,c, respectively). Scale bar = 10 μm.

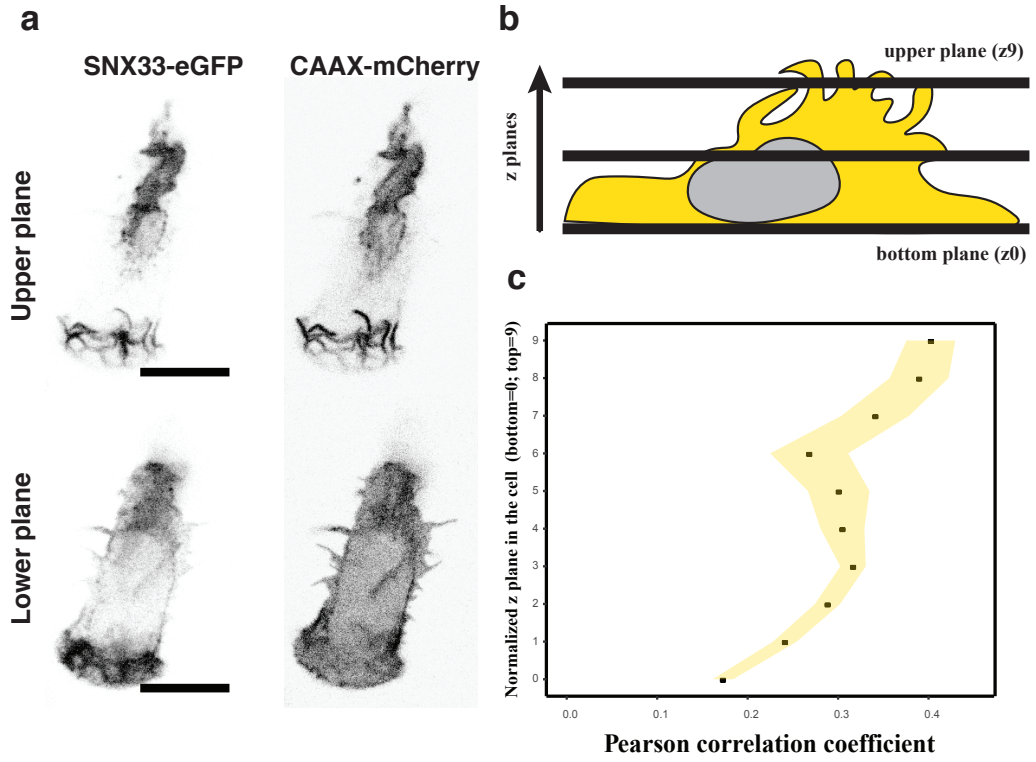

FIGURE 5.7: Snx33 is enriched at the top membrane folds. a. Confocal images of eGFP-Snx33 and mCherry-CAAX (membrane), upper and lower z-planes. b. Schematic illustrating experimental setup. c. Pearson correlation of eGFP-Snx33 and mCherry-CAAX in normalized z-planes. n = 10. Scale bar = 10 μm. Yellow indicates SEM.

part of the cell.

Additionally, we explored the PCC values of F-actin (visualized by phalloidin staining) and Snx33 fluorescence (Figure 5.8). F-actin signal had a PCC values around 0.2 (low, positive) at the extreme z-planes that correspond mostly to the lower and upper plasma membrane. In contrast, it reached values over 0.5 (high, positive) for middle z-planes, where the signal comes predominantly from the cytoplasm. The high positive PCC value of F-actin signal and Snx33 suggests that there is a considerable pool of cytoplasmatic protein that resides in the close proximity to F-actin. Previous studies are in agreement with our findings. First, Snx33 contains SH3 domain that is widely known to interact with a variety of cytoskeletal proteins (Kurochkina and Guha, 2012). SH3 domain is emerging as key, in for example I-BAR protein functions, in signal transduction and cell migration, so it could play a similar role in other BAR domain proteins, such as sorting nexins (Li et al., 2016). Second, Snx33 was already reported to partially localize cytoplasmatically (Zhang et al., 2009; Hicks et al., 2015). Third, there are reports stating that Snx33 interacts with human WASP (Zhang et al., 2009) and *Drosophila's* F-actin (Hicks et al., 2015), supporting the localization of Snx33 to the leading edge and its high correlation with F-actin.

Intriguingly, it has been never shown before that Snx33 localizes to the leading edge of migrating cells, which indicates that it could have an important role in actin polymerization and cell migration.

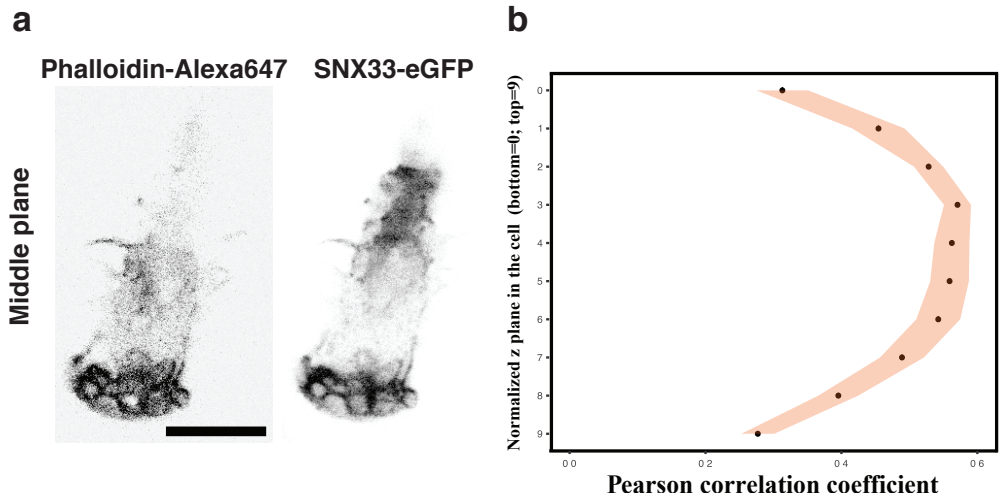

FIGURE 5.8: F-actin signal highly correlates with Snx33. a. Confocal images of Phalloidin-Alexa647 (F-actin) and eGFP-Snx33, middle z-plane. b. Pearson correlation of Phalloidin-Alexa647 and eGFP-Snx33 in normalized z-planes. n = 5. Scale bar = 10 μm.

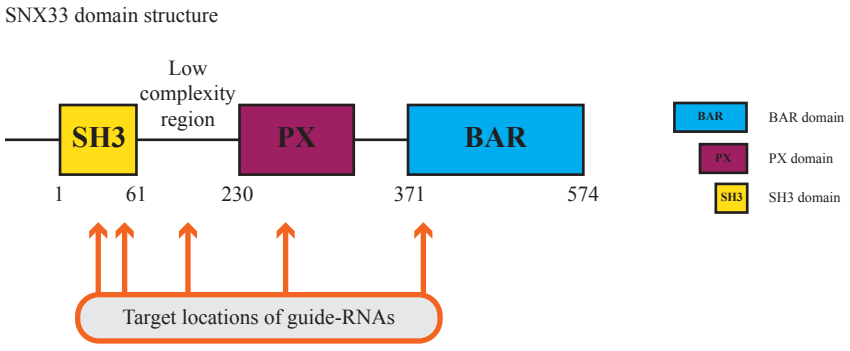

FIGURE 5.9: Schematic of locations targeted by guide-RNAs for Snx33 knockout generation.

5.3.2 Snx33 knockout cell line generation using CRISPR/Cas9 technology

In order to understand the role of Snx33, we decided to generate a Snx33 knockout cell line using CRISPR/Cas9 technology. We followed a similar strategy applied to HL-60 cells in previous studies (Graziano et al., 2017; Graziano et al., 2019; Methods 7.13). Shortly, wild type HL-60 cells were transduced using lentiviral vectors containing a puromycin-selectable gRNA targeting one of five different locations aimed at regions around 30 (SH3 domain), 56 (SH3 domain), 122 (low complexity region), 263 (PX domain) and 374 (BAR domain) amino acids (Figure 5.9). Ideally, gRNA's would be designed to target the beginning of the sequence corresponding to exon 1, but all the potential gRNA's for this region had predictions of low efficiency and high off-targets potential. Thus, additional gRNA's targeting further sequence regions were designed.

Following puromycin selection, cells were transduced using lentiviral vectors containing *S. pyrogenes* Cas9 sequence fused to BFP. After recovery and proliferation, BFP-positive cells were single-cell sorted. Single-cell clones were further assessed by

gDNA purification and sequencing (Figure 4.3).

Out of 110 single-cell clones screened by sequencing, 14 were identified as potential knockout cell lines because of deletion or insertions disrupting the reading frame. These clones were further validated using Western Blotting and clone #40 was identified as the best candidate as no signal was visible in the three consecutive blots at around 65 kDa, where the Snx33 bands should appear (Figure 5.10a-c). Clone #40 will be further referred to as the Snx33 knockout cell line. We validated differentiation efficiency of the Snx33 knockout cell line by CD11b staining quantified using a FACS (Methods 7.18). By doing so, we confirmed that the population of differentiated cells that will be used for further experiments do not show any defects in differentiation. Interestingly, there appears to be a slight shift of CD11b fluorescence in the population of undifferentiated cells. Namely, Snx33 knockout cells seem to spontaneously differentiate to a small extent, without the supplementation with 1.5% DMSO. Additionally, we tested the differentiation of the control HL-60 clones that did go through knockout generation procedure using CRISPR/Cas9 technology, but did not acquire sequence alterations. By this we confirmed that our knockout generation procedure does not affect differentiation. (Figure 5.10d).

Considering the reports showing that overexpression of Snx33 blocks cell division and induces micronucleation in HeLa cells (Zhang et al., 2009), we also tested the growth rate of the Snx33 knockout cell line. After 44 hours of growth, we could observe mild decrease in the cell number between Snx33 knockout and wild type cells (Figure 5.10e). The result was not as dramatic as in other cell lines which could be explained by cell type-specific control of proliferation as division was reported to be blocked in epithelial cells, not neutrophil-like cells used in our study. Additionally, based on the RNAseq data from HL-60 cells at various stages of differentiation, we know that RNA expression of Snx33 is considerably lower in the undifferentiated state (Figure 3.3). This, supports our hypothesis that in the undifferentiated HL-60 the role of Snx33 is limited. Importantly, in previous studies only overexpression or knockdown approaches were tested. Thus, it is plausible to suspect that knockout cell line may unravel distinct roles of Snx33.

5.3.3 Snx33 knockout cells show differences in cell shape and leading edge morphology

Motivated by the finding that Snx33 is enriched at the upper membrane folds at the leading edge of migrating cells, we wondered how Snx33 knockout affects leading edge morphology. To answer this question, we visualized F-actin in Snx33 knockout cells migrating on fibronectin-coated dishes using epifluorescent microscopy (Methods 7.23–7.25). To access cell shape and leading edge morphology, we developed image analysis methods for automatic cell and leading edge segmentation based on bright-field images (Methods 7.28). Consequently, we were able to quantify the F-actin signal in distinct parts of the cell (Methods 7.28). Cell shape quantification revealed that Snx33 knockout cells have a 32% increase in cell area compared to wild type cells (Figure 5.11b). Moreover, our leading edge morphology quantification analysis unveiled that Snx33 knockout cells have a 50% increase in leading edge size (Figure 5.11c). When we measured F-actin fluorescence, we observed decrease in total and leading edge F-actin signal as well as F-actin density in the leading edge in Snx33 knockout cells. (Figure 5.11d-f).

To make sure that the effects we observe are due to Snx33 function, we decided to perform rescue experiments. To do so, we took advantage of the Snx33 knockout cell line stably expressing an eGFP-tagged Snx33 (sorted by FACS for high expressors).

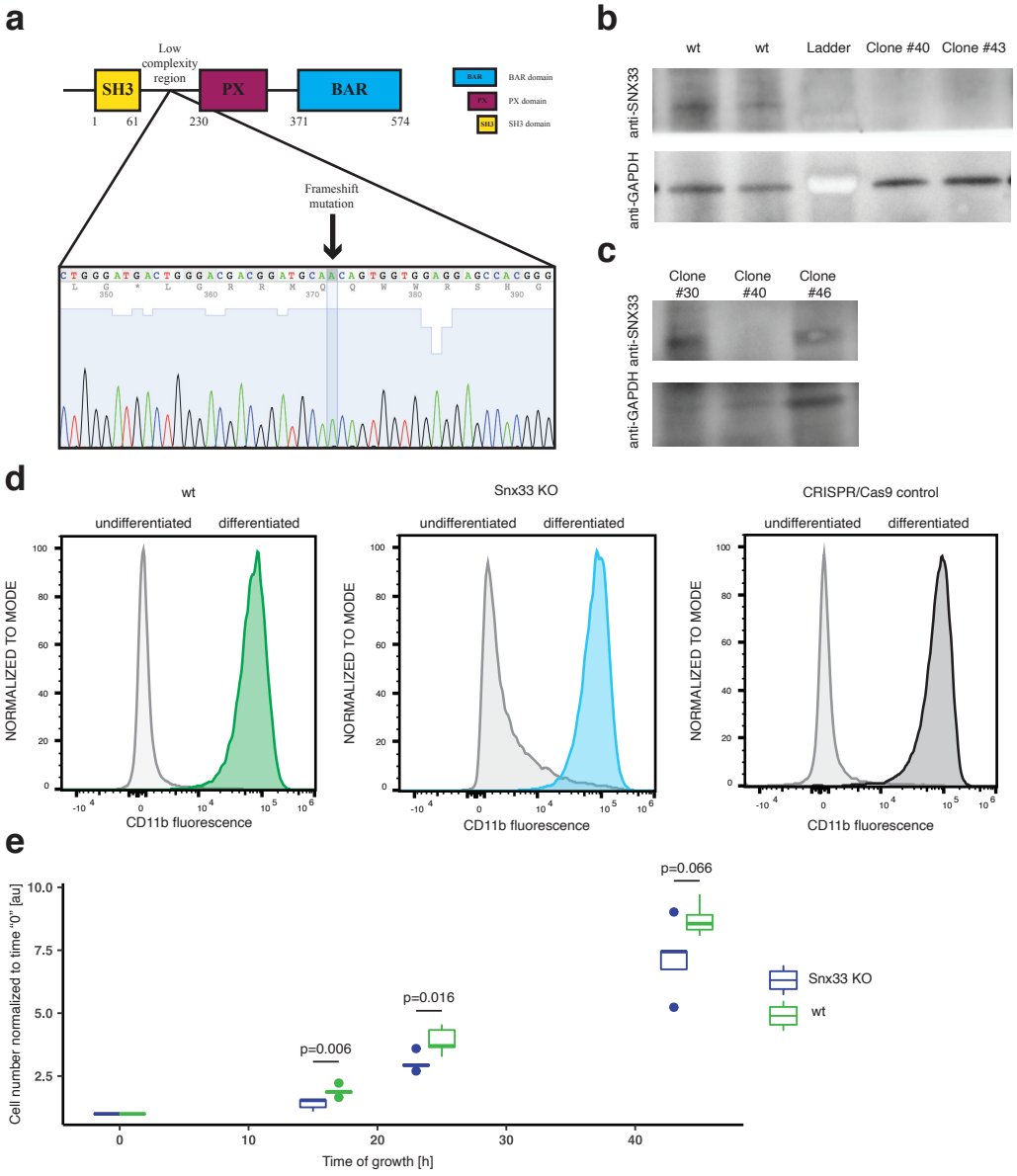

FIGURE 5.10: Snx33 knockout cell line validation. a. Clone #40 sequencing confirming a frameshift mutation. b. Snx33 and GAPDH Western Blots of wild type cells and promising Snx33 KO clones. c. Snx33 and GAPDH Western Blots of promising Snx33 KO clones. d. Representative histograms of CD11b intensity of wild type, Snx33 KO and CRISPR/Cas9 control of HL-60 cells before and after 5 days of differentiation in 1.5% DMSO. e. Growth curves of wild type and SNX33 KO cells from 3 independent experiments. Statistics: T-test and Mann-Whitney-U-Test.

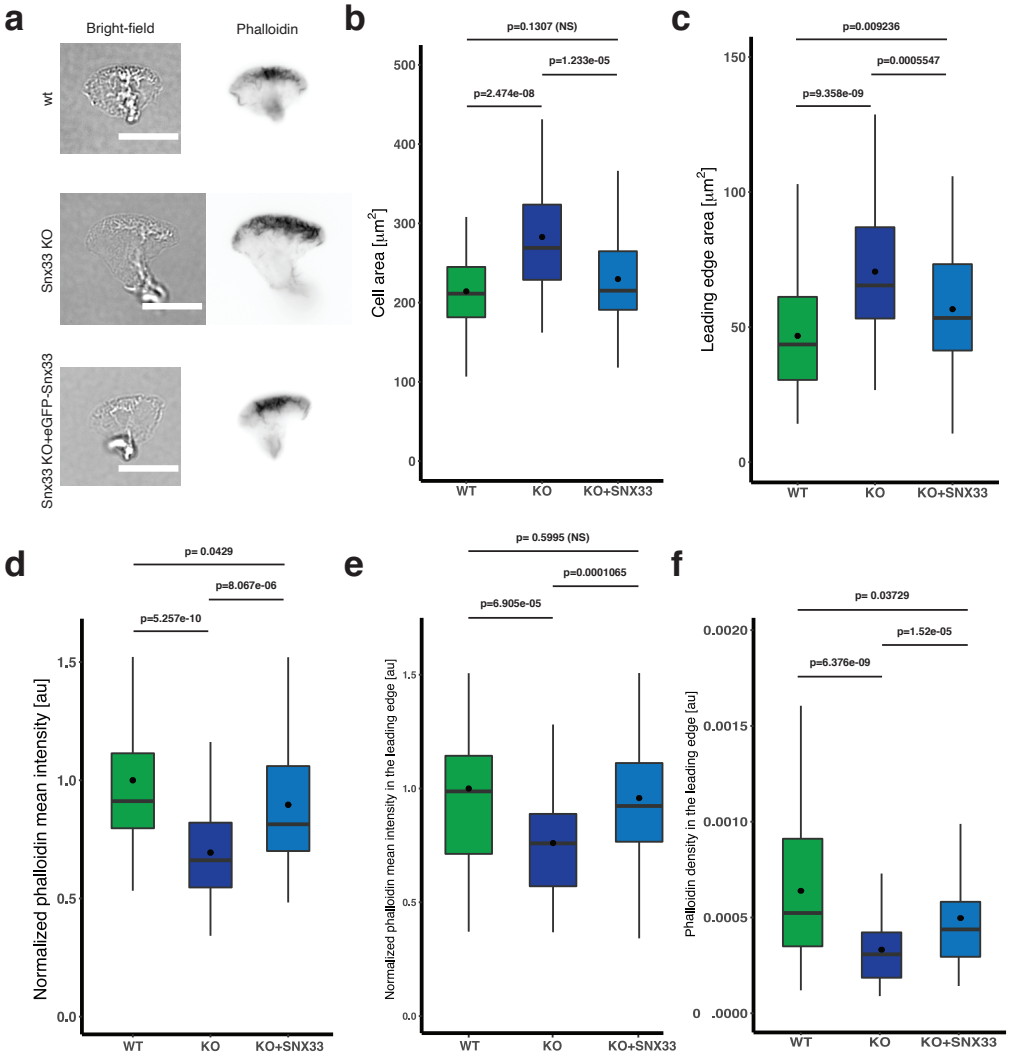

FIGURE 5.11: Cell and leading edge morphology. a. Example images of bright-field and phalloidin staining of wild type, Snx33 KO and Snx33 KO with eGFP-tagged Snx33 cells. Quantification of b. cell area, c. leading edge area, d. total phalloidin fluorescence inside the cell body, e. phalloidin fluorescence in the leading edge and f. phalloidin density in the leading edge. Data are from 3 independent experiments. n = 67 (wild type), n = 73 (Snx33 KO), n = 67 (Snx33 KO with eGFP-tagged Snx33). Data processed jointly with S. Dias Almeida (c-g). Statistics: T-test and Mann-Whitney-U-Test.

All presented knockout phenotypes were partially or fully restored by Snx33-eGFP, confirming that the observed phenotypes are Snx33 specific (Figure 5.11). To provide comparable conditions in the above-mentioned experiments regarding coating, fixation, staining and imaging, the cells from different conditions were always plated on the same dish. Wild type cells used in the experiments were a stable cell line expressing an eGFP-tagged H2B that labels nuclei of wild type cells, making them easily distinguishable from Snx33 knockout cells (without any nuclei staining) and an eGFP-tagged Snx33 cells with cytoplasmatic Snx33 signal.

5.3.4 Leading edge morphology of Snx33 knockout cells is not adhesion-dependent

We wanted to test whether adhesion plays a role in maintaining cell and leading edge morphology of Snx33 knockout cells. To do so, we probed characteristics of both cell types migrating on substrates with variable adhesion strength. Lower adhesion substrates were prepared by adding a protein blocker to fibronectin coating (Methods 7.29). It has been previously showed that the density of fibronectin is strongly correlated with the number of adhering neutrophil-like cells. Adhesion strength can be modulated by adding a protein blocker (BSA) to a fibronectin coating. While higher adhesion strength does not affect membrane tension, it decreases migration speed by slowing tail retraction and, consequently, cell translocation (Diz-Muñoz et al., 2016a).

As expected, adding protein blocker to the fibronectin coating significantly decreased the number of adherent wild type dHL-60 cells (Figure 5.12a-b). Next, we examined the impact of changes in adhesion strength on cell and leading edge morphology. Increased cell size in Snx33 knockout cells in comparison to wild type was adhesion-dependent, as upon lowering adhesion, we could not observe differences between the wild type and Snx33 knockout cells. (Figure 5.12c). Interestingly, the increase in the leading edge in the Snx33 knockout cells was not adhesion-dependent (Figure 5.12d). Similarly, regardless of the adhesion manipulation, we observed differences between wild type and Snx33 knockout cells in total F-actin intensity and F-actin density in the leading edge. As F-actin intensity in the leading edge in both types of cells remained unchanged, we concluded that differences in F-actin density were driven by larger leading edges in the Snx33 knockout cells (Figure 5.12e-f).

Our results indicate that Snx33 knockout has both adhesion-independent and adhesion-dependent effects on cell and leading edge morphology. This, in turn, suggests that Snx33 may affect cell and leading edge size through different mechanisms. We investigated Snx33 binding partners to look for a potential mechanism explaining the Snx33 knockout adhesion-dependent phenotypes. Interestingly, we found that Snx33 is a binding partner of several isoforms of ADAM15 (a disintegrin and metalloprotease 15) by its SH3 domain (Kleino et al., 2009). ADAM15 is known to affect neutrophil transmigration (Sun et al., 2010). Interestingly, it was also proposed that ADAM15 may modulate cell motility by cell surface expression of integrin $\beta 1$ (ITGB1) that is important for adhesion processes (Chen et al., 2008). In our cell line of interest integrin $\beta 1$ is highly expressed in the migratory state as confirmed by RNA expression analysis (Figure 5.13). Thus, it is plausible to suspect that ADAM15 may play an important role in regulating ITGB1 through interaction with Snx33. Regulation of ADAM proteins by sorting nexins may be a more general phenomenon as it has been also found that other proteins from Snx9 protein family, namely Snx9 and Snx18, regulate a different ADAM protein (ADAM9) at the cell surface (Mygind et al., 2018). Exploring this direction requires further experiments that are beyond the

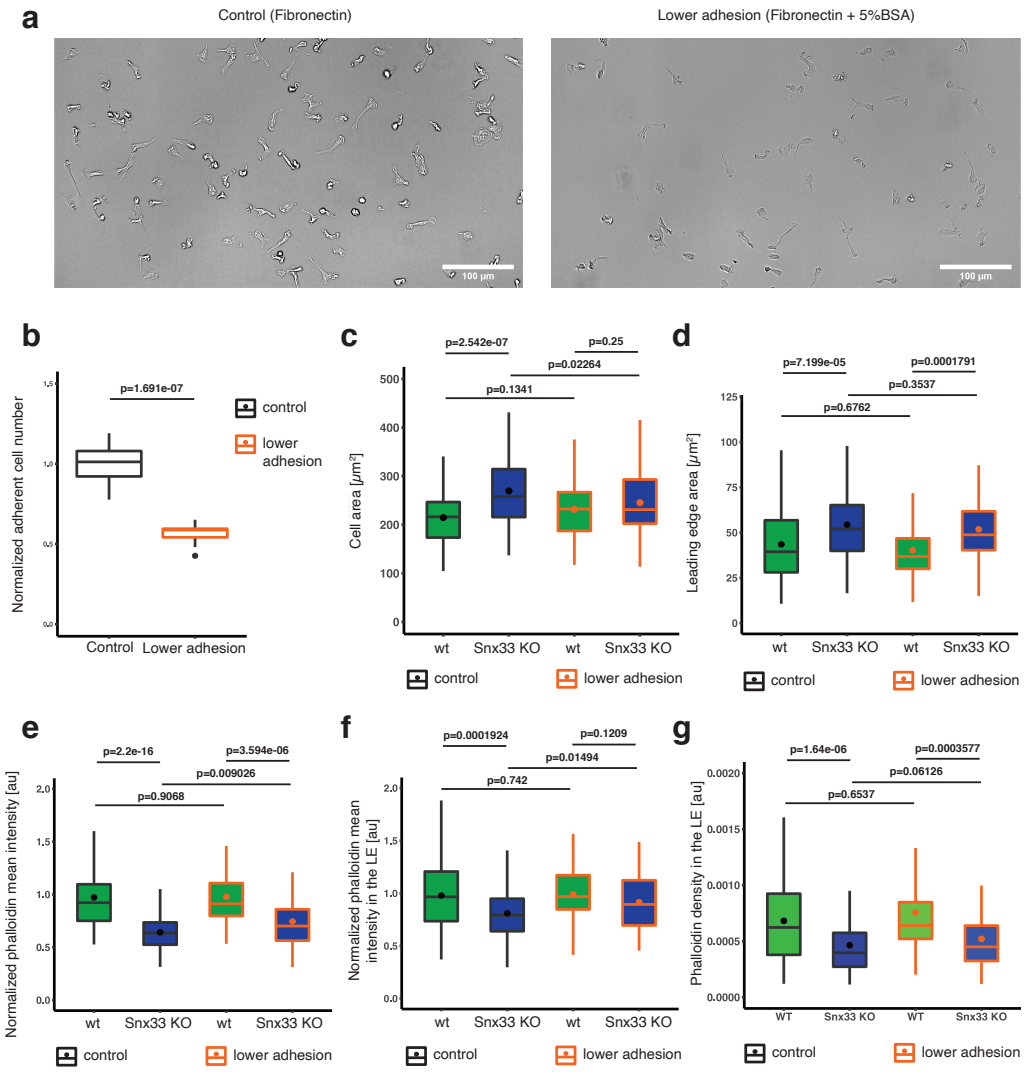

FIGURE 5.12: Contribution of substrate adhesion to cell and leading edge morphology in Snx33 knockout cells. a. Example bright-field images of wild type dHL-60 cells migrating on the control (fibronectin) and lower adhesion substrate (fibronectin with 5%BSA). Data from 2 independent experiments. b. Cell number quantification depending on the adhesion substrate. Quantification of c. cell area, d. leading edge area, e. total phalloidin (F-actin) fluorescence inside the cell body, f. phalloidin (F-actin) fluorescence in the leading edge and g. phalloidin (F-actin) density in the leading edge. Data from 3 independent experiments. Controls: n = 82 (wt), n = 102 (Snx33 KO); Lower adhesion: n = 53 (wt), n = 72 (Snx33 KO). Data processed jointly with S. Dias Almeida. Statistics: T-test and Mann-Whitney-U-Test.

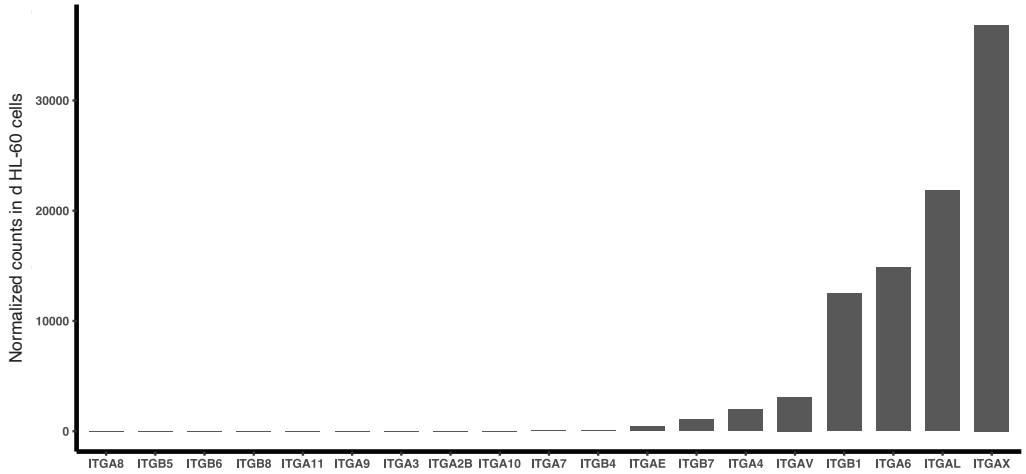

FIGURE 5.13: Normalized counts of integrins identified in differentiated HL-60 cells by RNAseq. Bars indicate mean of from 3 independent experiments.

scope of the work presented here. We decided to focus our efforts on understanding what is driving the adhesion-independent increase in the leading edge size in Snx33 knockout cells.

5.3.5 Leading edge enrichment of Snx33 is Arp2/3 and membrane tension-dependent

Arp2/3 complex orchestrates the formation of branched-actin networks that are a main driver of leading edge morphology as well as cellular responses to the environment (Pollard, 2007; Papalazarou and Machesky, 2021). We asked if the observed phenotypes in the Snx33 knockout could stem from the effects generated by Arp2/3 action. To test the relationship between Arp2/3-dependent leading edge morphology and Snx33, we imaged F-actin of the fixed dHL-60 cells with an eGFP-tagged Snx33 before and after the treatment with the Arp2/3 inhibitor CK-666. As expected, before treatment, the Snx33 signal was enriched in the leading edge, in the proximity of the F-actin signal. However, after CK-666 treatment, we observed that the F-actin signal disappeared from the leading edge and subsequently a 3 fold decrease in Snx33 fluorescence (Methods 7.12). Instead of clearly visible and structured ruffles to which F-actin and Snx33 localized, we could only observe a smear of F-actin, confirming that CK-666 treatment worked as expected. These results support the hypothesis that Snx33 localizes to the leading edge in the Arp2/3 dependent manner (Figure 5.14). Therefore, it is plausible to suspect that Snx33 could have some role upstream or downstream of Arp2/3 activation.

Generation of actin networks induced by Arp2/3 is known to have mechanical consequences for the plasma membrane. Arp2/3 contributes to the creation of the pushing forces against the membrane surface through establishing a branched actin network. On the other hand, the actin network can also resist membrane tension or other forces exerted on the cell (Papalazarou and Machesky, 2021). It has been shown that branched actin networks can adapt to mechanical load in various ways (Bieling et al., 2016), for example by adapting actin density (Mueller et al., 2017). Motivated by the reports suggesting a role for Snx33 in actin polymerization

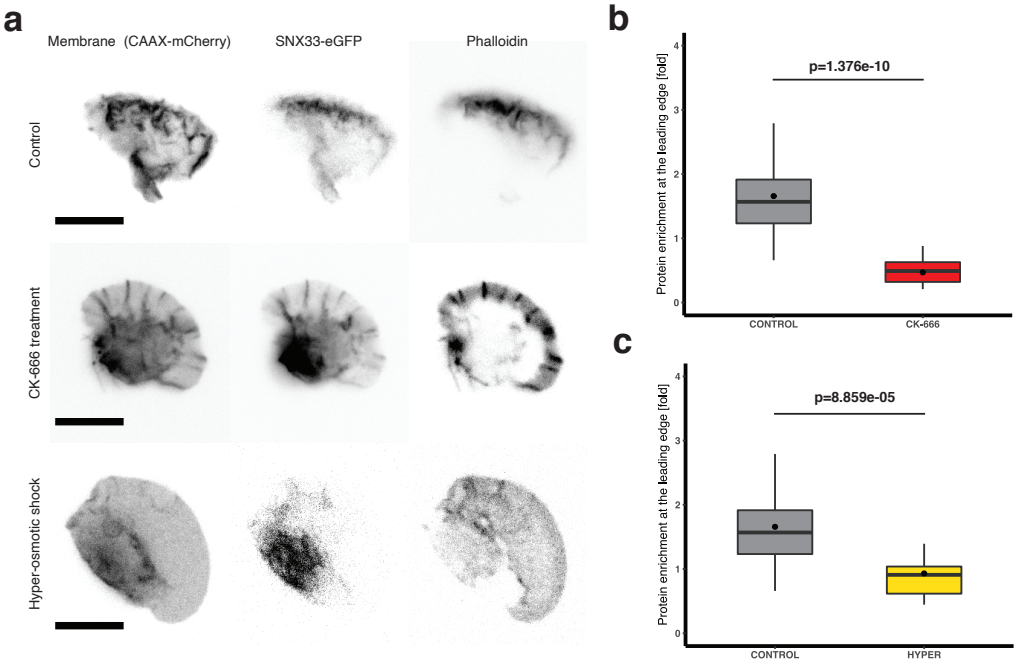

FIGURE 5.14: Leading edge enrichment of Snx33 is Arp2/3 and membrane tension-dependent. a. Example images of control, CK-666 and hyper-osmotically treated cells. b. Snx33 enrichment at the leading edge in control (n = 33) and CK-666 (n = 13) treated cells. c. SNX33 enrichment at the leading edge in control (n = 33) and hyper-osmotically treated (n = 11) treated cells. Statistics: Mann-Whitney-U-Test.

(Zhang et al., 2009), and intrigued by our data showing the decreased levels of F-actin in the leading edge, we next tested whether Snx33 enrichment could not only be Arp2/3-dependent, but more generally, membrane tension-dependent. To understand this, we tested the enrichment of Snx33 at the leading edge, but instead of Arp2/3 inhibitor, used hyper-osmotic shock that decreases membrane tension (Sens and Plastino, 2015; Diz-Muñoz, Fletcher, and Weiner, 2013). Similarly to Arp2/3 inhibition, the hyper-osmotic shock decreased by 1.5 fold Snx33 enrichment at the leading edge, which indicates that Snx33 localized to the leading edge in a tension dependent manner. Previous results using CK-666 inhibitor could be, thus, interpreted in two ways. First, that Snx33 localizes in an Arp2/3-dependent manner. Second, that Snx33 changes localization upon decrease of membrane tension as CK-666 treatment also decreases membrane tension (Diz-Muñoz et al., 2016a). Importantly, actin polymerization underlies positive and negative feedback loops that coordinate the growth or restriction of the leading edge (Graziano et al., 2019), so Snx33 could be also involved either a short-range or long-range feedback loop maintaining the plasma membrane homeostasis in migrating dHL-60 cells.

5.3.6 Snx33 affects membrane mechanics in dHL-60 cells

To further investigate the role of Snx33 in maintaining the plasma membrane homeostasis, we decided to directly measure tether force of the Snx33 knockout cells that, under certain assumptions, can be directly related to membrane tension. To achieve that, we performed static tether pulling experiments using Atomic Force Microscopy (Methods 7.19), as reported previously (Diz-Muñoz et al., 2016a; Graziano et al., 2019). In a typical experiment, we approach the cell with a cantilever coated with

concanavalin A, a plant lectin that binds to the mannose residues of various glycoproteins, and contact the cells. The subsequent retraction of the cantilever at a certain speed allows to pull a membrane tether that is initially actin-free. If this tether breaks before actin polymerizes inside it, we can measure the tether force - a force that the cantilever is experiencing - by analyzing the force experienced by the cantilever before and after the tether breaks (Figure 5.15).

We observed that Snx33 knockout cells have significantly increased tether force (mean = 57.16 pN) in static measurements in comparison with wild type cells (mean = 45.28 pN), these measurements correspond to membrane tension values of 153.26 μN/m and 96.17 μN/m, respectively (Methods 7.19, Figure 5.15a). To make sure that the observed change in tether force comes solely from the lack of Snx33 and not from previously unidentified effects of the knockout generation protocol or the effects of single-cell clones, we compared tether forces of wild type cells and single cell clone that went through the knockout generation protocol, but did not acquire desired mutations. We did not observe any differences between wild type (mean = 58.90 pN) and CRISPR control cells (mean = 56.50 pN) (Figure 5.15b). As the Snx33 knockout displayed an increase in tether force, we wondered whether this effect is specific for Snx33. We found that overexpression of an eGFP-tagged Snx33 in the knockout background could rescue the phenotype, confirming Snx33 specificity. Populations of wild type (mean = 61.58 pN) and Snx33 knockout cells with eGFP-tagged Snx33 (mean=65.56 pN) were not significantly different as a result of statistical testing, while Snx33 knockout cells (mean=75.25 pN) had significantly higher tether force, corresponding to membrane tension values of 177.87 μN/m, 201.61 μN/m, 265.62 μN/m, respectively (Figure 5.15c). To test if Snx33 is sufficient to decrease membrane tension we performed static tether pulling experiments comparing wild type cells overexpressing an eGFP-tagged Snx33 (mean = 56.20 pN) with control wild type cells (mean = 54.44 pN). We observed no changes in tether force, revealing that Snx33 overexpression is not sufficient to decrease tether force (Figure 5.15d).

Snx33 decreases tether force in the Snx33 knockout cells, but has no effect in the background of endogenous Snx33. We wondered what is the relationship between Snx33 expression levels and the measured tether force. As expected, in wild type cells there is no correlation between and eGFP-Snx33 protein levels and tether force (Pearson's R = 0.006, p = 0.7384) (Figure 5.16a). Interestingly, in Snx33 knockout we observed almost statistically significant weak negative correlation (Pearson's R = -0.322, p = 0.072) suggesting that tether force could scale to a small extent with Snx33 expression levels, but it is not a clear relationship (Figure 5.16b).

Important to note is that the measured tether force and calculated membrane tension values seem to vary across experiments for wild type (45.28-61.58 pN/96.17-177.88 μN/m) and Snx33 knockout (57.16-75.25 pN/153.26-265.62 μN/m) cells. Although the same AFM system was used for measurements and cantilevers were carefully calibrated, it may still not account for all imperfections of our experimental setup. Interestingly, the tether force difference between condition remains comparable across two experiments (11.88 pN and 13.67 pN).

Static tether force measured by AFM can be directly related to membrane tension using certain assumptions (Equation 1.1), but it intermingles two distinct contributions: in-plane membrane tension and MCA (Diz-Muñoz, Fletcher, and Weiner, 2013). Snx33 is not known as an MCA protein, but we cannot exclude that it could act as one. Its membrane binding activity by BAR domain is very well described, but to be defined as an MCA protein, it would also need to bind actin. To our knowledge, there is no reports about Snx33 direct binding to actin. However, it has been recently

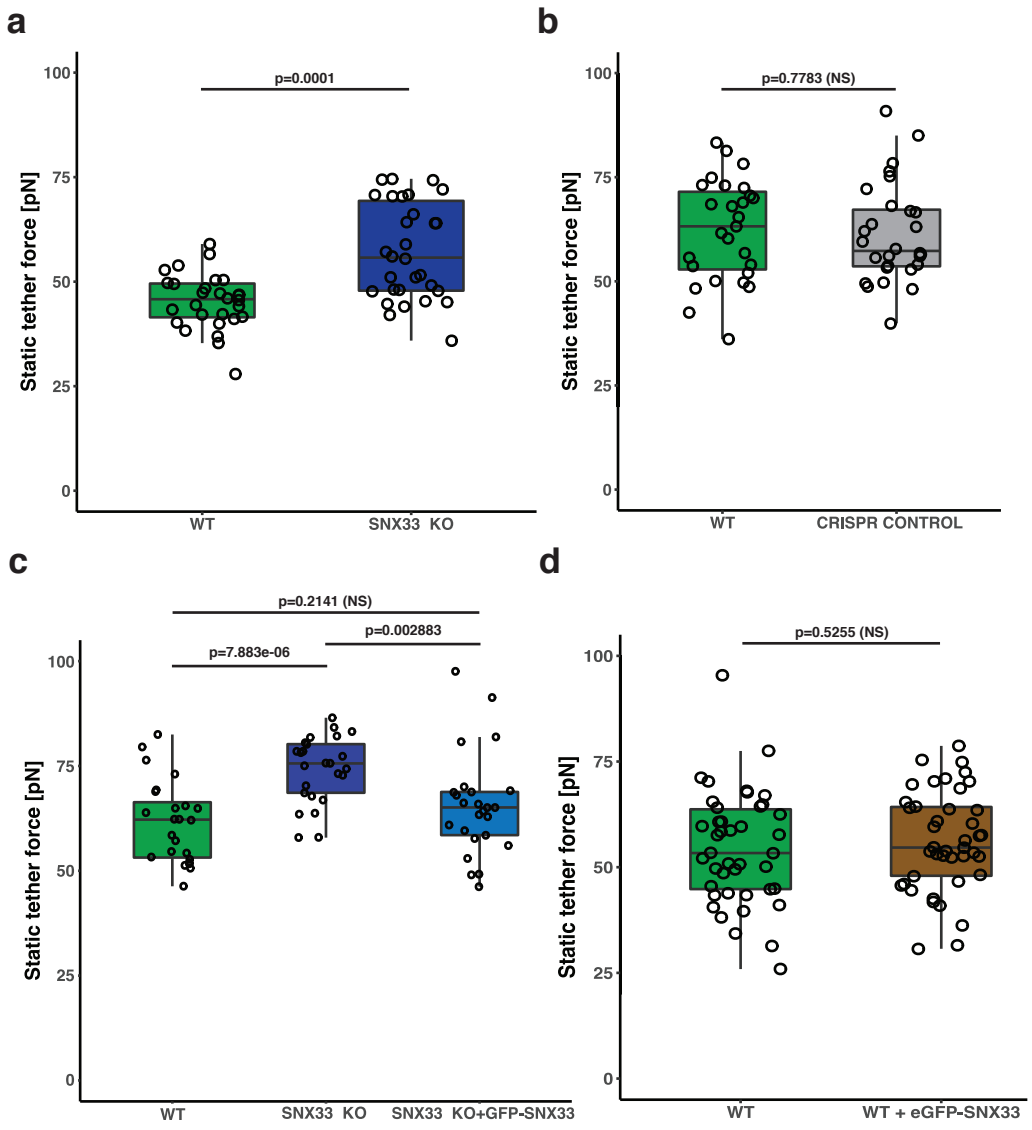

FIGURE 5.15: Snx33 knockout increases membrane tension in dHL-60 cells, while Snx33 over-expression restores the wild type phenotype. a. Mean static tether force of wild type (n = 28) and Snx33 KO (n = 30) dHL-60 cells from 5 independent experiments. b. Mean static tether force of wild type (n = 27) and CRISPR control (n = 28) dHL-60 cells from 4 independent experiments. c. Rescue experiments for Snx33 knockout: Mean static tether force of wild type (n = 24), Snx33 KO (n = 26) and Snx33 KO with overexpressed eGFP-SNX33 (n = 25) from 3 independent experiments. d. Mean static tether force of wild type (n = 42) and eGFP-SNX33 over-expressed (n = 42) dHL-60 cells from 6 independent experiments. For data presented in each plot, the data for all conditions was always collected with the same cantilever per one independent experiment to account for variability introduced by the system. Statistics: T-test and Mann-Whitney-U-Test.

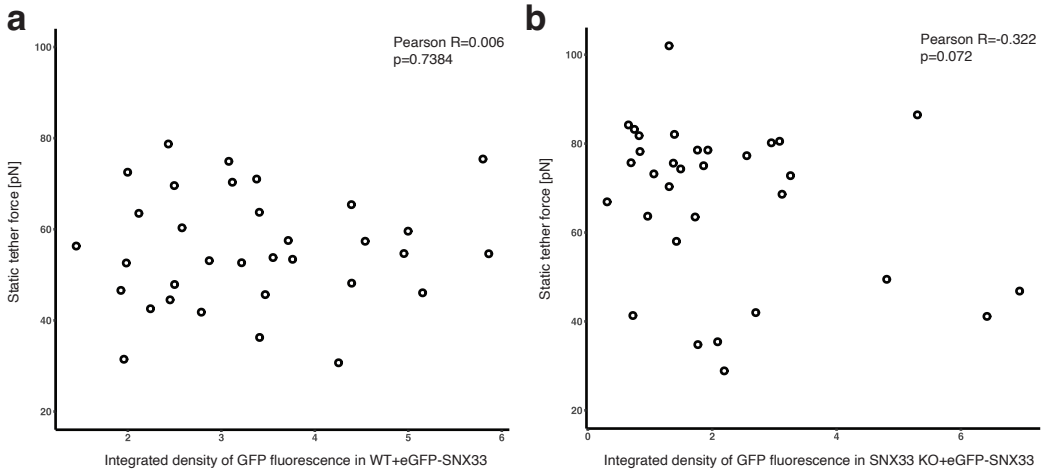

FIGURE 5.16: Pearson R correlation of static tether force and eGFP-Snx33 fluorescence a. Pearson R correlation of static tether force of and eGFP-Snx33 fluorescence in wild type cells (n = 33) dHL-60 cells from 3 independent experiments. b. Pearson R correlation of static tether force and eGFP-Snx33 fluorescence in Snx33 KO cells (n = 33) dHL-60 cells from 4 independent experiments.

found that some BAR domain proteins can associate with actin filaments. For example, the F-BAR domain of PACSIN2 is able to interact with actin filaments using the same concave surface employed to bind membranes (Kostan et al., 2014). Similarly, it was demonstrated that a BAR domain protein Bin1 and PDZ-BAR domain protein PICK1 can bind actin filaments polymerized *in vitro* (Rocca et al., 2008; Dräger et al., 2017). More recently, an N-BAR domain of ASAP1 was found to directly bind to F-actin and modulate the dynamics of higher order actin structures in cells (Chen et al., 2020). It is plausible to hypothesize that other BAR domain proteins could also bind actin filaments. Snx33 was indeed reported to interact with mouse β-actin in one high-throughput screen, suggesting its potential role as an MCA protein (Hein et al., 2015).

We decided to understand to which extent in-plane membrane tension and MCA contribute to increased tether force measured by AFM in the Snx33 knockout cell line. Thus, we performed dynamic tether pulling (Methods 7.30) experiments on wild type and Snx33 knockout cells. During measurements the same cell was probed multiple times at different retraction velocities. Tether force increases with increasing velocity and all parameters used to described this process (Equation 7.3) are assumed to be constant except for parameters describing the effects of MCA on plasma membrane viscosity. Therefore, we describe these parameters as α and measure it to approximate the effects of MCA. Interestingly, we observed a 2-fold decrease of the MCA parameter α value in Snx33 knockout in comparison to wild type cells (Figure 5.17). Considering that the relationship between in-plane membrane tension and MCA contributions is additive (Equation 1.1), it shows that the major change in tether force in the Snx33 knockout cells comes from in-plane membrane tension. On the other hand, a decrease in MCA parameter suggests that Snx33 either acts as a MCA protein or regulates some MCA proteins. Understanding of the nature of the MCA parameter value in the context of Snx33 needs to be further investigated.

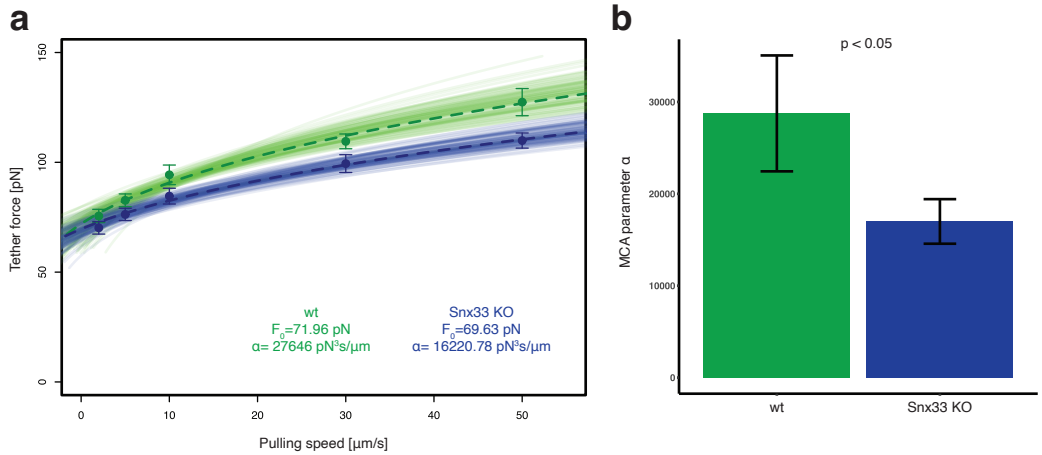

FIGURE 5.17: Membrane-to-Cortex attachments contribution to membrane tension in Snx33 knockout cells. a. Force-velocity curve from dynamic tether pulling on wild type (n = 12) and Snx33 knockout (n = 13) cells. Data points correspond to the mean tether force for indicated pulling velocity. Whiskers show SEM. Lines are Monte-Carlo fits of a model for dynamic tether formation used to extract the MCA parameter α. b. Mean and standard deviation of MCA parameter α for each condition. Data are from 3 independent experiments. Statistics: Z-test.

5.3.7 Snx33 controls cell migration and directionality in 2D

Leading edge morphology, cell shape and mechanics were previously reported to play an important for cell migration (Krause and Gautreau, 2014). Our previously described data confirm that Snx33 knockout cells differ in all of the above-mentioned aspects. Hence, we wondered how Snx33 knockout affects cell motility. To our knowledge, Snx33 was not reported to have effects on cell migration, in neither knockout, knockdown or by overexpression. To assess migration characteristics of Snx33 knockout cells, we imaged migrating dHL-60 cells with an mCherry-tagged CAAX, a membrane binding motif, using TIRFM (Methods 7.10). TIRFM allows to visualize a region of a cell in a close proximity to the coverslip. In TIRFM, fluorophores are excited by the evanescent field that is created at the interface between two media with different refractive indices. Consequently, TIRF modality is often used for visualizing the molecules at the membrane, as in comparison with the epi-fluorescent imaging, the membrane signal is significantly enhanced.

We followed the movements of membrane that is adhered to the substrate in 2-minute long movies of migrating wild type and Snx33 knockout cells using TIRFM (Figure 5.18a; Methods 7.10). For quantification, cells were segmented based on the membrane signal using Ilastic (Methods 7.31). Similarly to our previous results in fixed dHL-60 cells (Section 5.11), we observed increase in cell area (however, here it is cell area attached to the substrate) in Snx33 knockout compared to wild type cells (Figure 5.18b). Additionally, we revealed an increase in elongation and eccentricity of Snx33 knockout cells, although both types of cells are highly eccentric when migrating (Figure 5.18c-d.) Next, we identified the cell center of mass in every image and calculated the center of mass displacement between two consecutive frames (Figure 5.18e). Using the center of mass displacement we measured that cell speed increases in Snx33 knockout in comparison to wild type cells (Figure 5.18f). We also wondered if other parameters of migration, such as persistence, are affected in the

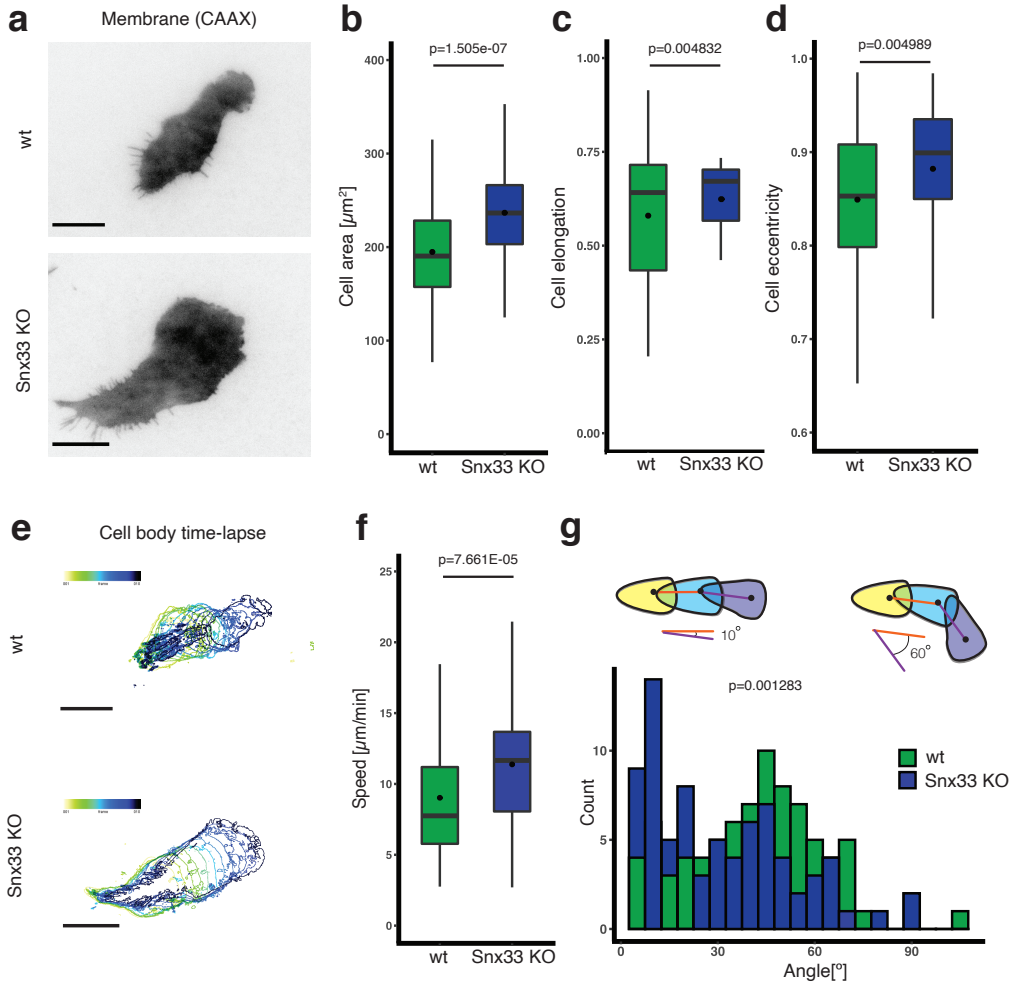

FIGURE 5.18: Snx33 affects cell shape, speed and directionality. a. Exemplary images of live-cell membrane imaging (mCherry-CAAX) of wt and Snx33 KO cells using TIRFM. b. Quantification of cell area, c. elongation, d. eccentricity and f. speed in wt and Snx33 KO cells. e. Visualization of cell body (membrane) time-lapse over 2 minutes. Images were taken every 5 seconds. g. Histograms of motion angles for wt and Snx33 KO cells. Data are from 3 independent experiments, n = 82 (wt), n = 78 (Snx33 KO). Data processed jointly with S. Dias Almeida. Statistics: T-test and Mann-Whitney-U-Test. Scale bar = 10 μm.

Snx33 knockout cell line. To assess that, we identified the angle between every three consecutive frames. We observed that the measured angle between three consecutive frames is considerably wider for wild type cells than Snx33 knockout cells (Figure 5.18g). Not only do Snx33 knockout cells move faster, but they are also moving more directionally and turn less in comparison to wild type cells.

5.3.8 Snx33 knockout cells differ in WAVE2 characteristics at the leading edge

As Snx33 knockout cells show clear differences in cell migration, we asked what are the origins of this behaviour. One known critical regulator of actin nucleation and directed cell migration in HL-60 cells is the WAVE2 complex (Weiner et al., 2006; Danson et al., 2007; Mendoza et al., 2011). We decided to investigate the contribution of the WAVE2 complex in Snx33 knockout cells. To do that, we generated wild type and Snx33 knockout cell lines with an eGFP-tagged Hem1 (WAVE2 complex subunit) and an mCherry-tagged CAAX (membrane binding motif) (Methods 7.7; 7.34). We performed time-lapse TIRFM imaging of migrating dHL-60 cells (Methods 7.10). To quantify the images, we took advantage of Ilastic for segmentation of cell body based on CAAX signal and WAVE2 based on Hem1 signal (Figure 5.19a). Because the cells are very dynamic and move in and out the TIRF illumination field, often a semi-manual curation of the segmentation was required to make sure that all part of the cells are segmented properly. Another challenge lied in the fact that the individual cells have different expression levels of CAAX and Hem1, so the segmentation parameters needed to be tailored to the variability of the signal. After successful implementation of an automatic segmentation of membrane and Hem1 signal, we wanted to compare Hem1 signal inside and outside of the leading edge. Leading edge is a region where WAVE2 activates the Arp2/3 complex to induce branched actin polymerization. To segment the leading edge of migrating dHL-60 cells, we developed a method to automatically segment the leading edge which defines it as the difference of two consecutive frames of CAAX signal (membrane), in which at least one pixel of Hem1 signal is present (Methods 7.31). Without taking into account the at least one pixel of Hem1 signal in the definition, the retracting fibers in the back of the cells were picked by our segmentation methods, but even such a permissive definition allowed to get rid of them very efficiently (Methods 7.31; Figure 7.4). After leading edge segmentation was completed, we quantified leading edge characteristics in migrating dHL-60 cells. We observed increase in the leading edge length and area in the Snx33 knockout cells compared to control (Figure 5.19b-d).

The segmentation of cell body, leading edge and Hem1 signal permitted us to describe the WAVE2 characteristics (Figure 5.20a). We measured the total segmented area covered by Hem1 in the cell body and in the leading edge. We observed no differences between the Hem1 total area in wild type and Snx33 knockout cells, confirming that both populations have comparable levels of fluorescence and the imaged cells are randomly obtained (Figure 5.20b). We revealed an increase in Hem1 area in the leading edge in the Snx33 knockout cells that could explain larger leading edges and faster migration of Snx33 knockout cells (Figure 5.20c). Next, we decided to understand where do these differences in the Hem1 area in the leading edge come from. We quantified the mean length and width of Hem1 patches and discovered that they are bigger in both dimensions (Figure 5.20d-f). As WAVE2 complex is generating branched actin polymerization, and thus, driving the cell protrusion formation, the changes of its pattern have possibly important consequences for the turnover of actin and the magnitude of the actin network.

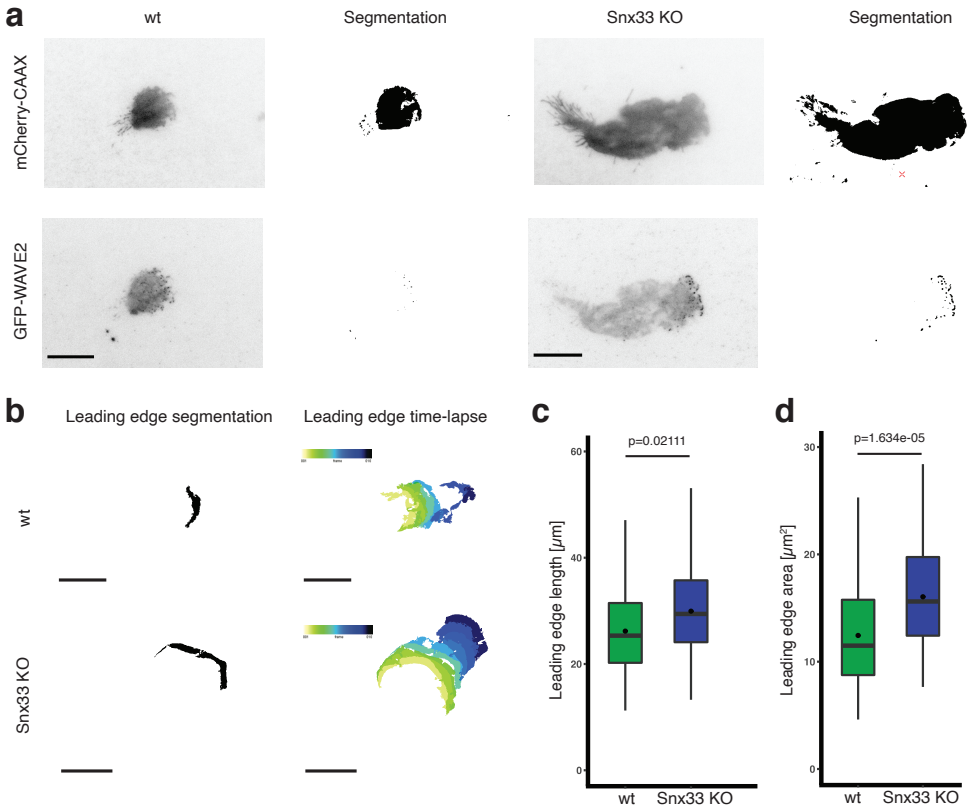

FIGURE 5.19: Snx33 affects leading edge size in migrating cells. a. Representative examples of TIRFM images and their segmentation of WAVE2-eGFP and membrane (CAAX-mCherry) in wt and Snx33 KO cells b. Exemplary images of segmented leading edge and their progression over time in wt and Snx33 KO cells. c. Quantification of leading edge length and d. leading edge area in wt and Snx33 KO cells. Data are from 3 independent experiments, n = 82 (wt), n = 78 (Snx33 KO). Data processed jointly with S. Dias Almeida. Statistics: T-test and Mann-Whitney-U-Test. Data processed jointly with S. Dias Almeida. Scale bar = 10 μm.

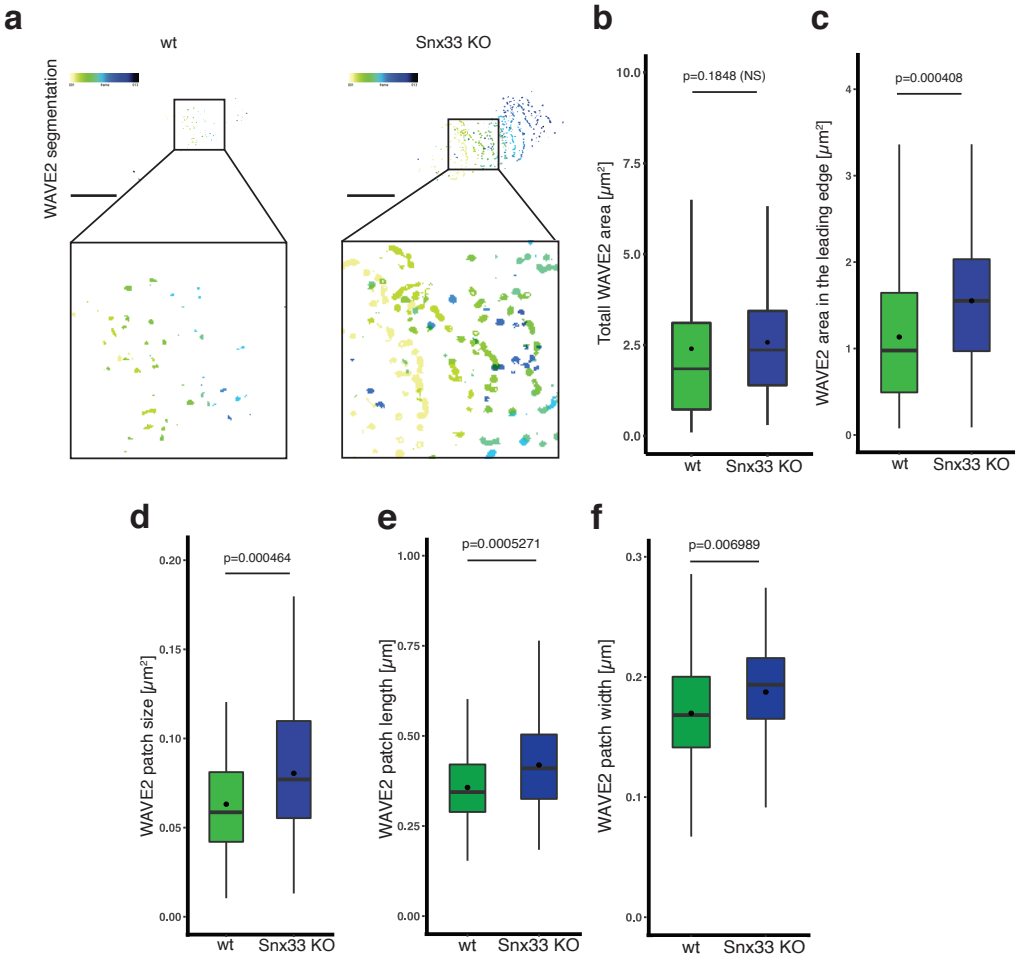

FIGURE 5.20: Snx33 knockout increases the WAVE2 patterning at the leading edge. a. Representative examples of WAVE2-eGFP TIRFM time-lapse movies segmentation in wt and Snx33 KO cells b. Quantification of total WAVE2 area, c. WAVE2 in the leading edge area, d. WAVE2 patches area, e. WAVE2 patch length f. WAVE2 patch width in wt and Snx33 KO cells. Data are from 3 independent experiments, n = 82 (wt), n = 78 (Snx33 KO). Data processed jointly with S. Dias Almeida. Statistics: T-test and Mann-Whitney-U-Test. Scale bar = 10 μm.

5.3.9 Snx33 and WAVE2 localization

WAVE2 patterning is strongly affected by the lack of Snx33, which results, among others, in larger leading edges and more efficient migration of dHL-60 cells. What is the exact relationship between Snx33 and the WAVE2 complex? Snx33 was shown to immunoprecipitate with WASP (Zhang et al., 2009), which belongs to the same family of proteins as WAVE2 that are fundamental for actin-cytoskeleton reorganization and widely conserved across species (Kurisu and Takenawa, 2009). It has been shown that WASP interacts with Snx33 through its VCA domain, but surprisingly, according the results from co-immunoprecipitation, Snx33 keeps its interaction with WASP by N-terminal SH3 and C-terminal BAR domain, independently. This is in contrast to SNX9, where only SH3 domain is crucial for the interaction with WASP (Zhang et al., 2009). So far, there is no evidence supporting the interaction between Snx33 and WAVE2 complex, but the VCA domain of WAVE2 could be a potential interaction site for Snx33. Interestingly, SH3 domains of other BAR domain proteins such as IRSp53 were shown to interact with WAVE2 (Miki et al., 2000a), and as Snx33 also contains a SH3 domain, it could be potentially involved in a similar type of interaction. These recent findings that Snx33 interacts with WASP via its BAR domain lead to the hypothesis that there could be more than one interaction mode of Snx33 and WASP. In case of WASP, GBD/CRIB domains are known to be critical for the control of its activity as they inhibit by binding the VCA domain which is released by competitive binding of GTP-bound Cdc42 and PIP_2 (Kim et al., 2000). Even though WAVE2 does not have a GBD/CRIB that could autoinhibit VCA domain, it has been several times reported that it is found in autoinhibited state in reconstitutions and *in vivo* (Abou-Kheir et al., 2008; Ismail et al., 2009). Yet, the clear mechanism by which this autoinhibition happens is not fully elucidated.

To understand the role of Snx33 in regulation of the WAVE2 complex patterning at the membrane, we decided to use confocal microscopy of the dHL-60 cells fixed while migrating (Methods 7.17; 7.23). We imaged a stable cell line with an eGFP-tagged Snx33 and an mCherry-tagged Hem1 (WAVE2 complex subunit) sorted for low and high expressors, respectively. As a result, we observed that fluorescence signal from Snx33 and Hem1 were overlapping to a large extent (Figure 5.21a). To quantify the relation between Snx33 and WAVE2 complex in the leading edge, we measured PCC value in the leading edge, segmented based on F-actin staining. As previously (Figure 5.7, and 5.8), we compared different cell z-sections. The first two normalized z-slices belonging to the cell bottom (closer to the coverslip) had significantly lower PCC values (0.2 and 0.4, positive) of an eGFP-Snx33 and an mCherry-WAVE2. In contrast, middle and top parts of cells had high PCC values, reaching over 0.6 (high, positive) (Figure 5.21b). Intriguingly, at the cell bottom, adjacent to the coverslip, often a wave of WAVE2 was visible at the protruding cell edge (Figure 5.21c).

Despite overall high overlap between Snx33 and WAVE2 signal, Snx33 signal at the protruding edge was missing. WAVE2 localization at the protrusion front of the bottom plasma membrane can be visualized by TIRFM (Figure 5.22), where it has been shown to reside at the propagating waves that organize the leading edge of a moving cell (Weiner et al., 2006).

Following the observation that Snx33 is excluded from the propagating Hem1 wave at the cell front made by confocal microscopy, we decided to perform TIRFM imaging that is more suitable to assess the protein localization at the bottom plasma membrane (Axelrod, 2008). In TIRFM, we could as expected observe propagating waves of Hem1 that were appearing clearly at the cell front. Snx33 signal was not

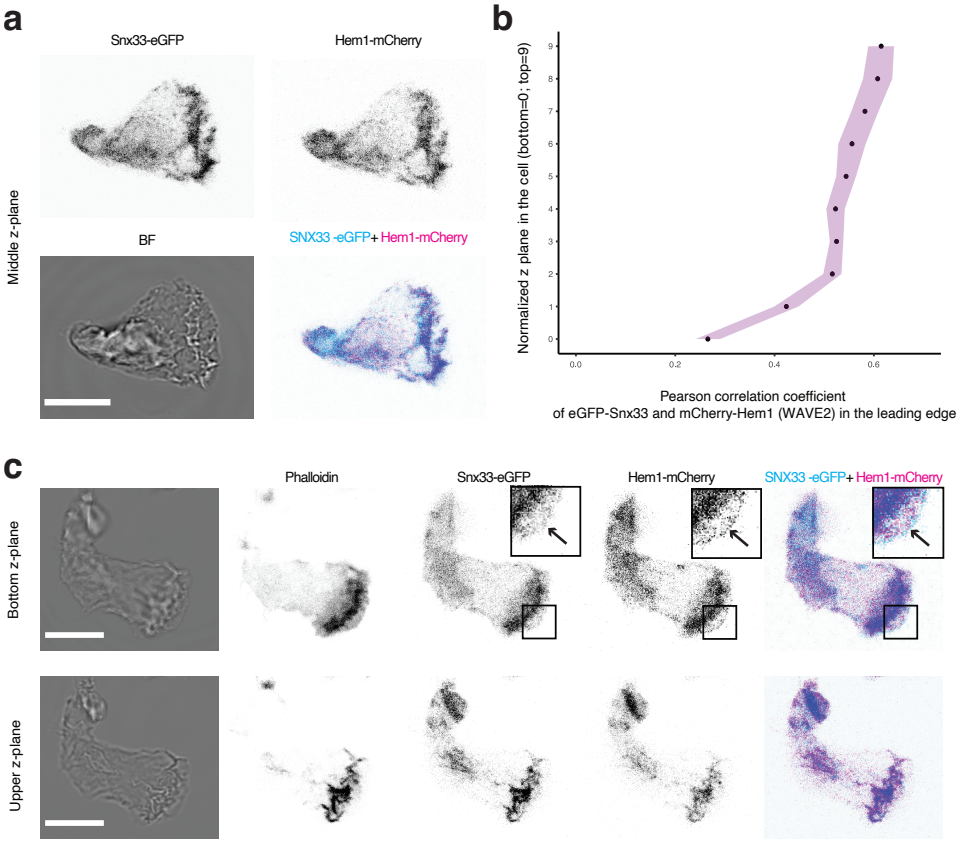

FIGURE 5.21: Snx33 and WAVE2 signal correlates, but SNX33 is excluded from a protruding edge. a. Confocal images of a migrating cell bright-field image, Snx33-eGFP and Hem1-mCherry (WAVE2) in the middle z-plane. b. Pearson correlation of Snx33-eGFP and Hem1-mCherry (WAVE2) in normalized z-planes (n = 10). Purple indicates SEM. c. Confocal images of a migrating cell bright-field image, Snx33-eGFP, Hem1-mCherry (WAVE2) and F-actin (Phalloidin-Alexa647) in the bottom and upper z-planes. Arrows indicate the most protruding edge at the cell bottom. Scale bar = 10 μm.

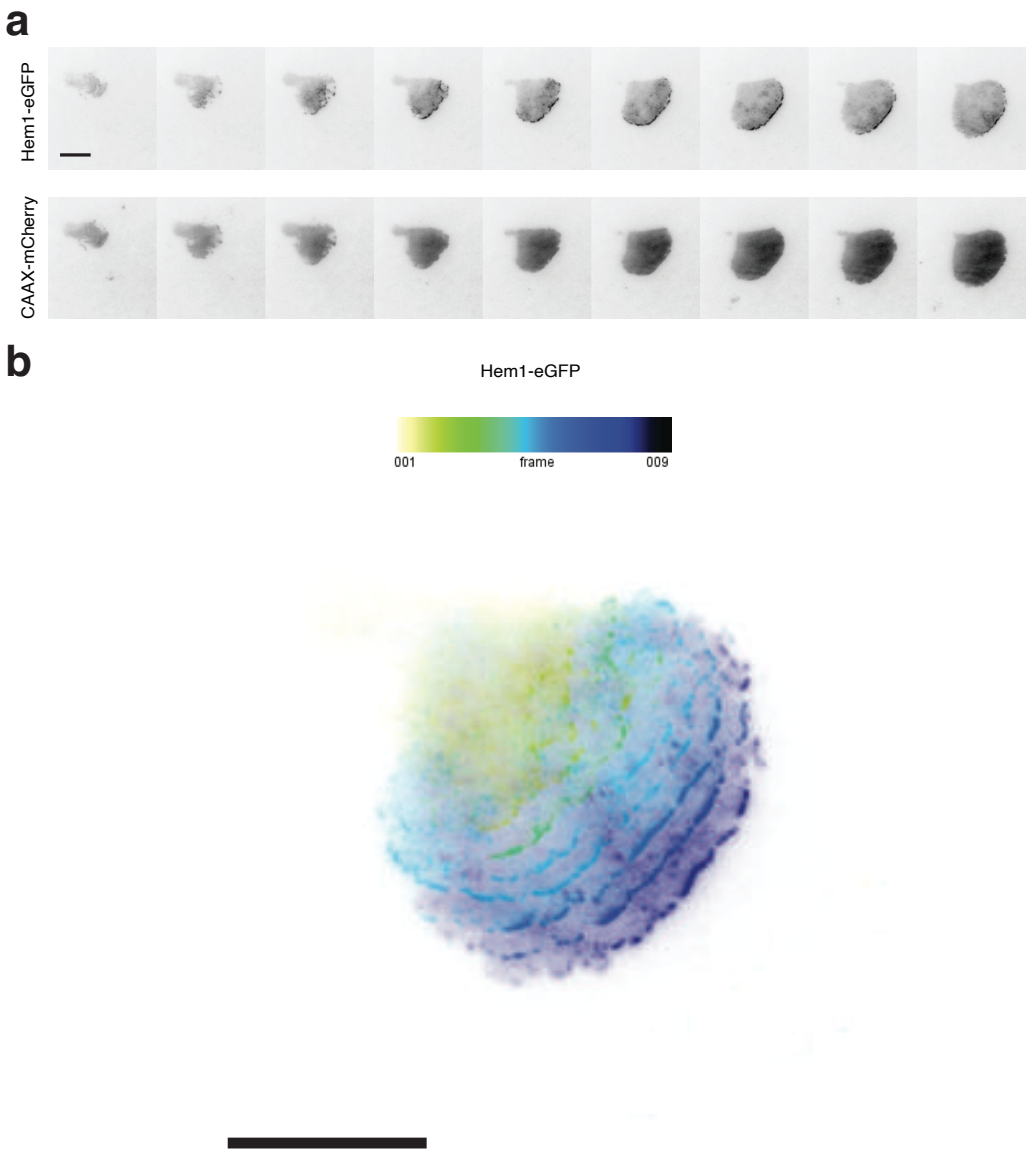

FIGURE 5.22: WAVE2 waves in migrating HL-60 cells. a. TIRFM images of Hem1-eGFP (WAVE2) and CAAX-mCherry (membrane) b. Color-coded time projection of Hem1-eGFP (WAVE2) to visualize WAVE2 waves progression. Time in-between frames is 5 seconds. Scale bar = 10 μm.

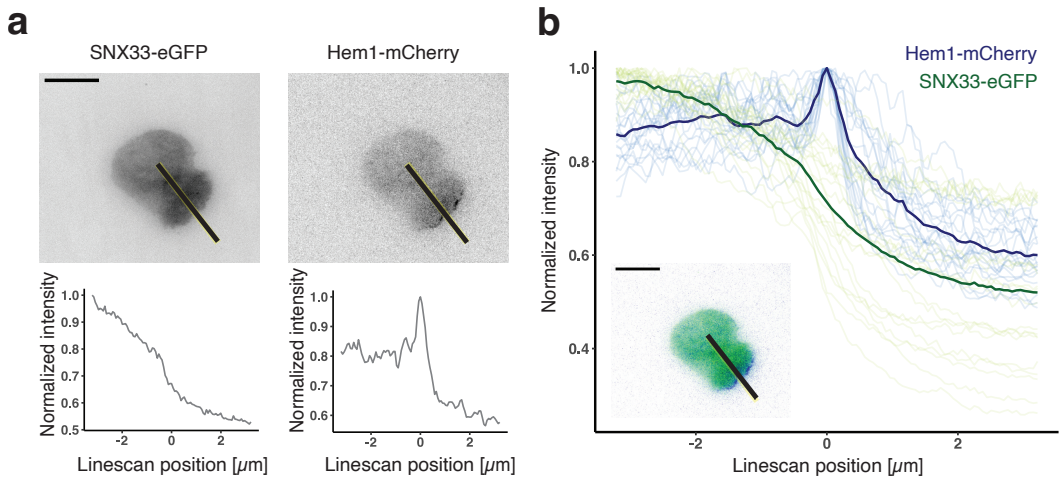

FIGURE 5.23: Snx33 and Hem1 (WAVE2) signal at the protruding edge. a. Exemplary images of a fluorescently-tagged Snx33 and Hem1 (component of WAVE2 complex) and representative linescans through the leading edge in migrating dHL-60 cells using TIRFM. b. Snx33 and Hem1 normalized intensity at the protrusion edge. Linescan position zero is set to highest normalized intensity of WAVE2 that corresponds to the protrusion edge (n=10). Scale bar = 10 μm.

enriched in these locations, confirming the results from confocal microscopy (Figure 5.23).

Changes in WAVE2 patterning at the plasma membrane in the Snx33 knockout clearly suggest a direct or indirect interaction between the two proteins. However, the nature of this interaction is not straightforward. It is plausible to hypothesize that this interaction depends on the binding to the membrane, as Snx33 shows the same localization pattern as Hem1 in the cytoplasmic fraction, but a different pattern when membrane-bound. Potentially, the difference between membrane-bound and cytosolic state could be connected to WAVE2 regulation of autoinhibition.

Together with our previous data on membrane mechanics, Snx33 exclusion from the leading edge is particularly interesting in the context of recent revision of the Brownian Ratchet Model by including MCA proteins into it. Based on the revised model, membrane protrusion are initiated by the release of MCA proteins that allows for actin-driven force exertion on the membrane (Bisaria et al., 2019; Welf et al., 2020). It was shown that the flat lamellipodia at the cell front were devoid of MCA protein Ezrin, while membrane signal remained unchanged (Welf et al., 2020). Snx33 behaves similarly to Ezrin in this regard - at the cell front where WAVE2 enrichment occurs, Snx33 is depleted. Furthermore, if this is the case, MCA proteins could not only play a role in protrusion initiation. Our results show that the depletion of Snx33 increases cell persistence and speed along with generating larger leading edges. The release provided by MCA proteins could also contribute to the formation and the size of cellular protrusions, which can be translated into the migration capacity.

5.3.10 Collision dynamics of migrating Snx33 knockout cells

We have previously shown that Snx33 knockout cells are more persistent, and thus, migrate faster in a 2D setting. As dHL-60 cells move at around 10 μm/min, if seeded densely enough, they often encounter other cells. Interestingly, we have observed that Snx33 knockout cells were found more often in contact with other cells

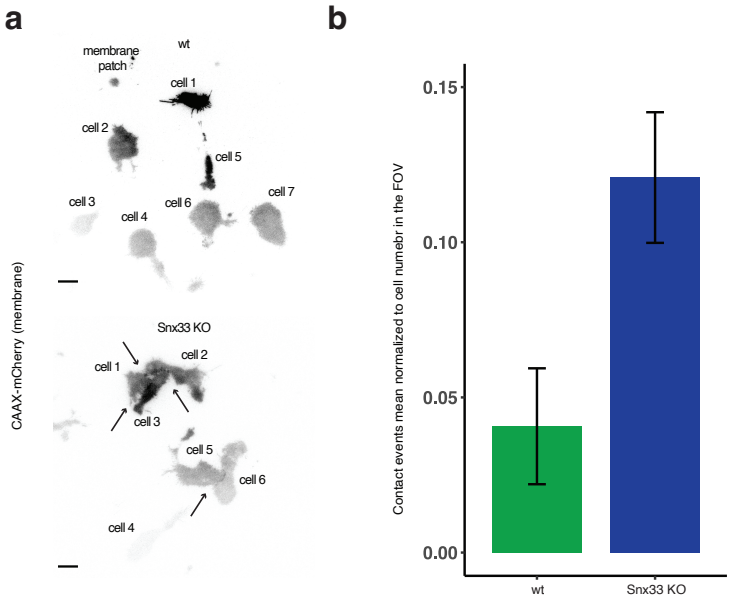

FIGURE 5.24: Snx33 knockout cells persist in cell-cell contact. a. Exemplary images of fluorescently-tagged CAAX (membrane marker) in migrating wt and Snx33 KO dHL-60 cells using TIRFM. Cells taken into consideration for quantification are labelled. Arrows point towards contact sites. b. Quantification of contact events in wt (n = 68) and Snx33 KO (n = 68) cells. Data from 3 biological replicates. Whiskers indicate SEM. Scale bar = 10 μm.

in comparison to wild type ones. To estimate the magnitude of this effect, we performed short time-lapse imaging of migrating wild type and Snx33 knockout cells using TIRFM. Imaging the bottom plasma membrane allowed us to access precisely whether cells were in contact. We defined the contact event as a situation when cells engage and persist in the interaction for more than 10 seconds. We quantified the number of contact events, taking into consideration the density of cells. We observed that the mean of contact events normalized to the cell density was almost 3-fold higher in Snx33 knockout cells than in the control (Figure 5.24).

Next, we followed the migration patterns of both cell types upon contact. To do this, we performed longer (2 minute) time-lapse TIRFM imaging on cells with a fluorescently-tagged Hem1 (WAVE2) and CAAX (membrane marker). We aimed at imaging the cells that were about to engage in a contact event. We automatically segmented cell membrane and WAVE2 (Methods 7.31) of interacting cell and observed striking differences in the cells behaviour when colliding (Figure 5.25a). First, we measured the length of contact interface and normalized it to the cell circumference. As a result, we found that Snx33 knockout cells had 1.7-fold higher percentage of cell circumference in contact than wild type cells (Figure 5.25b). It has been previously described that dHL-60 cells change direction upon contact or collision. The molecular basis of this behaviour lies in extinguishing of Hem-1 waves. As the waves collide with an obstacle, they do not continue to propagate. Instead, the waves of Hem1 in the leading edge or elsewhere that are not in direct contact with an obstacle expand and their propagation allows the cell to move away from barriers (Weiner et al., 2006). Hence, we wondered whether Snx33 could affect WAVE2 waves propagation. To test it, we measured the WAVE2 area covering the plasma membrane before and after a contact event. We revealed that the WAVE2 fold change is lower

in Snx33 knockout after a contact event (Figure 5.25c).

Our results support a hypothesis where Snx33 has an inhibitory effect on WAVE2. This effect could be especially important for controlling contact inhibition of cells. It is still not fully understood how the extinguishing of Hem-1 waves is controlled and how the waves are being inhibited at the contact site. To investigate it further, we decided to perform imaging on fluorescently-tagged Snx33 and Hem-1 (WAVE2) during a cell-cell contact in wild type cells. Interestingly, we observed that Snx33 was residing at the cell-cell interface, while Hem1 was excluded from this localization (Figure 5.26a). Moreover, the cells is re-polarizing in the direction indicated by Hem-1 signal that is opposite from the cell-cell contact interface covered with Snx33. This suggests that the leading edge protrusion is inhibited in the Snx33 enriched part of cell membrane. (Figure 5.26b-c).

5.3.11 Migration of Snx33 knockout cells in complex environments

Snx33 knockout changes the WAVE2 patterning at the plasma membrane that is crucial for the formation of the leading edge and polarization on the 2D substrate. Moreover, Snx33 knockout also affects speed and directionality of migration. Our results highlight the importance of Snx33 protein in steering cell migration. We wondered whether Snx33 protein was also crucial to facilitate navigation of the cells through complex environments, as recent studies showed that the WAVE2-dependent branched actin network is dispensable for microenvironments in which cells experience compression forces (Graziano et al., 2019). We decided to investigate the Snx33 knockout in complex environments using microfluidic devices, as previously (Section 4.3.4).

First, we exploited PDMS-based devices with long microchannels with a constriction in the middle, accommodating one cell in a single channel (Figure 5.27a; Methods 7.22). Cells were migrating in a gradient of chemoattractant (fMLP). The analysis of migration revealed that in comparison to control, Snx33 knockout cells were faster both when migrating through microchannels and when squeezing through constrictions, similarly to their higher speed on flat substrates (Figure 5.27b-d).

As a single constriction is a relatively simple obstacle, we took advantage of a more complex design of a PDMS-device having microchannels with a decision point in the middle (Figure 5.28a). The distribution of the frequency of choosing particular constriction sizes did not differ in wild type and Snx33 knockout cells (Figure 5.28b). Intriguingly, the latter cells were considerably slower at going through the decision point (Figure 5.28c-d). Taken together, these result support our previous findings that Snx33 knockout cells are faster and more persistent both when migrating on flat substrates and in microfluidic devices mimicking more complex environments. Curiously, a complexity of a decision point slows the Snx33 knockout cells down. This result might be connected to the fact that Snx33 knockout cells have diminished ability to change direction (Figure 5.18g), different WAVE2 patterning (Figure 5.20) and have higher contact interface with other objects (Figure 5.25).

Larger leading edges are connected to the increased cell speed and persistence in the Snx33 knockout cells. However, these same cells fall short when faced with a challenging environment, that pushes them to restrict protrusions to choose one path among others. The ability to restrict protrusion formation to only one leading edge has long been considered as a key feature of the cell movement in both single-cell and collective migration (Diz-Muñoz et al., 2016a; Plutoni et al., 2019). High activity of WAVE2 does not allow for efficient protrusion control, which results in impaired migration (Diz-Muñoz et al., 2016a). On the other hand, elimination of WAVE2 also

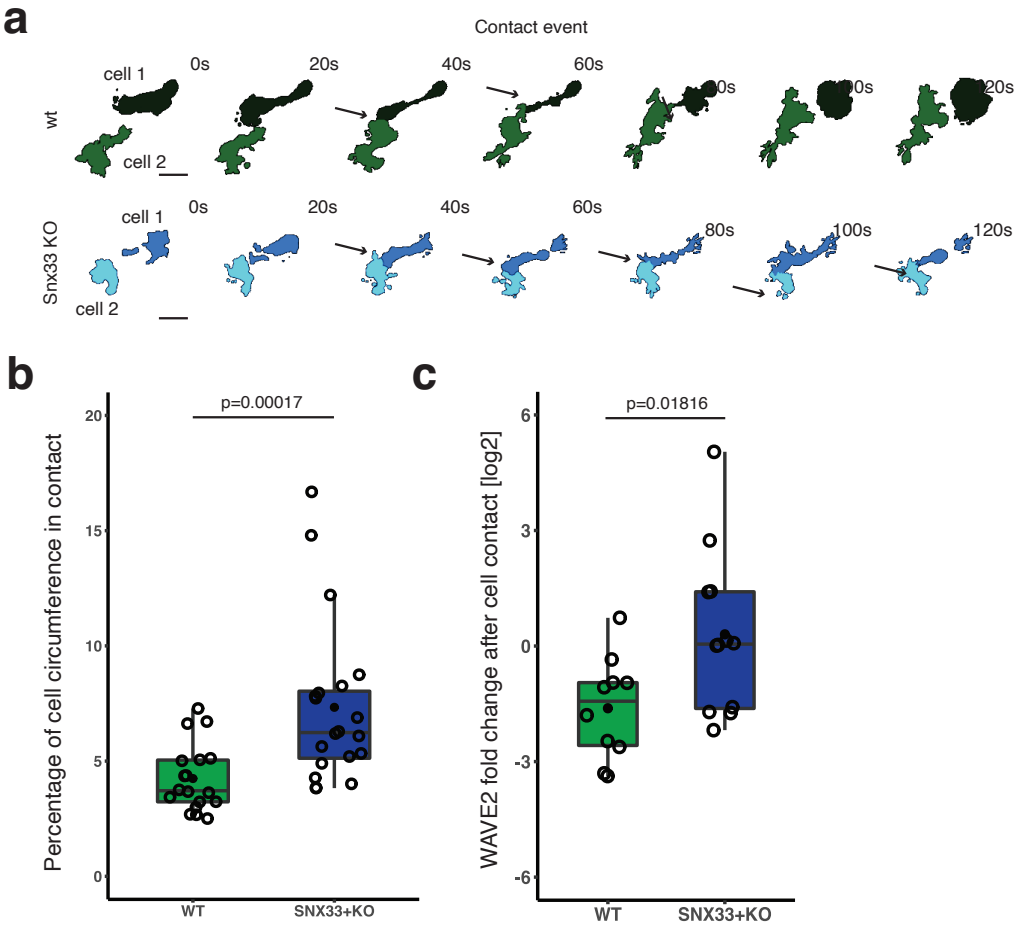

FIGURE 5.25: Snx33 inhibits WAVE2 complex at the plasma membrane restraining cell-cell contacts. a. Segmentation of a contact event between two wt (upper panel) or Snx33 KO (lower panel) dHL-60 cells. Arrows are pointing to contact interfaces. b. Percentage of cell circumference in contact with other cell in wt (n = 18) and Snx33 KO (n = 20) dHL-60 cells. e, WAVE2 fold change after cell-cell contact in wt (n = 9) and Snx33 KO (n = 10) dHL-60 cells. Data from 3 biological replicates. Data processed jointly with S. Dias Almeida. Scale bar = 10 μm.

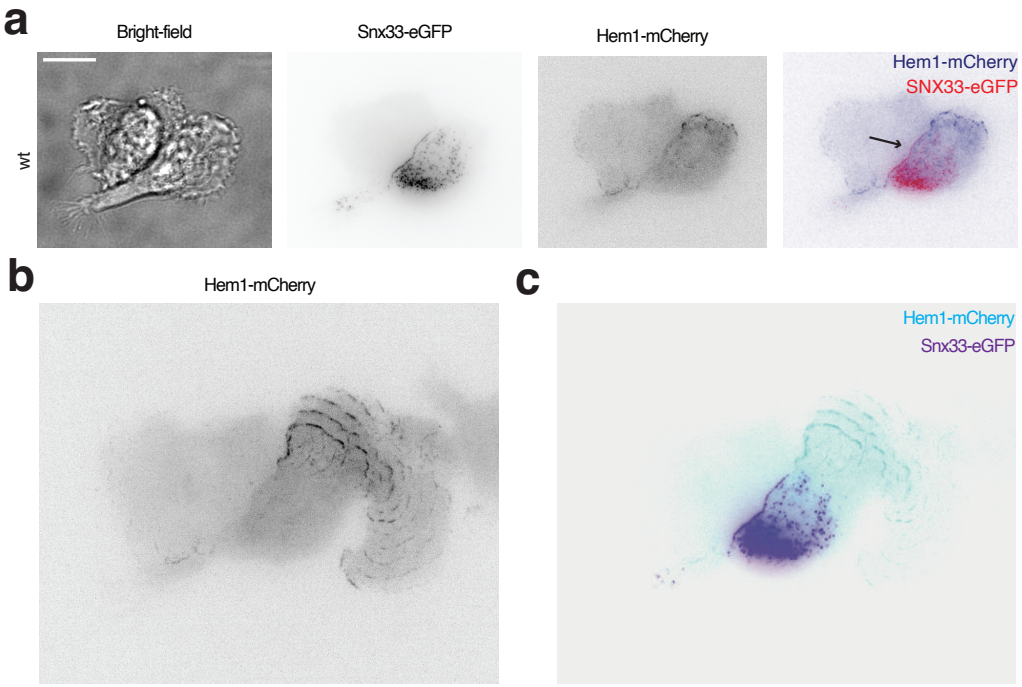

FIGURE 5.26: Snx33 localizes to the contact sites to restrict protrusion formation. a. Bright-field and TIRFM imaging of Snx33-eGFP and Hem1-mCherry in cell-cell contact. Arrow points towards the contact interface. b. Time projection of Hem1 (WAVE2) of 12 time points with 12 seconds in-between frames. c. Time projection of Hem1 (WAVE2) of 12 time points (12 seconds in-between frames) overlaid with Snx33-eGFP signal from the first time point. Scale bar = 10 μm.

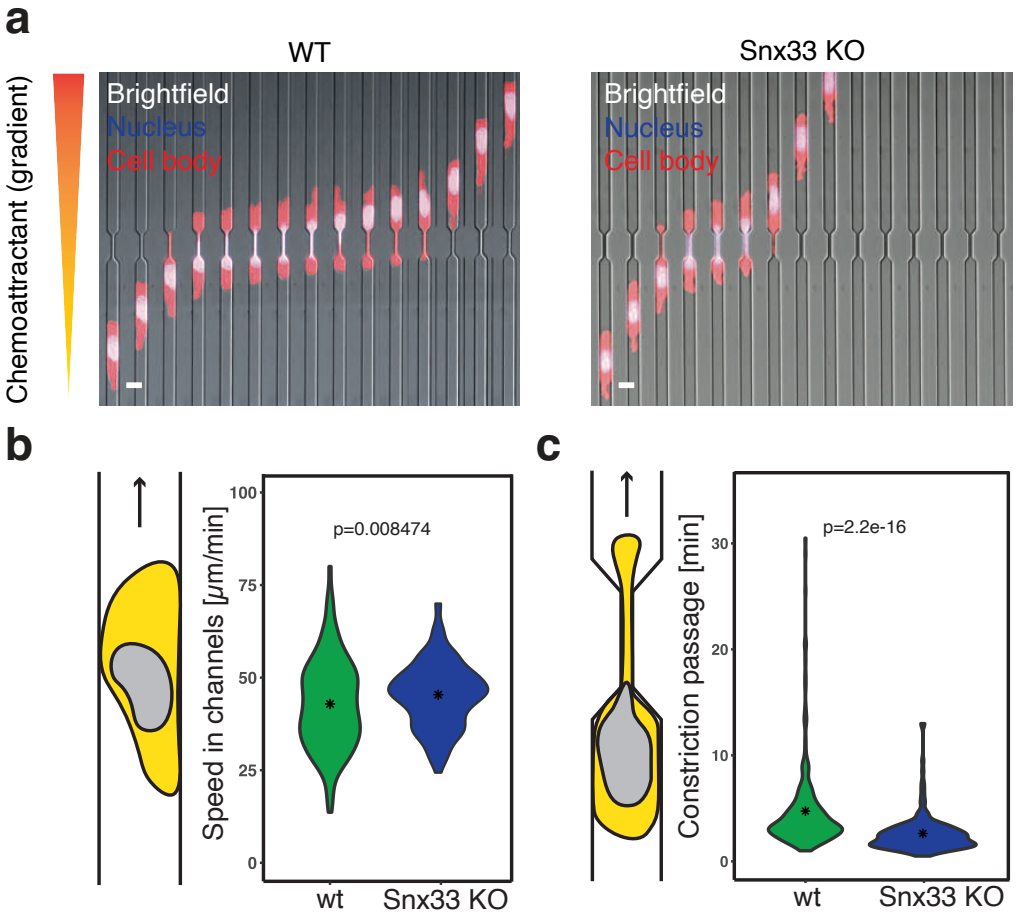

FIGURE 5.27: Speed and constriction passage time in microfluidic channels increases in Snx33 knockout cells. a. Time lapse of wt and Snx33 KO cells squeezing through constriction. Time in-between frames is 30 seconds. Scale bar = 10 μm. Schematic of migration assay using microfluidic devices and quantification of b. migration speed in straight channels (n = 235 for wt, n = 169 for Snx33 KO). c. constriction passage time (n = 234 for wt, n = 158 for Snx33 KO). Data acquired jointly with J. Stopp. Data from 3 independent biological replicates.

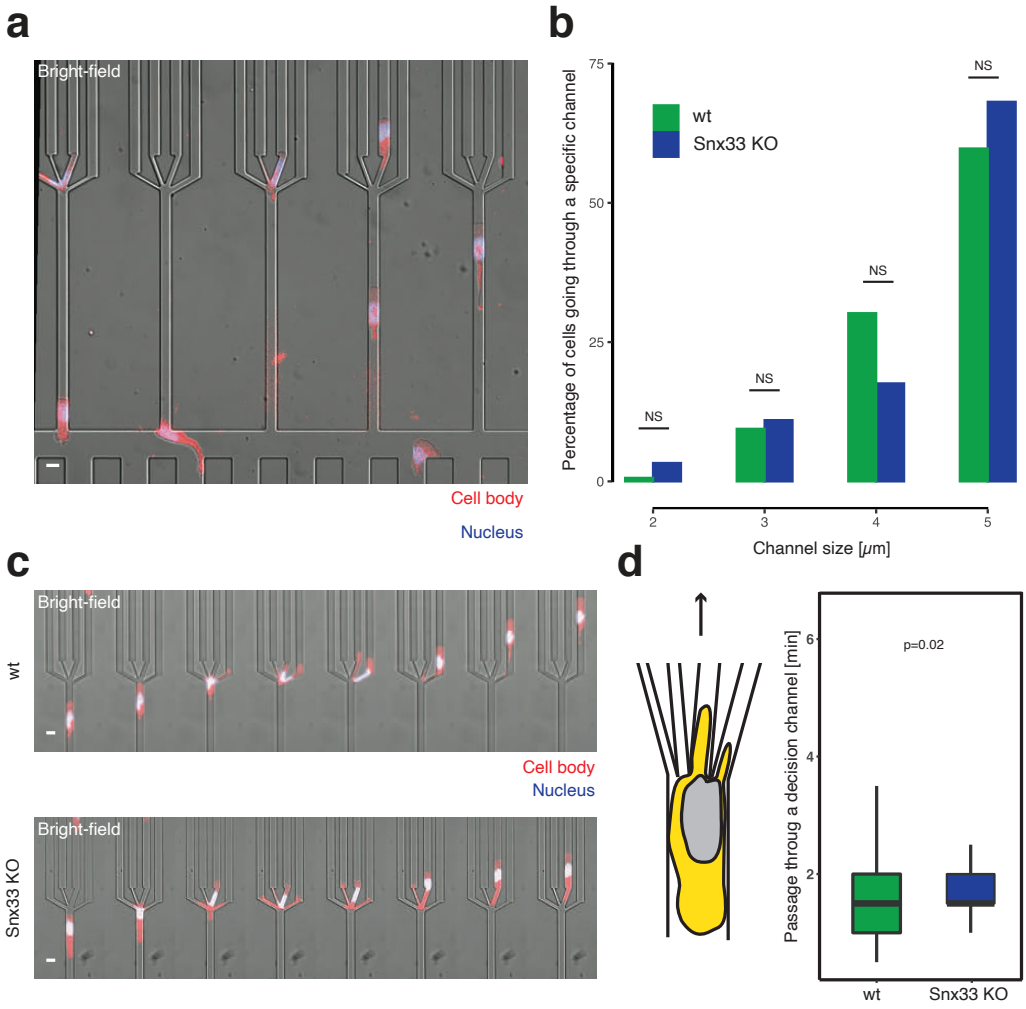

FIGURE 5.28: Snx33 knockout cells are less efficient at navigating through decision point. a. Overlay of bright-field, nuclei and cell body images of dHL-60 cells migrating in PDMS-based devices with a decision point. b. Frequency of wt and Snx33 KO dHL-60 cells choosing a channel of a certain size (n = 159 for wt, n = 91 for Snx33 KO). c. Time lapse of wt and Snx33 KO cells navigating through a decision point. Time in-between frames is 30 seconds. d Schematic of migration assay using microfluidic devices with a decision point and quantification of passage time (n = 159 for wt, n = 91 for Snx33 KO) in dHL-60 cells. Data acquired jointly with J. Stopp. Data from 3 independent biological replicates. Scale bar = 10 μm.

decreases the migration capabilities and generates diversified protrusions that slow the cell movement down. How is WAVE2 complex and actin assembly regulated in the Snx33 knockout? We observed that the F-actin network is more spread, but at the same time, more WAVE2 resides at the plasma membrane. This may suggest that depending on Snx33, WAVE2 can adopt a different spatial activity that modulates the actin network. Alternatively, as a BAR domain protein, Snx33 could also potentially indirectly affect WAVE2 localization and its subsequent activity by curvature regulation of the plasma membrane, but this needs to be further investigated (Leithner et al., 2016; Graziano et al., 2019).

5.3.12 Effects of individual Snx33 domains on filamentous actin organization and cell shape

As described in previous sections (Section 5.2.3), Snx33 is a protein with 574 amino acids residues which has several functional domains identified (SH3, PX, LC, BAR). The function and interaction partners of these individual domains are widely studied and well described (Kurochkina and Guha, 2012; Teasdale and Collins, 2011; Simunovic et al., 2019), albeit, how exactly do they interact to control lamellipodia formation and cell migration is not understood. For example, it has been demonstrated that the BAR domain is modulated by autoinhibition (Carman and Dominguez, 2018). Furthermore, is has also been shown recurrently that the binding of particular proteins to the SH3 domain of BAR domain proteins, among other effects, releases its membrane-binding surface, promoting their binding to the plasma membrane (AMPH2, ENTH [Meinecke et al., 2013], FCHSD2 [Stanishneva-Konovalova et al., 2016]). Unfortunately, only scarce data are available regarding the autoinhibition in sorting nexins. Very recently, the cryo-EM structure of yeast Mvp1, that shares conservation with the mammalian Snx8, revealed that the full-length protein forms an autoinhibited tetramer with the occluded membrane interacting PX-BAR domain (Sun et al., 2020). These findings suggest that autoinhibition of membrane-interacting interface could be conserved in other sorting nexins as well. For Snx33 in particular, the only structure available is of the PX-BAR domains (4AKV) forming dimers, but the contributions of the SH3 domain and the LC region and how are they spatially positioned remain unexplored.

Only a handful of studies investigates the importance of individual domains of Snx33. PX-BAR, but not the SH3 domain, turned out to be key for enabling homodimerization of Snx33 and its membrane tubulating activity in HeLa cells (Dislich, Than, and Lichtenthaler, 2011). In contradiction, the overexpression of Snx33 PX-BAR domain in HEK cells did not result into any localization to the plasma membrane (Wang et al., 2010) which was hypothesized by the authors to be due to the high overexpression perturbing the membrane recruitment or cell-type specificity. An independent study also encountered difficulties while working with Snx33. In their hands PX-BAR domain of Snx33 was unable to tubulate liposomes, unlike Snx18 and Snx9, but it generated extensive tubular network in HeLa cells (Håberg, Lundmark, and Carlsson, 2008). Lastly, another group reported that all truncated versions for protein that encompass domains in various configurations, except for LC region alone, do co-precipitate with WASP as well as inhibit cell proliferation in Hela cells (Zhang et al., 2009). All of the above findings suggest non-linear effects of the individual domains on cell machinery that are often challenging to interpret.

Here, we established a very robust experimental system, having a Snx33 knockout cell line that can be rescued using an eGFP-tagged Snx33 protein, proving the specificity of the knockout phenotypes arising from the lack of Snx33 protein solely.

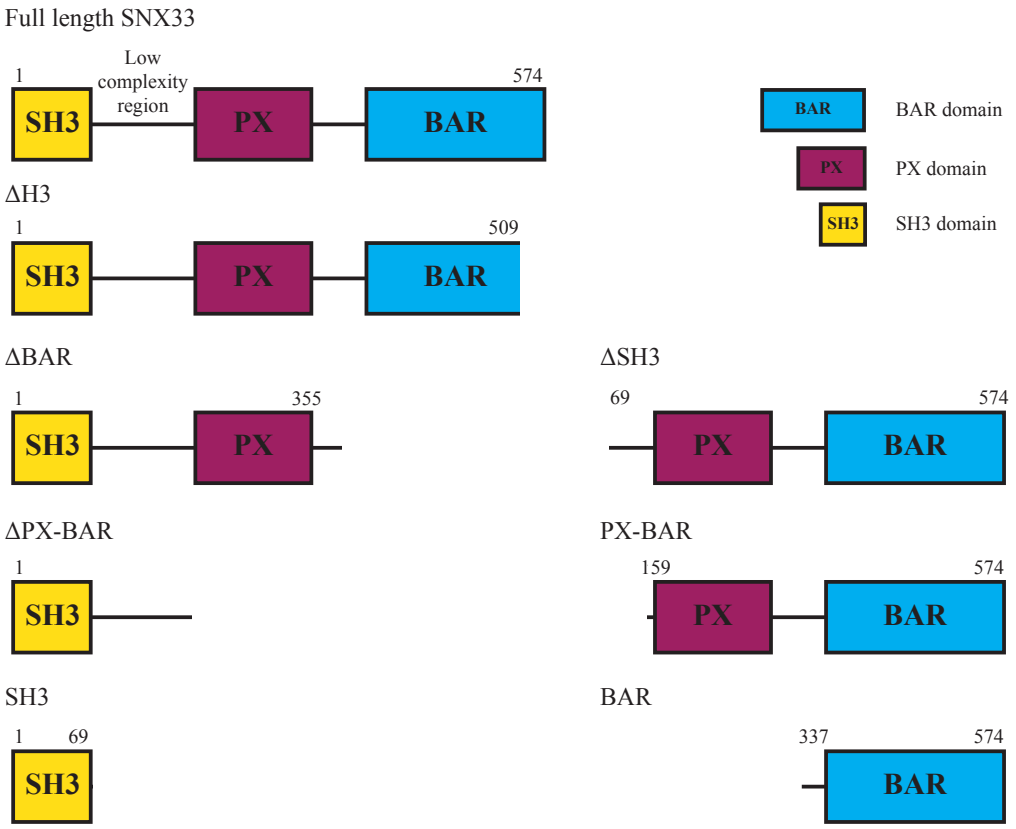

FIGURE 5.29: Schematic of Snx33 truncations. Domains size is not to scale.

Additionally, we showed that the highest achievable overexpression of the Snx33 in our system does not induce changes in the phenotype. Finally, the fact that migrating dHL-60 cells are not undergoing cell division as they are terminally differentiated allows us to investigate cell processes other than cell cycle progression, avoiding its confounding effects.

Consequently, we decided to shed some light on the roles of the individual domains of Snx33 for cytoskeleton organization and cell shape. To do so, we cloned several truncated versions of Snx33 and generated cell lines overexpressing them in wild type and Snx33 knockout cells with the aim of scrutinizing the role of membrane binding PX-BAR domain (Figure 5.29).

We imaged migrating dHL-60 cells and assessed the localization of all Snx33 truncations using epifluorescent microscopy (Figure 5.30; Methods 7.24). Surprisingly, localization of most of Snx33 truncations strongly resembled the localization of full-length Snx33 (Figure 5.5). In constructs with ΔH3, ΔBAR, ΔPX-BAR, SH3, ΔSH3 and PX-BAR we observed protein enrichment in the leading edge in both wild type and Snx33 knockout cells when imaging with a 40x objective (Methods 7.27). These results suggest that proper localization of Snx33 may depend on the interactions of its various domain with other proteins at the leading edge. Thus, truncations do not abort leading-edge localization. Interestingly, the BAR domain of Snx33 shows a cytoplasmatic and unexpected nuclear localization. Proteins with a molecular mass up to 40 kDa are able to enter nucleus by passive diffusion (Freitas and Cunha, 2009). However, a fluorescently tagged BAR domain of Snx33 is expected to have around

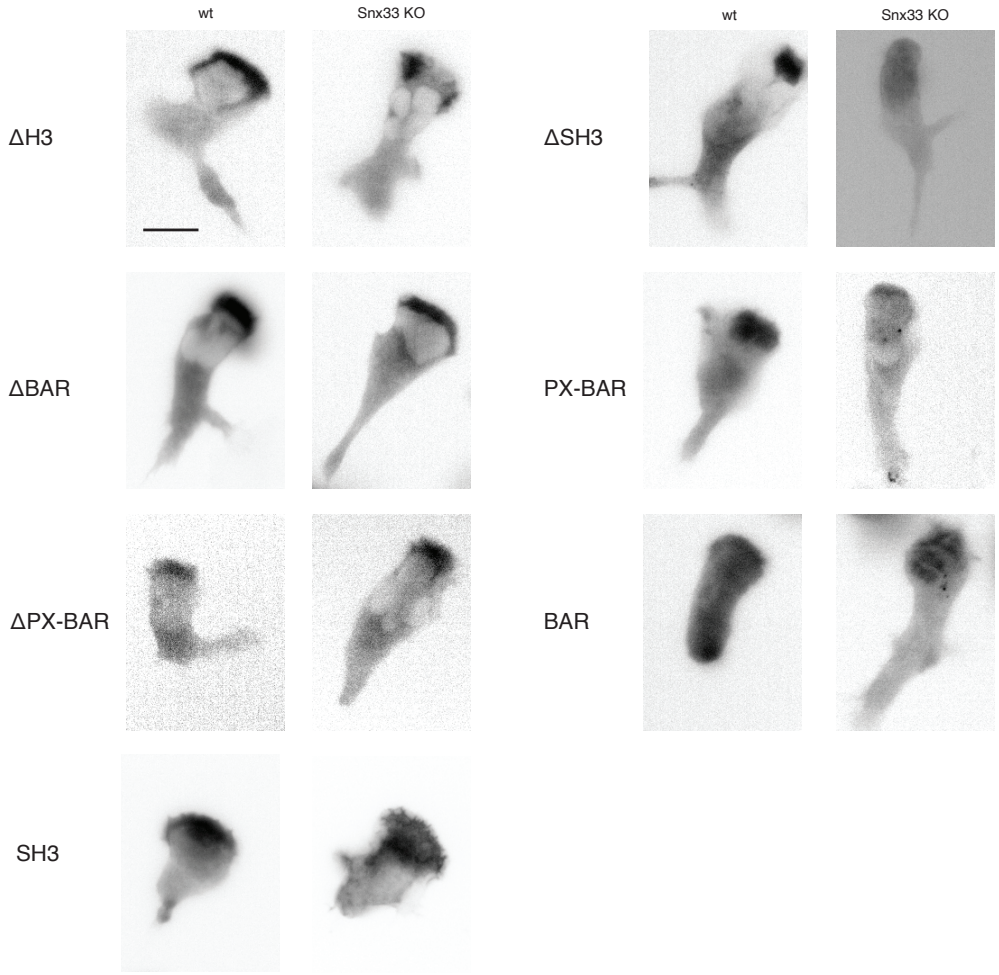

FIGURE 5.30: Epifluorescent imaging of Snx33 truncations (ΔH3, ΔBAR, ΔPX-BAR, SH3, ΔSH3, PX-BAR, BAR) in wild type and Snx33 knockout cells. Scale bar = 10 μm.

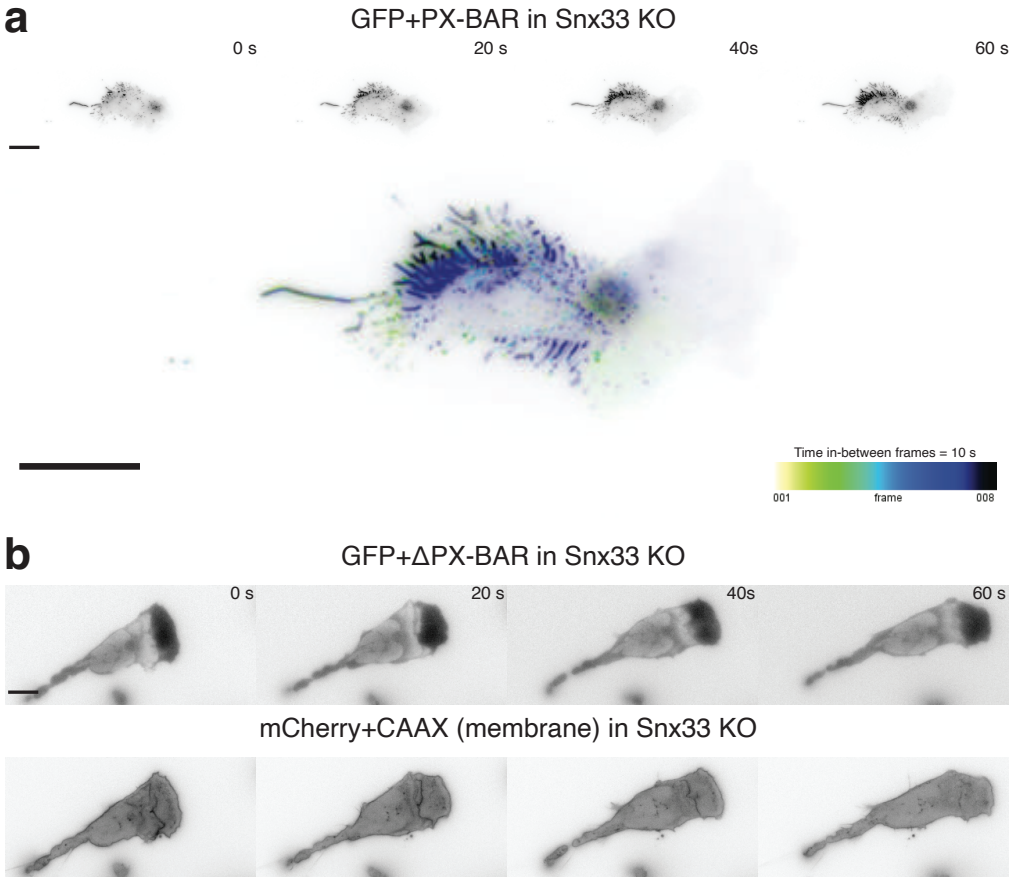

FIGURE 5.31: TIRFM and epifluorescent imaging of PX-BAR and ΔPX-BAR truncations. a. Time lapse of dHL-60 migrating cell with fluorescently tagged PX-BAR by TIRFM microscopy and time-encoded overlay. b. Time lapse of dHL-60 migrating cell with fluorescently tagged ΔPX-BAR using epifluorescent microscopy. Scale bar = 10 μm.

54 kDa, so it is not plausible that it resides in the nucleus. Further experiments are required to explain this phenomenon.

We decided to perform further experiments choosing two truncations, the ΔPX-BAR and the PX-BAR, as they had the most interesting phenotypes in the leading edge and at the membrane, respectively. In particular, we observed that the PX-BAR localizes to the bottom plasma membrane in the form of puncta that extend to create tubules (Figure 5.31a). This phenotype could not be observed with the full-length protein, but it corroborates the membrane tubulating activity of the PX-BAR domain, possibly partially inhibited in the full-length protein. We don't observe such tubules in the membrane ruffles at the leading edge of migrating cells, possibly due to the cytosolic signal, however, they could exist. On the other hand, cells with fluorescently tagged ΔPX-BAR show a strong signal enrichment in the leading edge (Figure 5.31b) which suggests that this truncation is potentially functional.

The experimental design and functional analysis of the PX-BAR and the ΔPX-BAR was performed as described previously (Section 5.3.3). Shortly, migrating Snx33 knockout and wild type cells stably expressing an eGFP-tagged PX-BAR and ΔPX-BAR were fixed, stained with F-actin and epifluorescently imaged (Figure 5.32a-b). The image analysis revealed that the PX-BAR and the ΔPX-BAR do rescue the cell

and leading edge area, similarly to the full-length Snx33 (Figure 5.32c-d).

The ΔPX-BAR truncation does partially rescue the F-actin intensity and density in the leading edge, similarly to the full-length Snx33 (Figure 5.32e-f). In contrast, the PX-BAR truncation partially rescues the F-actin density, but not F-actin intensity in the leading edge (Figure 5.32e-f). Interestingly, when we analyzed the total F-actin levels measured by phalloidin staining, neither of the tested truncations counterbalanced the effects of the Snx33 knockout, in contrast to the full-length protein (Figure 5.32g).

Apart from the important role of the full length Snx33 in regulation of the leading edge morphology, our experiments revealed its second role in modulating the F-actin polymerization in the cell body. This second role is possibly connected to perinuclear actin polymerization, as suggested previously (Zhang et al., 2009). Surprisingly, in our hands neither the PX-BAR nor the ΔPX-BAR truncations of Snx33 were able to restore the wild type levels of F-actin in the cell body. Two different hypotheses can be provided to explain these results. First, to keep the high F-actin levels in migrating cells, the concurrent binding of the plasma membrane and the SH3-LC domain effectors are required, which cannot be fulfilled by separated domains. Alternatively, the full-length cytosolic protein may exist in the autoinhibited form. In this form some (e.g. membrane binding) interfaces are occluded, but other interface could be released and available for binding of the F-actin machinery nucleators (such as WASP and WAVE). In conclusion, our data show that both the PX-BAR and the ΔPX-BAR truncations of Snx33 contribute to leading edge morphology, but further experiments are needed to understand the role of Snx33 in organizing the F-actin outside of the leading edge.

The role of BAR domain proteins in migration and curvature regulation has been intensively studied, but it is still not well understood how particular domains of these proteins act together to perform their specific functions. For example, recent *in vitro* studies showed that SH3 domain can recruit the BAR domain protein endophilin to membranes and tubulate them without electrostatic interactions between the lipids and BAR domain, but only by binding to the intracellular loops of GPCR receptors (Mondal et al., 2020). This exemplifies how various protein-protein interactions may drive unexpected functions. The regulation of the leading edge and the cell shape by both the PX-BAR and the ΔPX-BAR could be due to their independent mechanisms of action: ΔPX-BAR could regulate nucleation of actin polymerization by interactions with WASP or WAVE protein families, while PX-BAR construct could regulate actin assembly by binding to PIP_2 and resulting activation of PIP5K, as suggested for its family member Snx9.

5.3.13 Differential expression analysis of Snx33 knockout and wild type dHL-60 cells

As we found that Snx33 not only affects actin polymerization in the leading edge, but also outside of the leading edge, we wondered what other processes are affected by the knockout. To this end, we decided to perform an RNAseq experiment comparing wild type and Snx33 knockout cells at the 5^{th} day of differentiation. After collection of samples, total RNA was purified (Methods 7.4) and sequenced at the Genomics Core Facility (Methods 7.5). Principal component analysis (PCA) of the data showed little variation within every condition. The PC1 explains 89% of the variance that comes from the difference between the Snx33 knockout and wild type cells. The variation within each condition is, on the other hand, captured by PC2 that explains 7% of the variance. Alike, sample to sample distance map confirmed

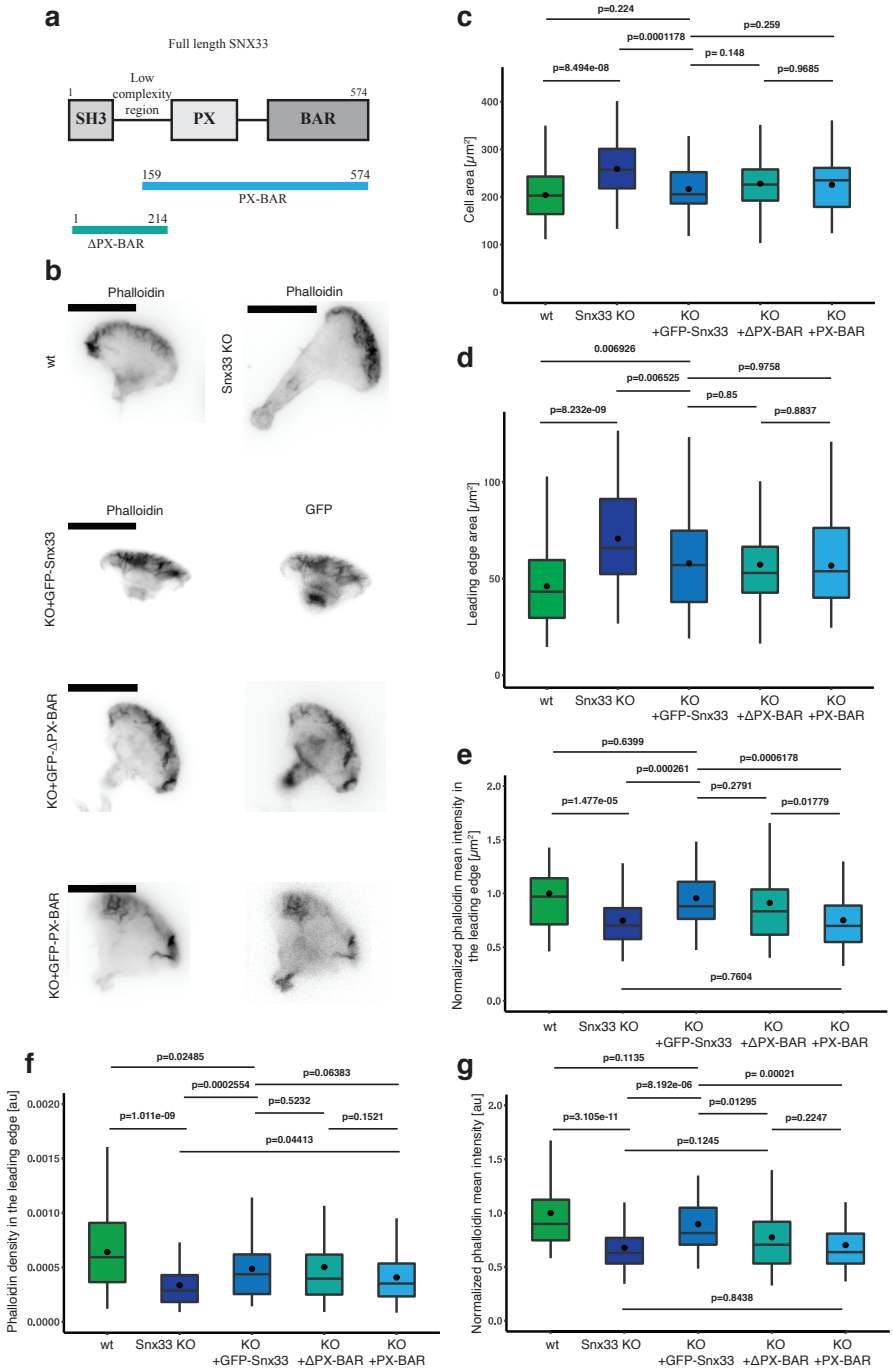

FIGURE 5.32: PX-BAR and ΔPX-BAR truncations of Snx33 contribute to cell and leading edge morphology. a. Schematic of full-length protein and Snx33 truncations. b. Example images of phalloidin staining and eGFP signal from wild type, Snx33 KO and Snx33 KO rescued with eGFP-Snx33, eGFP-ΔPX-BAR and GFP-PX-BAR. Quantification of c. cell area, d. leading edge area, e. phalloidin fluorescence in the leading edge, f. phalloidin density in the leading edge and g. phalloidin fluorescence in the cell for indicated conditions. Data are from 3 independent experiments. n = 72 (wt), n = 73 (Snx33 KO), n = 45 (KO + eGFP-Snx33), n = 74 (KO + eGFP-ΔPX-BAR), n = 57 (KO + eGFP-PX-BAR). Data processed jointly with S. Dias Almeida. Statistics: T-test and Mann-Whitney-U-Test. Scale bar = 10 μm.

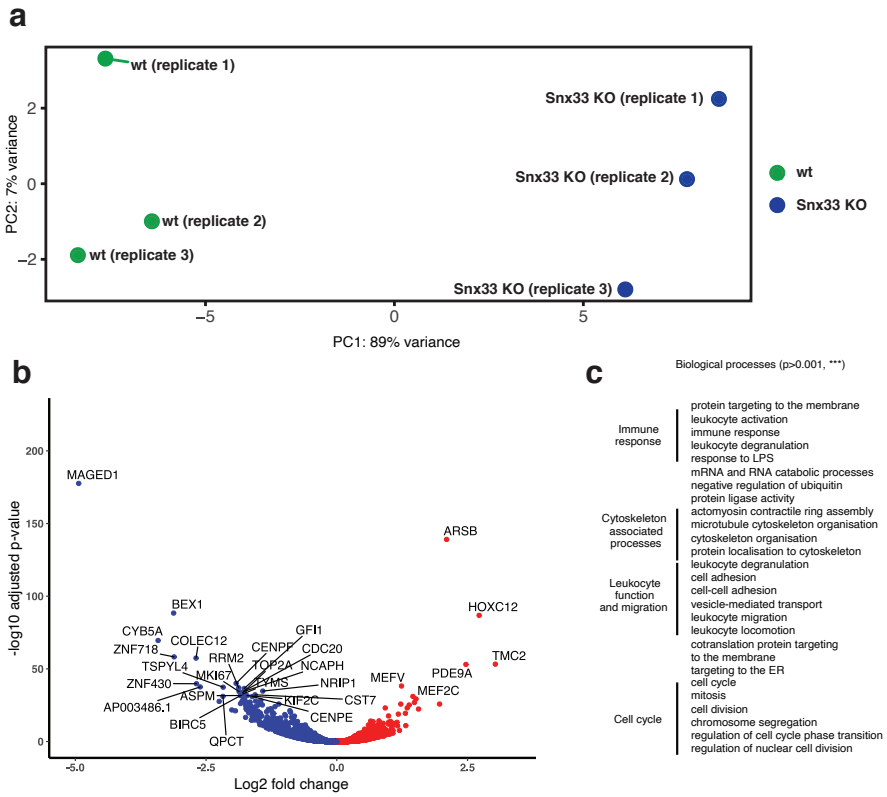

FIGURE 5.33: Differential expression analysis of Snx33 knockout and wild type dHL-60 cells a. Principal component analysis (PCA) plot from RNAseq experimet comparing wild type and Snx33 KO samples of 3 biological replicates. b. Volcano plot showing the distribution of differently regulated genes (FDR adjusted p-value < 0.05) between wild type and SNX33 KO dHL-60 cells. Points shown in blue are underexpressed and in red are overexpressed in Snx33 KO dHL-60 cells. Top 30 most significant hits are labelled. c. Statistically significant GO terms Biological Processes identified between wild type and Snx33 KO dHL-60 cells.

high correlation of the samples coming from the same condition. The sequencing results were analyzed taking the advantage of the differential expression analysis (DEseq2). We identified a total of 416 genes of significance (FDR adjusted p-value < 0.0001 and fold change > 1) affecting a variety of proteins. We used hits that had p-value < 0.05 for Gene Ontology (GO) analysis and determined several affected 'biological processes' including immune response, cytoskeleton, adhesion and cell migration, in agreement with our previous results. Interestingly, many highly differentially expressed genes are involved in the cell cycle regulation. Some reports suggested that Snx33 plays a role in cell division and cell cycle control (Zhang et al., 2009; Ma and Chircop, 2012; Carim et al., 2019). Both in HeLa cells and in *Drosphila*, Snx33 and its homologue in flies were shown to affect cytokinesis through cleavage furrow organization (Ma and Chircop, 2012; Carim et al., 2019). However, in HL-60 cells we could only observe mild differences in the growth rate. As Snx33 is widely expressed in a variety of cell types (Zhang et al., 2009), it is feasible to suspect that its functions may be cell type-specific.

Interestingly, one of the most highly overexpressed gene in the Snx33 knockout is MEF2C, known as transcription activator that acts in a Ca^{2+}-dependent signal

transduction cascade. We observed a similar pattern in the expression of TMC2, a protein involved in mechanoelectrocial transduction in auditory hair cells that involves calcium signaling (Giese et al., 2017; Beurg et al., 2019). This suggests that Snx33 knockout could be involved in Ca^{2+} storage and modulation of intracellular Ca^{2+} homeostasis.

5.3.14 Calcium homeostasis in migrating Snx33 knockout cells

Calcium signaling is essential for diverse biological processes, including muscle contraction, differentiation, proliferation and gene expression (Hogan, Lewis, and Rao, 2010). The cell surface is a key player in governing the mechanism of calcium influx, as the engagement of cell surface receptors initiates a signaling cascade. This signaling cascade leads to the phosphorylation of phospholipases that convert PIP_2 into DAG and IP_3. IP_3 then binds to its receptor on the ER and releases calcium from ER stores (Clemens and Lowell, 2015).

In cells, cytoplasmic levels of calcium are well regulated and kept low by a variety of calcium channels present in the plasma membrane (ORAI and TRPC protein family) and ER proteins (STIM protein family). Calcium levels are especially critical for immune cells as they affect mast cells degranulation, lysis of T cell targets as well as all cytokine responses and differentiation (Hogan, Lewis, and Rao, 2010). Several studies have linked calcium activity to cell speed, directionality and chemotaxis (Tsai and Meyer, 2012; Tsai et al., 2014). In HUVEC cells, cyclic calcium pulses trigger local retraction and adhesion of lamellipodia (Tsai and Meyer, 2012). At the leading lamella of fibroblasts, active calcium flickers promote cell turning (Wei et al., 2009), while in endothelial leader cells they regulate both directionality and speed of migration (Tsai et al., 2014).

Calcium signals also affect structure and polarity of the leading edge, for example, influx of calcium induced by fMLP was shown to be dependent on store-operated Ca^{2+} entry (SOCE) and affect activation of Akt, Src, Rac2, Cdc42 and polarization (Evans and Falke, 2007; Wei et al., 2009; Zou et al., 2012). More recently, it has been shown that Rac1, a key regulator of the actin cytoskeleton signaling upstream of WAVE2, potentiated translocation to the leading edge of ORAI1 (calcium channel in the plasma membrane). This, resulted in an increased surface exposure of ORAI1 which promoted membrane ruffling. In turn, ORAI1 knockout cells have reduced speed, directionality, smaller lamellipodia and are less polarized (Tsai et al., 2014; Lopez-Guerrero et al., 2020).

First, we decided to assess whether the Snx33 knockout interferes with fMLP-induced actin polymerization, a process that is known to be affected by calcium influx. To do so, we fixed non-adherent cells before and after the addition of fMLP at several time points and stained the cells with phalloidin (Methods 7.21). The median value of F-actin staining did not significantly differ before and after 10 minutes of fMLP stimulation. However, one minute after the fMLP stimulation it was significantly higher in the Snx33 knockout in comparison to the control (Figure 5.34b). At this time, fMLP induces an initial burst of F-actin polymerization in many regions in the cell. Later, F-actin polymerization is restricted to only one leading edge (Weiner et al., 1999). We wondered if the increased F-actin levels are the results of disturbed calcium homeostasis by the lack of Snx33. Next, we took advantage of a calcium indicator (Fluo-4-AM) to measure the calcium influx during cell polarization by flow cytometry (Methods 7.32). We observed that intracellular calcium levels were higher

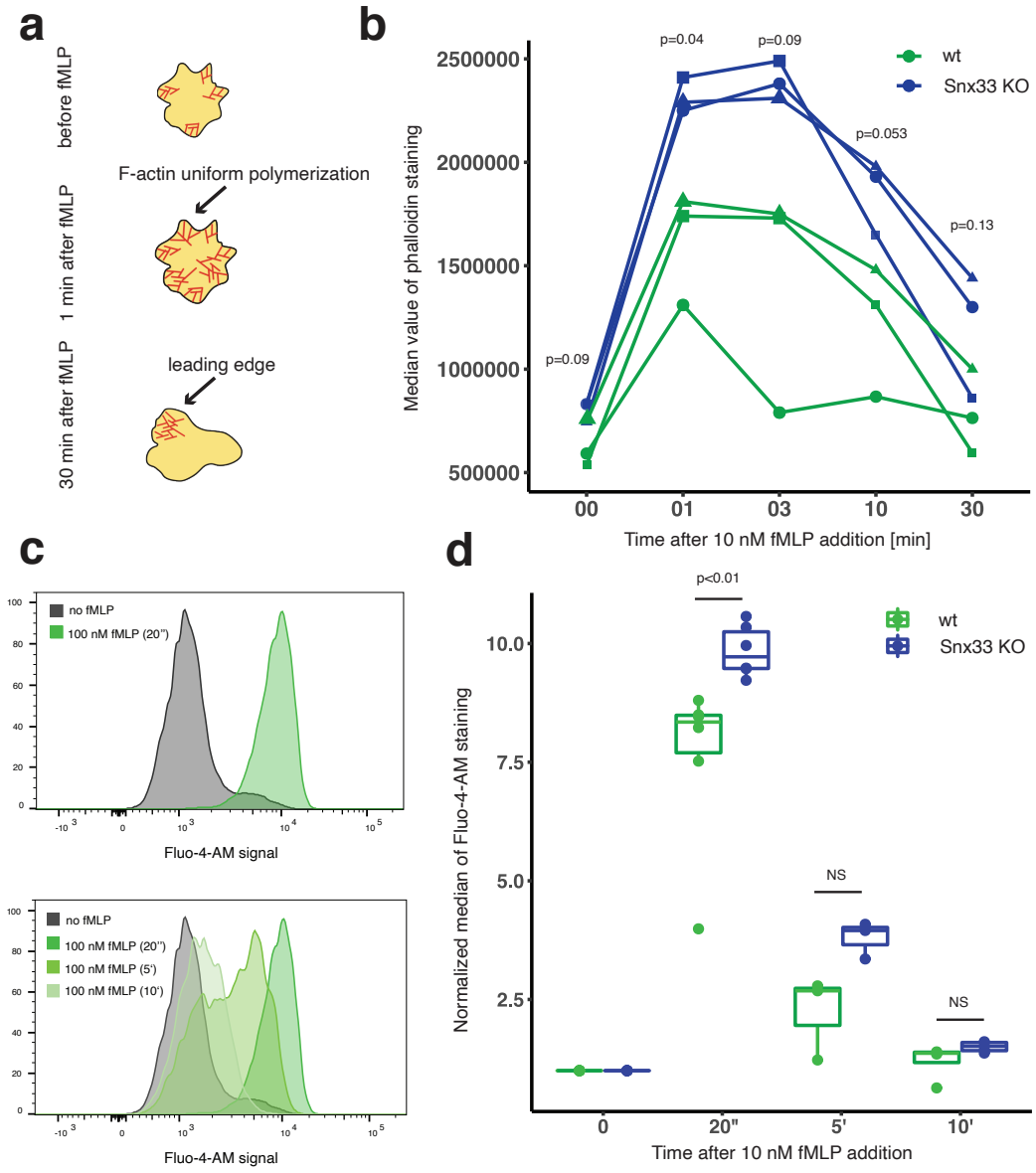

FIGURE 5.34: Snx33 knockout increases the F-actin initial polymerization and the intracellular calcium levels upon chemoattractant stimulation. a. Schematic of F-actin polymerization in HL-60 cells before and after 10 nM fMLP stimulation. b. Median value of phalloidin staining of fixed wt and Snx33 KO dHL-60 cells using FACS upon 10 nM fMLP stimulation. Data from 3 independent experiments. c. Representative histograms of Fluo-4-AM fluorescence in dHL60 wild type cells before and after 100 nM fMLP stimulation. d. Normalized Fluo-4-AM median fluorescence for wild type and Snx33 KO dHL60 cells upon 100 nM fMLP stimulation. Data points correspond to the individual measurements in two independent experiments. Statistics: T-test and Mann-Whitney-U-Test.

in the Snx33 knockout cells, confirming our hypothesis that Snx33 knockout deregulates calcium homeostasis (Figure 5.34c-d). How calcium signaling could be related to membrane mechanics, and in particular, to a curvature-sensitive protein Snx33?

Recent studies showed that intracellular calcium oscillations stemming from ER stores can be induced in response to mechanical forces (applied to the membrane of HMSC cells by optical laser tweezers) (Kim et al., 2015). The role of the cytoskeleton in the transmission of mechanical forces is crucial, as its disruption (by cytochalasin D, nocodazole or blebbistatin) eliminates the force-induced calcium oscillation and, in general inhibits extracellular calcium influx (Kim et al., 2015). Interestingly, new results show that curvature-sensitive proteins (septins) coordinate the architecture of the PM-ER junctions in which ORAI1 calcium channels are gated by STIM1 (that regulates store-dependent calcium entry into the cells). Super-resolution imaging of filamentous septins 4 and 5 revealed that they do not colocalize with the ER-PM junctions, but indirectly modulate STIM1-ORAI1-mediated calcium signaling, possibly by cytoskeletal or membrane rearrangements. Direct regulators remain unidentified (Sharma et al., 2013; Deb, Pathak, and Hasan, 2016; Katz et al., 2020). Intriguingly, we found that Septin 5 was downregulated in the Snx33 knockout cells (-0.78 log Fold change). However, it is possible that observed effects in calcium homeostasis deregulation does not come from changes in transcription, but from the Snx33 function in orchestrating cell surface regulation. As BAR domain proteins are (similarly to septins) curvature-sensitive, they could potentially be indirect or direct modulators of the PM-ER junction. Very recently, a BAR domain protein BIN2 was found to orchestrate calcium influx together with STIM1 and IP_3 receptor in platelets (Volz et al., 2020). Proteins from the sorting nexin family are particularly promising candidates to govern calcium influx as they have functions at the ER and, similarly to BIN2, contain an N-BAR domain.

5.3.15 Summary

In this Chapter, we presented the role of curvature-sensitive protein Snx33 in the context of cell migration and the regulation of the cell surface mechanics. Following high expression of Snx33 mRNA in migratory cells, we revealed that this protein is enriched in the leading edge of motile cells, and localizes specifically to curvature-rich membrane ruffles. Next, by generating and validating the Snx33 knockout cell line using CRISPR/Cas9 technology and establishing several quantification methods, we scrupulously showed the importance of Snx33 for the cell and leading edge morphology and adhesion. Further, linking leading edge characteristics to membrane mechanics, we discovered that cells devoid of Snx33 change their mechanical properties of the plasma membrane. Specifically, we found an increase in membrane tension and decrease in MCA parameter α value in the Snx33 knockout cells, suggesting that this protein is important for cell surface homeostasis regulation. Using a combination of machine learning-based segmentation for time-resolved TIRF microscopy and microfluidics, we demonstrated that motion persistence and directionality, in both freely moving and environmentally constrained cells, strongly depend on the Snx33. Particularly, we observed that Snx33 controls lamellipodia dynamics by regulating WAVE2-driven actin polymerization. Cells lacking Snx33 migrate faster and are more persistent during unobstructed migration, but fall short when a change in direction is required. By quantification of fluorescent imaging, we proposed a potential inhibitory effect of Snx33 on WAVE2 that is particularly important for cell-cell contact inhibition and cell turning. Additionally, we investigated the effects of the individual domains of Snx33 in the context of cell shape as well as and F-actin polymerization. We discovered that both parts of Snx33, the ΔPX-BAR and the PX-BAR, can independently rescue various Snx33 phenotypes, but the full-length protein is indispensable for an efficient total F-actin polymerization. Finally, we show that the cell surface homeostasis is also key for the regulation of calcium signaling. In summary, we demonstrated that Snx33, a curvature-sensitive BAR domain protein, is crucial for directed cell migration in complex environments as it orchestrates lamellipodia dynamics.

Part III

Concluding Remarks

Chapter 6

Concluding remarks

Despite many undertakings towards understanding the complexity of mechanochemical feedbacks that drive cellular functions, many questions of how mechanical properties are interpreted to steer the cell or tissue behaviour and *vice-versa* are still not fully understood. In this study, we focused on a versatile group of proteins, BAR domain proteins, that share only one simple characteristic - their shape allows for sensing and generation of plasma membrane curvature (Simunovic et al., 2019). The complexity of their biological roles arises from several aspects: the flexibility of membrane types and shapes that they bind to, mechanisms by which they curve membranes, a variety of protein-protein interactions they engage in, and the forces that can be exerted on the membrane with their assistance (Suetsugu, Toyooka, and Senju, 2010; Carman and Dominguez, 2018; Simunovic et al., 2019). To grasp the perplexing ways in which BAR domain proteins act together with other proteins and membranes, it is necessary to investigate a biological process than can capture their potential. Cell migration meets these conditions as it requires dynamic membrane and actin cytoskeleton remodeling that depends on the surrounding environment (Lämmermann and Sixt, 2009; Yamada and Sixt, 2019). During their movement, cells need to sense and respond to a variety of stimuli to perform their functions efficiently. Here, the cell surface is not only a barrier between the outside and inside of the cell, but a dynamic interface where the mechanical properties and the biochemical signaling can inform the cell function.

It remains very challenging to understand the relationship between the organization of the cell surface and migration, especially for mammalian cells, as they display a plethora of dynamic processes shaping their morphology and functions. To shed light on this topic, we decided to investigate one of the fastest migrating mammalian cells, namely, the neutrophil-like HL-60 cell line (Sitarska and Diz-Muñoz, 2020). In the future, it would be interesting to investigate immune cells *in vivo*, to both validate in more details functions of BAR domain proteins and get inspired for the design of more complex microfluidic devices by the natural environment and its challenges.

In this work, we found several BAR domain proteins that could be of most relevance for the interplay between the cell surface mechanical properties and cell migration. We focused our endeavours on the two of them, SH3BP1 and Snx33, and demonstrated that they indeed govern the regulation of the cell surface and are particularly important for orchestrating complex cellular movements. Investigation of other interesting BAR domain proteins was beyond the scope of this work, but nevertheless, it would be important to study them in the future. Many BAR domain proteins interact with other members from this group, so it is tempting to speculate that their interactions could also contribute to organization of the cell surface and resulting functions.

To our knowledge, SH3BP1 and Snx33 are the only BAR domain proteins identified to both response to, and directly change mechanical properties of the plasma membrane. Previously, it has been only suggested that BAR domain proteins could potentially act as membrane tension sensors. It was motivated by the relation between the differences in membrane tension levels and the changes in the curvature landscape as shown in the context of keeping the balance between endocytosis and exocytosis (Diz-Muñoz, Fletcher, and Weiner, 2013). Studies about another two BAR domain proteins, FBP17 and GRAF1, confirmed that they indeed response to membrane tension modulation induced by osmotic shocks by changing their subcellular localization (Tsujita, Takenawa, and Itoh, 2015; Vidal-Quadras et al., 2017). However, no BAR domain protein was formerly reported to change membrane tension levels by its depletion or overexpression, as we could show for SH3BP1 and Snx33. Further experiments investigating more BAR domain proteins could allow to evaluate if it is a general property of curvature-sensitive and curvature generating proteins or whether it requires a specific characteristic.

In terms of the several mechanisms of BAR domain proteins and their many facets, a picture emerge, in which by sensing or generate membrane curvature, they create molecular platforms that recruit and enable binding and activation or deactivation of various partners, leading to performing a plethora of finely-tuned cellular processes such as steering the protrusions during cell migration. We have identified that two proteins that share a BAR domain, SH3BP1 and Snx33, as novel regulators of cell surface mechanics by both responding to and affecting plasma membrane tension. Despite distinct mechanisms of action, they both contribute to the steering of cell migration by controlling cell protrusions. Although many crucial proteins for cell migration are well known, it is their complex interaction that makes a difference in the ever-changing environment. By studying BAR domain proteins that relate dynamics of the cell surface to cellular functions we can unravel the timely and spatially regulated feedback mechanisms and the physics of the cell surroundings with the biochemistry of the cell interior.

Part IV

Methods

Chapter 7

Methods

Materials and Methods are presented in the order of appearance.

7.1 HL-60 cells culture and differentiation

HL-60 cells were obtained thanks to the generosity of Prof. Dr. Orion Weiner (UCSF, USA). For all experiments the clone HL60MB8 was used. HL-60 cells were grown in 5-40 ml of RPMI 1640 media with 10% heat-inactivated FBS (#10500-064, Gibco) and 1% Penicillin-Streptomycin antibiotics solution (#15140-122, Gibco) in a humidified incubator at 37 °C with 5% CO_2. Two types of flasks were used: smaller (#353109, Falcon) and bigger (#430641U, Corning), depending on the needs. Counting was performed using plastic slides with grids (#87144E, KOVA). Cells were split when reaching the confluency of $1x10^6$-$1.5x10^6$ per ml.

Cell differentiation was achieved by adding 1.5 % of DMSO (#D2438, Sigma Aldrich) to split cells reaching around $1.5x10^5$ cells per ml. Cells were then incubated as usual, and used 5 days post-differentiation, if not indicated otherwise. For RNAseq samples, cells were used also after 1, 2, 3 and 4 days after differentiation. One biological replicate is defined as an independently differentiated batch of HL-60 cells.

If experiments required starvation, the HL-60 cells were spun in the centrifuge (Heraeus™ Megafuge™ 16, Thermo Fisher Scientific) at around 300-400 g for 5 minutes, resuspended in FBS-free RPMI medium and kept in the incubator for 1 hour.

For freezing, cells were spun down at 400 g for 5 minutes and resuspended in FBS with 10% of DMSO at $1x10^7$/ml, placed in -80 °C in the freezing container (#15542771, Thermo Fisher Scientific) and after at least 2-4 hours transferred to the liquid nitrogen containers.

For thawing, cells were quickly transferred from long-term storage to the water bath at 37 °C. As soon as the last ice was dissolved, 1 ml of cells was transferred to a 15 ml falcon tube (#352095, Corning) with 9 ml of growth media, mixed properly and spun at 300 g for 5 minutes. After aspiration of the supernatant, the cells were re-suspended in 10 ml of growth media and incubated as usual until they reached confluency.

7.2 Membrane curvature imaging using polarized TIRFM

The possibility of imaging using polarized TIRFM (pTIRFM) modality was inspired and implemented based on previous work (Sund, Swanson, and Axelrod, 1999; Oreopoulos and Yip, 2009b; Oreopoulos and Yip, 2009a; Oreopoulos et al., 2010; Anantharam, Axelrod, and Holz, 2010; Axelrod, 2008). We decided to realize the implementation of pTIRFM in our system (Eclipse Ti inverted light microscope from

Nikon) by using two orthogonally positioned polarizers in the excitation pathway placed in two metal cubes with 405/488/561/640 nm quad band filters and dichroic mirrors (Figure 7.1a-c). The quad band dichroic and emission filter enabled the excitation of fluorophores with all four available lasers, ensuring the possibility of choosing the most appropriate carbocyanine dye for the desired application. For presented data carbocyanine dye DiI (1 mg/ml) was used for membrane staining at 1 μl per 1 ml of culture medium (#D3911, ThermoFisher Scientific).

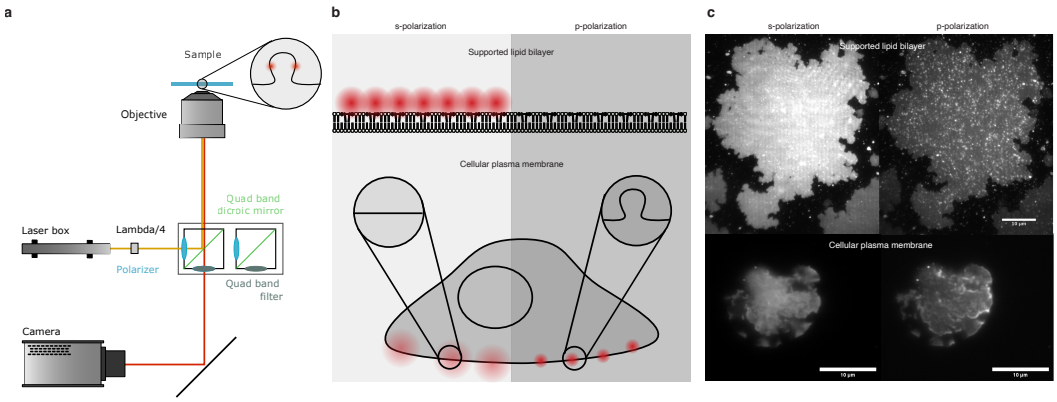

FIGURE 7.1: Setup, principle and validation of membrane curvature imaging by pTIRFM. a. Implementation of pTIRFM in our setup. b. Principle of membrane curvature imaging in Supported Lipid Bilayers (SBL) and cells by pTIRFM and c. exemplary images.

7.3 Quantitative PCR

7.3.1 RNA purification

RNA purification was performed using RNeasy MinElute CleanupKit (#74204, Qiagen) according to the manufacturer instructions with on column DNase digestion (#79254, Qiagen) to provide a high-quality total RNA perfectly suited for qPCR applications. The concentration of purified RNA was measured on the NanoDrop™ 2000 Spectrometer (#ND-2000, Thermo Fisher Scientific).

7.3.2 Reverse-transcription of RNA to cDNA

Total RNA samples were reverse-transcribed to complementary DNA (cDNA) using SuperScript® III First-Strand Synthesis System for RT-PCR (#18080-051). cDNA synthesis was performed as described below. First, the heatblocks were set to 65 °C and 85 °C. For all reactions the components were mixed in 1 ml RNase-free tubes (#AM12400, Thermo Fisher Scientific):

Next, the reaction was incubated for 65 °C for 5 minutes and placed on ice for 1-5 minutes. In the meantime, cDNA synthesis mix was prepared in small PCR tubes (#8610040, Ratiolab), according to the indicated order:

For every cDNA generation, 10 μl of RNA mixture (Table 7.1) was added to cDNA synthesis mix (Table 7.2), mixed and centrifuged briefly. After that, the reaction was incubated 50 minutes at 50 °C, then terminated at 85 °for 5 minutes and chilled on ice. Finally, the chilled reaction was incubated for 20 minutes at 37 °C with 1 ul of RNase H. cDNA samples were stored immediately at 20 °C as 5 μl aliquots in small PCR tubes. If in use, always kept one ice.

Component	Volume [μl]
mRNA ($\sim$ 2 ng/ul)	2.5 μl (5 μg)
50 μM oligo(dT)	1 μl
10 mM dNTP mix	1 μl
DEPC-treated H_2O	5.5 μl
Total volume	10 μl

TABLE 7.1: cDNA synthesis - step 1

Component	Volume [μl]
10xRT buffer	2 μl
25 mM $MgCl_2$	4 μl
0.1 M DTT	2 μl
RNaseOUT (40 U/μl)	1 μl
Superscript II RT (200 U/μl)	1 μl
Total volume	10 μl

TABLE 7.2: cDNA synthesis mix - step 2

7.3.3 Primers design and quality assessment

Primers for qPCR were designed using IDR tool RealTime qPCR Assay Entry or taken from PrimerBank (PCR Primers for Gene Expression Detection and Quantification run by Harvard Medical School. All primers used are listen below (Table 7.3).

Target	Forward primer sequence	Forward primer sequence	Working concentration
FBP17	AGCAGATTACTCATCCATTCTCC	GACTCTCCCATTCTCACAATCC	0.15 μM
SH3BP1	AGATTCAGGCCGATTACCATC	CAGCGACACCCCATACAC	0.1 μM
ASAP1	CTCACATTCATCGAGGGAGAAG	ACAAAGGACACTGGAAAGACC	0.1 μM
AMPH2	CAGTGCGTCCAGAATTTCAAC	CAATCGGGCTCATACACCTC	0.1 μM
IRSp53	CATGTCTCTGTCTCGCTCAG	CCAGTGCCTTCTCGTAATTCT	0.125 μM
β-actin	TCCCTGGAGAAGAGCTACGA	AGCACTGTGTTGGCGTACAG	0.125 μM
GAPDH	CTTTGTCAAGCTCATTTCCTGG	TCTTCCTCTTGTGCTCTTGC	0.125 μM
FCHSD1	AGGATGAGGTGGAGCAGG	TCCTCAAAGTCAGAAAGCTCAG	0.1 μM
FCHSD2	AGACTGAACAGATGGCTCATG	CCGGGCTTTTAACTTTACACTTG	0.1 μM
srGAP3	TTCTCCTCCAAAATCCGCAG	ACCAGATACCAACAGTTCACAG	0.1 μM
PACSIN2	TGATTCCGTTGGAGTAGAAGTG	AGTTCATGAGGTCGCTGC	0.1 μM

CIP4	CCGAAGTG-GAACAGGCTTAC	TGTACGAAGGACT-GTTGCTG	0.1 μM
SNX9	GGAGCCCAAA-GAAACACAAAC	CCAGTCTTCATC-CCAGTCATC	0.1 μM
APPL1	CCAGTGATCCCT-TATATGTGCC	GGTAGATGACAC-CAAGCCTG	0.1 μM
APPL2	AGTGATGGCCGTG-GATTG	CCACTCTTCATTTTC-CTTTCTGC	0.1 μM
ARHGAP26	CATG-CAAGCTTTGTCG-GAAG	ACTCTGGCT-GTCTTTGTTCG	0.05 μM
SH3GLB2	CTCAGTACATGGCA-GACGC	GTGGATAAAATCC-CTCTCCGC	0.1 μM
DNMBP	TCTCTAC-CTCCAGCACATCC	CGATGCACCCTCT-CAAACTG	0.1 μM
PIEZO1	GGCTACATCAAG-TACGACCTG	GCTCTTGTCAT-GCTCCTTGG	0.1 μM
FCHO1	AGCAGAACATCGA-GAACGTC	CACTGTATGCCTC-GAAGTCC	0.1 μM
FCHO2	CATCT-GCTTCATTGAGT-GCTG	TCCTGATTTCCAAG-GCTGAC	0.1 μM
PICK1	ACAAAGGGAT-GACGGAACAC	GAGAACACGTCCC-CAAAGG	0.1 μM
SNX18	CATCTGGC-TAACTTCCCGG	CTTCTGCACCTC-CATCTTCC	0.1125 μM
SNX33	AATGACCTCTTCCA-GATGCTG	TTGGCTCTC-CTTCACCTTG	0.1 μM
GRAF2	TGCACAGTTG-GATAAGATGGG	CTCTGGAC-CTTTGAACTCACC	0.1 μM
PLD2	CTACCTGCTTCC-CAAGTCTAC	GTAGGCATTGAG-GATGGAGTTC	0.1 μM
Toca-1	TCCATAAGAATGAG-GCTTGGC	GACTTTCTCGTCC-CTGTGTTAC	0.125 μM

TABLE 7.3: Primers for qPCR

To assess the optimal melting temperature of primers (T_m), PCR reaction with 1:10 dilution of cDNA was performed following the protocol below using Phusion® High-Fidelity DNA Polymerase (#F530L, Thermo Fisher Scientific). Following mixture was prepared (Table 7.4). The PCR reaction with a gradient of temperatures was run using the conditions below, to assess the T_m of every primer set (Table 7.5). To assess the optimal concentration of primers to use for qPCR experiments, qPCR experiments were performed using Fast SYBR™ Green PCR Master Mix from Applied Biosystems (#4309155, Thermo Fisher Scientific) on the StepOne Real-Time PCR System (#4376357, Applied Biosystems). For this, 8 different cDNA concentrations were used (serial dilution from 1:2 to 1:256). Content of every reaction is presented in the table (Table 7.6).

The standard reaction protocol available on the StepOne Real-Time PCR System (#4376357, Applied Biosystems) was used. The results were analyzed with the

Component	Volume [μl]
5xHF buffer	4 μl
10 nM dNTPs	0.4 μl
Forward primer 10 μm	1 μl
Reverse primer 10 μm	1 μl
cDNA 1:10 dilution	1 μl
Phusion polymerase	0.2 μl
Nuclease-free water	12.4 μl
Total volume	20 μl

TABLE 7.4: PCR mix of primers for qPCR

Temperature	Time	Cycles
98 °C	30 seconds	1
98 °C	10 seconds	
Gradient °C	20 seconds	30
72 °C	15 seconds	
72 °C	5 minutes	1
4 °C	infinity	

TABLE 7.5: PCR reaction with temperature gradient with cDNA

StepOne Software v2.3. Primers were considered efficient and optimal when reaching between 95 to 105 % efficiency, with melting curves clearly overlapping. The appropriate concentration of cDNA to be used was assessed based on the standard curve (quantity vs CT) results.

7.3.4 Quantitative PCR reaction

After measuring the optimal concentration of cDNA and primers that should be used, the qPCR experiments were setup by making a master mix (Table 7.6) and carefully pipetted into plates (4346906, Applied Biosystems) suited for the readout by StepOne Real-Time PCR System (Applied Biosystems), as previously. Before the run, the master mix was carefully pipetted into the plate in a RNase-free environment and spun down for 5 minutes at 1500 rpm in the Multifuge 3L-R Refrigerated Centrifuge (Heraeus). The results were analyzed using StepOne Software v2.3 and ExpressionSuite Software v1.1. GAPDH or β-actin were planned to be used as internal controls, but β-actin proved to be insufficiently stable. All qPCR results were obtained from at least 2 technical replicates and 3 biological replicates.

7.4 Total RNA purification and quality control

Total RNA purification was performed according the manufacturer instructions using RNeasy Mini Kit (#74104, Qiagen). Shortly, $1x10^7$ undifferentiated or differentiated at the desired day of differentiation HL-60 cell were spun and lysed in appropriate buffer immediately. After addition of 70 % of ethanol and mixing, the samples were transferred to RNeasy Mini spin column and centrifuged. The on column DNase digestion was performed according to the RNase-free DNase Set (#79254, Qiagen). After several washes with RW1 and RPE buffers, the RNA was eluted in

Component	Volume [μl]
SYBR-Green	10 μl
Forward primer e.g. 1 μM	2 μl (final: 0.1 μM)
Reverse primer e.g. 1 μM	2 μl (final: 0.1 μM)
cDNA dilution (1:2-1:256)	1 μl
Nuclease-free water	5 μl
Total volume	20 μl

TABLE 7.6: SYBR-Green reaction mix

around 30 μl of RNase-free water. The samples were stores at -20 °C. Before submitting to the Genomics Core Facility for sequencing, the RNA samples were run using Agilent RNA 6000 Nano Kit (#5067-1511-12, Agilent Technologies) on Agilent 2100 Bioanalyzer (Agilent Technologies) according to the instructions to assess RNA quality. Alternatively, instead of the using Agilent RNA 6000 Nano Kit, a regular 1% agarose gel was run with RNA samples.

7.5 RNA sequencing

RNA sequencing was performed by the Genomics Core Facility at EMBL, under the supervision of Dr. Vladimir Benes. High quality total RNA samples obtained from 3 biological replicates were submitted for RNA sequencing on a Illumina NextSeq 500 platform as NextSeqHigh-75 SE. RNA-Seq libraries were prepared according to the manufacturer's protocol. For sequence alignment the reference genome used was hg19. Differential expression analysis was performed with the custom-made Galaxy pipeline using DESeq2 package with the assistance of Dr. Charles Girardot and Dr. Jelle Scholtalbers from Genome Biology Computational Support at EMBL.

7.6 Cloning of BAR domain proteins:

DNA sequences were amplified using PCR of the designed primers with restriction sites for MluI/BsiWI or BsiWI/NotI (#R3198L, #R3553, #R3189 from New England Biolabs) or primers for Gibson cloning. Following protocols were used:

Component	Volume [μl]
5xHF buffer	10 μl
10 nM dNTPs	1 μl
Forward primer 2.5 μm	1 μl
Reverse primer 2.5 μm	1 μl
DNA template 5 ng/μl	1 μl
Phusion polymerase	1 μl
Nuclease-free water	33 μl
Total volume	50 μl

TABLE 7.7: Amplification of sequence by PCR

Temperature	Time	Cycles
98 °C	30 seconds	1
98 °C	10 seconds	
Desired °C	30 seconds	30
72 °C	15s/kb	
72 °C	5 minutes	1
4 °C	infinity	

TABLE 7.8: PCR reaction

Next, both pHR lentiviral vectors (with previously introduced eGFP) and amplified DNA sequences were cut according to manufacturer instructions. After running agarose gel electrophoresis, DNA was purified using QIAquick Gel Extraction Kit (#28706, Qiagen). Later, Quick Ligation™ Kit was used for ligation of constructs (#M2200, New England Biolabs). After running on agarose gels and purification, DNA constructs were validated using sequencing (Methods 7.14). Alternatively, Gibson assembly® method was used for cloning.

Plasmid including sequences for human BAR domain proteins were a kind gift from Dr. Rainer Pepperkok's Lab (AMPH2), Dr. Heidi Chial (APPL2), Dr. Safa Lucken Ardjomande Häsler (GRAF1), Prof. Pietro de Camilli (FBP17), Dr. Lars Hufnagel (PACSIN2), Prof. Maria Balda (SH3BP1) and Prof. Duanqing Pei (Snx33). BIN2 (#NM016293.4) was synthesized as a gBlock by Integrated DNA Technologies.

7.7 Generation of stable cell lines

7.7.1 Lentivirus production

HEK293T cells were grown in a 6-well plate (#140675, Thermo Fisher Scientific) up to 60-70% confluency. To achieve it, usually $5x10^5$ cells/well were seeded 24 hours in advance. For a single transfection, 1.5 μl of the transfer vector (lentiviral target) was mixed with 1.3 μl of CMV p8.91 and 0.167 μl of pMD2.G (#12259, Addgene). The prepared mixture was further added to 200 μl of Optimem (#51985-026, Gibco) and 8 μl of cold TransIT®-Lenti Transfection Reagent (#MIR6604, Mirus Bio) and incubated 15 minutes at RT. The mixture was added to one 6-well plate supplemented with the 3 ml of the fresh HEK293T medium. The plate was transferred to a cell culture incubator in an S2 lab.

After 48-72h, around 3 ml of the viral supernatant were collected using 0.22 μm filter (#SLGV033RS, Millipore) and concentrated using Lenti-X™ Concentrator (#631231, Clontech) by incubation at 4 °C for at least 1 hour. Concentrated viruses were spinned down for a minimum of 45 minutes at 1500 g at 4 °C and resuspended in around 75 ul (for one 6-well plate). Concentrated virus was used for infection immediately or kept at -80°C for long-term storage.

7.7.2 Lentiviral infection of HL-60 cells

For lentiviral infection, undifferentiated HL-60 cells were concentrated at $2x10^6$ per ml. 100 μl of concentrated virus solution was added to 130 μl of concentrated HL-60 cells, together with 80.5 μl of growth media and 12.9 μl of polybrene at 0.1 mg/ml (#TR-1003-G, Sigma-Aldrich) in a 24-well plate (#142474, Thermo Fisher Scientific).

After up to 24 hours and later growth media were added to the 24-well plate accordingly to HL-60 cells growth. Following the exchange of media by centrifugation and resuspention of cells at least three times, cells were sorting according to the needs on BD FACSAria^{TM} Fusion.

7.8 CK-666 treatment of HL-60 cells

For CK-666 treatment of dHL-60 cells, the cells were pre-incubated with 100 μM CK-666 (#3950, Tocris) and 100 nM fMLP (#F3506-5MG, Sigma Aldrich) for 10 minutes before the addition of a fixation buffer to a dish with migrating HL-60 cells (Methods 7.23).

7.9 Fibronectin Coating

For experiments with migration of differentiated HL-60 cells fibronectin-coated dishes were required. To coat the dishes, the glass bottom of of 35/10 mm dishes with one compartment (#627860, Greiner bio-one) were covered with 2 μl of 1 mg/ml human fibronectin (#356008, Corning) in 200 μl of dPBS for 30 minutes each. After that, the dishes were washed 3-4 times with 3 ml of dPBS. Dishes were used immediately or stored at 4 °C for couple of days. If different dishes were used, the coating was adjusted according the to surface area.

7.10 Total Internal Reflection Fluorescence Microscopy imaging of migrating HL-60 cells

For imaging experiments, the 35-mm glass-bottom dishes were coated for 30 min with fibronectin (Methods 7.9) or fibronectin supplemented with 5% BSA. Differentiated HL-60 cells were plated on each dish filled with growth media and allowed to adhere for at least 10 min at 37 °C. Next, cells were washed with HL-60 growth media and supplemented with 10 nM fMLP.

TIRFM images were acquired on a Nikon Ti Eclipse inverted microscope with a TIRF objective CFI Plan Apo Lambda 100x Oil (#MRD01905, Nikon) and sCMOS camera controlled by NIS-Elements (Nikon). Sample drift was reduced using an autofocus system (Perfect Focus, Nikon) in case of time lapse imaging. NIS-Elements was used for image acquisition. Usually, 488 and 561 nm laser lines were used. Cells were imaged every 5-20 seconds (depending on the numbers of channels acquired and purpose of imaging) with the exposure time of 100-500 ms of laser power 4-15%. Cells were used no longer than 1 hour for image acquisition and were at 37 °C in humidified chamber at 5 % CO_2.

7.11 Image analysis method of puncta quantification using CellProfiler

Image analysis method of puncta quantification using CellProfiler-3.0.0 was developed jointly with dr. Christian Tischer. Images used in the analysis were acquired on migrating dHL-60 cells with fluorescently labelled eGFP-tagged BAR domain proteins (first channel) and mCherry-labelled CAAX (second channel) with the use of TIRFM (Methods 7.10). Functions used in CellProfiler-3.0.0 and details about the

pipeline are presented in the table (Table 7.9). Exemplary images and the segmentation are shown in the Figure 7.2).

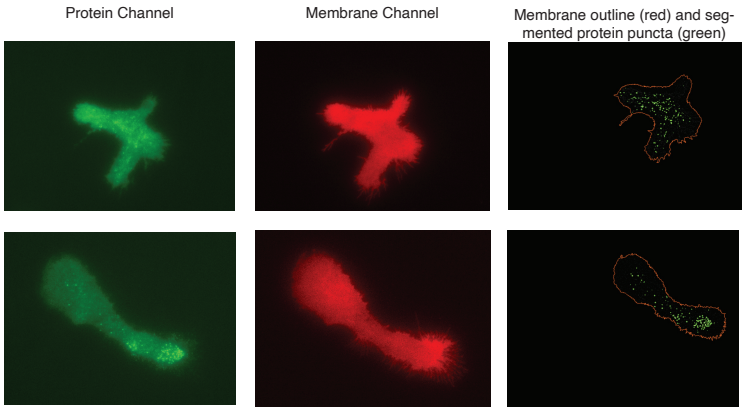

FIGURE 7.2: Exemplary images of puncta quantification using CellProfiler. Exemplary images of eGFP-tagged cells with BAR domain proteins and mCherry-tagged with CAAX (membrane marker). The outcome of CellProfiler pipeline is cell mask (red outline) and protein puncta (green dots). Original images and pipeline outcome are not at the same scale for visualization purposes.

7.12 Quantification of protein enrichment at the leading edge

Images of fixed dHL-60 cells, stained with phalloidin and tagged with protein of interest (with the fluorophore different than the one to which phalloidin was conjugated), were obtained with Eclipse Ti inverted light microscope (Nikon) with 40x objective (#MRD00405, Nikon). Only single cells (not touching other cells or image edge) with visible leading edge (characterized by the enrichment of phalloidin staining on one side of the cell) were considered for analysis. Images of single cells were background subtracted and total intensity of the protein of interest was measured using ImageJ. To quantify the intensity of protein of interest in the leading edge, the leading edge was manually segmented based on phalloidin signal. Phalloidin-based segmentation of the leading edge was then used for measuring the total intensity of protein of interest using ImageJ. By dividing the total intensity of protein of interest in the leading edge by the total intensity the protein in the cell, the enrichment in the leading edge measure was obtained.

7.13 Knockout cell lines generation using CRISPR/Cas9

We followed a protocol based on previous studies (Graziano et al., 2017; Graziano et al., 2019). Our strategy of choice was using a two vector system, where the expression of the first plasmid (lentiGuidePuro (#52963, Addgene), Sanjana, Shalem, and Zhang, 2014) generates the chimeric guide RNA (gRNA) and the second plasmid provides BFP-Cas9 expression. Both vectors were received thanks to the generosity of Dr. Brian Graziano.

Function in CellProfiler	Description
IdentifyPrimaryObjects	Cell are segmented based on membrane signal using 'object diameter' (50-500 pixels) and Thresholding Method (Minimum cross entropy)
MeasureObjectSizeShape	Here, indicated characteristics are measured based on membrane signal (eg. Eccentricity, Area, Compactness, Perimeter)
Smooth	Application of Gaussian Filter with typical artifact diameter 8 pixels.
Smooth	Application Gaussian Filter with typical artifact diameter 2 pixels.
ImageMath	Performs DoG (difference of Gaussian) of both smoothed images in order to visualize puncta.
Crop	Protein channel is cropped based on the mask from the membrane signal
IdentifyPrimaryObjects	Puncta are identified in every cropped protein channel. Identification is based on typical diameter (3-10 μm) and threshold.
MeasureObjectSizeShape	Applied on puncta, this function measures indicated characteristics (eg. Eccentricity, Area, Compactness, Perimeter).
RelateObjects	Puncta are related to segmented cells based on membrane signal.
ExportToSpreadsheet	CellProfilier exports all the chosen measured data to the excel file.
RescaleIntensity	Applied in order to see the puncta after saving the image.
OverlayOutlines	Puncta (green) and segmented cells (red outline) are saved for visual inspection of the results.

TABLE 7.9: Step-by-step puncta quantification analysis using CellProfiler

7.13.1 Cloning of the target guide sequence into LentiGuidePuro vector

Target guide sequence cloninig into LentiGuidePuro vector was performed according to the Gecko protocol. Shortly, 5 μl of the lentiviral vector was digested and dephosphorylated with 3 μl of Esp3I (#FD0454, Thermo Fisher Scientific), 3 μl of FastAP (#EF0654, Thermo Fisher Scientific), 6 μl of 10x FastDigest Buffer (#B64, Thermo Fisher Scientific), 0.6 μl of 100 mM DTT (#10197777001, Merck) and water was added up to 60 μl. The reaction was running for 30 minutes at 37 °C. Next, the reaction was run on a agarose gel and purified with QIAquick Gel Extraction Kit (#28706, Qiagen). Simultaneously, each pair of oligos was phorphorylated and annealed using S1000 Thermal Cycler (Biorad) in a following reaction: 1 μl of 100 μM oligo 1 and 2, 1 μl of 10x T4 Ligation Buffer (#B69, Thermo Fisher Scientific), 0.5 μl of T4 PNK (#M0201, NEB) in the total of 10 μl of H_2O. Thermocycler was programmed for 37 °C for 30 minutes, 95 °C for 5 minutes, concluding with the ramp down to 25 °C at the speed of 5 °C/min. Annealed oligos were diluted at 1:200 into

sterile water. To finalize the cloning of the LentiGuidePuro vector, a ligation reaction was set up for 10 minutes at RT using: 1 uμl of diluted, annealed oligos, 50 ng of Esp3I digested and purified LentiGuidePuro plasmid, 2 μl of 5x Rapid Ligase Buffer (#K1422, Thermo Fisher Scientific), 1 μl of Quick Ligase (#M2200S, NEB), filled up to 11 μl with H_2O. Required controls were performed at all stages. Competent bacteria were transformed by a heat shock (45 s at 42 °C) in a water batch with a 2 μl of the ligation mix and plated on a ampicillin resistant plates overnight. Bacteria were later amplified overnight in a 5 ml of LB media supplemented with ampicillin and purified using QIAprep Spin Miniprep Kit (#27104, Qiagen). To test whether the target guide sequence was properly colned into the LentiGuidePuro plasmid, the obtained plasmids were sequqnced using primers targeting human U6 promotor: cgatacaaggctgttagag (forward #1), cttgggtagtttgcagttt (forward #2).

7.13.2 Double transduction of HL-60 cells with gRNA's and Cas9

Lentivirus production of gRNA's and Cas9 was performed using general lentivirus production protocol for 293T cells (Methods 7.7.1). First, wild-type HL-60 cells were transduced (Methods 7.7.2) using viruses produced based on lentiviral vectors containing puromycin-selectable gRNA's targeting desired locations (Table 7.10). The gRNA's were designed to target preferably the sequences around starting codon or in exon one, if the efficiency and off-target effects predictions calculated in Benchling algorythms (Cloud-Based Informatics Platform for Life Science) were promising. Following puromycin (#P8833, Sigma Aldrich) selection at 1 μg/ml for 5 days, cells were again transduced using viruses produced from lentiviral vectors containing *S. pyrogenes* Cas9 sequence fused to BFP. Alternatively, lentiviral vectors containing *S. pyrogenes* Cas9 sequence fused to BFP were introduced by electroporation using Neon® Transfection System using manufacturer protocols for HL-60 cells (# MPK5000, Life technologies). Viral transduction was performed as described previously (Methods 7.7.2), with the change of doubling the volume of viruses added. After recovery and cell proliferation to around $1x10^6$ cells, BFP-positive cells were single-cell sorted using BD FACSAria™ Fusion at the EMBL Flow Cytometry Core Facility. Single-cell clones were amplified and later assessed by gDNA purification (Methods 7.13.3), amplification of regions flanking the Cas9 cut site by touchdown PCR (Methods 7.12) and sequencing (Methods 7.14). Sequencing results were analyzed using 4Peaks and ApE software to verify that a particular clone arose from a single cell as well as to search for deletion or insertions disrupting the reading frame. The clones identified as potential knockout cell lines were further validated using Western Blotting (Methods 7.15).

7.13.3 Genomic DNA purification

After 300-500 μl of confluent cells solution was spun at 300 g for 5 minutes, the supernatant was removed carefully using a pipette. For one sample, 50 μl of QuickExtract™ DNA Extraction Solution (#101094, Lucigen) was added to a 1 ml tube with cells and incubated for 10 minutes at RT. The solution was pipetted 5-10 times, vortexed (Scientific Industries SI™SI-0256, Thermo Fisher Scientific) 15 seconds, incubated 15 minutes at 65 °C and vortexed again for 15 seconds.

Target sequence	Forward guide sequence	Reverse guide sequence
SNX33 (#1)	CACCGCATCTTTAGCGA-GACCTCAC	aaacGTGAGGTCTCGCTAAA-GATGC
SNX33 (#2)	CACCGACGGACGATCTC-CACATAAG	aaacCTTATGTGGAGATCGTC-CGTC
SNX33 (#3)	CACCGctgggacgacGGATG-CACAG	aaacCTGTGCATCCgtcgtc-ccagC
SNX33 (#4)	CACCGTAGCGCCGGTA-GACGGGTG	aaacCACCCGTCTACCG-GCGCTAC
SNX33 (#5)	CACCGCAGGACGTGGAA-GATCGCG	aaacCGCGATCTTCCACGTC-CTGC
SH3BP1 (#1)	CACCGAGAGGCAGCTG-CACCGCATG	aaacCATGCGGTGCAGCTGC-CTCTC
SH3BP1 (#2)	CACCGtcgcccccAAGATGAT-GAAG	aaacCTTCATCATCTTgggggc-gaC

TABLE 7.10: List of designed target guide sequences

7.13.4 Genomic DNA amplification by Touchdown PCR

Genomic DNA was extracted as described in the section above (Methods 7.13.3). Genomic amplification using Touchdown PCR protocol was performed based on previous studies (Koch et al., 2018). Shortly, primers for Touchdown PCR were designed to span between 500-1500 bp in a final PCR product (Table 7.11).

Target sequence	Forward guide sequence	Reverse guide sequence
SNX33 (#1)	TCTTTCTATACCACCCAGC-CCAG	CTGGTGCGTAAACAT-GTGGGG
SNX33 (#2)	TCTTTCTATACCACCCAGC-CCAG	GCCGTAACCTCAAC-CGTTTCTC
SNX33 (#3)	AACTGTGTAAGCGC-CATTCAGC	CATGCTTTGTGCGTTCTG-GAGT
SNX33 (#4)	CATTGAAATGGGCC-CTCGTGG	TTCCAGGCCATCAGT-CATTCCT
SNX33 (#5)	TGCTTTGAAGAGGGGGA-GACTGGACAGCATCT	TCATTCTTGGGCT-GCTCAGCAAACATCTCCCC
SH3BP1 (#1)	AGGAATGGGCTTACCT-GCTTCC	GAAGAGA-GAGCAGGAGTCTGGC
SH3BP1 (#2)	AGGAATGGGCTTACCT-GCTTCC	tttacgacccctcaAGTCCTGC

TABLE 7.11: List of designed primers for Touchdown PCR

To amplify the region of interest HotStar HighFidelity PCR kit was used (#202602, Qiagen), and reactions were set up as following:

The region of interest was amplified using the following conditions: 1 cycle of 95 °C for 5 minutes, 2-21 cycles at 95 °C for 30 seconds (Anneal: start temperature at 5 °C higher than T_M of primers, -0.5 °C/cycle, 45 seconds; Extend: 72 °C, 0.5

Component	Volume [μl]
5x HotStar PCR buffer	4 μl
Primer forward (10μm)	2 μl
Primer reverse (10μm)	2 μl
Hotstar HighFidelity polymerase	1 μl
Q solution	4 μl
Template DNA (200 ng)	1-2 μl
ddH_2o	up to 20 μl

TABLE 7.12: Touchdown PCR reaction

kb/1min), finishing with 22-43 cycles at 95 °C for 30 seconds (Anneal: End temperature of last cycle = 5 °C lower than T_M of primers, 45 seconds; Extend: 72 °C, 0.5 kb/1min).

PCR products were later run on a 2% agarose gel and purified using MinElute Gel Extraction Kit (#28604,Qiagen) according to the manufacturer instructions. Usually single band was present in one sample but in case of multiple bands, multiple products were sequenced and analyzed.

7.14 Sequencing

Samples for sequencing were obtained by using QIAquick Gel Extraction Kit (#28115, Qiagen), MinElute Gel Extraction Kit (#28604,Qiagen) or QIAprep Spin Miniprep Kit (#27104, Qiagen). The amount of purified plasmids or DNA fragments was measured using NanoDrop™ 2000 Spectrometer (#ND-2000, Thermo Fisher Scientific). Samples were dilted to 50-80 ng/μl and send to sequencing to Eurofins (earlier GATC) using Supremerun Tube option.

7.15 Western-blotting

7.15.1 Protein sample preparation

$6x10^6$-$1.2x10^7$ undifferentiated or differentiated HL-60 cells were spun for 6 minutes at around 300-400 g. Supernatant was aspirated and the cells were washed with 10 ml of cold dPBS, twice. After a final aspiration of the supernatant, the cells were mixed with 500 μl of the RIPA Lysis and Extraction buffer (#89900, Thermo Scientific™) supplemented with recommended amounts of the protease inhibitors (#4693159001, Roche) and incubated on ice for 5 minutes. Very sticky lysed solution was then transferred to 1.5 ml Eppendorf tubes and spun at the top speed (15 000 rpm) at the benchtop centrifuge (Centrifuge 5417R, Eppendorf) for 10-20 minutes, until the solution was clear. Next, the supernatant was transferred to pre-colded fresh 1.5 ml tubes. The samples were immediately frozen in liquid nitrogen and transferred to -80 °C or supplemented with 4xLaemmli protein sample buffer (#161-0747, BioRad containing 10% β -mercaptoethanol (m6250, Sigma Aldrich) and stored at -20 °C.

7.15.2 Gel electrophoresis and transfer

For gel electrophoresis, the samples were supplemented with 4x Laemmli Sample Buffer (#161-0747, BioRad) containing 10% β -mercaptoethanol (#m6250, Sigma

Aldrich), boiled 5 minutes at 95 °C and centrifuged at the top speed in a benchtop centrifuge (5417R, Eppendorf). Precasted gels for electrophoresis with 10-15 wells (#np0321box, #np0323box, #np032115, Invitrogen) were mounted in a Mini-Gel-Tank (#A25977, Thermo Fisher Scientific) and Mini-Gel-Tank was filled with NuPAGE MOPS SDS Running buffer (1x solution: 50 mM MOPS (#m1254, Sigma Aldrich), 50 mM Tris (#t1503, Sigma Aldrich), 0.1%SDS (#20765.01, Serva), 1 mM EDTA (number, company), pH 7.7) prepared from the 20x stock solution stored at 4 °C. The wells were pipetted through to ensure the uniformity of the buffer. Samples and prestained Protein Ladder (#26618, Thermo Fisher Scientific) were pipetted carefully inside the wells. After placing the lid and plugging the cords into the power supply, the gel was run at 80 V for the first 5-15 minutes to ensure the proper entering the samples into the gel, which was followed by 150-200 V for the next 40-60 minutes. After a successful gel electrophoresis, the gel was taken out from the chamber, rinsed with double distilled water and places in a freshly prepared 1x transfer buffer (700 ml of cold ddH_20, 100 ml of 10 x Transfer buffer, 200 ml of methanol) for 10 minutes. 10 x Transfer buffer was obtained by formerly dissolving 30.3 g Tris Base (#t1503, Sigma Aldrich) and 144.1 g glycine (#G8898, Sigma Aldrich) in 1 l of ddH_20 and stored at RT. Previously pre-cut PVDF membrane (#IPVH00010, Millipore) was activated for 10 s in methanol and soaked in the 1 x transfer buffer, as well as the filter paper and sponges provided in the Mini Blot Module (#B1000, Thermo Fisher Scientific). Transfer sandwich was mounted according to the manufacturer instructions. Transfer buffer (1x) was added to the module core and to the chamber to make sure that the sandwich is completely submerged. The blot was run for 1-2 hours at constant voltage of 20 V. Next, the sandwich was carefully taken out from the chamber and unmounted using tweezers. The PVDF membrane with transferred proteins was either put directly into the blocking solution of 5% BSA in 1 x TBST (20 mM TrisHCl (#10812846001, Sigma Aldrich), 150 mM NaCl (#bp358-1, Fisher Bioreagents), 0.1% Tween 20 (#P9416 Sigma Aldrich) in ddH_20) or stained with Ponceau S (#P7170-1L, Sigma Aldrich) to check the quality of the transfer and later washed off with 1 x TBST, followed with incubation in the blocking solution for 2 hours at RT.

7.15.3 Antibodies probing and bands detection

After 2 hours at RT in the blocking solution, the membrane with transferred proteins was subsequently incubated with primary antibodies, washed 4 x 10 minutes with TBST, incubated with secondary antibodies and washed 4 x 10 minutes with TBST, always on a rocking shaker (#BR1000, Benchmark Scientific). Next, the bands were visualized using Pierce ECL Western Blotting Substrate (#32106, Thermo Fisher Scientific) that is a horseradish peroxidase substrate for enhanced chemiluminescence. Substrate was prepared according to the manufacturer's instructions and incubated in a dark place with a PVDF membrane for 10-15 minutes. Later, the bands were visualized using a ChemiDoc Touch Imaging System (Biorad).

7.16 Immunofluorescence staining

For immunofluorescent staining, cells were fixed as described (Methods 7.23). Later, they were permeabilized with 0.2% Triton X-100 (#T8787, Sigma Aldrich) and/or phalloidin coupled with TRITC (#P1951, Sigma Aldrich) for 30 minutes at 4 °C. Cells were then washed 3 times with dPBS. Next, cells were blocked for 1 hour in 2%BSA

Primary antibody	Secondary antibody	Antibody references
anti-SH3BP1 1:10 000	anti GAPDH: 1:10 000	#EB06271, Everest Biotech; #NB300-221, Novus Biologicals
anti-SNX33 1:1 000	anti GAPDH: 1:10 000	#orb331346, Biorbyt; #NB300-221, Novus Biologicals

TABLE 7.13: Primary and secondary antibodies used for Western Blots

in dPBS overnight at 4 °C. After washing the samples twice in dPBS, they were incubated with primary antibody for SH3BP1 at 2 μg/ml (#EB06271, Everest Biotech) in 2% BSA overnight at 4 °C. After washing with 2% BSA, secondary antibody anti-goat-IgG AlexaFluor 488 (#A11055, Molecular Probes) was incubated for 1 hour at RT and used for confocal imaging (Methods 7.17).

7.17 Imaging of fixed HL-60 cells using confocal microscopy

Confocal imaging was performed with the assistance of Advanced Light Microscopy Facility at EMBL. Shortly, fixed cells (Methods 7.23) were imaged with a silicone objective UPLSAPO 60X S (NA 1.3; WD 0.3mm) on a Olympus FV3000 inverted microscope. Laser lines 405 nm, 488 nm, 561 nm, 640 nm were used.

7.18 CD11b staining of HL-60 cells

After 1 hour of starvation, 1x10^5 of undifferentiated and differentiated HL-60 cells were pelleted at 300 g in the centrifuge (Heraeus™ Megafuge™ 16, Thermo Fisher Scientific). For differentiated HL-60, all pelleted cells were on the 5^{th} day of differentiation. Each samples was resuspended in 7 μl of Anti-Hu CD11b Alexa Fluor® 488 antibody solution (#A4-681-T100, Exbio) and incubated on ice for 40 minutes. Next, the cells were washed twice with ice-cold dPBS supplemented with 1% of FBS in a volume of at least 200 μl. Finally, the cells were resuspended in the same buffer at around 1x10^6 and transported immediately for analysis. The CD11b fluorescence was analyzed on the Cytek® Aurora (Cytek) at the EMBL Flow Cytometry Core Facility. Data were further analyzed and plotted using FlowJo software.

7.19 Tether force measurements in HL-60 cells

For tether force measurements, custom-cut 35-mm glass-bottom dishes were coated for 30 min with fibronectin (7.9). Differentiated HL-60 cells were plated on each dish in growth media and allowed to adhere for at least 10 min at 37 °C. Next, cells were washed with HL-60 growth media and supplemented with 10 nM fMLP. Before the cell seeding, the Olympus BioLevers (k = 60 pN/nm) from Bruker were calibrated using the thermal noise method and incubated for 1 h at room temperature in 2.5 mg/ml Concanavalin A (#C5275, Sigma Aldrich). Prior to the measurements, cantilevers were two or three rinsed in dPBS. Experiments were performed immediately after the cantilever preparation. Cells and the cantilever were located by bright-field

imaging using 20x objective (#MRH68200, Nikon). For tether measurement, the cantilever was position over the cell, preferably over the leading edge. Cells were at 30 °C and 5 %CO_2 for data acquisition, but they were not used longer than 1 h. Tethers were extruded using a CellHesion 200 Atomic Force Microscopy (AFM) from JPK mounted on an Eclipse Ti inverted light microscope (Nikon). Measurements parameters for static tether pulling experiments were as followed: approach velocity was set to 1 μm/s, contact force to 100–300 pN, contact time to 5–10 s, and retraction speed to 10 μm/s. After a 10 μm tether was pulled, the cantilever position was held constant until it broke, but no longer than 30 seconds. In every experimental repetition the conditions' order was randomized. For every cell we have obtained at least 3 different tether measurements. The analysis of the acquired data was performed using the JPK Data Processing Software. For assessing the magnitude of membrane tension based on tether force measurements, the following formula was used, similarly to Diz-Muñoz et al., 2016a:

$$T = \frac{F_0^2}{8B\pi^2} \tag{7.1}$$

where F_0 is the tether force measured by AFM, B is the bending rigidity of the plasma membrane. As we are not able to measure the bending rigidity of the membrane in migrating cells, we assume that it is invariable between different experimental conditions tested and for calculation we use the estimated value for the cells ($2.7x10^{-19}$ Nm) based on other measurements (Sens and Plastino, 2015; Hochmuth et al., 1996).

7.20 pAkt S473 staining of HL-60 cells

After 1 hour of starvation, $1x10^5$ of undifferentiated and differentiated HL-60 cells were pelleted at 300 g in the centrifuge (Heraeus™ Megafuge™ 16, Thermo Fisher Scientific). For differentiated HL-60, all pelleted cells were on the 5^{th} day of differentiation. If experiments required chemoattractant stimulation or osmotic shocks, the appropriate amounts of fMLP (to reach final concentration 10 nM) or miliQ H_2O with 0.2% BSA (to reach 75% of hypo-osmotic shock water to medium ratio was 3:1) were added to starved cells and followed by the incubation for 5 minutes at 37°C at 5% CO_2.

Next, cells were fixed by adding 1 ml of 2x fixation buffer to 1 ml of differentiated HL-60 cells in a dish. Fixation buffer (1x) is containing 3.7% paraformaldehyde (#28908, Thermo Scientific), 1x intracellular buffer (140 mM KCL, 1 mM $MgCl_2$, 2 mM EGTA, 20 mM HEPES, pH 7.5), 320 mM sucrose (#S0389-500G, Sigma Aldrich), 0.2% BSA (#A7030-10G, Sigma Aldrich), protease inhibitors (#4693159001, Roche) and PhosSTOP™ (#PHOSS-RO, Sigma Aldrich). After 30 minutes of incubation on ice, cells were pelleted at 300 g in the centrifuge (Heraeus™ Megafuge™ 16, Thermo Fisher Scientific).

Later, cells were washed carefully three times with dPBS supplemented with 40 mM NaF. While on ice, cells were permeabilized by addition of 40 μl of cold methanol (directly from -20 °C) followed by addition of 160 μl and incubation at -20 °C for 10 minutes or longer. Once incubation is completed, cells were spun and re-suspended in 200 μl of Staining Buffer (5% FBS, 40 mM NaF, 2 mM EDTA in dPBS without calcium and magnesium) for 10 minutes to allow the rehydration. For staining, samples were washed three times in Staining Buffer to remove residual

methanol and re-suspended in Staining buffer at 1:50 dilution of Anti-Akt pS473 and incubated for 1 hour at RT.

Next, samples were again washed three times in Staining buffer and re-suspended in Alexa Fluor 568 secondary antibody (# A-11036, Thermofisher) at 1:2000 for 30 minutes. Finally, the cells were resuspended in the Staining Buffer at around $1x10^6$ and transported immediately for analysis. The fluorescence was analyzed on the BD LSRFortessa™ (BD Biosciences) at the EMBL Flow Cytometry Core Facility. Data were further analyzed and plotted using FlowJo software and R.

7.21 F-actin staining of non-adherent HL-60 cells upon fMLP stimulation

Cells used for F-actin staining in a non-adherent conditions were starved for 1 hour at 37 °C with 5% CO_2 in humidified chamber by re-suspending in FBS-free RPMI medium. 6-well plates used for the cell starvation were coated with 0.2-03 % BSA in RPMI for 15 minutes to avoid loosing cell number by the cell sticking to the non-coated plastic. Cells were on the 5^{th} day of differentiation. Cells were fixed by adding an equal volume of 2x fixation buffer (7.25) to desired volume of cells in growth media or stimulated with 10 nM fMLP. The fixation was performed before, for control condition, or 1, 3, 10, 20 minutes after, for experimental conditions, supplementing the media with 10 nM fMLP by mixing equal volume of cells re-suspended in the growth media with growth media supplemented with 20 nM fMLP. Fixed cells in a 24 or 96-well plates were incubated at 4 °C for 1 hour. Cells were consecutively washed carefully with 1x intracellular buffer by plate centrifugation on a Multifuge 3L-R Refrigerated Centrifuge (Heraeus) or transferred to 1.5 ml tubes and centrifuged at 1000 g for 10 minutes and aspirated for three times. Next, they were re-suspended in intracellular buffer (1x) containing 0.2% of Triton X-100 (#T8787, Sigma Aldrich) and phalloidin coupled with TRITC (#P1951, Sigma Aldrich). Staining was performed for 30 minutes at 4 °C. Cells were then washed 3 times with intracellular buffer (1x) as previously. Finally, they were re-suspended in the FACS buffer containing 1 ml of 0.1 % BSA, 2.5 mM EDTA in dPBS and analyzed by Cytek® Aurora (Cytek) or BD LSRFortessa™ (BD Biosciences) at the EMBL Flow Cytometry Core Facility. Data were further analyzed and plotted using FlowJo software.

7.22 PDMS-based microfluidic devices preparation and migration assay's

PDMS-based microfluidic devices were prepared as previously described (Renkawitz et al., 2018; Renkawitz et al., 2019; Kopf et al., 2020). Shortly, microfluidic photomasks printed on chrome photomask at the resolution of 1 μm were obtained thanks to the courtesy of Prof. Dr. Micheal Sixt (IST Austria). The PDMS devices were made with Sylgard 184 (Dow Corning) using a 10:1 ratio of PDMS and PDMS curing agent. After mixing the PDMS in the Thinky mixing machine, it was poured on the wafer laying in the previously shaped aluminium foil into the circular tray and degassed in a vacuum desiccator several times until no air bubbles could be visible on the surface. Next, the PDMS on wafers was cured at 80 °C overnight up to couple of days. The cured PDMS was carefully cut off from the back of the wafer, then pealed off the wafer and cut into a single devices using a razor blade. Once single devices were cut, the 2 mm holes were punch using a microfluidic PDMS

puncher and a transparent sticky tape was used to protect the devices. Glass coverslips were sonicated for 5 minutes in 70 % ethanol and blown dry. Devices were cleaned using the transparent sticky tape, then bonded to the coverslips using oxygen plasma and finally left for securing the bond on the heating block at 85 % for 1 hour. Devices were stored at RT in plastic dishes (#150468, Thermo Fisher Scientific).

The devices used for HL-60 cells had heights of 2.8 μm and 3.13 μm for channels with decision point and channels with constriction, respectively. The decision channels had constrictions of 2 μm, 3 μm, 4 μm and 5 μm in two different arrangements. The channels with a single constrictions had 2 μm. Prior to introduction of the cells, the devices were rinsed with the growth media of HL-60 cells using plastic syringes and incubated for at least 1 hour at 37 °C with 5 % CO_2 after removal of air bubbles manually or using a vacuum desiccator couple of times. To visualize nuclei and cell body, Hoechst 33342 (#62249, Thermo Fisher Scientific) and 10 μM of TAMRA (Invitrogen) were incubated for 15 minutes and washed before the introduction into the PDMS device. The chemoattractant (fMLP) and cells were introduced in this order into the PDMS devices by pipetting out 15 μl of medium and exchanging it with a desired solution. Next, the cell migration were monitored on a tissue culture light microscope until they entered the patterns on the devices. Further, the cell migration was imaged on an inverted wide-field Nikon Eclipse microscope using 20x/0.5 PH1 air objective, equipped with a Lumencor light source (390 nm, 475 nm, 542/575 nm), an incubation chamber and the heated stage with CO_2. Images were taken every 30 seconds for 2-4 hours to avoid the bleaching and to not interfere with cell migration that is sensitive to extensive light exposure.

The acquired data were analyzed using ImageJ software. In brief, only single, non-interacting cells that moved through the entire channel were quantified to exclude the influence of neighbouring cells or inhomogeneities in chemoattractant distribution. All the parameters were quantified based on the nuclei signal from Hoechst 333242. The cell was considered to be in a constriction as long as any part of the nucleus was visible inside of the constriction. The data acquired by a custom-made ImageJ script was manually curated to make sure that all the signal analyzed was coming from the nuclei staining.

7.23 Fixation of migrating HL-60 cells

On the 5^th day post-differentiation, 1-2 ml of HL-60 cells were plated on fibronectin-coated dish for 10 minutes and left at 37 °C with 5% CO_2 humidified chamber. Unbound cells were washed with medium 2 times and stimulated with addition of 10 nM fMLP (#F3506-5MG, Sigma Aldrich) for 30 minutes at 37 °C with 5% CO_2 in humidified chamber. Next, cells were fixed by adding 1 ml of 2x fixation buffer to 1 ml of differentiated HL-60 cells in a dish. Fixation buffer (1x) is containing 3.7% paraformaldehyde (#28908, Thermo Scientific), 1x intracellular buffer (140 mM KCL, 1 mM $MgCl_2$, 2 mM EGTA, 20 mM HEPES, pH 7.5), 320 mM sucrose (#S0389-500G, Sigma Aldrich) and 0.2% BSA (#A7030-10G, Sigma Aldrich) and incubated at 4 °C for 1 hour. Cells were washed carefully three times with 1x intracellular buffer and stored in dPBS until further use.

7.24 Imaging of fixed HL-60 cells using epifluorescent microscopy

For epifluorescent imaging, dHL-60 cells were fixed as described previously (Methods 7.23). Cells with fluorescently-tagged proteins (Methods 7.34) or stained for F-actin (Methods 7.25) were imaged using Eclipse Ti inverted light microscope (Nikon) with a 20x, 40x or 100x objective (#MRH68200, Nikon;#MRD00405, Nikon; 100x#MRD01905, Nikon). Fluorescent and Bright-Field images were obtained with the SOLA SE II and 100W halogen lamps (Nikon) using appropriate filter sets.

7.25 F-actin staining of adherent HL-60 cells after fixation

After fixation of adherent HL-60 cells (7.23), dPBS in which the cells were stored was aspirated and cells were re-suspended in intracellular buffer (1x) containing 0.2% of Triton X-100 (#T8787, Sigma Aldrich) and phalloidin coupled with appropriate fluorophore (Alexa 488 (#A12379, Thermo Fisher Scientific), TRITC (#P1951, Sigma Aldrich), Alexa-647 (#A22287, Thermo Fisher Scientific). Staining was performed for 30 minutes at 4 °C. Cells were then washed 3-5 times with intracellular buffer (1x) or dPBS and stored at 4 °C in the dark or used immediately for imaging.

7.26 Pearson Correlation Coefficient (PCC) calculation for confocal imaging

The data was acquired using a Confocal Laser Scanning Microscope (FV3000, Olympus) and analyzed using ImageJ software. The z-planes containing the cell were identified as following: the line scan with the width covering the whole signal was drawn on the resliced maximum intensity z projection. Only the z-slices that had top 80 % of the intensity were considered for analysis. A channel of interest (ChoF) (e.g. channel with mCherry-CAAX labelling membrane) was used for preparing a mask based on automatic Otsu segmentation. A custom-made script allowed to calculate PCC for every z-plane of ChoF1 with ChoF2 based on the mask of ChoF1. Later, either the mean of the PCC was calculated for every cell, or the z-slices were assigned to 10 bins and the mean for every bin was calculated.

7.27 Time-lapse imaging of dHL-60 cells using epifluorescence

For imaging experiments, the 35-mm glass-bottom dishes were coated for 30 min with fibronectin (7.9) or fibronectin supplemented with 5 % BSA. Differentiated HL-60 cells were plated on each dish in growth media and allowed to adhere for at least 10 min at 37 °C. Next, cells were washed with HL-60 growth media and supplemented with 10 nM fMLP.

Epifluorescent images were acquired on a Nikon Ti Eclipse inverted microscope with a TIRF objective CFI Plan Apo Lambda 100X Oil (#MRD01905, Nikon) and sCMOS camera controlled by NIS-Elements (Nikon). Sample drift was reduced using an autofocus system (Perfect Focus, Nikon) in case of time-lapse imaging. NIS-Elements was used for image acquisition. A 488 and 561 nm laser lines were used. Cells were imaged every 2-20 seconds, depending on the numbers of channels acquired with the exposure time of 100-500 ms of laser power 4-15%. Cells were not

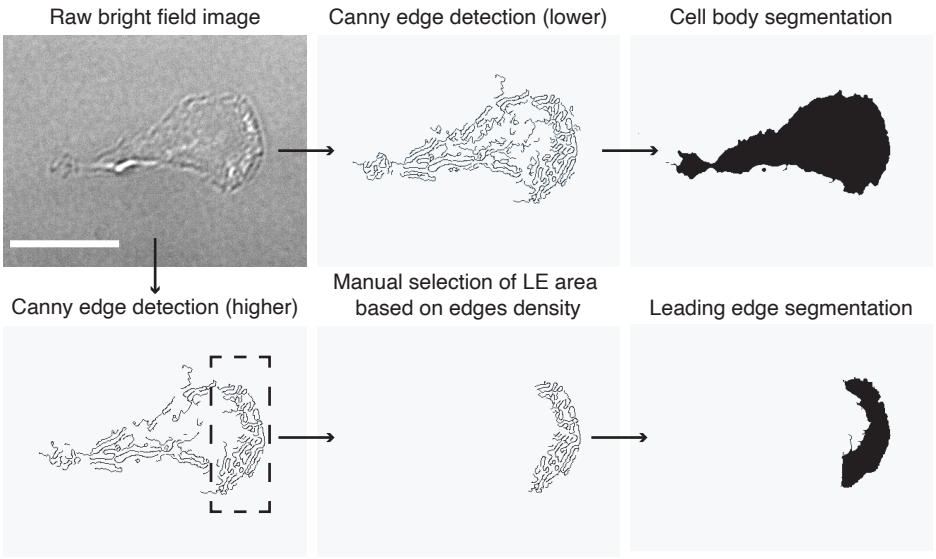

FIGURE 7.3: Cell body and leading edge segmentation pipeline using bright-field imaging. Data processed jointly with S. Dias Almeida. Scale bar = 10 μm.

used longer than 1 hour for image acquisition and were at 37 °C in humidified chamber at 5 % CO_2.

7.28 Cell body and leading edge segmentation using Canny edge detection

Bright-field images were obtained using Eclipse Ti inverted light microscope (Nikon) with 40x objective (#MRD00405, Nikon). Fluorescent and Bright-Field images were obtained with the SOLA SE II and 100W halogen lamps (Nikon) using appropriate filter sets. Cells were manually cut using ImageJ software from large FOV images. Only single cells (not touching other cells or image edge) with visible leading edge characterized by visible enrichment of phalloidin staining in one edge of the cells) were considered for analysis. To segment the cell body, in raw bright-field imaged the contrast was enhanced using equalize histogram function followed by running of the canny edge detection and the filling holes of previously semi-manual closing of the lines. To segment the leading edge, similar strategy was used, with the difference of semi-manual choosing of the cell region with the enriched edges after the canny edge detection with higher values step (Figure 7.3). After successful segmentation of the cell body and the leading edge, the pixel area of cell body, leading edge and their subtraction were measured as well as their average pixel intensity value of the phalloidin signal.

7.29 Manipulating adhesion in the substrates

Substrates with different adhesion properties were obtained by coating glass-bottom dishes with fibronectin (higher adhesion) or fibronectin supplemented with 5% molar BSA for 30 minutes, as described previously (Diz-Muñoz et al., 2016a). After

incubation at RT, glass-bottom dishes were washed with dPBS twice. Cells were plated as described previously (Methods 7.1).

7.30 Membrane-to-Cortex attachments (MCA) measurements in HL-60 cells

Samples and cantilever preparation was completed as described in the previous Section 7.19. To estimate the contribution of MCA, instead of previously described static tether pulling experiment, the dynamic tether pulling experiment was performed. We assume that membrane tension value is a result of force contributions coming from in-plane membrane tension (T_{in}) and MCA (T_{MCA}), which value is described as in Equation 1.1:

$$T = T_{in} + T_{MCA} = \frac{f_0^2}{8B\pi^2} \tag{7.2}$$

To estimate the contribution of MCA, the same cell can be probed multiple times at different retraction velocities (v) as the tether force (f) increases with increasing velocity. Bending rigidity was as previously assumed to be constant for different conditions (2.7x10^{-19} Nm). To interpret the measurements at different retraction velocities, the model described by Brochard-Wyart and colleagues (Brochard-Wyart et al., 2006) was applied using Monte-Carlo-based fitting:

$$f^3 - f f_0^2 = \alpha v = [(2\pi)^3 2\kappa^2 \eta \epsilon ln(\frac{R_c}{R_t})v \tag{7.3}$$

As the radius of the cell (R_c) » radius of the tether (R_t) and the bending rigidity (κ) are assumed to be constant, the tether force increase with retraction velocity depends solely on the surface viscosity (η) and the density of the MCA linkers (ϵ). Since we are not able to report the exact values for the surface viscosity (η) and the density of the MCA linkers (ϵ) independently, we report here the parameter α that being proportional to $\eta\epsilon$ reflects the effects of MCA on plasma membrane viscosity

7.31 Segmentation and analysis of TIRFM images using Ilastic

Images of eGFP-tagged Hem1 (WAVE2 complex component) and mCherry-tagged CAAX using TIRFM were obtained as previously described (Methods 7.10). To segment cell mask (based on membrane signal) and WAVE2 mask (based on Hem1 signal) machine learning-based ilastik software was used (Sommer et al., 2011; Berg et al., 2019). Further, image analysis was performed using an in-house built program implemented in Python. Angle at which cells are moving was calculated based on center of mass for 3 consecutive frames. The leading edge was defined as difference between two consecutive frames where at least one pixel of WAVE2 mask was present per cluster (Figure 7.4). Leading edge length was defined as number of pixels in the outside leading edge perimeter. For quantification of cells in contact the same methodology was used. Data processed jointly with S. Dias Almeida.

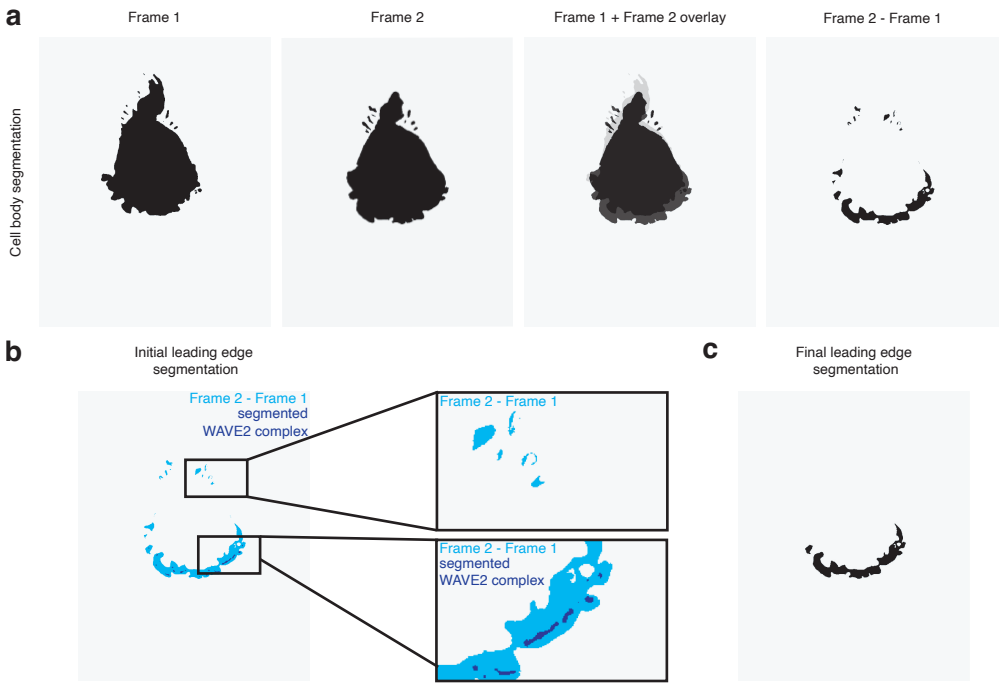

FIGURE 7.4: Leading edge segmentation pipeline in migrating cells. Data processed jointly with S. Dias Almeida.

7.32 Fluo-4-AM staining of live non-adherent HL-60 cells

24-well plates were coated with 0.2-03 % BSA in RPMI for 15 minutes to avoid loosing cell number by the cell sticking to the non-coated plastic. Fluo-4-AM (#F14201, Thermo Fisher Scientific) was added to 1 ml of differentiated cells at 4.5x10^5 at 1 μM and incubated for 30 minutes at 37 °C with 5% CO_2 in humidified chamber. Next, cells were spun down, washed three times and starved for 1 hour in FBS-free RPMI medium. 6-well plates used for the cell starvation were coated with 0.2-03 % BSA in RPMI for 15 minutes. After 30-60 minutes of starvation, the cells were moved to FACS sorting facility and analyzed on BD LSRFortessa™ at the EMBL Flow Cytometry Core Facility. Equal volumes of 20 nM fMLP were thoroughly mixed with starved cells stained with Fluo-4-AM just before analysis. Every sample was acquired for around 10-20 seconds depending on the density of cells (some were lost during the washing step).

7.33 Graphics and Statistics

Graphics and statistical analyses were performed using R, Microsoft Excel, Inkscape and Adobe Illustrator. P-values were calculated using T-test, after ensuring that data distribution was normal according to Shapiro-Wilk test. Otherwise, a non-parametric Mann-Whitney-U-test was used, if not indicated differently. In all box-plots, the lower and upper hinges correspond to the first and third quartiles (the 25th and 75th percentiles). The upper whisker extends from the hinge to the largest value, but no further than 1.5*IQR (distance between the first and third quartiles). The lower whiskers extends from the hinge to the smallest value, but no lower than

1.5*IQR of the hinge. Data beyond the end of the whiskers are plotted as black dots. Black line corresponds to the median.

7.34 List of generated cell lines

Cell line	Fluorophores
wt	AMPH2-eGFP, CAAX-mCherry
wt	APPL2-eGFP, CAAX-mCherry
wt	BIN2-eGFP, CAAX-mCherry
wt	GRAF1-eGFP, CAAX-mCherry
wt	FBP17-eGFP, CAAX-mCherry
wt	SH3BP1-eGFP, CAAX-mCherry
wt	Snx33-eGFP (high expression)
wt	Snx33-eGFP, CAAX-mCherry
wt	PACSIN2-eGFP, CAAX-mCherry
wt	FBP17-eGFP, CAAX-mCherry
SH3BP1 knockout	-
Snx33 knockout	-
Snx33 knockout	Snx33-eGFP (high expression)
Snx33 knockout	Snx33-eGFP, CAAX-mCherry
wt	WAVE2-eGFP, CAAX-mCherry
Snx33 knockout	WAVE2-eGFP, CAAX-mCherry
wt	Snx33-eGFP, Hem1-mCherry
wt	ΔH3-eGFP (from Snx33)
wt	ΔBAR-eGFP (from Snx33)
wt	ΔPX-BAR-eGFP (Snx33)
wt	SH3-eGFP (Snx33)
wt	ΔSH3-eGFP (Snx33)
wt	PX-BAR-eGFP (Snx33)
wt	BAR-eGFP (Snx33)
Snx33 knockout	ΔH3-eGFP (from Snx33)
Snx33 knockout	ΔBAR-eGFP (from Snx33)
Snx33 knockout	ΔPX-BAR-eGFP (Snx33)
Snx33 knockout	SH3-eGFP (Snx33)
Snx33 knockout	ΔSH3-eGFP (Snx33)
Snx33 knockout	PX-BAR-eGFP (Snx33)
Snx33 knockout	PX-BAR-eGFP (Snx33), CAAX-mCherry
Snx33 knockout	BAR-eGFP (Snx33)

TABLE 7.14: List of generated cell lines used in the study

List of Figures

List of Tables

Bibliography

Aaron, Jesse S, Aaron B Taylor, and Teng-Leong Chew (Feb. 2018). "Image co-localization – co-occurrence versus correlation". In: *Journal of Cell Science* 131.3, jcs211847–10.

Abercrombie, Michael et al. (1970). "The locomotion of fibroblasts in culture: II."Ruffling"". In: *Experimental cell research* 60.3, pp. 437–444.

Abou-Kheir, W et al. (Jan. 2008). "Membrane targeting of WAVE2 is not sufficient for WAVE2-dependent actin polymerization: a role for IRSp53 in mediating the interaction between Rac and WAVE2". In: *Journal of Cell Science* 121.3, pp. 379–390.

Akamatsu, Matthew et al. (2020). "Principles of self-organization and load adaptation by the actin cytoskeleton during clathrin-mediated endocytosis". In: *Elife* 9, e49840.

Almeida-Souza, Leonardo et al. (2018). "A flat BAR protein promotes actin polymerization at the base of clathrin-coated pits". In: *Cell* 174.2, pp. 325–337.

Almendinger, Johann et al. (Apr. 2011). "A Conserved Role for SNX9-Family Members in the Regulation of Phagosome Maturation during Engulfment of Apoptotic Cells". In: *PLoS ONE* 6.4, e18325–11.

Alto, Laura Taylor and Jonathan R Terman (2017). "Semaphorins and their signaling mechanisms". In: *Semaphorin Signaling*. Springer, pp. 1–25.

Anantharam, Arun, Daniel Axelrod, and Ronald W Holz (2010). "Polarized TIRFM reveals changes in plasma membrane topology before and during granule fusion". In: *Cellular and molecular neurobiology* 30.8, pp. 1343–1349.

Apodaca, Gerard (2002). "Modulation of membrane traffic by mechanical stimuli". In: *American Journal of Physiology-Renal Physiology* 282.2, F179–F190.

Axelrod, Daniel (2008). *Chapter 7 - Total Internal Reflection Fluorescence Microscopy*. 1st ed. Vol. 89. Elsevier Inc.

Barger, Sarah R et al. (2019). "Membrane-cytoskeletal crosstalk mediated by myosin-I regulates adhesion turnover during phagocytosis". In: *Nature communications* 10.1, pp. 1–18.

Batchelder, Ellen L et al. (2011). "Membrane tension regulates motility by controlling lamellipodium organization". In: *Proceedings of the National Academy of Sciences* 108.28, pp. 11429–11434.

Becalska, Agata N et al. (2013). "Formation of membrane ridges and scallops by the F-BAR protein Nervous Wreck". In: *Molecular biology of the cell* 24.15, pp. 2406–2418.

Bendris, Nawal et al. (2016). "SNX9 promotes metastasis by enhancing cancer cell invasion via differential regulation of RhoGTPases". In: *Molecular biology of the cell* 27.9, pp. 1409–1419.

Bennett, Vann and Anthony J Baines (2001). "Spectrin and ankyrin-based pathways: metazoan inventions for integrating cells into tissues". In: *Physiological reviews* 81.3, pp. 1353–1392.

Berchtold, Doris et al. (2012). "Plasma membrane stress induces relocalization of Slm proteins and activation of TORC2 to promote sphingolipid synthesis". In: *Nature cell biology* 14.5, pp. 542–547.

Berg, Stuart et al. (2019). "Ilastik: interactive machine learning for (bio) image analysis". In: *Nature Methods*, pp. 1–7.

Bergert, Martin et al. (2015). "Force transmission during adhesion-independent migration". In: *Nature cell biology* 17.4, pp. 524–529.

Bergert, Martin et al. (2020). "Cell Surface Mechanics Gate Embryonic Stem Cell Differentiation". In: *Cell Stem Cell*.

Beurg, Maryline et al. (2019). "A Tmc1 mutation reduces calcium permeability and expression of mechanoelectrical transduction channels in cochlear hair cells". In: *Proceedings of the National Academy of Sciences* 116.41, pp. 20743–20749.

Bhatia, Vikram K et al. (2009). "Amphipathic motifs in BAR domains are essential for membrane curvature sensing". In: *The EMBO journal* 28.21, pp. 3303–3314.

Bieling, Peter et al. (Jan. 2016). "Force Feedback Controls Motor Activity and Mechanical Properties of Self-Assembling Branched Actin Networks". In: *Cell* 164.1-2, pp. 115–127.

Bigay, Joëlle and Bruno Antonny (2012). "Curvature, lipid packing, and electrostatics of membrane organelles: defining cellular territories in determining specificity". In: *Developmental cell* 23.5, pp. 886–895.

Bisaria, Anjali et al. (2019). "Membrane proximal F-actin restricts local membrane protrusions and directs cell migration". In: *BioRxiv*, p. 705509.

Blaser, Heiko et al. (2006). "Migration of zebrafish primordial germ cells: a role for myosin contraction and cytoplasmic flow". In: *Developmental cell* 11.5, pp. 613–627.

Bo, Lin and Richard E Waugh (1989). "Determination of bilayer membrane bending stiffness by tether formation from giant, thin-walled vesicles". In: *Biophysical journal* 55.3, pp. 509–517.

Bodor, Dani L et al. (2020). "Of Cell Shapes and Motion: The Physical Basis of Animal Cell Migration". In: *Developmental Cell* 52.5, pp. 550–562.

Boulant, Steeve et al. (2011). "Actin dynamics counteract membrane tension during clathrin-mediated endocytosis". In: *Nature cell biology* 13.9, pp. 1124–1131.

Bridges, Andrew A and Amy S Gladfelter (2015). "Septin form and function at the cell cortex". In: *Journal of Biological Chemistry* 290.28, pp. 17173–17180.

Brochard-Wyart, F et al. (May 2006). "Hydrodynamic narrowing of tubes extruded from cells." In: *Proceedings of the National Academy of Sciences* 103.20, pp. 7660–7663.

Broussard, Joshua A et al. (2012). "The endosomal adaptor protein APPL1 impairs the turnover of leading edge adhesions to regulate cell migration". In: *Molecular biology of the cell* 23.8, pp. 1486–1499.

Burridge, Keith and Christophe Guilluy (2016). "Focal adhesions, stress fibers and mechanical tension". In: *Experimental cell research* 343.1, pp. 14–20.

Cao, Huiren et al. (2013). "FCHSD1 and FCHSD2 are expressed in hair cell stereocilia and cuticular plate and regulate actin polymerization in vitro". In: *PLoS One* 8.2, e56516.

Carim, Sabrya C et al. (Mar. 2019). "IPIP27 Coordinates PtdIns(4,5)P2 Homeostasis for Successful Cytokinesis". In: *Current Biology* 29.5, 775–789.e7.

Carman, Peter J and Roberto Dominguez (Dec. 2018). "BAR domain proteins-a linkage between cellular membranes, signaling pathways, and the actin cytoskeleton." In: *Biophysical reviews* 10.6, pp. 1587–1604.

Chapuis, J et al. (2013). "Increased expression of BIN1 mediates Alzheimer genetic risk by modulating tau pathology". In: *Molecular psychiatry* 18.11, pp. 1225–1234.

Charest, Pascale G and Richard A Firtel (2006). "Feedback signaling controls leading-edge formation during chemotaxis". In: *Current opinion in genetics & development* 16.4, pp. 339–347.

Charras, Guillaume and Ewa Paluch (2008). "Blebs lead the way: how to migrate without lamellipodia". In: *Nature reviews Molecular cell biology* 9.9, pp. 730–736.

Chen, Pei-Wen et al. (2016). "The Arf GTPase-activating protein, ASAP1, binds non-muscle myosin 2A to control remodeling of the actomyosin network". In: *Journal of Biological Chemistry* 291.14, pp. 7517–7526.

Chen, Pei-Wen et al. (2020). "The BAR domain of the Arf GTPase-activating protein ASAP1 directly binds actin filaments". In: *Journal of Biological Chemistry*, jbc–RA119.

Chen, Qin et al. (2008). "ADAM15 suppresses cell motility by driving integrin $\alpha 5\beta 1$ cell surface expression via Erk inactivation". In: *The international journal of biochemistry & cell biology* 40.10, pp. 2164–2173.

Chen, Zhucheng et al. (2010). "Structure and control of the actin regulatory WAVE complex". In: *Nature* 468.7323, pp. 533–538.

Chou, Ai Mei et al. (2017). "Redundant functions of I-BAR family members, IRSp53 and IRTKS, are essential for embryonic development". In: *Scientific reports* 7.1, pp. 1–11.

Chugh, Priyamvada and Ewa K Paluch (2018). "The actin cortex at a glance". In: *Journal of cell science* 131.14, jcs186254.

Cicchetti, Piera et al. (1992). "Identification of a protein that binds to the SH3 region of Abl and is similar to Bcr and GAP-rho". In: *Science* 257.5071, pp. 803–806.

Cicchetti, Piera et al. (1995). "3BP-1, an SH3 domain binding protein, has GAP activity for Rac and inhibits growth factor-induced membrane ruffling in fibroblasts." In: *The EMBO Journal* 14.13, pp. 3127–3135.

Clemens, R A and C A Lowell (Oct. 2015). "Store-operated calcium signaling in neutrophils". In: *Journal of Leukocyte Biology* 98.4, pp. 497–502.

Cohen, Adam E and Zheng Shi (2020). "Do Cell Membranes Flow Like Honey or Jiggle Like Jello?" In: *BioEssays* 42.1, p. 1900142.

Craig, AW (2012). "FES/FER kinase signaling in hematopoietic cells and leukemias". In: *Front Biosci (Landmark Ed)* 17, pp. 861–875.

Dai, Jianwu, H Ping Ting-Beall, and Michael P Sheetz (1997). "The secretion-coupled endocytosis correlates with membrane tension changes in RBL 2H3 cells". In: *The Journal of general physiology* 110.1, pp. 1–10.

Damiano-Guercio, Julia et al. (2020). "Loss of Ena/VASP interferes with lamellipodium architecture, motility and integrin-dependent adhesion". In: *Elife* 9, e55351.

Danson, C M et al. (Dec. 2007). "Phosphorylation of WAVE2 by MAP kinases regulates persistent cell migration and polarity". In: *Journal of Cell Science* 120.23, pp. 4144–4154.

De Belly, Henry et al. (2020). "Membrane Tension Gates ERK-Mediated Regulation of Pluripotent Cell Fate". In: *Cell Stem Cell*.

De Rossi, Pierre et al. (2020). "Neuronal BIN1 Regulates Presynaptic Neurotransmitter Release and Memory Consolidation". In: *Cell reports* 30.10, pp. 3520–3535.

Deb, Bipan Kumar, Trayambak Pathak, and Gaiti Hasan (May 2016). "Store-independent modulation of Ca2+ entry through Orai by Septin 7". In: *Nature Communications* 7.1, pp. 549–16.

Dimova, Rumiana (2014). "Recent developments in the field of bending rigidity measurements on membranes". In: *Advances in colloid and interface science* 208, pp. 225–234.

Ding, Youming et al. (2016). "APPL1-mediating leptin signaling contributes to proliferation and migration of cancer cells". In: *PLoS One* 11.11, e0166172.

Dislich, Bastian, Manuel E Than, and Stefan F Lichtenthaler (Jan. 2011). "Specific amino acids in the BAR domain allow homodimerization and prevent heterodimerization of sorting nexin 33". In: *Biochemical Journal* 433.1, pp. 75–83.

Diz-Muñoz, Alba, Daniel A Fletcher, and Orion D Weiner (Feb. 2013). "Use the force: membrane tension as an organizer of cell shape and motility." In: *Trends in Cell Biology* 23.2, pp. 47–53.

Diz-Muñoz, Alba, Orion D Weiner, and Daniel A Fletcher (2018). "In pursuit of the mechanics that shape cell surfaces". In: *Nature physics* 14.7, pp. 648–652.

Diz-Muñoz, Alba et al. (2010). "Control of directed cell migration in vivo by membrane-to-cortex attachment". In: *PLoS Biol* 8.11, e1000544.

Diz-Muñoz, Alba et al. (June 2016a). "Membrane Tension Acts Through PLD2 and mTORC2 to Limit Actin Network Assembly During Neutrophil Migration". In: *PLoS Biology* 14.6, e1002474–30.

Diz-Muñoz, Alba et al. (2016b). "Steering cell migration by alternating blebs and actin-rich protrusions". In: *BMC biology* 14.1, pp. 1–13.

Doherty, Gary J et al. (2011). "The endocytic protein GRAF1 is directed to cell-matrix adhesion sites and regulates cell spreading". In: *Molecular biology of the cell* 22.22, pp. 4380–4389.

Dräger, Nina M et al. (Oct. 2017). "Bin1 directly remodels actin dynamics through its BARdomain". In: *EMBO reports* 18.11, pp. 2051–2066.

Elbediwy, Ahmed et al. (2012). "Epithelial junction formation requires confinement of Cdc42 activity by a novel SH3BP1 complexSpatial control of Cdc42 and junction formation". In: *The Journal of cell biology* 198.4, pp. 677–693.

Elvers, Margitta et al. (2012). "The GRAF family member oligophrenin1 is a RhoGAP with BAR domain and regulates Rho GTPases in platelets". In: *Cardiovascular research* 94.3, pp. 526–536.

Endris, Volker et al. (2011). "SrGAP3 interacts with lamellipodin at the cell membrane and regulates Rac-dependent cellular protrusions". In: *Journal of cell science* 124.23, pp. 3941–3955.

Engler, Adam J et al. (Aug. 2006). "Matrix Elasticity Directs Stem Cell Lineage Specification". In: *Cell* 126.4, pp. 677–689.

Evans, E and A Yeung (1989). "Apparent viscosity and cortical tension of blood granulocytes determined by micropipet aspiration". In: *Biophysical journal* 56.1, pp. 151–160.

Evans, John H and Joseph J Falke (Oct. 2007). "Ca2+ influx is an essential component of the positive-feedback loop that maintains leading-edge structure and activity in macrophages." In: *Proceedings of the National Academy of Sciences* 104.41, pp. 16176–16181.

Falcone, Sestina et al. (2014). "N-WASP is required for Amphiphysin-2/BIN 1-dependent nuclear positioning and triad organization in skeletal muscle and is involved in the pathophysiology of centronuclear myopathy". In: *EMBO molecular medicine* 6.11, pp. 1455–1475.

Farsad, Khashayar et al. (2001). "Generation of high curvature membranes mediated by direct endophilin bilayer interactions". In: *Journal of Cell Biology* 155.2, pp. 193–200.

Fehon, Richard G, Andrea I McClatchey, and Anthony Bretscher (2010). "Organizing the cell cortex: the role of ERM proteins". In: *Nature reviews Molecular cell biology* 11.4, pp. 276–287.

Francis, Monika K et al. (2015). "Endocytic membrane turnover at the leading edge is driven by a transient interaction between Cdc42 and GRAF1". In: *Journal of cell science* 128.22, pp. 4183–4195.

Freitas, Natália and Celso Cunha (Dec. 2009). "Mechanisms and signals for the nuclear import of proteins." In: *Current genomics* 10.8, pp. 550–557.

Friedl, Peter, Stefan Borgmann, and Eva-B Bröcker (2001). "Amoeboid leukocyte crawling through extracellular matrix: lessons from the Dictyostelium paradigm of cell movement". In: *Journal of leukocyte biology* 70.4, pp. 491–509.

Fritz-Laylin, Lillian K et al. (2017). "Actin-based protrusions of migrating neutrophils are intrinsically lamellar and facilitate direction changes". In: *Elife* 6, e26990.

Frost, Adam et al. (2008). "Structural basis of membrane invagination by F-BAR domains". In: *Cell* 132.5, pp. 807–817.

Funamoto, Satoru et al. (2002). "Spatial and temporal regulation of 3-phosphoinositides by PI 3-kinase and PTEN mediates chemotaxis". In: *Cell* 109.5, pp. 611–623.

Gallop, Jennifer L et al. (2006). "Mechanism of endophilin N-BAR domain-mediated membrane curvature". In: *The EMBO journal* 25.12, pp. 2898–2910.

Gauthier, Nils C, Thomas A Masters, and Michael P Sheetz (Oct. 2012). "Mechanical feedback between membrane tension and dynamics." In: *Trends in Cell Biology* 22.10, pp. 527–535.

Giese, Arnaud PJ et al. (2017). "CIB2 interacts with TMC1 and TMC2 and is essential for mechanotransduction in auditory hair cells". In: *Nature communications* 8.1, pp. 1–13.

Goehring, Nathan W and Stephan W Grill (2013). "Cell polarity: mechanochemical patterning". In: *Trends in cell biology* 23.2, pp. 72–80.

Goudarzi, Mehdi et al. (2012). "Identification and regulation of a molecular module for bleb-based cell motility". In: *Developmental cell* 23.1, pp. 210–218.

Graham, Todd R and Michael M Kozlov (2010). "Interplay of proteins and lipids in generating membrane curvature". In: *Current opinion in cell biology* 22.4, pp. 430–436.

Grashoff, Carsten et al. (2010). "Measuring mechanical tension across vinculin reveals regulation of focal adhesion dynamics". In: *Nature* 466.7303, pp. 263–266.

Graziano, Brian R et al. (2017). "A module for Rac temporal signal integration revealed with optogenetics". In: *Journal of Cell Biology* 216.8, pp. 2515–2531.

Graziano, Brian R et al. (Oct. 2019). "Cell confinement reveals a branched-actin independent circuit for neutrophil polarity." In: *PLoS Biology* 17.10, e3000457.

Guerrier, Sabrice et al. (2009). "The F-BAR domain of srGAP2 induces membrane protrusions required for neuronal migration and morphogenesis". In: *Cell* 138.5, pp. 990–1004.

Håberg, Karin, Richard Lundmark, and Sven R Carlsson (May 2008). "SNX18 is an SNX9 paralog that acts as a membrane tubulator in AP-1-positive endosomal trafficking." In: *Journal of Cell Science* 121.Pt 9, pp. 1495–1505.

Hak, Laura Chan Wah et al. (Aug. 2018). "FBP17 and CIP4 recruit SHIP2 and lamellipodin to prime the plasma membrane for fast endophilin- mediated endocytosis". In: *Nature Cell Biology*, pp. 1–15.

He, Yuan et al. (2013). "Mammalian target of rapamycin and Rictor control neutrophil chemotaxis by regulating Rac/Cdc42 activity and the actin cytoskeleton". In: *Molecular biology of the cell* 24.21, pp. 3369–3380.

Hein, Marco Y et al. (Oct. 2015). "A Human Interactome in Three Quantitative Dimensions Organized by Stoichiometries and Abundances". In: *Cell* 163.3, pp. 712–723.

Heiseke, Andreas et al. (July 2008). "The Novel Sorting Nexin SNX33 Interferes with Cellular PrP ScFormation by Modulation of PrP cShedding". In: *Traffic* 9.7, pp. 1116–1129.

Heisenberg, Carl-Philipp and Yohanns Bellaïche (May 2013). "Forces in Tissue Morphogenesis and Patterning". In: *Cell* 153.5, pp. 948–962.

Helfrich, Peter and Eric Jakobsson (1990). "Calculation of deformation energies and conformations in lipid membranes containing gramicidin channels". In: *Biophysical journal* 57.5, pp. 1075–1084.

Helfrich, Wolfgang (1973). "Elastic properties of lipid bilayers: theory and possible experiments". In: *Zeitschrift für Naturforschung C* 28.11-12, pp. 693–703.

Henne, William Mike et al. (2007). "Structure and analysis of FCHo2 F-BAR domain: a dimerizing and membrane recruitment module that effects membrane curvature". In: *Structure* 15.7, pp. 839–852.

Hetrick, Byron et al. (2013). "Small molecules CK-666 and CK-869 inhibit actin-related protein 2/3 complex by blocking an activating conformational change". In: *Chemistry & biology* 20.5, pp. 701–712.

Hicks, L et al. (Nov. 2015). "Depletion or over-expression of Sh3px1 results in dramatic changes in cell morphology". In: *Biology Open* 4.11, pp. 1448–1461.

Hochmuth, F M et al. (Jan. 1996). "Deformation and flow of membrane into tethers extracted from neuronal growth cones." In: *Biophysical Journal* 70.1, pp. 358–369.

Hochmuth, Robert M (2000). "Micropipette aspiration of living cells". In: *Journal of biomechanics* 33.1, pp. 15–22.

Hogan, Patrick G, Richard S Lewis, and Anjana Rao (Mar. 2010). "Molecular Basis of Calcium Signaling in Lymphocytes: STIM and ORAI". In: *Annual Review of Immunology* 28.1, pp. 491–533.

Houk, Andrew R et al. (2012). "Membrane tension maintains cell polarity by confining signals to the leading edge during neutrophil migration". In: *Cell* 148.1-2, pp. 175–188.

Hu, Jinghui et al. (2011). "Cdc42-interacting protein 4 is a Src substrate that regulates invadopodia and invasiveness of breast tumors by promoting MT1-MMP endocytosis". In: *Journal of cell science* 124.10, pp. 1739–1751.

Huse, Morgan (July 2017). "Mechanical forces in the immune system". In: *Nature Reviews Immunology* 17.11, pp. 679–690.

Iden, Sandra and John G Collard (2008). "Crosstalk between small GTPases and polarity proteins in cell polarization". In: *Nature reviews Molecular cell biology* 9.11, pp. 846–859.

Iglesias, Pablo A and Peter N Devreotes (2012). "Biased excitable networks: how cells direct motion in response to gradients". In: *Current opinion in cell biology* 24.2, pp. 245–253.

Iijima, Miho and Peter Devreotes (2002). "Tumor suppressor PTEN mediates sensing of chemoattractant gradients". In: *Cell* 109.5, pp. 599–610.

Ismail, Ayman M et al. (Apr. 2009). "The WAVE regulatory complex is inhibited". In: *Nature Structural & Molecular Biology* 16.5, pp. 561–563.

Itoh, Toshiki et al. (2005). "Dynamin and the actin cytoskeleton cooperatively regulate plasma membrane invagination by BAR and F-BAR proteins". In: *Developmental cell* 9.6, pp. 791–804.

Jain, Rakesh K, John D Martin, and Triantafyllos Stylianopoulos (2014). "The role of mechanical forces in tumor growth and therapy". In: *Annual review of biomedical engineering* 16, pp. 321–346.

Jarsch, Iris K, Frederic Daste, and Jennifer L Gallop (2016). "Membrane curvature in cell biology: An integration of molecular mechanisms". In: *Journal of Cell Biology* 214.4, pp. 375–387.

Kameritsch, Petra and Jörg Renkawitz (Oct. 2020). "Principles of Leukocyte Migration Strategies". In: *Trends in Cell Biology* 30.10, pp. 818–832.

Kast, David J and Roberto Dominguez (2019a). "IRSp53 coordinates AMPK and 14-3-3 signaling to regulate filopodia dynamics and directed cell migration". In: *Molecular biology of the cell* 30.11, pp. 1285–1297.

— (2019b). "Mechanism of IRSp53 inhibition by 14-3-3". In: *Nature communications* 10.1, pp. 1–14.

Katz, Zachary B et al. (Oct. 2020). "Septins organize endoplasmic reticulum-plasma membrane junctions for STIM1-ORAI1 calcium signalling". In: *Scientific Reports*, pp. 1–17.

Kelkar, Manasi, Pierre Bohec, and Guillaume Charras (2020). "Mechanics of the cellular actin cortex: from signalling to shape change". In: *arXiv preprint arXiv:2005.11854*.

Keren, Kinneret (2011). "Cell motility: the integrating role of the plasma membrane". In: *European Biophysics Journal* 40.9, p. 1013.

Keren, Kinneret et al. (2008). "Mechanism of shape determination in motile cells". In: *Nature* 453.7194, pp. 475–480.

Kim, A S et al. (Mar. 2000). "Autoinhibition and activation mechanisms of the Wiskott-Aldrich syndrome protein." In: *Nature* 404.6774, pp. 151–158.

Kim, Tae-Jin et al. (Feb. 2015). "Distinct mechanisms regulating mechanical force-induced Ca2+ signals at the plasma membrane and the ER in human MSCs". In: *eLife* 4, R1586–14.

Kleino, Iivari et al. (Nov. 2009). "Alternative splicing of ADAM15 regulates its interactions with cellular SH3 proteins". In: *Journal of Cellular Biochemistry* 108.4, pp. 877–885.

Knævelsrud, Helene et al. (July 2013). "Membrane remodeling by the PX-BAR protein SNX18 promotes autophagosome formation". In: *The Journal of Cell Biology* 202.2, pp. 331–349.

Koch, Birgit et al. (May 2018). "Generation and validation of homozygous fluorescent knock-in cells using CRISPR–Cas9 genome editing". In: *Nature Publishing Group* 13.6, pp. 1465–1487.

Koduru, Suresh et al. (2010). "Cdc42 interacting protein 4 (CIP4) is essential for integrin-dependent T-cell trafficking". In: *Proceedings of the National Academy of Sciences* 107.37, pp. 16252–16256.

Kopf, Aglaja et al. (May 2020). "Microtubules control cellular shape and coherence in amoeboid migrating cells". In: *The Journal of Cell Biology* 219.6, pp. 193–24.

Kostan, J et al. (Nov. 2014). "Direct interaction of actin filaments with F-BAR protein pacsin2". In: *EMBO reports* 15.11, pp. 1154–1162.

Kovacs, Eva M, Robert S Makar, and Frank B Gertler (2006). "Tuba stimulates intracellular N-WASP-dependent actin assembly". In: *Journal of cell science* 119.13, pp. 2715–2726.

Krause, Matthias and Alexis Gautreau (Aug. 2014). "Steering cell migration: lamellipodium dynamics and the regulation of directional persistence". In: *Nature Reviews Molecular Cell Biology*, pp. 1–14.

Kreuk, Bart-Jan de and Peter L Hordijk (2012). "Control of Rho GTPase function by BAR-domains". In: *Small GTPases* 3.1, pp. 45–52.

Kreuk, Bart-Jan de et al. (2011). "The F-BAR domain protein PACSIN2 associates with Rac1 and regulates cell spreading and migration". In: *Journal of cell science* 124.14, pp. 2375–2388.

Krieg, Michael, Alexander R Dunn, and Miriam B Goodman (2014). "Mechanical control of the sense of touch by β-spectrin". In: *Nature cell biology* 16.3, pp. 224–233.

Krieg, Michael et al. (2008). "Tensile forces govern germ-layer organization in zebrafish". In: *Nature cell biology* 10.4, pp. 429–436.

Kruger, Philipp et al. (Mar. 2015). "Neutrophils: Between Host Defence, Immune Modulation, and Tissue Injury". In: *PLoS pathogens* 11.3, e1004651–23.

Kruse, Karsten et al. (2005). "Generic theory of active polar gels: a paradigm for cytoskeletal dynamics". In: *The European Physical Journal E* 16.1, pp. 5–16.

Kurisu, Shusaku and Tadaomi Takenawa (2009). "The WASP and WAVE family proteins." In: *Genome biology* 10.6, pp. 226–9.

Kurochkina, Natalya and Udayan Guha (June 2012). "SH3 domains: modules of protein–protein interactions". In: *Biophysical reviews* 5.1, pp. 29–39.

Kurten, R C, D L Cadena, and G N Gill (May 1996). "Enhanced degradation of EGF receptors by a sorting nexin, SNX1." In: *Science* 272.5264, pp. 1008–1010.

Ladoux, Benoit and René-Marc Mège (2017). "Mechanobiology of collective cell behaviours". In: *Nature reviews Molecular cell biology* 18.12, pp. 743–757.

Lämmermann, Tim and Michael Sixt (2009). "Mechanical modes of 'amoeboid'cell migration". In: *Current opinion in cell biology* 21.5, pp. 636–644.

Le Roux, Anabel-Lise et al. (2019). "The plasma membrane as a mechanochemical transducer". In: *Philosophical Transactions of the Royal Society B* 374.1779, p. 20180221.

Lee, Chunghee et al. (2000). "Inhibition of phospholipase D by amphiphysins". In: *Journal of Biological Chemistry* 275.25, pp. 18751–18758.

Lehman, Heather K and Brahm H Segal (June 2020). "The role of neutrophils in host defense and disease". In: *Journal of Allergy and Clinical Immunology* 145.6, pp. 1535–1544.

Leithner, Alexander et al. (2016). "Diversified actin protrusions promote environmental exploration but are dispensable for locomotion of leukocytes". In: *Nature cell biology* 18.11, pp. 1253–1259.

Li, Ang et al. (2011). "Rac1 drives melanoblast organization during mouse development by orchestrating pseudopod-driven motility and cell-cycle progression". In: *Developmental cell* 21.4, pp. 722–734.

Li, Lushen et al. (2016). "The SH3 domain distinguishes the role of I-BAR proteins IRTKS and MIM in chemotactic response to serum". In: *Biochemical and biophysical research communications* 479.4, pp. 787–792.

Liu, Suxuan et al. (2015a). "F-BAR family proteins, emerging regulators for cell membrane dynamic changes—from structure to human diseases". In: *Journal of hematology & oncology* 8.1, p. 47.

Liu, Yan-Jun et al. (2015b). "Confinement and low adhesion induce fast amoeboid migration of slow mesenchymal cells". In: *Cell* 160.4, pp. 659–672.

Liu, Yin et al. (2012). "Constitutively active ezrin increases membrane tension, slows migration, and impedes endothelial transmigration of lymphocytes in vivo in mice". In: *Blood, The Journal of the American Society of Hematology* 119.2, pp. 445–453.

Liu, Yunhao et al. (2005). "Mislocalization or reduced expression of Arf GTPase-activating protein ASAP1 inhibits cell spreading and migration by influencing Arf1 GTPase cycling". In: *Journal of Biological Chemistry* 280.10, pp. 8884–8892.

Lopez-Guerrero, Aida M et al. (Apr. 2020). "RAC1-Dependent ORAI1 Translocation to the Leading Edge Supports Lamellipodia Formation and Directional Persistence." In: *Scientific Reports* 10.1, pp. 6580–18.

Lorentzen, Anna et al. (2011). "An ezrin-rich, rigid uropod-like structure directs movement of amoeboid blebbing cells". In: *Journal of cell science* 124.8, pp. 1256–1267.

Lou, Hsin-Ya et al. (2019). "Membrane curvature underlies actin reorganization in response to nanoscale surface topography". In: *Proceedings of the National Academy of Sciences* 116.46, pp. 23143–23151.

Low, Boon Chuan et al. (2014). "YAP/TAZ as mechanosensors and mechanotransducers in regulating organ size and tumor growth". In: *FEBS letters* 588.16, pp. 2663–2670.

Ma, Maggie P C and Megan Chircop (Sept. 2012). "SNX9, SNX18 and SNX33 are required for progression through and completion of mitosis." In: *Journal of Cell Science* 125.Pt 18, pp. 4372–4382.

Machesky, Laura M and Robert H Insall (1998). "Scar1 and the related Wiskott–Aldrich syndrome protein, WASP, regulate the actin cytoskeleton through the Arp2/3 complex". In: *Current biology* 8.25, pp. 1347–1356.

Masters, Thomas A et al. (2013). "Plasma membrane tension orchestrates membrane trafficking, cytoskeletal remodeling, and biochemical signaling during phagocytosis". In: *Proceedings of the National Academy of Sciences* 110.29, pp. 11875–11880.

Mattila, Pieta K and Pekka Lappalainen (2008). "Filopodia: molecular architecture and cellular functions". In: *Nature reviews Molecular cell biology* 9.6, pp. 446–454.

Mattila, Pieta K et al. (2007). "Missing-in-metastasis and IRSp53 deform PI (4, 5) P2-rich membranes by an inverse BAR domain–like mechanism". In: *The Journal of cell biology* 176.7, pp. 953–964.

Mayer, Mirjam, Guillaume Salbreux, and Stephan W Grill (2012). "Biophysics of cell developmental processes: a lasercutter's perspective". In: *Comprehensive Biophysics* 7, pp. 194–207.

McMahon, Harvey T and Emmanuel Boucrot (2015). "Membrane curvature at a glance". In: *Journal of cell science* 128.6, pp. 1065–1070.

McMahon, Harvey T and Jennifer L Gallop (2005). "Membrane curvature and mechanisms of dynamic cell membrane remodelling". In: *Nature* 438.7068, pp. 590–596.

Meinecke, Michael et al. (Mar. 2013). "Cooperative recruitment of dynamin and BIN/amphiphysin/Rvs (BAR) domain-containing proteins leads to GTP-dependent membrane scission." In: *The Journal of biological chemistry* 288.9, pp. 6651–6661.

Mendoza, Michelle C et al. (Mar. 2011). "ERK-MAPK Drives Lamellipodia Protrusion by Activating the WAVE2 Regulatory Complex". In: *Molecular Cell* 41.6, pp. 661–671.

Miermont, Agnes et al. (2019). "Quantitative screening of the effects of hyper-osmotic stress on cancer cells cultured in 2-or 3-dimensional settings". In: *Scientific reports* 9.1, pp. 1–10.

Miki, H et al. (Dec. 2000a). "IRSp53 is an essential intermediate between Rac and WAVE in the regulation of membrane ruffling." In: *Nature* 408.6813, pp. 732–735.

Miki, Hiroaki et al. (2000b). "IRSp53 is an essential intermediate between Rac and WAVE in the regulation of membrane ruffling". In: *Nature* 408.6813, pp. 732–735.

Millard, Thomas H et al. (2005). "Structural basis of filopodia formation induced by the IRSp53/MIM homology domain of human IRSp53". In: *The EMBO journal* 24.2, pp. 240–250.

Mim, Carsten and Vinzenz M Unger (2012). "Membrane curvature and its generation by BAR proteins". In: *Trends in biochemical sciences* 37.12, pp. 526–533.

Min, Lingqiang et al. (2015). "Overexpression of Ras-GTPase-activating protein SH3 domain-binding protein 1 correlates with poor prognosis in gastric cancer patients". In: *Histopathology* 67.5, pp. 677–688.

Mogilner, Alex and George Oster (2003). "Polymer motors: pushing out the front and pulling up the back". In: *Current biology* 13.18, R721–R733.

Mogilner, Alexander and George Oster (1996). "Cell motility driven by actin polymerization". In: *Biophysical journal* 71.6, pp. 3030–3045.

Mondal, Samsuzzoha et al. (2020). "Endophilin recruitment drives membrane curvature generation through coincidence detection of GPCR loop interactions and negative lipid charge". In: *Journal of Biological Chemistry*, jbc–RA120.

Mueller, Jan et al. (2017). "Load adaptation of lamellipodial actin networks". In: *Cell* 171.1, pp. 188–200.

Müller, Daniel J and Yves F Dufrêne (2011). "Atomic force microscopy: a nanoscopic window on the cell surface". In: *Trends in cell biology* 21.8, pp. 461–469.

Müller, T et al. (2010). "ASAP1 promotes tumor cell motility and invasiveness, stimulates metastasis formation in vivo, and correlates with poor survival in colorectal cancer patients". In: *Oncogene* 29.16, pp. 2393–2403.

Mygind, Kasper J et al. (May 2018). "Sorting nexin 9 (SNX9) regulates levels of the transmembrane ADAM9 at the cell surface". In: *Journal of Biological Chemistry* 293.21, pp. 8077–8088.

Niles, Brad J et al. (2012). "Plasma membrane recruitment and activation of the AGC kinase Ypk1 is mediated by target of rapamycin complex 2 (TORC2) and its effector proteins Slm1 and Slm2". In: *Proceedings of the National Academy of Sciences* 109.5, pp. 1536–1541.

Oreopoulos, John and Christopher M Yip (2009a). "Combinatorial microscopy for the study of protein–membrane interactions in supported lipid bilayers: Order parameter measurements by combined polarized TIRFM/AFM". In: *Journal of structural biology* 168.1, pp. 21–36.

— (2009b). "Probing membrane order and topography in supported lipid bilayers by combined polarized total internal reflection fluorescence-atomic force microscopy". In: *Biophysical journal* 96.5, pp. 1970–1984.

Oreopoulos, John et al. (2010). "Peptide-induced domain formation in supported lipid bilayers: direct evidence by combined atomic force and polarized total internal reflection fluorescence microscopy". In: *Biophysical journal* 98.5, pp. 815–823.

Paluch, Ewa and Carl-Philipp Heisenberg (2009). "Biology and physics of cell shape changes in development". In: *Current Biology* 19.17, R790–R799.

Paluch, Ewa K, Irene M Aspalter, and Michael Sixt (2016). "Focal adhesion–independent cell migration". In: *Annual review of cell and developmental biology* 32, pp. 469–490.

Paluch, Ewa K and Erez Raz (2013). "The role and regulation of blebs in cell migration". In: *Current opinion in cell biology* 25.5, pp. 582–590.

Papalazarou, Vassilis and Laura M Machesky (Feb. 2021). "The cell pushes back: The Arp2/3 complex is a key orchestrator of cellular responses to environmental forces". In: *Current Opinion in Cell Biology* 68, pp. 37–44.

Parrini, Maria Carla et al. (2011). "SH3BP1, an exocyst-associated RhoGAP, inactivates Rac1 at the front to drive cell motility". In: *Molecular cell* 42.5, pp. 650–661.

Peter, Brian J et al. (2004). "BAR domains as sensors of membrane curvature: the amphiphysin BAR structure". In: *Science* 303.5657, pp. 495–499.

Petrie, Ryan J and Kenneth M Yamada (2012). "At the leading edge of three-dimensional cell migration". In: *Journal of cell science* 125.24, pp. 5917–5926.

Petrie, Ryan J et al. (2012). "Nonpolarized signaling reveals two distinct modes of 3D cell migration". In: *Journal of Cell Biology* 197.3, pp. 439–455.

Pinot, Mathieu et al. (2014). "Polyunsaturated phospholipids facilitate membrane deformation and fission by endocytic proteins". In: *Science* 345.6197, pp. 693–697.

Pipathsouk, Anne et al. (2019). "WAVE complex self-organization templates lamellipodial formation". In: *BioRxiv*, p. 836585.

Plutoni, Cédric et al. (2019). "Misshapen coordinates protrusion restriction and actomyosin contractility during collective cell migration". In: *Nature communications* 10.1, pp. 1–16.

Pollard, Thomas D (June 2007). "Regulation of Actin Filament Assembly by Arp2/3 Complex and Formins". In: *Annual Review of Biophysics and Biomolecular Structure* 36.1, pp. 451–477.

— (2016). "Actin and actin-binding proteins". In: *Cold Spring Harbor perspectives in biology* 8.8, a018226.

Poulsen, Lisbeth Rosager, RL López-Marqués, and MG Palmgren (2008). "Flippases: still more questions than answers". In: *Cellular and molecular life sciences* 65.20, p. 3119.

Prevedel, Robert et al. (2019). "Brillouin microscopy: an emerging tool for mechanobiology". In: *Nature methods* 16.10, pp. 969–977.

Raduwan, Hamidah et al. (2020). "RhoGAP RGA-8 supports morphogenesis in C. elegans by polarizing epithelia". In: *Biology open* 9.11.

Raftopoulou, Myrto and Alan Hall (2004). "Cell migration: Rho GTPases lead the way". In: *Developmental biology* 265.1, pp. 23–32.

Raucher, Drazen and Michael P Sheetz (2000). "Cell spreading and lamellipodial extension rate is regulated by membrane tension". In: *The Journal of cell biology* 148.1, pp. 127–136.

Razinia, Ziba et al. (Nov. 2017). "Stiffness-dependent motility and proliferation uncoupled by deletion of CD44". In: *Scientific Reports*, pp. 1–10.

Ren, Chunguang et al. (2019). "Leukocyte cytoskeleton polarization is initiated by plasma membrane curvature from cell attachment". In: *Developmental cell* 49.2, pp. 206–219.

Renkawitz, Jamp x000F6 rg et al. (Mar. 2019). "Nuclear positioning facilitates amoeboid migration along the path of least resistance". In: *Nature*, pp. 1–29.

Renkawitz, Jörg et al. (2018). *Micro-engineered "pillar forests" to study cell migration in complex but controlled 3D environments*. 1st ed. Vol. 147. Elsevier Inc.

Reversat, Anne et al. (2020). "Cellular locomotion using environmental topography". In: *Nature*, pp. 1–4.

Ridley, Anne J et al. (2003). "Cell migration: integrating signals from front to back". In: *Science* 302.5651, pp. 1704–1709.

Ridone, Pietro, Massimo Vassalli, and Boris Martinac (2019). "Piezo1 mechanosensitive channels: what are they and why are they important". In: *Biophysical reviews*, pp. 1–11.

Riggi, Margot et al. (2018). "Decrease in plasma membrane tension triggers PtdIns (4, 5) P 2 phase separation to inactivate TORC2". In: *Nature cell biology* 20.9, pp. 1043–1051.

Roberts, Rhiannon and Maurice Hallett (Mar. 2019). "Neutrophil Cell Shape Change: Mechanism and Signalling during Cell Spreading and Phagocytosis". In: *International Journal of Molecular Sciences* 20.6, pp. 1383–15.

Roca-Cusachs, Pere, Vito Conte, and Xavier Trepat (2017). "Quantifying forces in cell biology". In: *Nature cell biology* 19.7, pp. 742–751.

Roca-Cusachs, Pere et al. (Apr. 2013). "Integrin-dependent force transmission to the extracellular matrix by α-actinin triggers adhesion maturation." In: *Proceedings of the National Academy of Sciences of the United States of America* 110.15, E1361–70.

Rocca, Daniel L et al. (Feb. 2008). "Inhibition of Arp2/3-mediated actin polymerization by PICK1 regulates neuronal morphology and AMPA receptor endocytosis". In: *Nature Cell Biology* 10.3, pp. 259–271.

Rossy, Jérémie et al. (2007). "Ezrin/moesin in motile Walker 256 carcinosarcoma cells: signal-dependent relocalization and role in migration". In: *Experimental cell research* 313.6, pp. 1106–1120.

Ruprecht, Verena et al. (2015). "Cortical contractility triggers a stochastic switch to fast amoeboid cell motility". In: *Cell* 160.4, pp. 673–685.

Saarikangas, Juha et al. (2008). "ABBA regulates plasma-membrane and actin dynamics to promote radial glia extension". In: *Journal of cell science* 121.9, pp. 1444–1454.

Saarikangas, Juha et al. (2009). "Molecular mechanisms of membrane deformation by I-BAR domain proteins". In: *Current biology* 19.2, pp. 95–107.

Saci, Abdelhafid, Lewis C Cantley, and Christopher L Carpenter (2011). "Rac1 regulates the activity of mTORC1 and mTORC2 and controls cellular size". In: *Molecular cell* 42.1, pp. 50–61.

Saengsawang, Witchuda et al. (2012). "The F-BAR protein CIP4 inhibits neurite formation by producing lamellipodial protrusions". In: *Current Biology* 22.6, pp. 494–501.

Saha, Suvrajit, Tamas L Nagy, and Orion D Weiner (Apr. 2018). "Joining forces: crosstalk between biochemical signalling and physical forces orchestrates cellular polarity and dynamics". In: *Philosophical Transactions of the Royal Society B: Biological Sciences* 373.1747, pp. 20170145–9.

Salbreux, Guillaume, Guillaume Charras, and Ewa Paluch (2012). "Actin cortex mechanics and cellular morphogenesis". In: *Trends in cell biology* 22.10, pp. 536–545.

Sanjana, Neville E, Ophir Shalem, and Feng Zhang (July 2014). "Improved vectors and genome-wide libraries for CRISPR screening". In: *Nature Methods*, pp. 1–2.

Schlam, Daniel et al. (2015). "Phosphoinositide 3-kinase enables phagocytosis of large particles by terminating actin assembly through Rac/Cdc42 GTPase-activating proteins". In: *Nature communications* 6.1, pp. 1–12.

Schöbel, Susanne et al. (May 2008). "A Novel Sorting Nexin Modulates Endocytic Trafficking and α-Secretase Cleavage of the Amyloid Precursor Protein". In: *Journal of Biological Chemistry* 283.21, pp. 14257–14268.

Sens, Pierre and Julie Plastino (July 2015). "Membrane tension and cytoskeleton organization in cell motility." In: *Journal of physics. Condensed matter : an Institute of Physics journal* 27.27, p. 273103.

Shah, Enas Abu and Kinneret Keren (2013). "Mechanical forces and feedbacks in cell motility". In: *Current opinion in cell biology* 25.5, pp. 550–557.

Sharma, Sonia et al. (July 2013). "An siRNA screen for NFAT activation identifies septins as coordinators of store-operated Ca2+ entry". In: *Nature*, pp. 1–7.

Shi, Zheng et al. (2018). "Cell membranes resist flow". In: *Cell* 175.7, pp. 1769–1779.

Shibue, Tsukasa et al. (2012). "The outgrowth of micrometastases is enabled by the formation of filopodium-like protrusions". In: *Cancer discovery* 2.8, pp. 706–721.

Simionescu-Bankston, Adriana et al. (2013). "The N-BAR domain protein, Bin3, regulates Rac1-and Cdc42-dependent processes in myogenesis". In: *Developmental biology* 382.1, pp. 160–171.

Simunovic, Mijo and Gregory A Voth (2015). "Membrane tension controls the assembly of curvature-generating proteins". In: *Nature communications* 6.1, pp. 1–8.

Simunovic, Mijo et al. (Oct. 2019). "Curving Cells Inside and Out: Roles of BAR Domain Proteins in Membrane Shaping and Its Cellular Implications". In: *Annual Review of Cell and Developmental Biology* 35.1, pp. 111–129.

Sinha, Bidisha et al. (2011). "Cells respond to mechanical stress by rapid disassembly of caveolae". In: *Cell* 144.3, pp. 402–413.

Sitarska, Ewa and Alba Diz-Muñoz (2020). "Pay attention to membrane tension: Mechanobiology of the cell surface". In: *Current Opinion in Cell Biology* 66, pp. 11–18.

Smith, Alyson S et al. (2018). "Myosin IIA interacts with the spectrin-actin membrane skeleton to control red blood cell membrane curvature and deformability". In: *Proceedings of the National Academy of Sciences* 115.19, E4377–E4385.

Sommer, Christoph et al. (2011). "Ilastik: Interactive learning and segmentation toolkit". In: *2011 IEEE international symposium on biomedical imaging: From nano to macro*. IEEE, pp. 230–233.

Sorre, Benoît et al. (2012). "Nature of curvature coupling of amphiphysin with membranes depends on its bound density". In: *Proceedings of the National Academy of Sciences* 109.1, pp. 173–178.

Spanjaard, Emma and Johan de Rooij (2013). "Mechanotransduction: vinculin provides stability when tension rises". In: *Current Biology* 23.4, R159–R161.

Stanishneva-Konovalova, Tatiana B et al. (Sept. 2016). "Coordinated autoinhibition of F-BAR domain membrane binding and WASp activation by Nervous Wreck." In: *Proceedings of the National Academy of Sciences of the United States of America* 113.38, E5552–61.

Stewart, Martin P et al. (2011). "Hydrostatic pressure and the actomyosin cortex drive mitotic cell rounding". In: *Nature* 469.7329, pp. 226–230.

Suetsugu, Shiro, Shusaku Kurisu, and Tadaomi Takenawa (2014). "Dynamic shaping of cellular membranes by phospholipids and membrane-deforming proteins". In: *Physiological reviews* 94.4, pp. 1219–1248.

Suetsugu, Shiro, Kiminori Toyooka, and Yosuke Senju (2010). "Subcellular membrane curvature mediated by the BAR domain superfamily proteins". In: *Seminars in cell & developmental biology*. Vol. 21. 4. Elsevier, pp. 340–349.

Sun, C et al. (June 2010). "ADAM15 regulates endothelial permeability and neutrophil migration via Src/ERK1/2 signalling". In: *Cardiovascular Research* 87.2, pp. 348–355.

Sun, Dapeng et al. (Oct. 2020). "The cryo-EM structure of the SNXâ€"BAR Mvp1 tetramer". In: *Nature Communications*, pp. 1–10.

Sund, Susan E, Joel A Swanson, and Daniel Axelrod (1999). "Cell membrane orientation visualized by polarized total internal reflection fluorescence". In: *Biophysical journal* 77.4, pp. 2266–2283.

Svitkina, Tatyana M (2020). "Actin Cell Cortex: Structure and Molecular Organization". In: *Trends in Cell Biology*.

Svitkina, Tatyana M et al. (1997). "Analysis of the actin–myosin II system in fish epidermal keratocytes: mechanism of cell body translocation". In: *Journal of Cell Biology* 139.2, pp. 397–415.

Tan, Yinfei et al. (2016). "Appl1 and Appl2 are expendable for mouse development but are essential for HGF-induced Akt activation and migration in mouse embryonic fibroblasts". In: *Journal of cellular physiology* 231.5, pp. 1142–1150.

Tao, Yiming et al. (2016). "SH3-domain binding protein 1 in the tumor microenvironment promotes hepatocellular carcinoma metastasis through WAVE2 pathway". In: *Oncotarget* 7.14, p. 18356.

Tarricone, C et al. (2001). "The structural basis of Arfaptin-mediated cross-talk between Rac and Arf signalling pathways". In: *Nature* 411.6834, pp. 215–219.

Tata, Aleksandra et al. (2014). "An image-based RNAi screen identifies SH3BP1 as a key effector of Semaphorin 3E–PlexinD1 signaling". In: *Journal of Cell Biology* 205.4, pp. 573–590.

Teasdale, Rohan D and Brett M Collins (Dec. 2011). "Insights into the PX (phox-homology) domain and SNX (sorting nexin) protein families: structures, functions and roles in disease". In: *Biochemical Journal* 441.1, pp. 39–59.

Tsai, Feng-Chiao and Tobias Meyer (May 2012). "Ca2+ Pulses Control Local Cycles of Lamellipodia Retraction and Adhesion along the Front of Migrating Cells". In: *Current Biology* 22.9, pp. 837–842.

Tsai, Feng-Chiao et al. (Jan. 2014). "A polarized Ca2+, diacylglycerol and STIM1 signalling system regulates directed cell migration". In: *Nature Cell Biology* 16.2, pp. 133–144.

Tsai, Tony Y-C et al. (2019). "Efficient front-rear coupling in neutrophil chemotaxis by dynamic myosin II localization". In: *Developmental cell* 49.2, pp. 189–205.

Tsuboi, Shigeru et al. (2009). "FBP17 mediates a common molecular step in the formation of podosomes and phagocytic cups in macrophages". In: *Journal of Biological Chemistry* 284.13, pp. 8548–8556.

Tsujita, Kazuya, Tadaomi Takenawa, and Toshiki Itoh (2015). "Feedback regulation between plasma membrane tension and membrane-bending proteins organizes cell polarity during leading edge formation". In: *Nature cell biology* 17.6, pp. 749–758.

Tsujita, Kazuya et al. (2006). "Coordination between the actin cytoskeleton and membrane deformation by a novel membrane tubulation domain of PCH proteins is involved in endocytosis". In: *The Journal of cell biology* 172.2, pp. 269–279.

Ukken, Fiona P et al. (2016). "BAR-SH3 sorting nexins are conserved interacting proteins of Nervous wreck that organize synapses and promote neurotransmission". In: *Journal of cell science* 129.1, pp. 166–177.

Unwin, Nigel (2005). "Refined structure of the nicotinic acetylcholine receptor at 4 Å resolution". In: *Journal of molecular biology* 346.4, pp. 967–989.

Van Helvert, Sjoerd, Cornelis Storm, and Peter Friedl (2018). "Mechanoreciprocity in cell migration". In: *Nature cell biology* 20.1, p. 8.

Vidal-Quadras, Maite et al. (2017). "Endocytic turnover of Rab8 controls cell polarization". In: *Journal of Cell Science* 130.6, pp. 1147–1157.

Vining, Kyle H and David J Mooney (2017). "Mechanical forces direct stem cell behaviour in development and regeneration". In: *Nature reviews Molecular cell biology* 18.12, pp. 728–742.

Volz, Julia et al. (2020). "BIN2 orchestrates platelet calcium signaling in thrombosis and thrombo-inflammation". In: *The Journal of Clinical Investigation* 130.11, pp. 6064–6079.

Wakayama, Yuki et al. (2015). "Cdc42 mediates Bmp-induced sprouting angiogenesis through Fmnl3-driven assembly of endothelial filopodia in zebrafish". In: *Developmental cell* 32.1, pp. 109–122.

Wang, Jack T H et al. (Oct. 2010). "The SNX-PX-BAR Family in Macropinocytosis: The Regulation of Macropinosome Formation by SNX-PX-BAR Proteins". In: *PLoS ONE* 5.10, e13763–13.

Wang, Jing et al. (2012). "The Arf GAP ASAP1 provides a platform to regulate Arf4- and Rab11–Rab8-mediated ciliary receptor targeting". In: *The EMBO journal* 31.20, pp. 4057–4071.

Wang, Jingjing et al. (2018). "SH3BP1-induced Rac-Wave2 pathway activation regulates cervical cancer cell migration, invasion, and chemoresistance to cisplatin". In: *Journal of cellular biochemistry* 119.2, pp. 1733–1745.

Wang, Qi et al. (2009). "Molecular mechanism of membrane constriction and tubulation mediated by the F-BAR protein Pacsin/Syndapin". In: *Proceedings of the National Academy of Sciences* 106.31, pp. 12700–12705.

Weering, Jan R T van, Paul Verkade, and Peter J Cullen (June 2010). "SNXâ€"BAR proteins in phosphoinositide-mediated, tubular-based endosomal sorting". In: *Seminars in Cell and Developmental Biology* 21.4, pp. 371–380.

Wei, Chaoliang et al. (Feb. 2009). "Calcium flickers steer cell migration". In: *Nature*, pp. 1–6.

Weiner, O D et al. (June 1999). "Spatial control of actin polymerization during neutrophil chemotaxis." In: *Nature Cell Biology* 1.2, pp. 75–81.

Weiner, Orion D et al. (2002). "A PtdInsP 3-and Rho GTPase-mediated positive feedback loop regulates neutrophil polarity". In: *Nature cell biology* 4.7, pp. 509–513.

Weiner, Orion D et al. (2006). "Hem-1 complexes are essential for Rac activation, actin polymerization, and myosin regulation during neutrophil chemotaxis". In: *PLoS Biol* 4.2, e38.

Weiner, Orion D et al. (2007). "An actin-based wave generator organizes cell motility". In: *PLoS Biol* 5.9, e221.

Welf, Erik S et al. (2020). "Actin-membrane release initiates cell protrusions". In: *Developmental Cell*.

Whitacre, Johanna L et al. (2001). "Generation of an isogenic collection of yeast actin mutants and identification of three interrelated phenotypes". In: *Genetics* 157.2, pp. 533–543.

Wood, William et al. (2002). "Wound healing recapitulates morphogenesis in Drosophila embryos". In: *Nature cell biology* 4.11, pp. 907–912.

Woodham, Emma F and Laura M Machesky (2014). "Polarised cell migration: intrinsic and extrinsic drivers". In: *Current opinion in cell biology* 30, pp. 25–32.

Worby, Carolyn A and Jack E Dixon (Dec. 2002). "Sorting out the cellular functions of sorting nexins". In: *Nature Reviews Molecular Cell Biology* 3.12, pp. 919–931.

Yamada, Kenneth M and Michael Sixt (Nov. 2019). "Mechanisms of 3D cell migration". In: *Nature Reviews Molecular Cell Biology*, pp. 1–15.

Yamamoto, Hayato et al. (2011). "Requirement for FBP17 in invadopodia formation by invasive bladder tumor cells". In: *The Journal of urology* 185.5, pp. 1930–1938.

Yang, Hee Won, Sean R Collins, and Tobias Meyer (2016). "Locally excitable Cdc42 signals steer cells during chemotaxis". In: *Nature cell biology* 18.2, pp. 191–201.

Yang, Jian et al. (Mar. 2019). "The emerging role of sorting nexins in cardiovascular diseases". In: *Clinical Science* 133.5, pp. 723–737.

Yip, Ai Kia, Keng-Hwee Chiam, and Paul Matsudaira (2015). "Traction stress analysis and modeling reveal that amoeboid migration in confined spaces is accompanied by expansive forces and requires the structural integrity of the membrane–cortex interactions". In: *Integrative biology* 7.10, pp. 1196–1211.

Yoneda, M and K Dan (1972). "Tension at the surface of the dividing sea-urchin egg". In: *Journal of Experimental Biology* 57.3, pp. 575–587.

Yumura, Shigehiko, Hiroshi Mori, and Yoshio Fukui (1984). "Localization of actin and myosin for the study of ameboid movement in Dictyostelium using improved immunofluorescence." In: *The Journal of cell biology* 99.3, pp. 894–899.

Zago, Giulia et al. (2019). "A family affair: A Ral-exocyst-centered network links Ras, Rac, Rho signaling to control cell migration". In: *Small GTPases* 10.5, pp. 323–330.

Zhang, Hongfeng et al. (Mar. 2018). "The Retromer Complex and Sorting Nexins in Neurodegenerative Diseases". In: *Frontiers in Aging Neuroscience* 10, pp. 1337–11.

Zhang, Juan et al. (Aug. 2009). "Sorting nexin 33 induces mammalian cell micronucleated phenotype and actin polymerization by interacting with Wiskott-Aldrich syndrome protein." In: *Journal of Biological Chemistry* 284.32, pp. 21659–21669.

Zimmerberg, Joshua and Michael M Kozlov (2006). "How proteins produce cellular membrane curvature". In: *Nature reviews Molecular cell biology* 7.1, pp. 9–19.

Zou, Wenying et al. (2012). "Store-operated Ca2+ entry (SOCE) plays a role in the polarization of neutrophil-like HL-60 cells by regulating the activation of Akt, Src, and Rho family GTPases." In: *Cellular physiology and biochemistry : international journal of experimental cellular physiology, biochemistry, and pharmacology* 30.1, pp. 221–237.